UNIVERSITÉ DE GENÈVE
Département de physique
nucléaire et corpusculaire

FACULTÉ DES SCIENCES
Professeur Maria Novella Kienzle Focacci

Study of the $K^0_S K^0_S$ Final State and the K^0_S Inclusive Production in Two-Photon Collisions with the L3 Detector at LEP

THÈSE

présentée à la Faculté des Sciences de l'Université de Genève
pour obtenir le grade de Docteur ès Sciences, mention physique

par

Saverio BRACCINI

de Arezzo, Italie

Thèse N° 3255

GENÈVE
Atelier d'impression de la Section de physique
2001

L'aspetto più entusiasmante della scienza
è che essa incoraggia l'uomo
a insistere nei suoi sogni.

Guglielmo Marconi

Remerciements, Acknowledgments, Ringraziamenti

J'aimerais d'abord remercier sincèrement le directeur de ce travail de thèse, M^{me} le Professeur Maria Novella Focacci-Kienzle, pour le soutien et la confiance qu'elle m'a toujours temoignés et pour la liberté qu'elle m'a laissée dans mes recherches. Ses conseils et ses observations ont toujours été precieux.

Je remercie sincèrement les Professeurs C. Amsler et A. Blondel pour avoir accepté de faire partie du jury de cette thèse, ainsi que pour leurs commentaires constructifs.

Je remercie les Professeurs P. Extermann et M. Bourquin pour m'avoir accueilli dans leur groupe de recherche et pour m'avoir toujours soutenu dans mes initiatives.

Un grand merci va au Dr. J. H. Field pour sa constante disponibilité et pour nos discussions très constructives et fondamentales dans la résolution de mes problèmes de physique.

Mes remerciements vont ensuite à tous les membres du groupe de Genève pour la sympathie et pour l'amitié qu'ils m'ont toujours montrées. Je garderai des souvenirs très profonds des moments de vie professionelle et personnelle que j'ai partagés avec P. Argentin, B. Burger, C. Cecchi, M. Chamizo, E. Delmeire, P. Emonet, D. Ferrere, L. Fredj, F. Muheim, D. Sciarrino et G. Susinno. Un merci particulier va à mon "fils" P. Achard, maintenant véritable papa, et à "monsieur ordinateur" P. Déglon pour le bon temps passé ensemble comme collègues au CERN et comme amis en dehors du travail. Je remercie mon "enfant" B. Echenard que j'ai eu le plaisir d'introduire dans les secrets de L3 et L. Malgeri dont je garderai toujours le souvenir pour sa disponibilité et sa compétence.

I would like to thank all the members of the L3 collaboration at CERN and, in particular, all the members of the two-photon analysis group. This thesis work would have never been possible without their help and their constructive remarks. I would like to thank my friend M. Wadhwa for the many fruitful discussions, for his kindness and for having introduced me to Indian culture. I would like to acknowledge the invaluable help of the online coordinators, Dr. J. J. Blaising and Prof. C. Luci, always precious to solve all the problems we faced with the TEC trigger, and of Prof. S. Gentile, analysis coordinator.

Vorrei ringraziare la Prof. A. M. Cartacci dell'Univrsità di Firenze che per prima mi ha avvicinato al mondo della fisica delle particelle elementari. Un caro pensiero va alla Prof. B. Monteleoni, recentemente scomparsa, la cui gentilezza e i cui insegnamenti rimarranno sempre vivi in me.

Vorrei ricordare tutti i miei amici con cui ho condiviso momenti indimenticabili e che mi hanno fatto sempre sentire il legame che ci unisce.

Il più grosso grazie, con tutto il cuore, va ai miei genitori che hanno sempre creduto in me e mi sono stati vicino nei momenti belli e nei momenti difficili. Senza di loro, in tutti i sensi, non sarei qui!

Contents

Chapter 1

Résumé

1.1 Introduction

L'étude des composants fondamentaux de la matière et des leurs interactions est le but de la physique des hautes énergies. Notre connaissance actuelle des particules élémentaires et de leurs interactions est incorporée dans un modèle, appelé Modèle Standard. Dans ce cadre, les particules élémentaires qui constituent la matière sont des fermions de spin 1/2, les quarks et les leptons. Ils interagissent par l'intérmediaire des bosons porteurs des forces fondamentales. Il existe quatre interactions fondamentales: les interactions forte, faible, électromagnétique et gravitationnelle. Les fermions se divisent en trois familles contenant deux quarks et deux leptons chacune. Les quarks ont des charges électriques fractionnaires, +2/3 ou -1/3, et interviennent dans toutes les interactions fondamentales. Les leptons ont des charges électriques entières, -1 ou 0, et ne participent pas aux interactions fortes. A chaque fermion correspond un antifermion avec une charge électrique et des nombres quantiques opposés. Dans le Modèle Standard, chaque interaction est interpretée par l'échange de bosons de jauge qui dérivent directement de la symétrie fondamentale du modèle $SU(3)\times SU(2)\times U(1)$. L'interaction forte est portée par huit gluons qui sont responsables de la formation des états liés de trois quarks, les baryons, ou d'un quark avec un antiquark, les mésons. La force électromagnétique est portée par un boson de jauge sans masse, le photon. L'interaction faible est portée par trois bosons de jauge massifs (W^+, W^- et Z) qui ont été observés pour la première fois au collisionneur

SPS au CERN en 1983.

Le collisionneur LEP (Large Electron Positron collider) a été construit au CERN afin de tester la validité du Modèle Standard avec une très grande précision. Depuis 1989, les quatre expériences ALEPH, DELPHI, L3 et OPAL ont etudié des collisions électron-positron à des énergies du centre de masse autour de la masse du boson Z. La production du boson Z et l'étude de ses différents modes de désintégration ont permis d'établir l'existence de seulement trois familles de fermions "légers". Depuis 1996, l'énergie du centre de masse a depassé le seuil de production de couples W^+W^-. Le programme LEP s'est terminé en novembre 2000 après avoir atteint une énergie du centre de masse de 208 GeV.

Bien que les équations de Maxwell interdisent les interactions d'ondes électromagnétiques entre elles, l'électrodynamique quantique prédit la possibilité d'interaction entre les photons. Selon le principe d'indétermination, un photon peut fluctuer en deux particules chargées et interagir ainsi avec un autre photon. Les électrons et les positrons qui circulent dans un synchrotron sont des sources de photons virtuels de haute énergie et peuvent être utilisés pour produire des interactions photon-photon. Le LEP est donc également un collisionneur de photons et les expériences au LEP peuvent étudier les collisions photon-photon à travers la réaction

$$e^+e^- \rightarrow e^+e^-X, \tag{1.1}$$

où l'état final X peut être un couple de leptons chargés, un couple baryon-antibaryon ou méson-antiméson, un état résonant ou un état à plusieurs hadrons.

A très hautes energies, le photon peut fluctuer dans un couple quark-antiquark et la réaction $\gamma\gamma \rightarrow$hadrons peut être utilisée pour vérifier la validité des prédictions de la théorie des interactions fortes, la Chromodynamique Quantique (QCD). En particulier, l'étude de la production inclusive de particules comme le méson K^0_S dans la réaction $\gamma\gamma \rightarrow$hadrons permet d'obtenir des informations importantes tant dans la région non-perturbative que dans la région perturbative de la QCD.

La formation d'états résonants dans les collisions photon-photon permet l'étude des états mésoniques dans un environnement expérimental très favorable puisque seuls les produits de la désintégration de l'état résonant sont détectés. Comme le photon se couple à la charge électrique, la fonction d'onde des quarks dans le méson et les effets de mélange peuvent être mis en évidence. Selon la QCD, les gluons

peuvent interagir entre eux et il peut exister des états liés contenant uniquement des gluons. Ces états sont appelés "glueballs" et, jusqu'à présent, il n'existe pas de preuve expérimentale de leur existence. Par contre, des candidats glueball ont été répérés dans les interactions hadroniques. Comme les photons ne se couplent pas directement aux gluons, les glueballs ne se couplent que très faiblement aux deux photons. Les spectres d'états résonants formés dans la collision de deux photons vont donc être dominés par la formation d'états mésoniques et, en même temps, caractérisés par l'absence des candidats glueballs. L'étude de la formation des états résonants dans les collisions photon-photon joue donc un rôle important dans la recherche des glueballs.

Ce travail de thèse est structuré comme suit. Après une introduction générale dans le Chapitre 2, le Chapitre 3 contient une introduction à la physique des collisions photon-photon aux collisionneurs électron-positron. Le collisionneur LEP et l'expérience L3 sont présentés dans le Chapitre 4. Le Chapitre 5 est dedié au système de déclenchement de premier niveau pour les particules chargées qui a été une des nos responsabilités au sein de la Collaboration L3. Le Chapitre 6 décrit la reconstruction des traces chargées, des vertex primaires et secondaires ainsi que la mesure de la perte d'énergie par ionisation (dE/dx). Les deux derniers chapitres sont dédiés à deux analyses physiques sur les collisions photon-photon. Dans le Chapitre 7, l'étude de la production inclusive des mésons K^0_S est présentée. Le Chapitre 8 est dédié à l'état final $K^0_S K^0_S$ et à ses implications dans la recherche des glueballs.

1.2 Le collisionneur LEP

Le LEP est le plus grand collisionneur pour électrons et positrons qui ait jamais été construit. Sa circonférence est de 26.7 km et a été choisie aussi grande que possible, en tenant compte des contraintes imposées par la géologie et les coûts de construction, de façon à réduire la perte d'énergie due à la radiation synchrotron. L'énergie perdue par révolution est en effet proportionnelle à E^4/ρ où E est l'énergie du faisceau et ρ son rayon de courbure. L'anneau du LEP comporte huit sections droites et huit sections courbées. Chacune des huit sections courbées contient un ensemble de trente et une cellules magnétiques standards constituées de dipôles magnétiques et d'aimants quadripôlaires et sextupôlaires de focalisation. Dans la première phase du

LEP, un ensemble de 128 cavités radiofréquence (RF) de cuivre, alimentées par 16 klystrons de 1 MW fut utilisé pour l'accélération des faisceaux. Pour atteindre des énergies toujours plus élévées, les cavités radiofréquence de cuivre ont été remplacées progressivement par des cavités supraconductrices de niobium.

Pour la pré-accélération des électrons et des positrons, le LEP utilise des systèmes déjà existants. D'abord, les électrons et les positrons sont produits puis accélérés à 600 MeV dans l'injecteur linéaire du LEP, le LIL. Ces particules sont ensuites injectées dans l'accumulateur d'électrons et de positrons, l'EPA, qui les regroupe en paquets. Ces paquets sont ensuite injectés dans le Synchrotron à Proton (PS) et accélérés jusqu'à 3.5 GeV. Après injection dans le Super Synchrotron à Proton (SPS), ils sont accélérés à 22 GeV. Finalement, les paquets sont injectés dans l'anneau du LEP où ils sont accélérés jusqu'à l'énergie maximale.

1.3 Le detecteur L3

Le détecteur L3 (Figure 4.3) a été construit pour étudier les collisions e^+e^- jusqu'à 200 GeV dans le centre de masse avec, en particulier, une bonne résolution sur la mesure de l'énergie des électrons, des muons et des photons. Les détecteurs sont installés dans un aimant de 7800 tonnes fournissant un champ magnétique de 0.5 T.

Les détecteurs sont supportés par un tube d'acier de 32 m de long et 4.45 m de diamètre. Le tube est concentrique avec la ligne de faisceau et permet l'alignement de tous les détecteurs de L3 relativement aux faisceaux du LEP. Le spectromètre à muons est composé de trois couches de chambres concentriques autour du faisceau, montées sur l'extérieur du tube support. La partie centrale du tube support abrite les détecteurs internes, arrangés comme les éléments d'un tonneau autour du tuyau du faisceau et comme des éléments de bouchons dans les directions avant et arrière. Nous décrivons ici uniquement les sous-détecteurs qui sont importants pour notre étude, c'est à dire le détecteur de traces central, le calorimètre électromagnétique et le calorimètre hadronique.

1.3.1 Le détecteur de traces central

Le détecteur de traces central est constitué d'un détecteur de vertex au silicium, le SMD, et d'une chambre à fils à dérive, la TEC. L'ensemble est entouré de deux chambres proportionelles à géométrie cylindrique, les chambres Z. Dans les régions avant et arrière, où l'efficacité de la TEC est limitée par le petit nombre de fils touchés, deux plans de tubes à dérive, les FTC, viennent compléter le tout.

Le SMD (Figure 4.7) a été installé dans L3 en 1993 pour augmenter la précision de la reconstruction des traces et, en particulier, pour pouvoir effectuer la reconstruction des vertex secondaires produits par des mésons avec le quark "beauté". Le SMD est constitué de deux couches d'échelles au silicium. Il a une résolution de 8 μm dans le plan $r-\phi$ et de 14 μm dans le plan $r-z$. La couverture angulaire du SMD correspond à $21^\circ < \theta < 159^\circ$.

La TEC (Figure 4.8) est constituée de deux chambres à dérive concentriques de haute précision placées autour de la ligne du faisceau: la TEC interne, s'étend de 8.5 cm à 14.3 cm radialement et la TEC externe jusqu'à 45.7 cm. La TEC interne est divisée en 12 secteurs, ayant chacun 30 degrés de couverture dans l'angle azimuthal ϕ. La TEC externe est divisée en 24 secteurs, chacun avec une couverture de 15 degrés. La couverture angulaire de la TEC correspond à $25^\circ < \theta < 175^\circ$. Le gaz utilisé est un mélange de 80% de CO_2 avec 20% de $i-C_4H_{10}$.

Le volume de dérive est divisé en une région de dérive avec un faible champ électrique homogène et une région d'amplification avec un fort champ électrique. Les deux régions sont séparées par une grille de fils.

Chaque secteur contient respectivement 8 fils anodiques de la TEC interne et 54 de la TEC externe. Il y a trois types de fils d'anode:

- Les fils standard qui sont lus à une seule extrémité et fournissent une mesure précise dans le plan $r-\phi$.

- Les fils "Charge Division" (CD), lus de chaque côté, qui permettent une mesure de la coordonée z, en comparant l'amplitude des deux signaux.

- Les fils "Left-Right" (LR) qui permettent de résoudre l'ambiguité gauche-droite en lisant 5 fils de grille de chaque côté et en comparant les signaux induits par les ions positifs. Pour les particules chargées traversant la TEC interne et la TEC

externe, l'ambiguité gauche-droite peut également être résolue en associant les traces des deux chambres.

1.3.2 Le calorimètre électromagnétique

Le calorimètre électromagnétique (Figure 4.11) consiste en environ 11000 cristaux de BGO ($Bi_4Ge_3O_{12}$) et est composé d'un tonneau et de deux bouchons.

Les cristaux de BGO ont été choisis pour leur petite longueur de radiation (X_0 = 1.12 cm) permettant ainsi la construction d'un calorimètre très compact. Les cristaux sont de forme pyramidale tronquée d'une longueur de 24 cm ($\approx 22X_0$) et pointant vers la région d'interaction. Chaque cristal est lu par deux photodiodes placées sur sa face arrière.

La précision de la mesure d'énergie obtenue dans la région du tonneau est de 5% à 100 MeV et de 1.4% au dessus de 2 GeV. Pour des énergies au dessus de 1 GeV, la précision angulaire est de 0.5°.

La partie tonneau du calorimètre électromagnétique couvre une région d'angle polaire $42° < \theta < 138°$. La couverture angulaire des deux bouchons correspond à $12° < \theta < 38°$ pour la région avant et à $142° < \theta < 168°$ pour la région arrière.

1.3.3 Le calorimètre hadronique

Le calorimètre hadronique (Figure 4.13) est constitué d'un tonneau et d'un système avant-arrière couvrant 99.5 % de l'angle solide total.

Le calorimètre hadronique est constitué de plaques de 5 mm d'absorbeur d'uranium appauvri, intercalées avec des chambres à fils proportionnelles. Le gaz utilisé est un mélange de 80% d'Ar et 20% de CO_2.

Le tonneau du calorimètre hadronique couvre une région angulaire allant de 35° à 145° en θ. Il est formé de 9 anneaux de 16 modules chacun. Les bouchons du calorimètre hadronique couvrent les régions angulaires $5.5° < \theta < 35°$ et $145° < \theta < 174.5°$. Chaque bouchon est formé de trois anneaux, un anneau externe et deux anneaux internes. La résolution en énergie est

$$\frac{\sigma(E)}{E} = \left(\frac{55}{\sqrt{E}} + 5\right)\% \tag{1.2}$$

où E est mesurée en GeV.

1.3.4 Déclenchement et acquisition des données

A chaque croisement des faisceaux, les systèmes de déclenchement de L3 décident si l'événement doit être enregistré ou non. En cas de réponse positive, toutes les informations relatives à l'événement sont lues et transférées sur bande magnétique. Les système de déclenchement est composé de trois sous-systèmes de complexité croissante appelés niveau-un, niveau-deux et niveau-trois. Une telle configuration minimise les temps morts et fournit un taux d'événements acceptés de l'ordre de 2 Hz.

1.4 Le système de déclenchement de niveau-un pour les particules chargées

Le déclenchement pour les particules chargées analyse les signaux analogiques générés par la TEC. L'algorithme est basé sur la recherche de traces pointant vers le point d'interaction dans le plan normal à l'axe du faisceau. Dès que les traces sont répérées, on y recherche des couples de traces coplanaires. Un seul couple suffit pour une décision positive du système de déclenchement afin que l'événement soit gardé. Les événements de bruit de fond produits par les interactions entre le faisceau et le tube à vide ou entre le faisceau et le gaz résiduel sont caracterisés par la présence de traces de basse impulsion concentrées à petite distance de l'axe du faisceau. Pour cette raison, les secteurs de la TEC interne ne sont pas utilisés par ce système qui est basé uniquement sur les signaux des 14 fils "Left-Right" de chaque secteur externe. Ces fils sont distribués approximativement comme 1/R, entre R = 178 mm et R = 413 mm. Pour satisfaire les conditions temporelles imposées par le temps de dérive et par l'intervalle de temps entre les collisions, une technique parallèle, capable d'effectuer la procédure du déclenchement en moins d'une microseconde, est utilisée. Ce système de déclenchement a été conçu de façon que la plupart des paramètres puissent être ajustés par ordinateur selon les différentes conditions de bruit de fond de l'accélérateur. Les paramètres variables sont les suivants:

- les différents intervalles d'angles polaires des traces
- les différents intervalles d'impulsion transverse des traces

- le groupement des fils dans les sous-secteurs via les fonctions booléennes AND ou OR
- le nombre minimal de fils touchés afin qu'une trace soit considerée
- l'angle minimal d'acoplanarité pour la recherche des paires de traces.

A la fin de la période de prise de données de 1997, la haute luminosité de LEP produisait un taux important d'événements acceptés ayant pour conséquence un temps mort trop élévé. Afin de limiter le taux d'événements acceptés par ce système, plusieurs configurations ont été étudiées. Depuis 1998, une nouvelle configuration a été adoptée qui réduit le taux du déclenchement de 30% environ sans provoquer de perte en efficacité trop importante sur les canaux physiques.

1.5 Reconstruction des traces chargées, des vertex et mesure du dE/dx

Le détecteur de traces central est utilisé pour mesurer la position, l'impulsion et la perte spécifique d'énergie par ionisation des traces chargées. La reconstruction des traces s'effectue en recherchant d'abord les signaux produits dans le SMD et dans la TEC par une même particule chargée. Les quantités physiques de la particule dans le plan $r-\phi$ sont calculées a travers l'ajustement de sa trajectoire circulaire. Les quantités dans le plan $r-z$ sont ensuite calculées en utilisant les informations provenant des fils "Charge-Division", des chambres Z et du SMD.

Une fois que la position du vertex primaire d'interaction est déterminée (à l'aide d'environ 200 événements hadroniques consécutifs), la position des vertex secondaires peut être determinée. En particulier, les vertex formés par la désintégration $K^0_S \to \pi^+\pi^-$ peuvent être reconstruits. Les vertex secondaires sont repérés en déterminant l'intersection des trajectoires circulaires des traces de charges opposées dans le plan $r-\phi$. Un ajustement est ensuite effectué pour calculer les quantités dans le plan $r-z$ avec la contrainte du vertex secondaire.

La charge collectée par les fils anodiques de la TEC permet de mesurer la perte spécifique d'énergie par ionisation, appelée dE/dx. Pour chaque "hit" de chaque trace, la valeur de la charge collectée et mesurée par un flash ADC est multipliée

par $\sin\theta$ et divisée par une constante de calibration g_{wire} qui tient en compte les différences entre les fils de la TEC. Pour réduire les effets des fluctuations, le dE/dx est ensuite calculé comme la moyenne coupée à 80% de ces valeurs. La précision de la mesure du dE/dx est ensuite améliorée par des corrections qui tiennent compte des effets dus à la distance de dérive et à des asymétries géométriques. La résolution du dE/dx est de 9% environ. Le dE/dx peut être utilisé efficacement pour l'identification des particules chargées d'impulsion inférieure à 1 GeV.

1.6 La production inclusive de mésons K^0_S

1.6.1 Sélection des événements

Les événements produits par la réaction

$$e^+e^- \to e^+e^- \text{ hadrons} \tag{1.3}$$

sont sélectionnés selon les critères suivants:

- Six particules (pions chargés ou photons) au minimum doivent être détectées.
- L'énergie mesurée par le calorimètre électromagnétique doit être supérieure à 500 MeV et inférieure à 50 GeV. L'énergie mesurée par les calorimètres (électromagnétique et hadronique) doit être inférieure au 40% de l'énergie dans le centre de masse e^+e^-.
- Les événements avec des dépôts d'énergie dans le moniteur de luminosité supérieurs à 30 GeV sont exclus.
- La masse effective W_{vis}, calculée à partir des quadrivecteurs des photons et des pions chargés, doit être supérieure à 5 GeV.

Les mésons K^0_S sont sélectionnés dans l'ensemble des événements hadroniques produits dans les collisions de deux photons à l'aide de la reconstruction des vertex secondaires.

- La distance entre les vertex primaire et secondaire dans le plan $r-\phi$ doit être supérieure à 3 mm.

- L'angle entre la direction de vol et le vecteur impulsion totale des deux particules formant le vertex dans le plan $r - \phi$ doit être inférieur à 0.075 mrad.

Les données utilisées pour cette analyse ont été collectées par le détecteur L3 au LEP dans les années 1998 et 1999 pour des énergies du centre de masse e^+e^- entre 189 et 202 GeV. La luminosité intégrée totale est de 410 pb^{-1}. Avec les coupures précédemment décrites, 516540 événements sont sélectionnés.

1.6.2 Résultats

La section efficace de production des mésons K^0_S en fonction de l'impulsion transverse p_t et de la pseudorapidité $\eta = -\log[\tan(\theta/2)]$ est mesurée. Deux mesures sont effectuées, une pour $W_{\gamma\gamma} > 5$ GeV et l'autre pour $W_{\gamma\gamma} > 10$ GeV, où $W_{\gamma\gamma}$ est la masse effective des deux photons. Pour $0.4 < p_t < 2.0$ GeV et $|\eta| < 1.5$, la section efficace différentielle en fonction de p_t est bien décrite par une fonction exponentielle avec $\langle p_t \rangle = 342 \pm 8$ MeV. Ce comportement exponentiel est typique des intéractions hadroniques de basse énergie. Pour $p_t > 2.0$ GeV, la section efficace différentielle de production des mésons K^0_S est supérieure à la fonction exponentielle. Ceci confirme l'existence du processus d'interaction "durs" du photon décrits par la QCD et la QED. Un bon accord est trouvé entre les données expérimentales et les prédictions théoriques de QCD d'ordre supérieur ("Next to Leading Order") calculées par Kniehl. Un bon accord est aussi trouvé avec les résultats de l'expérience OPAL au LEP.

1.7 L'état final $K^0_S K^0_S$ dans les collisions photon-photon

1.7.1 Sélection des événements

Les événements exclusifs produits par la réaction

$$e^+e^- \to e^+e^-K^0_S K^0_S \tag{1.4}$$

sont sélectionnés en utilisant la désintégration $K^0_S \to \pi^+\pi^-$ et en reconstruisant le vertex secondaire ainsi produit. Les critères de sélection sont les suivants:

- L'énergie mesurée par les calorimètres électromagnétique et hadronique doit être inférieure à 30 GeV.
- Quatre traces de charge totale nulle doivent être détectées.
- Deux vertex secondaires avec une distance du vertex primaire supérieure à 1 mm dans le plan $r-\phi$ sont requis. En même temps, cette distance doit être supérieure à 3 mm pour au moins un de ces vertex. En outre, l'angle entre la direction de vol et le vecteur impulsion totale des deux particules formant le vertex dans le plan $r-\phi$ doit être inférieur à 0.3 mrad. Les deux vertex doivent être dos-à-dos à 0.3 rad près.
- Le carré de l'impulsion transverse totale des quatre traces chargées doit être inférieur à 0.1 GeV^2.
- Les événements contenant des photons sont exclus.
- Les masses effectives $m_i(\pi^+\pi^-)$ des deux candidats K^0_S doivent verifier:

$$\sqrt{[m_1(\pi^+\pi^-) - m(K^0_S)]^2 + [m_2(\pi^+\pi^-) - m(K^0_S)]^2} < 40 \quad \mathrm{MeV}.$$

Les données utilisées pour cette analyse ont été collectées par le détecteur L3 au LEP, de 1991 à 1999. La luminosité intégrée totale est de 588 pb^{-1}, dont 143 pb^{-1} collectés autour du pôle du boson Z et 445 pb^{-1} à haute énergie. Avec les coupures précédemment décrites, 802 événements sont sélectionnés.

1.7.2 Résultats

Le spectre de masse effective $K^0_S K^0_S$ (Figure 8.16) est caracterisé par la présence de trois signaux résonants sur un faible bruit de fond.

- A 1300 MeV environ, un petit signal résonant dû à l'interférence destructive entre les mésons tenseurs $f_2(1270)$ et $a_2(1320)$ est observé.
- Le spectre de masse $K^0_S K^0_S$ est dominé par la formation du méson tenseur $f'_2(1525)$ dans un état de spin deux et hélicité deux. La largeur partielle de

désintégration en deux photons mesurée est:

$$\Gamma_{\gamma\gamma}\Big(\mathrm{f}_2'(1525)\Big) \times \mathrm{Br}\Big(\mathrm{f}_2'(1525) \to \mathrm{K\bar{K}}\Big) = 76 \pm 6 \pm 11 \text{ eV}.$$

Cette valeur est actuellement la mesure la plus précise de cette quantité. Ce résultat conduit à l'évaluation de l'angle de mélange θ_M de l'octet des mésons tenseurs

$$\theta_M = (27.5^{+0.7}_{-0.8})^\circ.$$

Ceci met en évidence une déviation, petite mais significative, par rapport à l'hypothèse d'un mélange idéal ($\theta_M \simeq 35^\circ$).

- Un signal dû à la formation de l'état résonant $\mathrm{f_J}(1710)$ est observé et la première étude de cet état dans les collisions photon-photon est effectuée. Ce signal est dominé par un état de spin deux et hélicité deux. Une fraction de 24±16% de l'onde 0^{++} est aussi observé dans la région de masse entre 1640 et 2000 MeV. La composante tensorielle peut être interprétée comme la formation de la première excitation radiale d'un état mésonique tensoriel. Sa largeur partielle de désintégration en deux photons mesurée est:

$$\Gamma_{\gamma\gamma}\Big(\mathrm{f}_2(1750)\Big) \times \mathrm{Br}\Big(\mathrm{f}_2(1750) \to \mathrm{K\bar{K}}\Big) = 49 \pm 11 \pm 13 \text{ eV}.$$

- Aucun signal résonant n'est observé dans la region de masse autour de 2.2 GeV. La limite supérieure de la largeur partielle de désintégration en deux photons pour le candidat glueball $\xi(2230)$

$$\Gamma_{\gamma\gamma}(\xi(2230)) \times \mathrm{Br}(\xi(2230) \to \mathrm{K^0_S K^0_S}) < 1.4 \text{ eV}$$

est déterminée avec un niveau de confiance de 95%. Ce resultat conduit à la détermination de la limite inférieure de la "stickiness" de l'état $\xi(2230)$

$$S_{\xi(2230)} > 74$$

avec un niveau de confiance de 95%. Cette valeur est largement plus élévée que les valeurs qui caracterisent les états $q\bar{q}$ connus. Si l'existence de l'état $\xi(2230)$ se confirme dans les réactions hadroniques, ce résultat sera en faveur de son interprétation comme glueball tensorielle.

Chapter 2

Introduction

The study of the elementary constituents of matter and the understanding of their interactions is the aim of particle physics. Our present knowledge of elementary particles is based on a theory, the Standard Model, to which all the known natural phenomena can be reconducted. According to the Standard Model, matter is made of spin 1/2 fermions which interact via bosonic force carriers. There are four fundamental interactions: electromagnetic, weak, strong and gravitational. Fermions are divided into quarks and leptons. There are three families of quarks and leptons, as presented in Table 2.1. Quarks have a fractional charge (+2/3 for u, c, t and -1/3 for d, s, b) and participate to all the interactions. Leptons do not participate to strong interactions and have a charge -1 (e, μ and τ) or are neutral (neutrinos). To each fermion corresponds an antifermion with the same mass and opposite electric charge and quantum numbers. The fundamental interactions, except for the gravitational force which at present cannot be included in the Standard Model, derive directly by the gauge principle applied to the symmetry group SU(3)×SU(2)×U(1). Strong interactions are mediated by eight "coloured" gluons which are responsible for the formation of bound states of three quarks, the baryons, and of a quark and a anti-quark, the mesons. The electromagnetic interactions are mediated by one massless gauge boson, the photon, while the weak interactions are mediated by three heavy vector bosons (Z, W^+ and W^-), discovered at CERN in 1983.

To test the Standard Model, and in particular its electro-weak sector, with a very high precision, the Large Electron Positron Collider (LEP) was built at CERN. From 1989 to 1995 the four LEP experiments, ALEPH, DELPHI, L3 and OPAL, collected

Leptons		Quarks	
Electron (e)	Neutrino e (ν_e)	Up (u)	Down (d)
Muon (μ)	Neutrino μ (ν_μ)	Charm (c)	Strange (s)
Tau (τ)	Neutrino τ (ν_τ)	Top (t)	Bottom (b)

Table 2.1: The tree families of spin 1/2 matter elementary particles.

data at the Z peak, producing many important results which set the Standard Model on a solid footing. In particular, data showed the existence of only three families of "light" quarks and leptons. From 1996 the threshold for the production of W^+W^- pairs was crossed and the center of mass energy was continuously increased up to 208 GeV in the year 2000.

According to the indetermination principle, a photon can fluctuate into a pair of oppositely charged particles and photon-photon interactions can be produced. Since accelerated charged particles emit virtual photons, the beams of LEP can be used as sources of very high energy photons and the LEP experiments can study two-photon interactions. The L3 detector is well suited for two-photon physics and many results from LEP are signing a remarkable progress in this field. LEP is the most powerful photon-photon collider ever built which allows to study two-photon processes at the highest photon-photon effective masses and the search for new resonant states.

Since the photon can fluctuate into a pair of quarks, the photon behaves like a hadron at high energies and the reaction $\gamma\gamma \rightarrow$hadrons is well suited to test Quantum Chromo Dynamics (QCD). In particular, the study of inclusive single particle production can be used to test perturbative QCD predictions.

The formation of resonant states allows the investigation of meson spectra in a clean experimental environment. Since the photon couples to the electric charge, the quark structure of mesons and the presence of mixing effects can be studied. In QCD theory gluons can interact with themselves and form bound states called glueballs. The experimental existence of the glueballs is not firmly established and some candidates have been observed in hadronic interactions. Since photons do not couple directly to gluons, glueballs are weakly coupled to two photons. The study of the formation of resonant states in two-photon collisions provides therefore important and unique information on glueball searches.

The present thesis is organized as follows. A review of the theoretical framework of two-photon physics at the e^+e^- colliders is presented in Chapter 3. Chapter 4 contains a concise description of LEP and the L3 detector. Chapter 5 is dedicated to the level-one charged particle trigger which has been one of my responsibilities within the L3 Collaboration. The reconstruction of the tracks, of the primary and secondary vertices and the measurement of the specific ionization loss are described in Chapter 6. In Chapter 7 and Chapter 8 the experimental analysis of two photon-photon interaction processes is presented. The study of inclusive K^0_S production is described in Chapter 7 and Chapter 8 is dedicated to the study of the $K^0_S K^0_S$ exclusive final state and its implications for glueballs.

Chapter 3

Two-photon physics at the e^+e^- colliders

3.1 Introduction

The investigation of the nature and the behaviour of light is one of the most fascinating subjects of human speculation [1]. Light fills our world, our universe and is responsible for many fundamental natural phenomena at the basis of our own existence.

It is very probably Pythagoras, in the sixth century B.C., who first proposed the idea that light consists of small particles sent out by objects toward the eye of the viewer. It was attributed to Euclid, the great mathematician of the third century B.C., the idea that the eye sends out visual rays which then strike an object and cause the sensation of sight. After the birth of modern science, Isaac Newton (1642-1727) demonstrated that white light can be separated into different colours by a prism but that light of a single colour cannot be separated again. According to Newton, white light is composed of small particles of different nature. In the same period, Christian Huygens (1629-1695) formulated the earliest wave theory of light that was capable to explain phenomena like interference and diffraction. Light is therefore characterized by phenomena which are typical of a particle and, at the same time, by phenomena typical of a wave. This particle-wave dualism on the nature of light is one of the main problems physicists had to face up to the conception of quantum mechanics

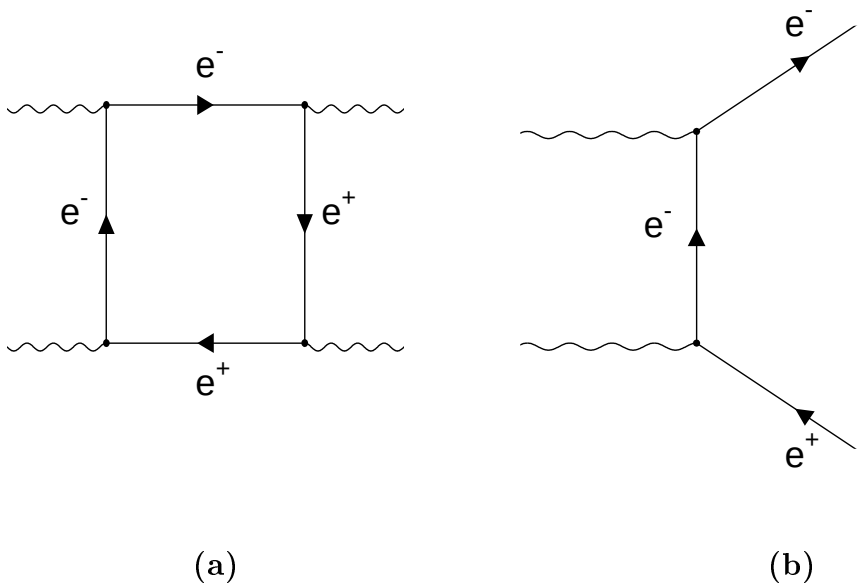

Figure 3.1: Elastic (a) and inelastic (b) photon-photon scattering.

which overcomes the problem by unifying the two concepts and by introducing a probabilistic interpretation of nature.

According to classical electrodynamics, light consists of electromagnetic waves. Since Maxwell equations are linear in the electric and in the magnetic field, light cannot interact with itself. Light-by-light interaction is therefore a phenomenon that can be predicted and explained only in terms of quantum mechanics. In 1905 Einstein proposed a revolutionary theory of the photoelectric effect. Starting from Plank's "energy quanta", he proposed that light consists of "light quanta", the photons [1], carrying a quantum of energy $h\nu$. In the modern theory of Quantum Electro Dynamics (QED), light is made of photons which are the carriers of the electromagnetic force that is produced by the coupling between photons and charged particles. According to Heisemberg's indetermination principle, a photon can fluctuate into a pair of oppositely charged particles making possible its interaction with another photon. This process has a non negligible probability if the energy of the photon is of the order of the mass of the created particles. Since the lightest particle in nature is the

[1] The name *photon* was proposed in 1926 by Lewis [2].

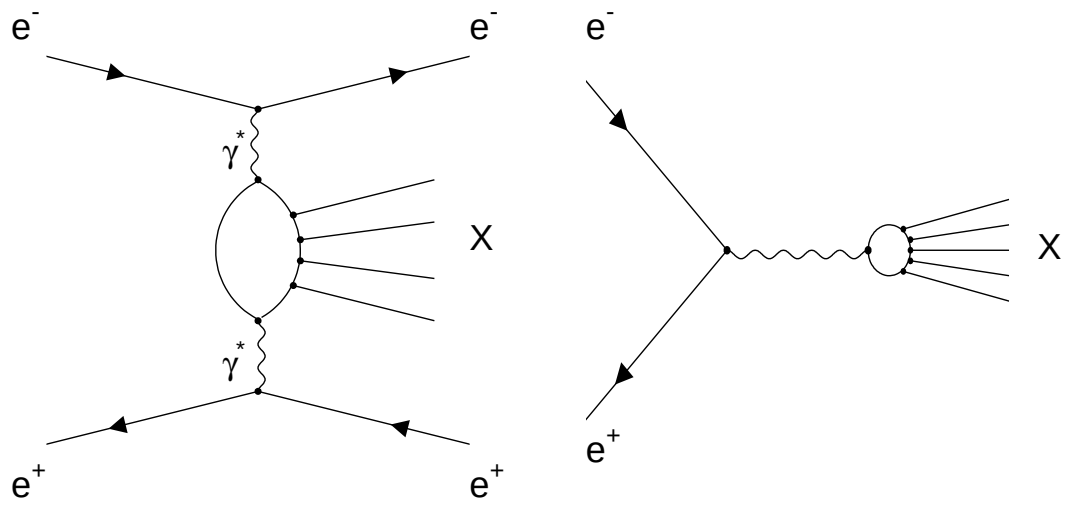

(a) (b)

Figure 3.2: The two-photon (a) and the annihilation (b) processes at e^+e^- colliders.

electron, the two-photon process is practically observable only if the energy of the photon is at least equal to the mass of the electron.

The cross section for photon-photon elastic scattering was first calculated by Euler and Kockel [3] in 1935 using the box diagram in Figure 3.1(a). They obtained $\sigma = 129(W_{\gamma\gamma}/m_e)^6$nb, where $W_{\gamma\gamma}$ is the effective mass of the two photons. For visible light ($W_{\gamma\gamma} \simeq 2.5$ eV) this result gives the practically unobservable value of 10^{-30}nb. The cross section rises to experimentally observable values of about 100 nb for photon energies of the order of the mass of the electron. It is interesting to report that the very first experimental attempt to detect photon-photon scattering was made in 1930 by Huges and Jauncey [4] by using sunlight as the source and the human eye as the detector. They obtained an upper limit for the cross section of $3 \cdot 10^{-20}$ cm^2. The cross section for the $\gamma\gamma \rightarrow e^+e^-$ inelastic process in Figure 3.1(b) was found [5] to be peaked at about 10^5 nb for photon energies just above the mass of the electron. Unfortunately photon beams of such energies were not available at the time of these calculations.

Up to the conception and the construction of the first e^+e^- storage rings, very little experimental progress was achieved in the field of two-photon interactions.

Already in 1924 Fermi [6] first proposed the idea of using accelerated charged particles as sources of virtual photons. This is at the basis of two-photon physics at e^+e^- colliders where photon-photon interactions are studied using the reaction

$$e^+e^- \rightarrow e^+e^-\gamma^*\gamma^* \rightarrow e^+e^-X \tag{3.1}$$

where γ^* is a virtual photon and X is the final state formed by the two photons, as shown in Figure 3.2(a). In 1960 Low [7] proposed to measure the lifetime of the π^0 meson via the process $e^+e^- \rightarrow e^+e^-\pi^0$ and Calogero and Zemach [8] calculated the cross section of the process $e^+e^- \rightarrow e^+e^-\pi^+\pi^-$. The first experimental observation of the two-photon reaction $e^+e^- \rightarrow e^+e^-e^+e^-$ came only in 1971 at VEPPII [9] storage ring in Novosibirsk, thirty-seven years after the first calculation of this process by Landau and Lifshitz [10]. In 1974 di-muon production by photon-photon scattering was observed at ADONE [11] at LNF in Frascati. Since then, a large number of e^+e^- colliders, such as DORIS and PETRA at DESY, SPEAR and PEP at SLAC, TRISTAN at KEK, CESR at Cornell and finally LEP at CERN, have been built with continuously increasing luminosities and energies, producing a very remarkable amount of results and progress in this field.

Two-photon physics is not the main goal of e^+e^- colliders which are generally built to study the annihilation process shown in Figure 3.2(b). In the annihilation process the mass of the final state X is fixed to $2E$, where E is the beam energy, and its quantum numbers to $J^{PC}=1^{--}$. The cross section for this process decreases with the beam energy as $\frac{\alpha^2}{E^2}$, where α is the fine structure constant. In contrast, the two-photon process gives access to a continuum mass range of final states with C=+1 and is characterized by a cross section that rises with the energy as $\alpha^4 \ln^2(\frac{E}{m_e})$. Despite the higher order in α, it is the dominant process already at energies of a few GeV. The continuously higher energies and luminosities of the LEP machine offer therefore a unique environment for the study of photon-photon interactions and the large number of results from LEP are signing a very remarkable progress in this field. Figure 3.3 shows the cross section as a function of the e^+e^- center of mass energy $\sqrt{s} = 2E$ for the main physical channels studied at LEP. The two-photon process clearly dominates the cross section, especially at LEP2 with center of mass energies above the W^+W^- threshold. The importance of the study of two-photon physics at LEP [12] comes not only from the fact that this process represents the main source

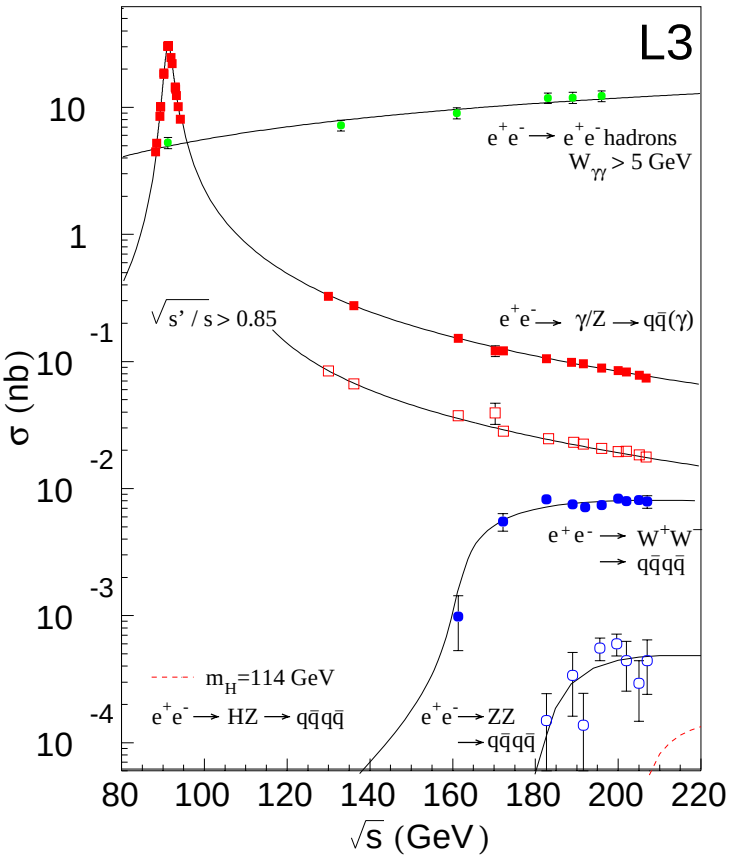

Figure 3.3: The cross section as a function of the e^+e^- center of mass energy ($\sqrt{s} = 2E_{beam}$) for the main processes studied at LEP. The experimental measurements by the L3 experiment are also shown.

of background for the search of new physics but mainly because the large amount of data at high energies allows the exploration of two-photon interactions at higher masses and the search for new resonant states.

Electron-positron colliders are at present the only experimental environment to study two-photon interactions. Only recently the first experimental evidence for light-by-light scattering involving only real photons has been obtained at SLAC [13] using a laser and an electron beam. This result can be the first step toward a photon-photon collider which will be probably built in future [14].

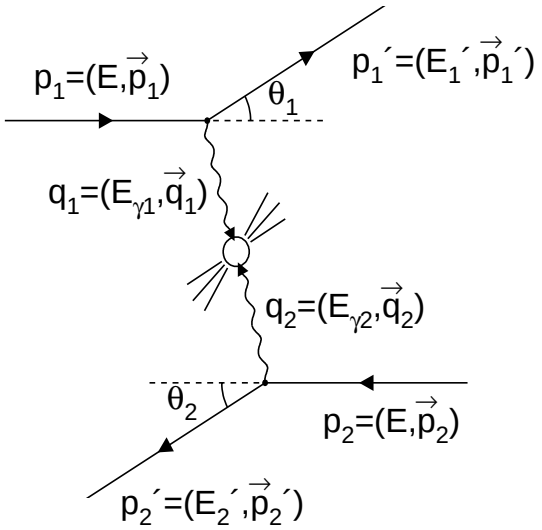

Figure 3.4: Kinematics of the two-photon reaction $e^+e^- \to e^+e^-X$.

3.2 Kinematics

The kinematics of the two-photon reaction is completely determined by the four momenta of the incoming and outgoing electron and positron, as shown in Figure 3.4. For unpolarized beams, five variables are necessary to determine the two-photon system at a given beam energy E. The following five variables are usually used in the laboratory system:

- the energies E_1' and E_2' of the scattered electron and positron
- their angles θ_1 and θ_2 with respect to the beam axis
- the angle Φ between their two scattering planes.

The energies and the normalized energies of the two virtual photons are

$$E_{\gamma 1} = E - E_1^{'} \quad , \quad E_{\gamma 2} = E - E_2^{'}$$
$$\omega_1 = E_{\gamma 1}/E \quad , \quad \omega_2 = E_{\gamma 2}/E$$

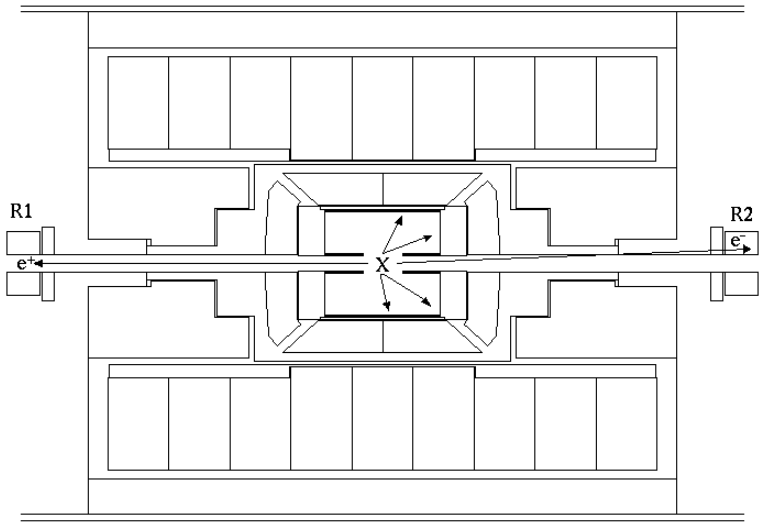

Figure 3.5: The "single-tag" case: one of the scattered electrons is detected by one of the low angle detectors (R1 and R2).

and their space-like effective masses

$$q_i^2 = (p_i - p_i')^2 = 2m_e^2 - 2EE_i' \cdot \left(1 - \sqrt{1 - \left(\frac{m_e}{E}\right)^2} \cdot \sqrt{1 - \left(\frac{m_e}{E_i'}\right)^2} \cdot \cos\theta_i\right). \quad (3.2)$$

For $E > E_i' >> m_e$ this expression reduces to

$$q_i^2 \simeq -2EE_i'(1 - \cos\theta_i). \quad (3.3)$$

Neglecting the contributions of the order m_e^2, the effective two-photon mass $W_{\gamma\gamma}$ is

$$W_{\gamma\gamma}^2 = (q_1 + q_2)^2 \simeq 4E_{\gamma 1}E_{\gamma 2} - 2E_1'E_2' \cdot (1 - \cos\theta_1 \cdot \cos\theta_2 - \sin\theta_1 \cdot \sin\theta_2 \cdot \cos\Phi) \quad (3.4)$$

that for $q_i^2 << m_e^2$ reduces to

$$W_{\gamma\gamma}^2 \simeq 4E_{\gamma 1}E_{\gamma 2}. \quad (3.5)$$

Since the propagator of the photon has the form $\frac{1}{q^2}$, the two photons are emitted at very small angles of the order $\frac{m_e}{E}$ with respect to the beam line and have small energies, typical of the bremsstralhung spectrum $\frac{1}{E_\gamma}$. This implies that the electron and positron are scattered at very low angles and carry nearly the full beam energy. The two-photon system is therefore characterized by a small mass $W_{\gamma\gamma} << E$, producing low transverse momentum and low multiplicity decay products. Since the two photons have not the same energy, the two-photon system has a typical boost along the beam line.

The experiments at e^+e^- colliders are usually equipped with low angle detectors, as shown in Figure 3.5. The two outgoing electrons are usually scattered inside the beam pipe of the accelerator and are not detected at all. In this case, according to Equation (3.3), the two photons are quasi-real and the two-photon system is characterized by a very small transverse momentum. This is the most probable kinematical configuration called "*no-tag*". If the q^2 of one of the two photons is sufficiently large, the corresponding scattered lepton is detected by one of the two low angle detectors. This is the configuration "*single-tag*". Much less probable than the "*single-tag*" is the "*double-tag*" configuration when both the scattered electrons are detected.

3.3 The helicity structure of the cross section

The matrix element for the two photon process is

$$\mathcal{M}_{e^+e^-\to e^+e^-X} = \frac{e^2}{q_1^2 q_2^2} \cdot \bar{u}(p_1', s_1')\gamma_\mu u(p_1, s_1) \cdot \bar{v}(p_2', s_2')\gamma_\nu v(p_2, s_2) \cdot M^{\mu\nu} \qquad (3.6)$$

where $u(p, s)$ and $v(p, s)$ are the Dirac spinors of the electron and the positron with four-momenta p_i and spin s_i. This expression is the product of three terms. The first two correspond to the lepton-photon vertices, describing the emission of the two photons in terms of QED, and the last term $M^{\mu\nu}$ describes the annihilation of the two photons into the final state X. Apart for di-lepton QED final states, the third term cannot be calculated and is a quantity to be measured.

The factorization of the cross section into a part which describes the flux of the photons and another part which describes the two-photon fusion process allows to

consider e^+e^- storage rings as photon-photon colliders. The complete derivation of this factorization can be found in Reference [15]. The fundamental points are described here and more details can be found in References [16, 17, 18, 19].

The transition matrix element of the $\gamma\gamma \to X$ subprocess depends on the polarization states of the two-photons ϵ_1^ν and ϵ_2^μ and can be written as

$$\langle X|T|\gamma\gamma\rangle = \epsilon_1^\mu \epsilon_2^\nu A_{\mu\nu}^X \tag{3.7}$$

where the tensor $A_{\mu\nu}^X$ contains the helicity structure of the transition.

The differential cross section, obtained by multiplying the square of the matrix element with a Lorentz invariant phase-space factor and by dividing by the incoming flux, can be written as

$$\sigma(e^+e^- \to e^+e^- X) = \frac{\alpha^2}{64\pi^4 E^2 q_1^2 q_2^2} \cdot \rho_1^{\mu\nu} \rho_2^{\mu'\nu'} M_{\mu\nu\mu'\nu'}^X \cdot \frac{d^3p_1' d^3p_2'}{E_1' E_2'} \tag{3.8}$$

where

$$\rho_i^{\mu\nu} = \frac{-[q_i^2 g_{\mu\nu} + 2(p_i'^\mu p_i^\nu + p_i^\mu p_i'^\nu)]}{q_i^2}. \tag{3.9}$$

The tensor

$$M_{\mu\nu\mu'\nu'}^X = 8\pi^2 \int A_{\mu\nu}^X \cdot A_{\mu'\nu'}^X \delta(q_1 + q_2 - P_f) d\Gamma_f \tag{3.10}$$

describes the formation of the final state X and $d\Gamma_f$ is the Lorentz invariant phase space factor of the final state of four-momentum P_f. Not all the $4^4 = 256$ components of the tensor $M_{\mu\nu\mu'\nu'}^X$ are independent. The conservation of the electromagnetic current imposes $q_{i\mu}\epsilon_i^\mu = 0$ and each photon can therefore be expressed by a 3-vector $\vec{\epsilon_i}$. This reduces to $3^4 = 81$ the number of the independent components of this tensor. When parity conservation, time reversal invariance and the conservation of the total helicity are considered, only 8 independent components are left. They reduce to 6 for unpolarized electron and positron beams. In this case the cross section can be expressed by a linear combination of 6 independent Lorentz covariants σ_{IJ} and τ_{IJ} whose coefficients ρ^{ab} are fully calculable functions of p_i and p_i' only. The cross

section can therefore be written as

$$\sigma(e^+e^- \to e^+e^- X) = \frac{\alpha^2\sqrt{(q_1q_2)^2 - q_1^2q_2^2}}{32\pi^4 E^2 q_1^2 q_2^2} \cdot \frac{d^3p_1' d^3p_2'}{E_1' E_2'} \cdot \Big[4\rho_1^{++}\rho_2^{++}\sigma_{TT} + 2\rho_1^{++}\rho_2^{00}\sigma_{TL} + 2\rho_1^{00}\rho_2^{++}\sigma_{LT} + \rho_1^{00}\rho_2^{00}\sigma_{LL} + 2|\rho_1^{+-}\rho_2^{+-}|\tau_{TT}\cos 2\Delta\phi - 8|\rho_1^{+0}\rho_2^{+0}|\tau_{TL}\cos\Delta\phi\Big] \quad (3.11)$$

where $\Delta\phi$ is the angle between the scattering planes of the colliding leptons in the two-photon centre of mass system. The expression for the coefficients ρ^{ab} can be found in Reference [15]. The subscript T stands for a transverse photon with helicity ± 1 and the subscript S for a longitudinal photon with helicity 0. If the azimuthal correlation between the scattered leptons is not explicitly measured, the last two terms average out to zero. Furthermore, for $q_i^2 \to 0$, i.e. for quasi-real photons, only the term with two-transverse photons σ_{TT} contributes to the cross section. This corresponds to the experimental case of "no-tag" that allows the approximation of only transverse photons. In this case the cross section reduces to

$$d\sigma(e^+e^- \to e^+e^- X) = \frac{\alpha^2\sqrt{(q_1q_2)^2 - q_1^2q_2^2}}{32\pi^4 E^2 q_1^2 q_2^2} \cdot \frac{d^3p_1' d^3p_2'}{E_1' E_2'} \cdot 4\rho_1^{++}\rho_2^{++} \cdot \sigma_{TT}(W_{\gamma\gamma}, q_1^2, q_2^2) \quad (3.12)$$

where

$$2\rho_1^{++} = X^{-1}(2p_1q_2 - q_1q_2)^2 + 1 + \frac{4m_e^2}{q_1^2} \quad (3.13)$$

$$2\rho_2^{++} = X^{-1}(2p_2q_1 - q_1q_2)^2 + 1 + \frac{4m_e^2}{q_2^2} \quad (3.14)$$

$$X = (q_1q_2)^2 - q_1^2q_2^2. \quad (3.15)$$

3.3.1 The luminosity function

In analogy with the formalism used for electron-positron scattering, the differential luminosity function

$$\frac{d^5L_{\gamma\gamma}^{TT}}{d\omega_1 d\omega_2 d\cos\theta_1 d\cos\theta_2 d\Phi} = \frac{\alpha^2}{16\pi^3} \cdot \frac{E_1'E_2'}{q_1^2q_2^2} \cdot \sqrt{(q_1q_2)^2 - q_1^2q_2^2} \cdot 4 \cdot \rho_1^{++}\rho_2^{++} \quad (3.16)$$

is introduced. In this way, the differential cross section (3.12) for the process $e^+e^- \to e^+e^-X$

$$\frac{d^5\sigma(e^+e^- \to e^+e^-X)}{d\omega_1 d\omega_2 d\cos\theta_1 d\cos\theta_2 d\Phi} = \frac{d^5L^{TT}_{\gamma\gamma}}{d\omega_1 d\omega_2 d\cos\theta_1 d\cos\theta_2 d\Phi} \cdot \sigma_{TT}(W_{\gamma\gamma}, q_1^2, q_2^2) \qquad (3.17)$$

is given by the product of the QED calculable differential luminosity function, giving the flux of the photons, with the cross section of the process $\gamma\gamma \to X$. The luminosity function can be evaluated via a Monte Carlo integration and is found to be peaked at low values of $W_{\gamma\gamma}$ and to increase with respect to the beam energy.

In order to obtain an analytical expression for the luminosity function, some approximations have to be applied. The $\rho_1^{++}\rho_2^{++}$ term contains the variables of both of the photons but, if $q_i^2 \to 0$ and $q_i^2 << W_{\gamma\gamma}^2$, it is possible to write the luminosity function as the product of two fluxes, each coming from only one $ee\gamma$ vertex. In this approximation $\theta_i << 1$ and $W_{\gamma\gamma}^2 \simeq 4E_{\gamma 1}E_{\gamma 2}$. After an integration over the angular distribution of the leptons, the factorized expression of the luminosity function

$$\frac{d^2L^{TT}_{\gamma\gamma}}{d\omega_1 d\omega_2} = \frac{dN_\gamma(\omega_1)}{d\omega_1} \cdot \frac{dN_\gamma(\omega_2)}{d\omega_2} \qquad (3.18)$$

is obtained where

$$\frac{dN_\gamma(\omega)}{d\omega} = \frac{\alpha}{2\pi}\frac{1}{\omega}\Big[[1+(1-\omega)^2]\cdot \ln\frac{q^2_{max}}{q^2_{min}} - (1-\omega)\Big(1-\frac{q^2_{min}}{q^2_{max}}\Big)\Big]. \qquad (3.19)$$

This factorization is called the "equivalent photon" or "Weizsäcker-Williams" approximation of the luminosity function.

For the tagged mode, the minimum and the maximum values of q^2, q^2_{min} and $q^2_{max} << W^2_{\gamma\gamma}$, are given by

$$\frac{q^2_{max}}{q^2_{min}} = \frac{\theta^2_{max}}{\theta^2_{min}} \qquad (3.20)$$

where θ_{min} and θ_{max} correspond to the acceptance of the low angle tagging detector. For the case of no-tag, q^2_{min} is given by the kinematical limit

$$q^2_{min} = m_e^2\frac{\omega}{\omega-1} + o(m_e^4) \qquad (3.21)$$

and q^2_{max} by the acceptance of the tagging detector according to Equation (3.3). If no tagging condition is considered, the maximum value allowed by Equation (3.3)

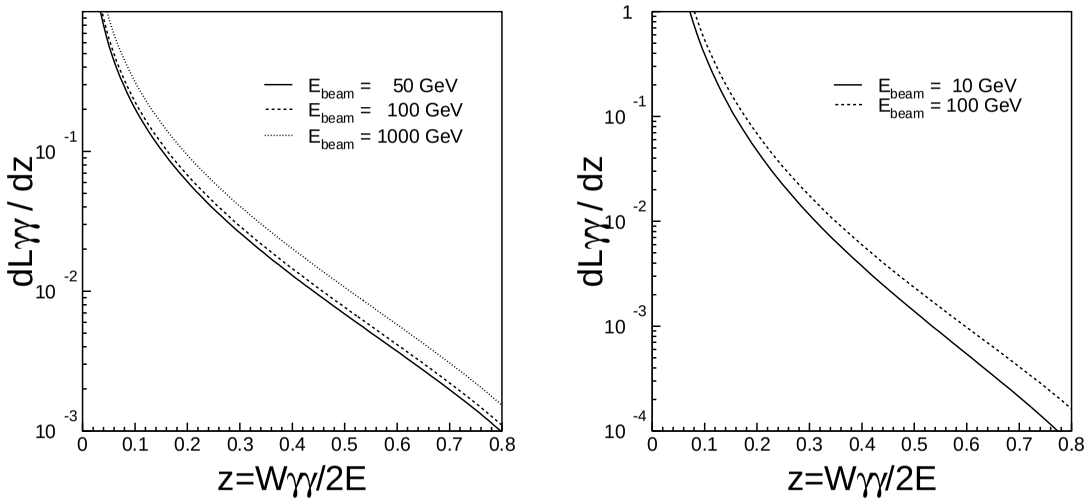

(a) (b)

Figure 3.6: The luminosity function for various beam energies using the Low approximation (a) and the improved equivalent photon approximation by Schuler (b).

$q^2_{max} = 4E^2\omega$ can be used. If only the leading logarithmic term is retained, the expression of the two-photon flux reduces to

$$\frac{dN_\gamma(\omega)}{d\omega} = \frac{\alpha}{\pi\omega} \cdot [1 + (1-\omega)^2] \cdot \ln\eta \tag{3.22}$$

where $\eta = 2E/m_e$ for the no-tag and $\eta = \theta_{max}/\theta_{min}$ for the tagged mode.

After an integration of Equation (3.18), taking into account the condition $W^2_{\gamma\gamma} \simeq 4E_{\gamma 1}E_{\gamma 2}$, the following approximated expression for the luminosity function

$$\frac{dL^{TT}_{\gamma\gamma}}{dW_{\gamma\gamma}} = \frac{4\alpha^2}{\pi^2 W_{\gamma\gamma}} \cdot (\ln\eta)^2 \cdot f\left(\frac{W_{\gamma\gamma}}{2E}\right) \tag{3.23}$$

is obtained where

$$f(z) = (2+z^2)^2 \cdot \ln\frac{1}{z} - (1-z^2)(3+z^2). \tag{3.24}$$

Equation (3.23) is called the "Low approximation" [7] and overestimates the luminosity function of about 20% but reproduces quite well its shape for small values of $z = W_{\gamma\gamma}/2E < 0.8$.

Figure 3.6(a) shows the luminosity function in the Low approximation as a function of z for various beam energies for the no-tag mode. The typical bremsstralhung rise at low z is visible together with the logarithmic rise with respect to the beam energy.

An improved equivalent-photon approximation method has been recently proposed by Schuler [20] taking into account beyond-leading-logarithmic effects and scalar photon contributions. Figure 3.6(b) shows the luminosity function in this approximation for the no-tag mode using a value of $\theta_{max} = 30$ mrad, typical for LEP detectors.

3.4 The two-photon final states

Two-photon interactions lead to five main categories of final states.

- The $\gamma\gamma \to l^+l^-$ process, where $l = \mathrm{e}, \mu, \tau$, is completely described by QED and can be used as a test for experimental set-ups. The study of the azimuthal correlations and of the "single-tag" events lead to new interesting results on the structure of the photon [21].

- The reaction $\gamma\gamma \to m\bar{m}$, where m is a meson, allows the study of non resonant di-meson production mechanisms.

- The process $\gamma\gamma \to b\bar{b}$, where b is a baryon (p, Λ, Σ, etc.), allows the test of three-quark and quark-diquark baryon models.

- The formation of a single resonant state R via the reaction $\gamma\gamma \to$ R is a fundamental process for the investigation of the structure of mesons and for the search for gluonium states. Since there are no other particles produced, the study of the resonant state can be performed in a very clean experimental environment. This case will be described in detail in Sections 3.5, 3.6 and 3.8.

- The process $\gamma\gamma \to$ *hadrons* allows tests of QCD both in the perturbative and non-perturbative regions. The study of "single-tag" and "double-tag" events is fundamental for the understanding of the hadronic structure of the photon. This process is described in more detail in Section 3.9.

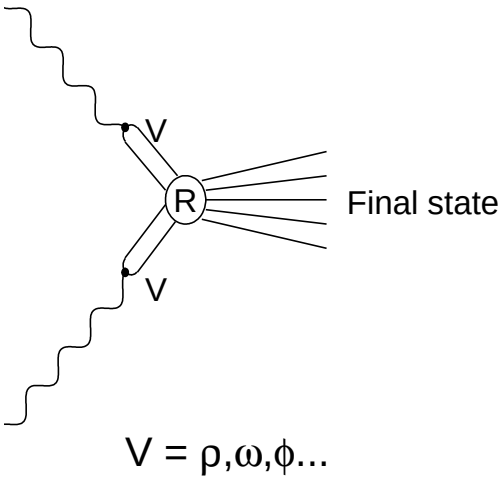

Figure 3.7: The formation of a resonant state in a photon-photon collision according to the Vector Dominance Model.

3.5 Resonance formation

The cross section σ_{TT} for the formation of a resonance R is given by the Breit-Wigner function

$$\sigma_{TT}(\gamma\gamma \to \mathrm{R}) = 8\pi(2J_R+1)\frac{\Gamma_{\gamma\gamma}(\mathrm{R})\Gamma(\mathrm{R})}{(W_{\gamma\gamma}^2 - m_R^2)^2 + m_R^2\Gamma^2(\mathrm{R})} \cdot F^2(q_1^2, q_2^2) \tag{3.25}$$

where m_R, J_R, $\Gamma_{\gamma\gamma}(\mathrm{R})$ and $\Gamma(\mathrm{R})$ are the mass, spin, two-photon partial width and total width of the resonance, respectively. The q_i^2 dependence of the cross section is modeled by the transition form factor $F^2(q_1^2, q_2^2)$ which for quasi real photons satisfies

$$F^2(q_1^2 \to 0, q_2^2 \to 0) = 1. \tag{3.26}$$

According to the Vector Dominance Model (VDM), one or both of the photons can fluctuate into a vector meson V=$\rho, \omega, \phi, ...$ before the interaction, as shown in Figure 3.7. This introduces a cutoff in q_i^2 of the order of the mass of the vector meson

which is expressed by the VDM transition form factor

$$F^2(q_1^2, q_2^2) = \sum_{V_1,V_2} \frac{A_{V_1}}{1 - q_1^2/m_{V_1}^2} \cdot \frac{A_{V_2}}{1 - q_2^2/m_{V_2}^2} \tag{3.27}$$

where

$$\sum_{V_i} A_{V_i} = 1. \tag{3.28}$$

The differential luminosity function of Equation (3.16) and the Breit-Wigner function (3.25) lead to a complete description of the process of resonance formation by two quasi-real photons. This result is implemented in the EGPC Monte Carlo program [22] that is used to model this process. It is important to remark that combining Equations (3.17) and (3.25) leads to the proportionality relation between the e^+e^- cross section and the two-photon partial width $\Gamma_{\gamma\gamma}(R)$

$$\sigma(e^+e^- \to e^+e^-R) = \mathcal{K} \cdot \Gamma_{\gamma\gamma}(R). \tag{3.29}$$

The proportionality factor $\mathcal{K}$ is evaluated by a Monte Carlo integration and is used to determine the two-photon partial width of the resonance from the measurement of the cross section.

For a very narrow resonance and for quasi real photons, an analytical formula for the cross section can be derived by approximating the Breit-Wigner function with a Dirac's delta according to

$$\sigma_{TT}(\gamma\gamma \to R) \simeq 8\pi^2 \cdot (2J+1) \cdot \frac{\Gamma_{\gamma\gamma}}{m_R} \cdot \delta(W_{\gamma\gamma}^2 - m_R^2). \tag{3.30}$$

Using Equations (3.17), (3.23) and (3.30), the "Low formula" for the cross section

$$\sigma_{TT}(e^+e^- \to e^+e^-R) \simeq 16\alpha^2 \cdot \frac{(2J+1)}{m_R^3} \cdot \left(\ln\frac{E}{m_e}\right)^2 \cdot f\left(\frac{m_R}{2E}\right) \cdot \Gamma_{\gamma\gamma} \tag{3.31}$$

is obtained.

The quantum numbers of the resonance must be compatible with the initial state of the two quasi-real photons and only a neutral, unflavoured state with even charge conjugation (C=+1), J≠1 and helicity-zero (λ=0) or two (λ=2) can be formed. The condition J≠1 is due to the Landau-Yang theorem [23] which is based on parity and

helicity conservation principles for real photons. If one of the two-photons is highly virtual, as in the tagged mode, J=1 states are allowed.

According to the quark model, a meson is a quark-antiquark bound state with quantum numbers

$$\begin{aligned} P &= -(-1)^L \\ C &= (-1)^{L+S} \end{aligned}$$

where P is the parity, L the orbital angular momentum and S the spin. If only the three lightest quarks u, d and s are considered, mesons are classified in nonets of a given J^{PC} according to the $SU_f(3)$ symmetry group. Each nonet is subdivided into an octet and a singlet S_1 and has three neutral members

$$\begin{aligned} S_1 &= \sqrt{\frac{1}{3}} \cdot (u\bar{u} + d\bar{d} + s\bar{s}) \\ S_8 &= \sqrt{\frac{1}{6}} \cdot (u\bar{u} + d\bar{d} - 2s\bar{s}) \\ V_8 &= \sqrt{\frac{1}{2}} \cdot (u\bar{u} - d\bar{d}). \end{aligned} \tag{3.32}$$

V_8 is called isovector since it has I=1 and I_3=0, where I and I_3 are the isospin and the third component of the isospin, respectively. S_1 and S_8 are called isosinglets having I=0 and I_3=0. Since these two states have the same quantum numbers, they can mix as

$$\begin{aligned} S &= S_8 \cdot \sin\theta_M + S_1 \cdot \cos\theta_M \\ S' &= S_8 \cdot \cos\theta_M - S_1 \cdot \sin\theta_M \end{aligned} \tag{3.33}$$

where θ_M is the mixing angle. Since photons couple to charged particles, the two-photon production mechanism is very suitable to probe the quark content of mesons and in particular to study mixing effects.

The study of resonance formation in two-photon collisions is a very interesting and active field and a lot of important results have been achieved in the last twenty years and, in particular, in the last decade when CESR and LEP storage rings became operational [24, 25, 26].

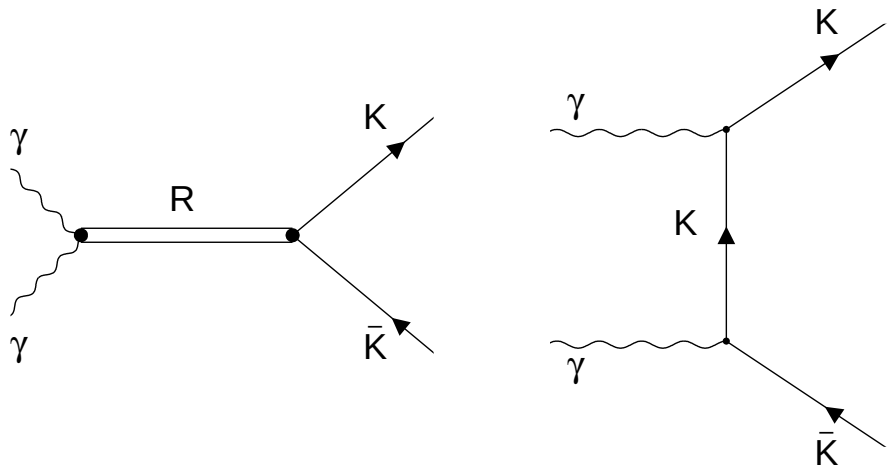

Figure 3.8: Diagrams contributing to the $K\bar{K}$ final state: *s*-channel resonance formation (a) and *t*-channel meson exchange process (b).

3.5.1 The $K^0_S K^0_S$ final state

In this thesis work, the study of the reaction

$$e^+e^- \rightarrow e^+e^-R \rightarrow e^+e^-K^0_S K^0_S \tag{3.34}$$

is performed. Since the K mesons are scalar bosons, the total angular momentum J of the $K^0_S K^0_S$ system is equal to the orbital momentum L and P=$(-1)^L$=+1 because of Bose symmetry. This translates into the condition

$$J^{PC} = (\text{even})^{++}. \tag{3.35}$$

The $K^0_S K^0_S$ final state in two-photon collisions is in particular very much suited for the study of 0^{++} scalar and 2^{++} tensor states. Two main processes contribute to the $K\bar{K}$ final state in two-photon collisions [27], as shown in Figure 3.8. The *t*-channel meson exchange process is responsible for a non resonant continuum contribution that can interfere with resonant states. For charged di-meson final states, such as $\pi^+\pi^-$ or K^+K^-, the interference with the continuum is very important and cannot

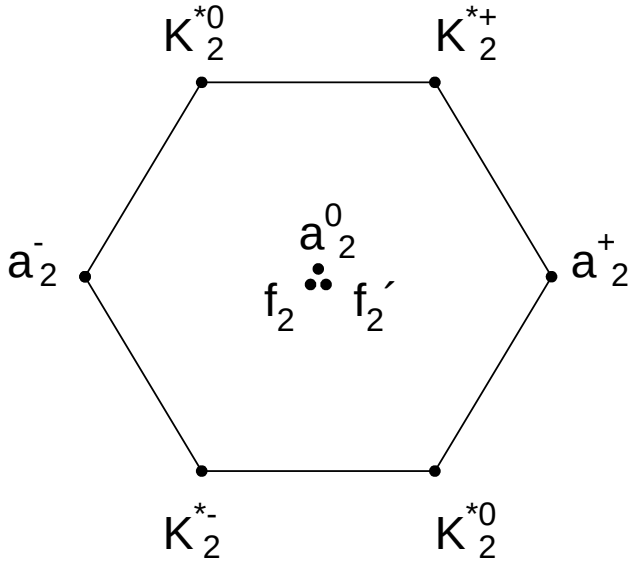

Figure 3.9: The tensor meson nonet.

in general be neglected. Since K^0 mesons are neutral, the non resonant t-channel meson exchange process is highly suppressed in the $K^0\bar{K}^0$ final state and the $K^0_S K^0_S$ final state is therefore dominated by resonance formation.

3.6 Tensor mesons

The 2^{++}, 1^3P_2 tensor meson nonet is shown if Figure 3.9. The three neutral members, the $f_2(1270)$, the $a_2^0(1320)$ and the $f_2'(1525)$, are characterized by a quite large two-photon width and a branching ratio into $K\bar{K}$ ranging from 5% up to 90%, as shown in Table 3.1. They are therefore very well suited to be studied in the $K^0_S K^0_S$ final state in two-photon collisions. However, since these three states are close in mass, interferences must be taken into account. The $f_2(1270)$ interferes constructively with the $a_2^0(1320)$ in the K^+K^- final state but destructively in the $K^0\bar{K}^0$ final state [29, 30]. Despite its smaller two-photon width, the $f_2'(1525)$ is therefore expected to dominate

the $K^0_S K^0_S$ final state.

The $f_2(1270)$–$a^0_2(1320)$ interference is due to the $SU_f(3)$ structure of the tensor meson nonet. This nonet is with good approximation ideally mixed with $\sin\theta_M = \frac{\sqrt{3}}{3}$ and $\theta_M \simeq 35.3^\circ$. In this case Equations (3.32) and (3.33) reduce to

$$\begin{aligned} a^0_2(1320) &= \frac{1}{\sqrt{2}} \cdot (u\bar{u} - d\bar{d}) \\ f_2(1270) &= \frac{1}{\sqrt{2}} \cdot (u\bar{u} + d\bar{d}) \\ f'_2(1525) &= -s\bar{s} \end{aligned} \tag{3.36}$$

where the $f'_2(1525)$ is a pure $s\bar{s}$ state which decays predominantly into $K\bar{K}$ according to the Okubo-Zweig rule. Since charged K mesons contain the quark u and the $u\bar{u}$ terms of the wave functions (3.36) for the $f_2(1270)$ and the $a^0_2(1320)$ have the same sign, a constructive interference is produced. On the other hand, since K^0 mesons contain d quarks, the opposite signs for the $d\bar{d}$ terms are responsible for the destructive interference.

The cross section for the process $\gamma\gamma \to T \to K\bar{K}$, where T is a tensor meson, can be written as [16]

$$\begin{aligned} \sigma_{\gamma\gamma\to K\bar{K}}(W_{\gamma\gamma}) &= (\tfrac{40\pi}{W^2_{\gamma\gamma}})|[\Gamma(f_2 \to \gamma\gamma) \cdot \mathrm{Br}(f_2 \to K\bar{K})]^{1/2} \cdot BW(f_2) \\ &\pm[\Gamma(a_2 \to \gamma\gamma) \cdot \mathrm{Br}(a_2 \to K\bar{K})]^{1/2} \cdot BW(a_2) \\ &+[\Gamma(f'_2 \to \gamma\gamma) \cdot \mathrm{Br}(f'_2 \to K\bar{K})]^{1/2} \cdot BW(f'_2)|^2 \end{aligned}$$

where

$$BW(R) = m_R\sqrt{\Gamma}/[m^2_R - W^2_{\gamma\gamma} - im_R\Gamma]$$

Meson	Mass (MeV)	Width (MeV)	$\Gamma_{\gamma\gamma}$(keV)	Br($K\bar{K}$) (%)
$f_2(1270)$	1275.4 ± 1.2	$185.1^{+3.4}_{-2.6}$	$2.71^{+0.26}_{-0.23}$	4.6 ± 0.5
$a_2(1320)$	1318.0 ± 0.6	107 ± 5	1.00 ± 0.06	4.9 ± 0.8
$f'_2(1525)$	1525 ± 5	76 ± 10	0.096 ± 0.013	88.8 ± 3.1

Table 3.1: The main parameters of the three neutral tensor mesons according to the Particle Data Group [28].

is the relativistic Breit-Wigner amplitude. The "+" sign applies to the K^+K^- while the "-" sign to the $K^0\bar{K}^0$ final state.

The mixing angle can be calculated using the Gell-Mann−Okubo mass formula [28, 31, 32]

$$\tan^2\theta_M = \frac{m_{88}^2 - m_{f_2'}^2}{m_{f_2}^2 - m_{88}^2} \tag{3.37}$$

where

$$m_{88}^2 = \frac{1}{3}(4m_{K^*}^2 - m_{a_2}^2) \tag{3.38}$$

and m_{K^*} is the mass of the $K_2^*(1430)$. This formula gives a value of $\theta_M = 28°$, indicating a small deviation from ideal mixing. A value of 26° is predicted by the linear Gell-Mann−Okubo mass formula which is obtained from Equation (3.37) by replacing m^2 by m.

The study of the formation of tensor mesons in two-photon collisions can probe their quark structure and put in evidence possible deviations from ideal mixing. The two-photon width of a meson R can be written as [16, 19]

$$\Gamma_{\gamma\gamma}(R) = C \cdot g_{R\gamma\gamma}^2 \cdot m_R^3 \tag{3.39}$$

where C is a constant of the nonet, m_R the mass of the meson and $g_{R\gamma\gamma}$ is the coupling constant of the process $\gamma\gamma \to R$. The coupling constant depends on the quark composition as

$$g_{R\gamma\gamma} = \sum_q c_q e_q^2 \tag{3.40}$$

where e_q is the charge of the quark and c_q is the coefficient of the corresponding $q\bar{q}$ term in the meson wave function. Equation (3.39) leads to

$$g_{a_2\gamma\gamma}^2 : g_{f_2\gamma\gamma}^2 : g_{f_2'\gamma\gamma}^2 = \frac{\Gamma_{\gamma\gamma}(a_2)}{m_{a_2}^3} : \frac{\Gamma_{\gamma\gamma}(f_2)}{m_{f_2}^3} : \frac{\Gamma_{\gamma\gamma}(f_2')}{m_{f_2'}^3}. \tag{3.41}$$

Using Equations (3.32), (3.33) and (3.40), the expression

$$\frac{\Gamma_{\gamma\gamma}(a_2)}{m_{a_2}^3} : \frac{\Gamma_{\gamma\gamma}(f_2)}{m_{f_2}^3} : \frac{\Gamma_{\gamma\gamma}(f_2')}{m_{f_2'}^3} = \tag{3.42}$$

$$9 : 3 \cdot (\sin\theta_M + 2\sqrt{2} \cdot \cos\theta_M)^2 : 3 \cdot (\cos\theta_M - 2\sqrt{2} \cdot \sin\theta_M)^2$$

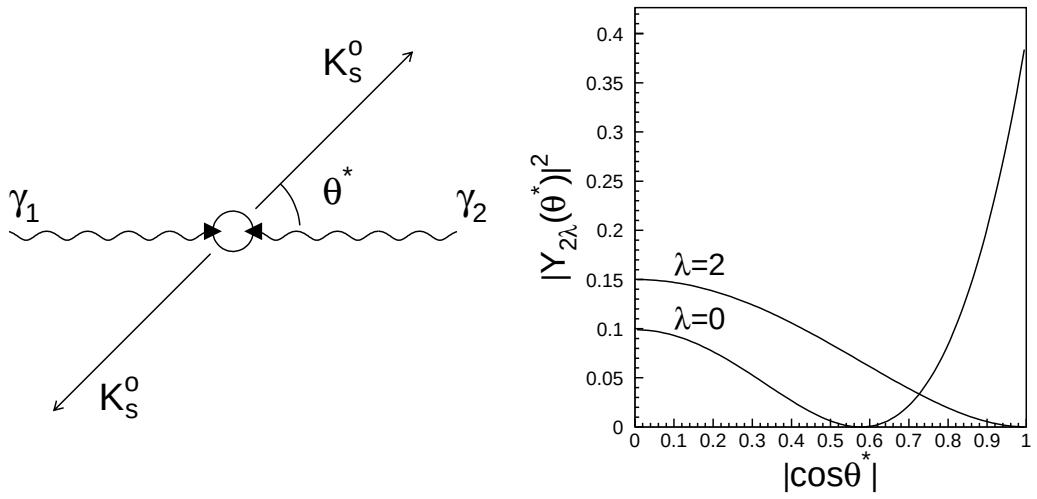

Figure 3.10: The angular distributions as a function of the angle θ^* for a spin-two state decaying into two spin-zero mesons.

is derived. In case of ideal mixing it reduces to

$$\frac{\Gamma_{\gamma\gamma}(\mathrm{a}_2)}{m^3_{\mathrm{a}_2}} : \frac{\Gamma_{\gamma\gamma}(\mathrm{f}_2)}{m^3_{\mathrm{f}_2}} : \frac{\Gamma_{\gamma\gamma}(\mathrm{f}'_2)}{m^3_{\mathrm{f}'_2}} = 9 : 25 : 2.$$

In a collision between two quasi-real photons, a tensor meson can be formed in two different helicity states $\lambda = 0$ or $\lambda = 2$. The corresponding angular distribution for two spin zero mesons produced by its decay is given by the spherical harmonic function squared $|Y^\lambda_2(\cos\theta^*)|^2$. As shown in Figure 3.10, the two angular distributions are very different, especially in the forward region where the acceptance of the detectors is usually very limited, leading to very different detection efficiencies in the two cases. Using only the helicity and the angular momentum conservation, helicity-two tensor states are found to be formed with a ratio 6:1 with respect to helicity-zero states. Moreover, the coupling constant of a tensor meson to two photons of opposite helicity $g_{T,+-}$ is found to be much larger than the coupling constant to two photons of the same helicity $g_{T,++}$. Helicity-two is therefore expected to largely dominate over helcity-zero [33].

Besides the states of the tensor meson nonet 1^3P_2, radially excited tensor states n^3P_2 with n> 1 can be formed. A quite remarkable amount of results on radial excitations has been achieved in the last few years [34] and in particular theoretical predictions for the mass and the two-photon width have been formulated following the OGE-SRM model [35]. The predictions for the excited tensor meson states are reported in Table 3.2. In particular the first radial excitations of the $a_2(1320)$ and the $f_2(1270)$ have a quite large two-photon width and therefore could be observed experimentally. It is interesting to remark that the f_2'' is predicted to have a surprisingly high value of the two-photon width of about 1 keV. Furthermore, the first radially excited f_2 meson is predicted at a mass of 1745 MeV by Celenza et al. [36] and at 1820 MeV by Godfrey and Isgur [37].

The first observation of a radially excited state in two-photon collisions has been recently reported by the L3 Collaboration at LEP [38] in the reaction $\gamma\gamma \to \pi^+\pi^-\pi^0$. The mass spectrum is shown in Figure 3.11 and is dominated by the formation of the $a_2(1320)$ tensor meson. At a mass of $1752 \pm 21 \pm 4$ MeV a clear enhancement is visible and it is found to be dominated by the 2^{++}, helicity 2 wave. This signal has a total width of $\Gamma = 150 \pm 110 \pm 34$ MeV and can be interpreted as the formation of a radial recurrence of the a_2 for which $\Gamma_{\gamma\gamma}(a_2'(1752)) \times BR(a_2'(1752) \to \pi^+\pi^-\pi^0) = 0.29 \pm 0.04 \pm 0.02$ keV in agreement with theoretical predictions and confirming the observation of the CERN-IHEP Collaboration [39] in the reaction $\pi^-p \to \pi^-\pi^-\pi^+p$.

State	Mass (MeV)	$\Gamma_{\gamma\gamma}$(eV)
a_2'	1740	376
a_2''	1820	353
f_2''	1740	1040
f_2'''	1820	982
f_2''''	2130	53
f_2'''''	2160	76

Table 3.2: The predicted values for the mass and the two-photon width for the radially excited tensor mesons [35]

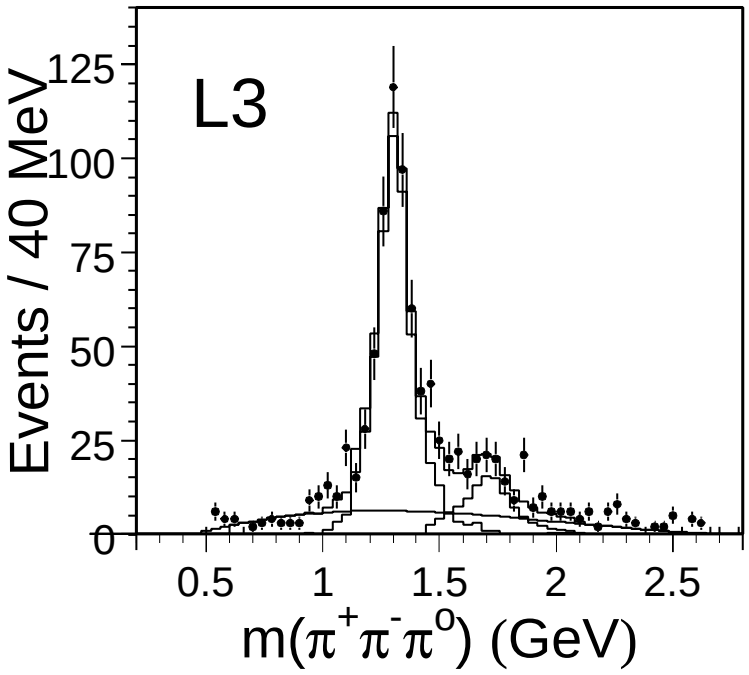

Figure 3.11: The $\pi^+\pi^-\pi^0$ mass spectrum measured by L3.

3.7 Scalar mesons

In contrast to tensor mesons, the scalar meson nonet is not well established and the identification of its members is a long-standing puzzle. The study of scalar resonances is very difficult because of their large decay widths causing overlap between different states and their interference with the scalar wave continuum. Moreover, more than nine scalar meson candidates have been observed experimentally [28]. In particular, more than three neutral scalar states have been established and cannot fit in only one nonet. A summary of the neutral scalar states reported by the Particle Data Group [28] is given in Table 3.3.

3.8 Two-photon collisions and glueball searches

Quantum Chromo Dynamics is a non-abelian gauge theory based on the symmetry group $SU_c(3)$. The eight carriers of the strong interactions, the gluons, interact with themselves and can form bound states called glueballs. In contrast to baryons and mesons which are bound states of fermions kept together by gauge bosons, glueballs are the only form of matter made exclusively by bosonic force carriers. The existence of such bound states is predicted since the very beginning of QCD, before the existence of quarks was set on a solid footing. In 1972 Fritzsch and Gell-Mann [40] predicted the existence of bound states of two gluons which, having the same quantum numbers of mesons, can be put in evidence if ten states with the same J^{PC} are observed instead of nine. In 1975 Fritzsch and Minkowski [41] proposed to extend the Zweig rule to glueball decays. The decay of a glueball proceeding through the coupling of the gluons to a $q\bar{q}$ pair is therefore inhibited if the quark-gluon coupling is sufficiently small. Consequently, a glueball which is below the threshold of decay into two other glueballs and has a mass above ~ 1 GeV is expected to be relatively narrow and to be observed as a resonant state.

Glueballs are expected to be formed in gluon rich hadronic reactions like proton-antiproton annihilations, proton-proton central production and radiative J/ψ decays. Gluons couple equally to quarks of any flavour and the decay of a glueball is expected to be "flavour blind". Since gluons do not couple directly to photons, the two photon width of a glueball is expected to be very small. Figure 3.12 shows the lowest-

State	Mass (MeV)	Width (MeV)	Isospin	J^{PC}
$f_0(400\text{-}1200)$	400 - 1200	600 - 1000	0	0^{++}
$f_0(980)$	980 ± 10	40 - 100	0	0^{++}
$f_0(1370)$	1200 - 1500	200 - 500	0	0^{++}
$f_0(1500)$	1500 ± 10	112 ± 10	0	0^{++}
$f_J(1710)$	1715 ± 7	125 ± 12	0	0^{++} or 2^{++}
$a_0(980)$	984.8 ± 1.4	50 - 100	1	0^{++}
$a_0(1450)$	1474 ± 19	265 ± 13	1	0^{++}

Table 3.3: The scalar states reported by the Particle Data Group [28].

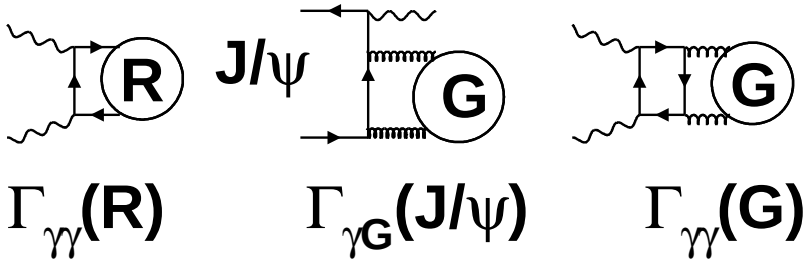

Figure 3.12: The coupling of a meson R to two photons and of a glueball G to two gluons and to two photons.

order diagrams for the two-photon formation of a meson and a glueball and for the production of a gluonium bound state in a radiative J/ψ decay. Of these three mechanisms, only the coupling of a glueball to two photons proceeds via a quark loop and is therefore suppressed. A state that can be formed in a gluon rich environment but not in two photon fusion has the typical signature of a glueball. Two-photon physics plays therefore a fundamental role in this field.

According Lattice QCD calculations [42], the ground state glueball has $J^{PC} = 0^{++}$ and a mass between 1400 and 1800 MeV. The 2^{++} tensor glueball is expected in the mass region around 2200 MeV while the 0^{-+} pseudoscalar glueball is predicted to be heavier.

Since the study of the $K^0_S K^0_S$ final state in two-photon collisions concerns only the scalar and the tensor glueball, the status of the searches for these two gluonium states is briefly reviewed. A summary of the Lattice QCD predictions for their masses is reported in Table 3.4.

3.8.1 The scalar glueball

More than three neutral 0^{++} states have been experimentally observed [28] and one scalar nonet is not sufficient for their classification. Moreover, some of them have a mass in the range 1400-1800 MeV where the scalar glueball is expected. Since 0^{++}

isoscalar mesons and the scalar glueball have the same quantum numbers, mixing effects must be taken into account. They can be responsible for significant changes in the value of the glueball mass with respect to Lattice QCD predictions where these effects are neglected. Moreover, a $q\bar{q}$ glueball mixed state is not expected to be characterized by "flavour blind" decays. The identification of the scalar meson nonet and the evidence of the scalar glueball are therefore two inseparable problems.

According to Amsler and Close [46, 47], the properties of the $f_0(1370)$ and the $f_0(1500)$ are incompatible with being both $q\bar{q}$ states. The $f_0(1370)$ appears to be dominantly $n\bar{n}$, where n is a non strange quark u or d, decaying predominantly into pions. The strong coupling of the $f_0(1500)$ to pions and its low coupling to $K\bar{K}$ imply this state cannot be the $s\bar{s}$ member of the nonet. The $f_0(1500)$ is therefore indicated as the scalar glueball and a new $s\bar{s}$ state, the $f_0'(1500\text{-}1800)$, is predicted to complete the nonet together with the $f_0(1370)$ and the $a_0(1450)$. The $f_0(980)$ and the $a_0(980)$ are considered $K\bar{K}$ molecules.

Very recently Close and Kirk [48] have proposed a model involving the $f_0(1370)$, the $f_0(1500)$ and the $f_0(1710)$, i.e. the $f_J(1710)$ with J=0. These three states are the effect of the mixing of the pure glueball $|G\rangle = |gg\rangle$, the pure $s\bar{s}$ $|S\rangle = |s\bar{s}\rangle$ and the pure non-strange isoscalar $|N\rangle = |u\bar{u} + d\bar{d}\rangle/\sqrt{2}$ state. The mixing between glueball and quarkonia is described by the mass matrix

$$\begin{pmatrix} M_G & f & \sqrt{2}f \\ f & M_S & 0 \\ \sqrt{2}f & 0 & M_N \end{pmatrix} \tag{3.43}$$

where M_G, M_S and M_N are the bare masses of the states before the mixing and $f =$

Reference	m(0^{++}) MeV	m(2^{++}) MeV
[43]	1550 ± 50	2270 ± 100
[44]	$1730 \pm 50 \pm 80$	$2400 \pm 25 \pm 120$
[45]	1648 ± 58	2267 ± 104
[42]	$1611 \pm 30 \pm 160$	$2232 \pm 220 \pm 220$

Table 3.4: The Lattice QCD predicted values for the mass of the ground state scalar and tensor glueball.

$\langle G|M|S|\rangle = \langle G|M|N|\rangle\sqrt{2}$ is the mixing strength between glueball and quarkonia. The three physical states are expressed by

$$\begin{pmatrix} |\mathrm{f}_0(1710)\rangle \\ |\mathrm{f}_0(1500)\rangle \\ |\mathrm{f}_0(1370)\rangle \end{pmatrix} = U \begin{pmatrix} |G\rangle \\ |S\rangle \\ |N\rangle \end{pmatrix} \tag{3.44}$$

where U is a unitary mixing matrix that can be calculated by a fit involving the partial decay widths of the observed states. The result

$$\begin{aligned} |\mathrm{f}_0(1710)\rangle &= 0.39|G\rangle + 0.91|S\rangle + 0.14|N\rangle \\ |\mathrm{f}_0(1500)\rangle &= -0.69|G\rangle + 0.37|S\rangle - 0.62|N\rangle \\ |\mathrm{f}_0(1370)\rangle &= 0.60|G\rangle - 0.13|S\rangle - 0.79|N\rangle \end{aligned} \tag{3.45}$$

indicates a strong mixing between glueball and quarkonia.

Strong mixing is found also by Burakowsky and Page [49] and by Lee and Weingarten [50] using a very similar approach. These two results indicate a dominant glueball component for the higher mass state.

It is interesting to note [51] that in the limit of strong mixing and if M_G lies between M_N and M_S, Equation (3.43) reduces to

$$\begin{aligned} |\mathrm{f}_0(1710)\rangle &\simeq 1/\sqrt{2}\Big(|q\bar{q}(1)\rangle + |G\rangle\Big) \\ |\mathrm{f}_0(1500)\rangle &\simeq |q\bar{q}(8)\rangle + \epsilon|G\rangle \\ |\mathrm{f}_0(1370)\rangle &\simeq 1/\sqrt{2}\Big(|q\bar{q}(1)\rangle - |G\rangle\Big) \end{aligned} \tag{3.46}$$

where $|q\bar{q}(1)\rangle$ and $|q\bar{q}(8)\rangle$ are S_1 and S_8 of Equation (3.32) and ϵ is close to zero. This means that the mixing makes the glueaball leak away from the central mass position towards the lightest and the heaviest states.

Minkowski and Ochs [52] propose a different scenario. In their model, the $\mathrm{a}_0(980)$, the $\mathrm{f}_0(980)$ and the $\mathrm{f}_0(1500)$ are identified as the three neutral members of the scalar nonet with a mixing similar to that of pseudoscalars. The $\mathrm{f}_0(400\text{-}1200)$ and the $\mathrm{f}_0(1370)$ are considered as different signals from a single broad resonance, called "the red dragon", which is identified as the lowest lying 0^{++} glueball, in agreement with the extended Zweig rule. The $\mathrm{a}_0(1450)$ is left out and can be interpreted as a radially excited state.

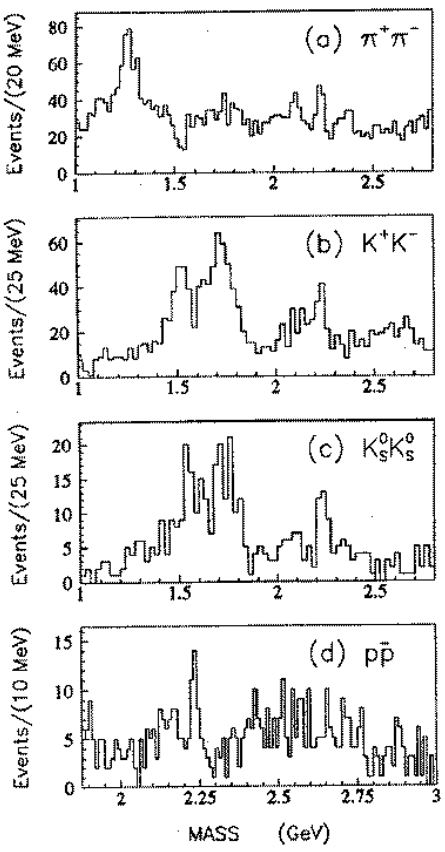

Figure 3.13: The $\pi^+\pi^-$, K^+K^-, $K^0_SK^0_S$ and $p\bar{p}$ mass spectra from radiative J/ψ decays by BES, reporting the observation of the $\xi(2230)$.

According to Gastaldi [53], the coupling of the $f_0(1500)$ and of the $f_0(1370)$ to $K\bar{K}$ are found to be similar, after a reanalysis of bubble chamber data. This leads to the conclusion that the scalar nonet is not ideally mixed and the $f_0(980)$, the $f_0(1370)$ and the $f_0(1500)$ can be interpreted as the isoscalar members of the nonet mixed with the scalar glueball. The $f_0(1370)$ is indicated to have a dominant gluonium component.

3.8.2 The tensor glueball

According to Lattice QCD predictions, the tensor glueball is expected to be in the mass region around 2.2 GeV. Being sufficiently far away from tensor mesons, mixing

effects are expected to be negligible. Because of its mass value, it is expected to be observed as a narrow resonant state, in agreement with the extended Zweig rule.

The $\xi(2230)$ [28], indicated also as the $f_J(2230)$, has a mass of 2231.1 ± 3.5 MeV and a total width of 23 ± 8 MeV and, up to present, is observed only in radiative decays of the J/ψ. Due to its mass value, its narrow width and its production in a gluon rich environment, it is considered a good candidate for the tensor glueball. It was first observed by the Mark III Collaboration [54] in the K^+K^- and $K^0_S K^0_S$ final states. This observation was not confirmed by the DM2 Collaboration [55], even if some activity was seen in the 2.2 GeV mass region. The BES Collaboration recently reported the observation of the $\xi(2230)$ in five different final states K^+K^-, $K^0_S K^0_S$, $\pi^+\pi^-$, $p\bar{p}$ [56] and $\pi^0\pi^0$ [57]. The mass spectra reported by BES [56] are shown in Figure 3.13 where the signals of the $\xi(2230)$ are visible. Since the $\xi(2230)$ is observed in the $p\bar{p}$ final state, it should be observable in $p\bar{p}$ annihilations. The $\xi(2230)$ has been searched by the Crystal Barrel Collaboration at LEAR in $p\bar{p}$ annihilations but no observation has been reported [58]. According to Amsler [47] the $p\bar{p}$ decay width measured by BES is inconsistent with the non observation by Crystal Barrel. A further confirmation of the $\xi(2230)$ in gluon rich environments other than radiative J/ψ decays and its non observation in two-photon collisions are therefore mandatory to support its interpretation as the tensor glueball.

Due to its copious production in radiative J/ψ decays and its observation in proton-proton central production, the $f_J(1710)$, with J=2, is considered a candidate for the tensor glueball by some authors like Minkowski and Ochs [52]. The determination of the spin of this state is therefore very important for the search of the scalar and of the tensor glueball.

Kada, Kessler and Parisi [59] have calculated the two-photon width for the tensor glueball candidates using a non-relativistic gluon bound-state model. They report $\Gamma_{\gamma\gamma}(f_2(1710)) \cdot \mathrm{Br}(K\bar{K}) = 85$ eV and $\Gamma_{\gamma\gamma}(\xi(2230)) \cdot \mathrm{Br}(K\bar{K}) = 1.2$ eV.

3.9 The reaction $\gamma\gamma \rightarrow$hadrons

According to the indetermination principle, a high energy photon can fluctuate into a quark-antiquark pair and interact via strong interactions [60, 61]. In Figure 3.14 four different processes contributing to the production of hadrons in photon-photon

interactions are shown. According to QED, two photons can interact as point-like

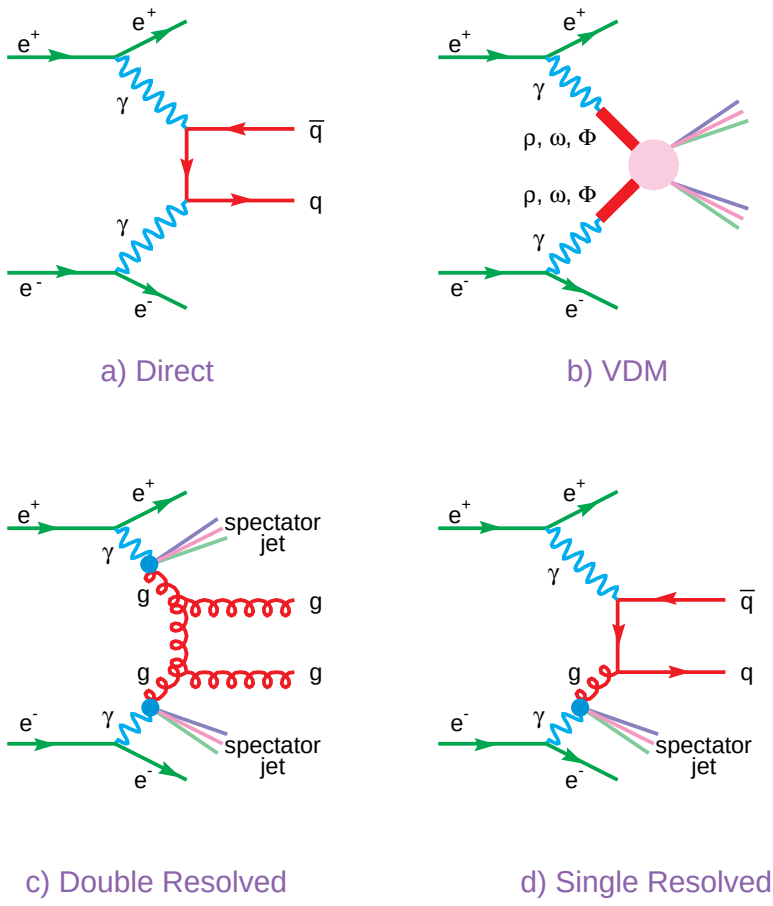

Figure 3.14: Four different contributions to the process $e^+e^- \to e^+e^-$ hadrons.

particles (Figure 3.14(a)), coupling directly to a quark-antiquark pair which will successively fragment into hadrons. As shown in Figure 3.14(b), a photon can also fluctuate into a vector meson (ρ, Φ, ω, ...) and the two-photon interaction can be modeled by assuming the interaction between two vector mesons. This is the Vector Dominance Model (VDM) that dominates soft interactions and opens up all the possibilities of hadronic interactions like Regge poles and Pomeron exchange.

According to QCD, three different processes contribute to the hard interaction of two photons at leading order: the direct (Figure 3.14(a)), the double-resolved

(Figure 3.14(c)) and the single-resolved (Figure 3.14(d)). The single and double-resolved processes are due to the hadronic structure of the photon which is resolved into partons, i.e. into quarks and gluons. The interaction of the hadronic components of the photon depends on the probability of finding a parton in the photon carrying a certain fraction of its momentum. This probability is parametrized by parton density functions.

The dual nature of the photon is taken into account by considering the physical photon as a superposition of a "bare photon" and virtual hadronic states having the same quantum numbers. This translates into the expression

$$|\gamma\rangle = \sqrt{Z_3}|\gamma_{bare}\rangle + \frac{e}{f_{q\bar{q}}}|q\bar{q}\rangle + \frac{e}{f_{q\bar{q}^*}}|q\bar{q}^*\rangle \tag{3.47}$$

where the first term describes the point-like behaviour of the photon, the state $|q\bar{q}\rangle$ corresponds to the superposition of the vector mesons ρ, ω and ϕ and $\pi^+\pi^-$ and the state $|q\bar{q}^*\rangle$ represents the hard interaction. The hadronic interactions are therefore divided into soft and hard interactions, according to the $|q\bar{q}\rangle$ and $|q\bar{q}^*\rangle$ decomposition. Soft and hard interactions are divided by a transverse momentum cutoff p_t^{cut} and the subprocesses involving transverse momenta larger than this scale are calculated by perturbative QCD. A part for the direct QED calculable process, the description of the VDM and QCD parts need some phenomenological input, usually taken from other hadronic processes. The coupling constants and the effective intercepts of the reggeon and the pomeron are needed to model the VDM component and the parton density functions of the photon are needed for the QCD part.

These processes are implemented into Monte Carlo programs which are used to model the reaction $e^+e^- \rightarrow e^+e^-$hadrons. Since an exact calculation of the cross section is not possible, a probabilistic approach to divide the process into several phases is used. First photons are radiated from the colliding beams according to the luminosity function. Then, the quasi-real photons interact via a sub-process, according to Figure 3.14 and Table 3.5. For the hard processes, the parton density functions of the photon are used to select the interacting parton and to initiate the elementary subprocess. A parton shower is then generated and, finally, the partons are converted into hadrons which are allowed to decay.

To model the process $e^+e^- \rightarrow e^+e^-$hadrons, we have used two Monte Carlo programs: PHOJET [62] and PYTHIA [63].

VDM	Models
Direct	$\gamma\gamma \to q\bar{q}$
Single resolved	$\gamma q \to qg$
	$\gamma g \to q\bar{q}$
Double resolved	$gg \to q\bar{q}$
	$gg \to gg$
	$qq' \to qq'$
	$\vdots$

Table 3.5: The sub-processes used by the event generators.

PHOJET is a general purpose Monte Carlo generator for hadronic pp, ep and $\gamma\gamma$ interactions by Engel and Ranft. The interactions are described within the Dual Parton Model (DPM) [64] in terms of reggeon and pomeron exchanges. The probabilities $e^2/f^2_{q\bar{q}}$ and $e^2/f^2_{q\bar{q}^*}$ to find the photon in one of the hadronic states, the coupling constants of the reggeon and the pomeron and the effective intercepts are treated as free parameters and are extracted from cross section fits on photoproduction data. In this way, once these parameter are fixed, two-photon collisions can be described without further new parameters.

PYTHIA is a general purpose Monte Carlo generator of high-energy particle physics reactions. The generation of hadron production in two-photon collisions is based on the SaS approach by Schuler and Sjöstrand [65] that aims at a smooth superposition of hadron-like and point-like photon interactions. Also here, the parameters describing soft and hard processes are tuned on γp data. PYTHIA is conceived to deal only with real photons. In L3 we have implemented into the program a luminosity function with a Q^2 cut of $Q^2 < m^2_\rho$.

LEP2 is well suited for the study of the process $e^+e^- \to e^+e^-$hadrons. The high beam energies give the possibility to reach high values of $W_{\gamma\gamma}$ and to produce high transverse momentum particles. This allows to reach the perturbative regime where reliable QCD predictions for hard processes can be formulated. Moreover, being far away from the Z pole, the background coming from e^+e^- annihilation can be easily reduced to a negligible fraction, allowing to test perturbative QCD predictions in a good experimental environment.

3.10 Inclusive single hadron production and QCD predictions

The study of inclusive single hadron production is an important testing ground for the theory of strong interactions. In particular, large transverse momentum particles are produced by hard hadronic interactions which can be described by perturbative QCD. The study of high p_t hadron production is today an alternative and complementary way to test QCD predictions with respect to jet production. The study of high p_t hadrons was in fact one of the first proofs of the partonic structure of the hadrons and hence of QCD.

The high energies available at LEP2 allow to reach the high p_t perturbative regime also in two-photon collisions. The high p_t spectrum is therefore expected to be dominated by the QCD processes examined in the previous paragraph, i.e. the direct, the single resolved and the double resolved, while at low p_t the VDM process is expected to be dominant. The cross section as a function of the transverse momentum is therefore expected to show an exponential decrease, typical of hadronic interactions, at low p_t. At high p_t the hard processes are expected to produce a rise above the experimental VDM exponential.

The cross section of inclusive single hadron production is given by the convolution of the parton-parton scattering cross section with the parton density function of the initial state and the fragmentation functions which characterize the transition between the partons coming out of the interaction and the final hadrons. While the partonic cross sections can be perturbatively calculated from QCD Feynman diagrams, the parton density functions and the fragmentation functions have to be determined from experimental data.

In the Next-to-Leading Order (NLO) QCD approximation, diagrams of higher order in α_s are considered to compute the cross section. Figure 3.15 shows the Leading Order processes together with the higher order α_s processes which are considered in the NLO approximation. The higher order α_s processes are characterized by the emission of a real gluon or by the presence of a virtual gluon. Binnewies, Kniehl and Kramer have recently formulated theoretical QCD predictions for the inclusive production of charged hadrons [66] in photon-photon collision in the NLO approximation, using the Gordon and Storrow [67] parameterization for the parton density

functions.

3.11 The K^0_S inclusive production

The study of K^0_S inclusive production in hadronic two-photon collisions is complementary with respect to the study of charged hadron production. Since K^0_S's contain the quark s, the VDM contribution is given mainly by the fluctuation of the photon into a ϕ vector meson. Considering QCD hard processes and neglecting quark masses, direct strange quark production is suppressed by a factor 16 with respect to direct charm production. Therefore a large fraction of the K^0_S's produced in hadronic two-photon collisions come from the decay of primary charm quarks. The detection of K^0_S mesons can therefore be used as a charm quark tagging method. However, since a substantial number of strange quarks come from the VDM process and from the fragmentation of u and d quarks, a good modeling of these processes is mandatory in order to have a good charm tagging. At present, this method of charm tagging has been used only by TOPAZ [68].

NLO QCD predictions for K^0_S inclusive production in photon-photon interactions have been formulated by Kniehl and the OPAL Collaboration [69] has performed a study of this process at LEP2. In this thesis work, a study of this process is performed with the L3 detector at LEP2. The experimental results are compared with the QCD theoretical predictions and with the results published by OPAL.

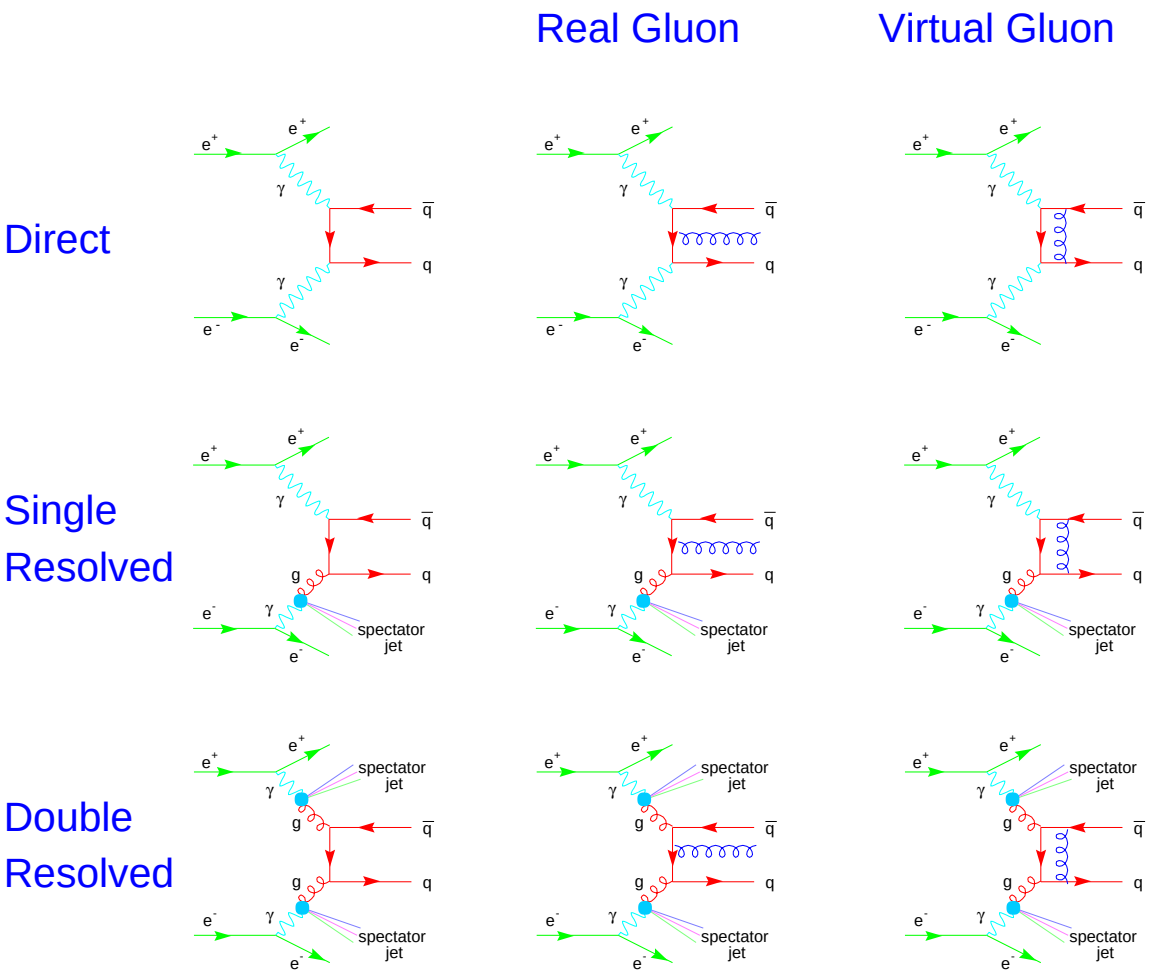

Figure 3.15: Some diagrams contributing to hadron production in $\gamma\gamma$ collisions in the Next-to-Leading Order QCD approximation.

Chapter 4

LEP and the L3 detector

4.1 The Large Electron Positron collider

The Large Electron Positron collider (LEP) [70] is the largest circular accelerator which has been built at CERN to study e^+e^- collisions at centre of mass energies from the Z pole up to 200 GeV. The aim of the LEP project is to perform very high precision tests of the Standard Model of fundamental interactions based on the study of the Z boson and of W^+W^- pairs produced in electron-positron annihilations. As mentioned in Chapter 3, LEP is also the most powerful photon-photon collider available at present.

The first studies for the construction of the LEP machine were performed at CERN [71] in 1976, seven years before the discovery of the weak force boson carriers W^+, W^- and Z. LEP was approved in 1981 and its construction started in 1983. Since the first e^+e^- collisions at the Z pole in 1989, LEP has been characterized by a continuously increasing performance in terms of energy and of luminosity producing a very remarkable amount of data and results. The LEP program ended in November 2000 after having reached the centre of mass energy value of 208 GeV, well above the design maximum energy.

LEP is situated by the French-Swiss border near Geneva and has a circumference of about 26.7 Km, as shown in Figure 4.1. The tunnel is located between 50 and 150 meters underground and is inclined at an angle of 0.8° with respect of the horizontal plane for geological reasons. The LEP ring is made of eight straight and eight

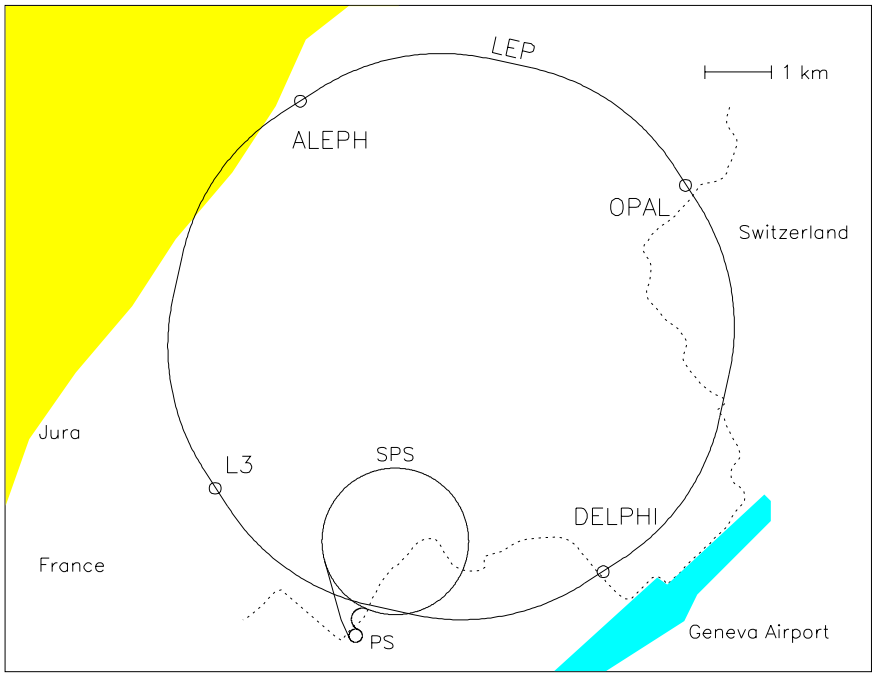

Figure 4.1: Schematic view of LEP with the four experiments ALEPH, DELPHI, L3 and OPAL.

curved sections. The curved sections are equipped with bending dipole and focusing quadrupole and sextupole magnets. LEP was originally equipped with 128 copper radio-frequency (RF) cavities giving an accelerating voltage of 300 MV. The energy loss due to the emission of synchrotron radiation is proportional to E^4/ρ, where E is the beam energy and ρ the radius of the accelerator. At 45 GeV the loss is about 85 MeV per turn which increases above 2 GeV for beam energies above 100 GeV. To reach higher and higher energies and to compensate the energy losses due to synchrotron radiation, the copper cavities have been replaced during the years by super conducting niobium cavities. The accelerating voltage in the year 2000 was of 3650 MV with 56 copper and 288 niobium cavities.

In the beam pipe of LEP four (eight in 1995) bunches of electron and positrons circulate in opposite directions and collide in four of the eight straight sections of

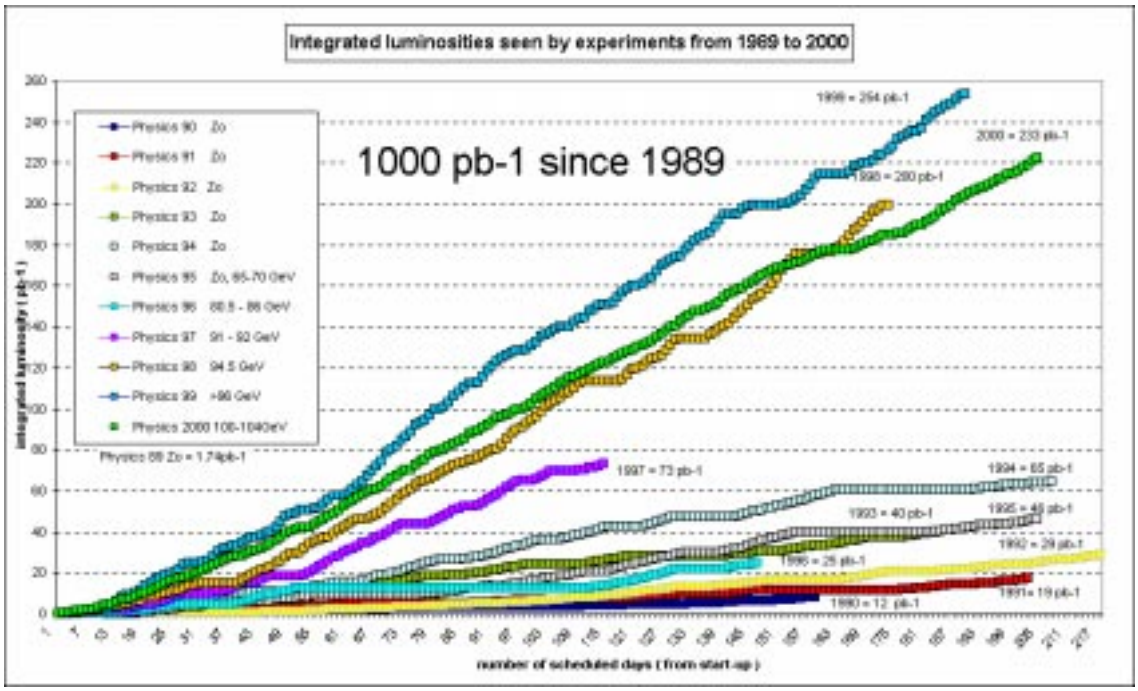

Figure 4.2: The integrated LEP luminosity per experiment as a function of the number of days of data taking for the years 1989-2000.

the accelerator. These four collision points are equipped with four general purpose detectors ALEPH, DELPHI, L3 and OPAL.

The luminosity delivered by an electron-positron collider is given by

$$\mathcal{L} = \frac{N_{e^+} N_{e^-} N_b f_{rev}}{4\pi\sigma_x\sigma_y} \tag{4.1}$$

where N_{e^+} and N_{e^-} are the number of electrons and positrons per bunch, N_b the number of bunches, σ_x and σ_y are the transverse dimensions of the beams at the colliding points and f_{rev} is the revolution frequency. To maximize the luminosity, the beams are focussed by a doublet of quadrupole magnets on each side of the interaction points. The beam dimensions in these points are about 10 μm vertically and about 250μm horizontally.

To reach the high energies of the LEP machine, a chain of injectors is used. Electron and positron beams are produced by two linacs of 200 and 600 MeV. They

are then directed toward the Electron-Positron Accumulator (EPA) where are stored in bunches of about 10^{10} particles. These bunches are then injected into the Proton Synchrotron (PS) where they reach the energy of 3.5 GeV. To be further accelerated, the electron and positron bunches are injected into the Super Proton Synchrotron (SPS). Here they reach the energy of 22 GeV and are successively injected into the LEP machine. When the LEP ring is filled with about $5 \cdot 10^{11}$ particles per bunch, the energy is increased to its final value. After the filling and accelerating phases, the beams keep colliding up to when the beam current is too low and the beams are dumped. The full duty cycle of LEP lasts about eight hours at the Z pole and about four hours at high energies.

The measurement of the beam energy is performed with several methods among which the main one is based on resonant depolarization. The beam energy is determined with a precision of better than 1 MeV at LEP1 and of about 25 MeV at LEP2 [72].

Figure 4.2 shows the luminosity delivered by LEP to each of the four experiments as a function of time for several years of data taking. Continuous improvements on the energy and integrated luminosity have characterized the LEP program, in particular during the data taking at high energies.

4.2 The L3 detector

The L3 experiment [73] is situated about 50 meters underground and is the largest among the four LEP detectors. The design of L3 is optimized to measure muons, electrons and photons with high precision.

A perspective of the L3 detector is shown in Figure 4.3. All the subdetectors are surrounded by a magnet of 7800 t producing a uniform solenoidal field of 0.5 T directed along the beam line. Inside the magnet, a 240 t steel support tube with a diameter of 4.45 m and a length of 32 m divides the detector into two parts. In the part between the magnet and the support tube, the three layer high precision muon spectrometer is located while all the other subdetectors are contained inside the support tube. As shown in Figure 4.4, the following main subdetectors are situated inside the support tube:

- the central tracking system composed by a silicon microvertex detector and a

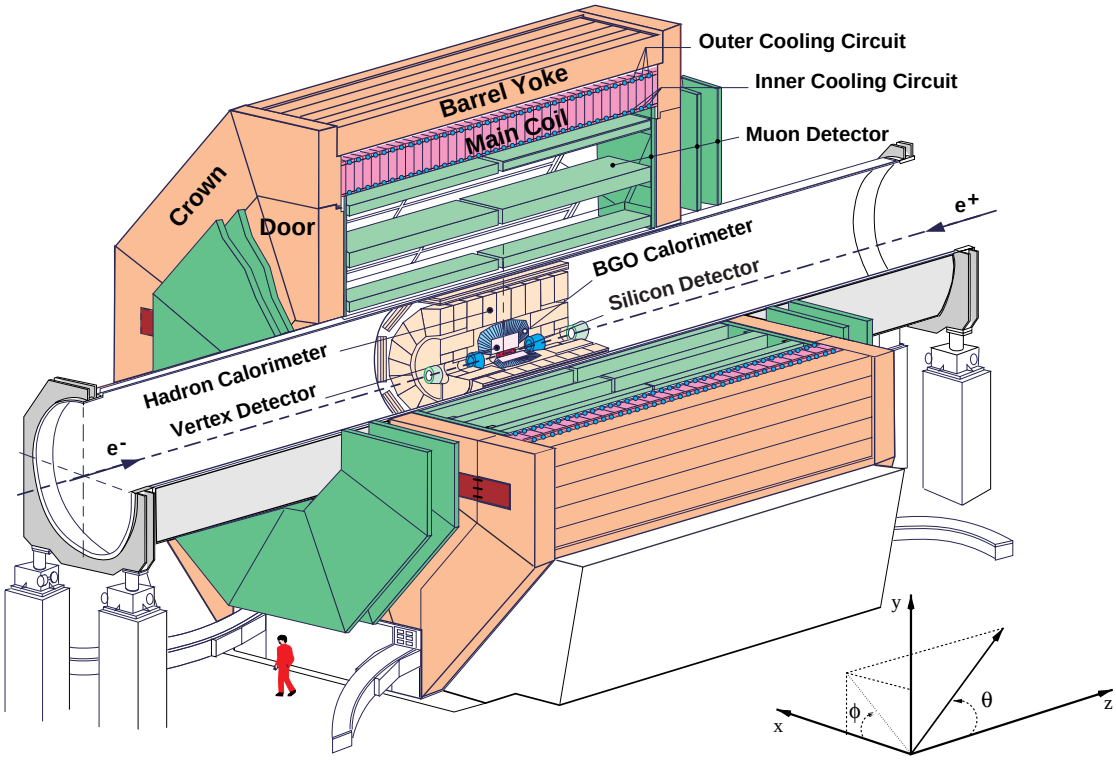

Figure 4.3: Perspective of the L3 detector.

drift chamber

- the high resolution electromagnetic calorimeter made by BGO crystals
- the sampling hadron calorimeter made by depleted uranium absorber and wire proportional chambers.

The right-handed L3 coordinate system is defined as follows, according to Figure 4.3. The origin is situated in the e^+e^- interaction point, the x axis is pointing towards the center of LEP, the y axis is directed upwards and the z axis is parallel to the beam line in the direction of the electron beam and the magnetic field. The polar angle $\theta \in [0, \pi]$ is defined with respect to the positive z direction and the azimuthal angle $\phi \in [0, 2\pi]$ is the angle in the xy-plane with respect to the positive x direction.

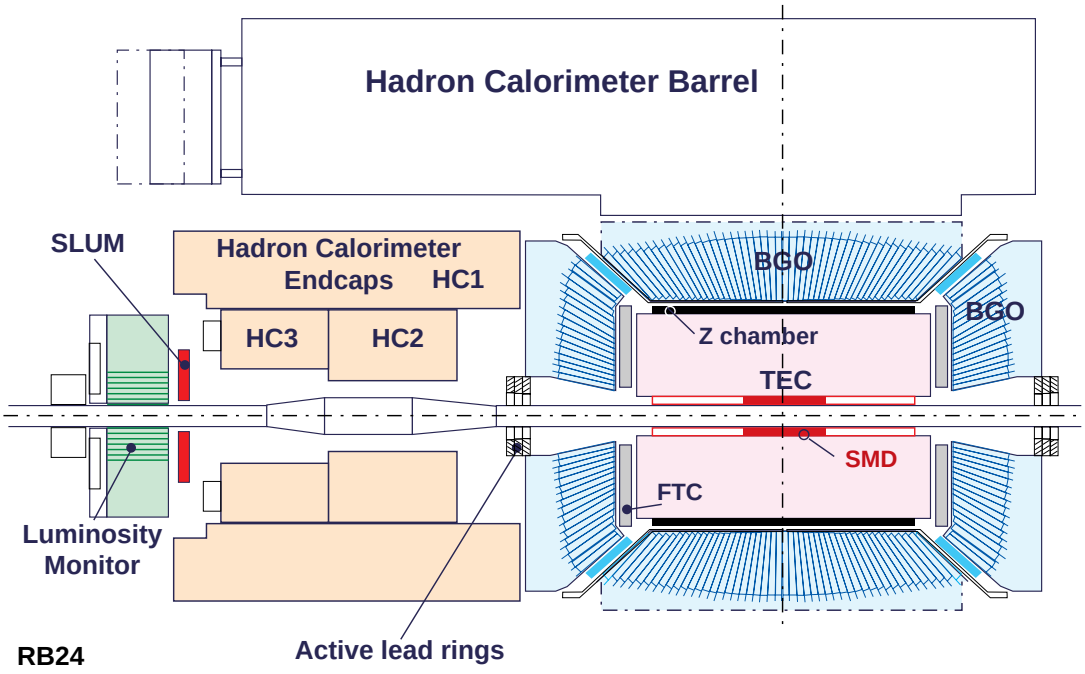

Figure 4.4: Side view of the inner part of the L3 detector.

4.3 The central tracking system

The central tracking system is used to measure the momentum, the charge, the position and the ionization loss dE/dx of charged particles produced by the e^+e^- interaction. Furthermore it is used to determine the position of the interaction point of the LEP beams and to determine secondary vertices formed by particles with a lifetime larger than 10^{-13} seconds. The signals from the central tracking system are also used by the charged particle trigger of L3. The compact design of the inner detector contained inside the support tube and the relatively low value of the magnetic field made the conception and the construction of the L3 central tracking system a difficult and challenging task.

The central tracking system is composed by four subdetectors:

- the Silicon Microvertex Detector (SMD)

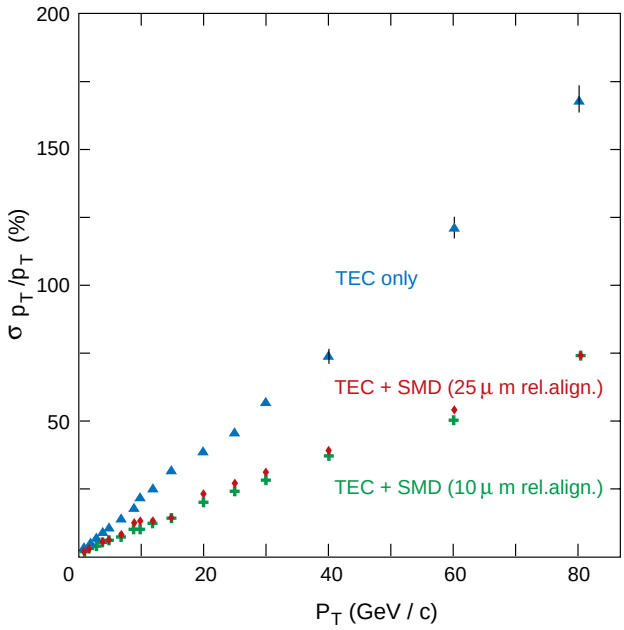

Figure 4.5: Transverse momentum resolution of the central tracking system for tracks with and without SMD hits.

- the Time Expansion Chamber (TEC)
- the Z chambers
- the Forward Tracking Chambers (FTC).

Figure 4.5 shows the resolution of the central tracking system as a function of the the transverse momentum for tracks with and without hits in the SMD. For tracks without SMD hits the resolution can be parametrized as $1.7\% p_t(\mathrm{GeV}) + 3\%$. The resolution for the angle ϕ is estimated to be better than 0.9 mrad.

Figures 4.6(a, b, c, d) show the resolution for $1/p_t$ and for the DCA calculated with 45 GeV muons. The improvement on the resolution due to the SMD is about a factor two for $1/p_t$ and a factor three for the DCA.

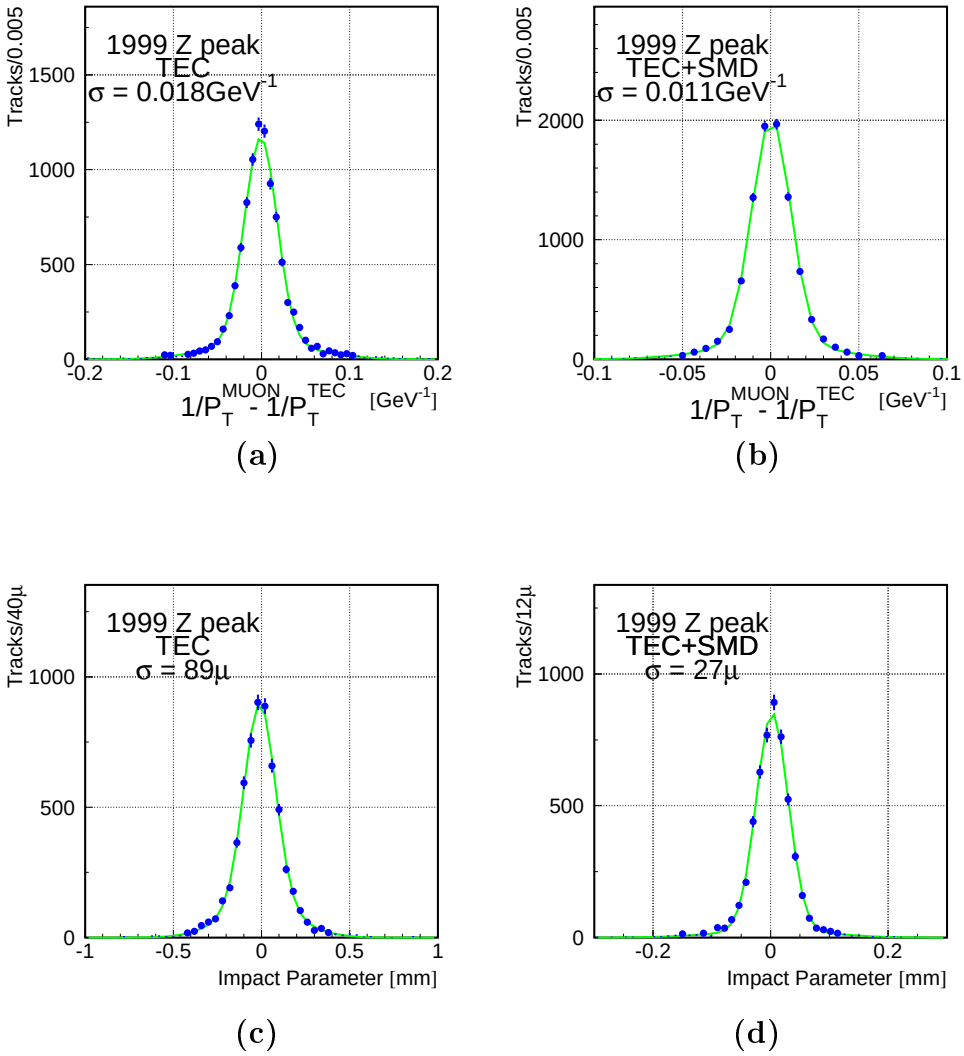

Figure 4.6: The resolution of the central tracking system for $1/p_t$ and for the DCA without (a, c) and with (b, d) the SMD calculated with 45 GeV muons.

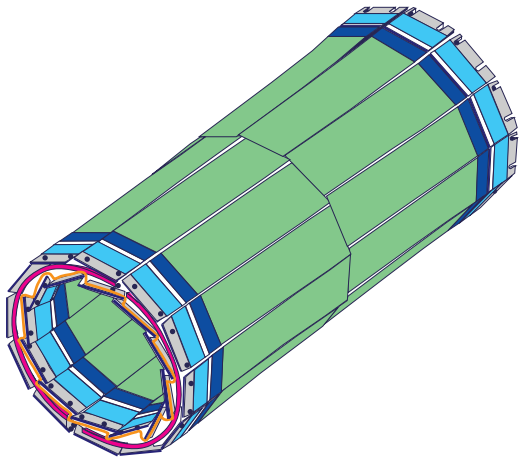

Figure 4.7: Perspective view of the Silicon Microvertex Detector.

4.3.1 The silicon microvertex detector

The Silicon Microvertex Detector (SMD) [74], shown in Figure 4.7, was installed in the L3 detector in 1993 to improve the tracking resolution, in particular for the reconstruction of very near secondary vertices as in the decay of mesons containing the quark bottom. It is made of two layers of double-sided silicon microstrips at radial distances of 6 and 8 cm from the interaction point. Each layer consists of 12 ladders in ϕ and each ladder is made of four wafers of silicon. The resolution of this detector is of 7 μm in the r-ϕ plane and of 14 μm in the r-z plane. The angular coverage in θ is between 21° and 159°.

4.3.2 The Time Expansion Chamber

The Time Expansion Chamber (TEC) is shown in Figure 4.8 and consists of two concentric high precision drift chambers which share the same gas volume and the same end flange plates. The TEC has an inner radius of 8.5 cm, an outer radius of 45.7 cm, a length of 97 cm and a lever arm of 37 cm. The angular coverage in θ is between 25° and 175°. The Inner TEC extends radially from 8.5 to 14.3 cm and is subdivided into 12 sectors covering 30° in ϕ. The Outer TEC is divided in 24 sectors covering 15°. Since the lever arm is constrained by the limited available space, this

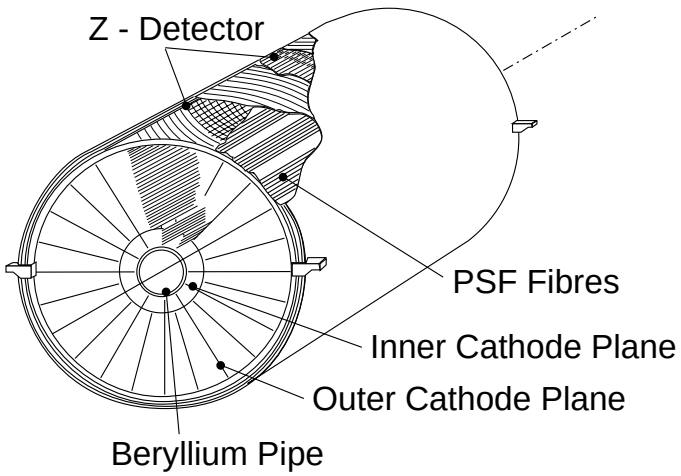

Figure 4.8: Perspective view of the Time Expansion Chamber.

configuration is chosen in order to have the largest possible ratio of the drift volume over the detection volume, a factor which maximizes the spatial resolution.

To obtain a good spatial and momentum resolution, the TEC operates according to the principle [75] shown in Figure 4.9(a). The electrons, produced by the ionization induced by a charged particle, drift towards the anode wires in a low electric field zone which is separated from the amplification region by a grid wire plane. The low drift velocity of about 6 μm/ns allows a precise measurement of the centroid of the time distribution of the signal on the anode wires. In this way resolutions of 56 μm and 46 μm are obtained for a single wire in the Inner and in the Outer TEC, respectively. These values have to be compared with the standard resolution of 125 μm typical for a drift chamber.

In the radial direction 62 anode wires are present, 8 belonging to the Inner and 54 to the Outer TEC, respectively. The wires are arranged as shown in Figure 4.9(b). The asymmetry in the number of sectors between the Inner and the Outer TEC is used to resolve the left-right ambiguity. Each sector of the TEC is equipped with three different categories of wires:

- 37 (6 in the Inner TEC) standard anode wires

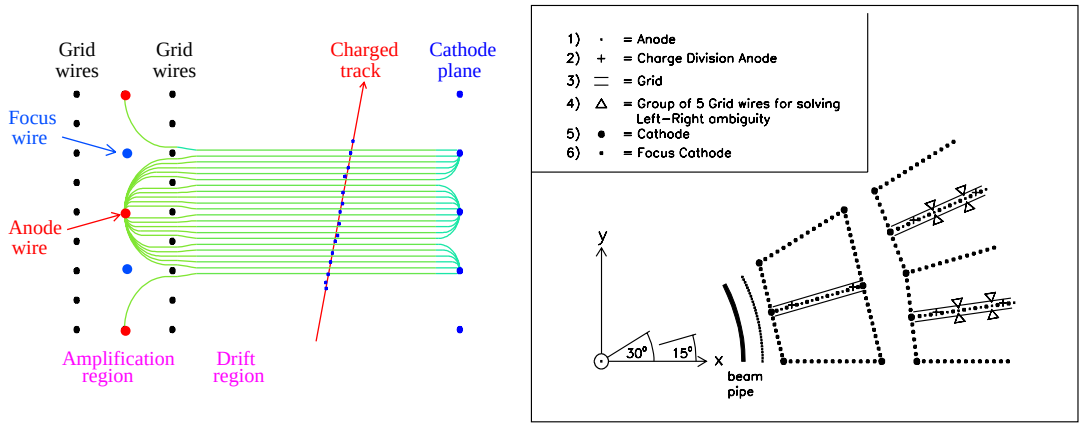

(a) (b)

Figure 4.9: (a) Scheme of the drift and of the avalanche gas amplification in the TEC. (b) Configuration of the wires in a Inner TEC sector with a part of the corresponding two Outer TEC sectors.

- 11 (2 in the Inner TEC) Charge Division (CD) wires
- 14 Left-Right (LR) wires.

The standard anode wires are read out only at one end and are optimized for a high precision measurement in the transverse plane. The Charge Division wires are used to determine the hit position in both the transverse plane and the z direction. The signals collected at both the extremities of these wires are read out and the z coordinate is determined using the charge division method with a precision of about 2 cm. In correspondence of the Left-Right wires the signal of five nearby grid wires is read out on both sides. This information is used to resolve the left-right ambiguity together with the geometrical asymmetry between the inner and the outer sectors [76].

The TEC operates with a gas mixture of carbon dioxide CO_2 (80%) and isobutane $i{-}C_4H_{10}$ (20%). The quantity of oxygen is kept below one part per billion in order to minimize recombination and aging effects. Since the drift velocity depends on the electric field E, on the pressure p, on the temperature T and of the fraction of isobutane f as $v_d \sim \mathrm{ET}f/p$ all these quantities are continuously monitored with

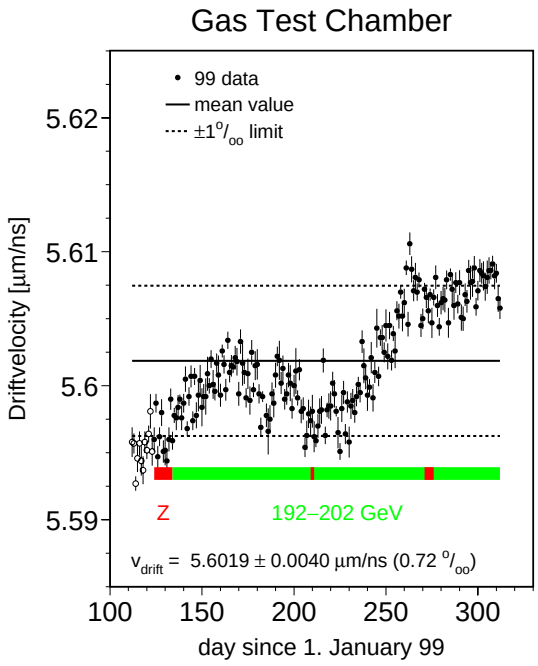

Figure 4.10: The drift velocity as a function of time for the 1999 data taking.

high precision. In particular, the stability of the drift velocity is controlled with a precision of about $2 \cdot 10^{-3}$ by using a gas test chamber, as shown in Figure 4.10. A Plastic Scintillating Fibers (PSF) system is also used to monitor the drift velocity.

4.3.3 The Z chambers

The Z chambers consist of a double layer of cylindrical proportional wire chambers covering the outside cylinder of the TEC. They are designed to provide additional information about the z coordinate of the tracks. Their length is 1068 mm and are composed by 920 cathode strips with an angular coverage of $45° < \theta < 135°$. The resolution is 320 μm for tracks crossing the chambers perpendicularly.

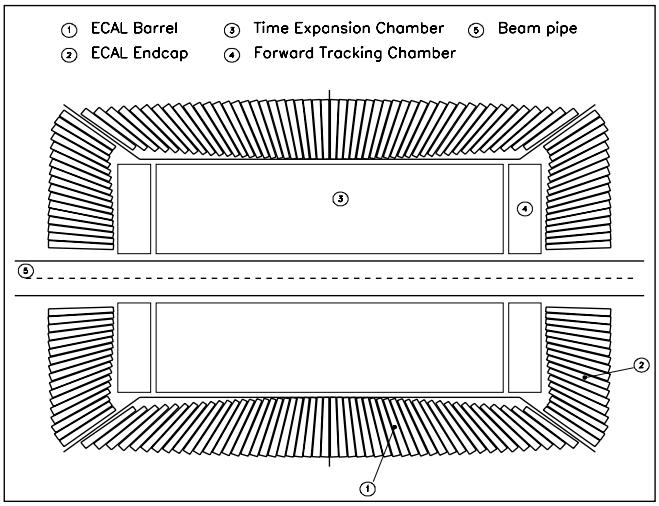

Figure 4.11: Side view of the electromagnetic calorimeter.

4.3.4 The Forward Tracking Chambers

The Forward Tracking Chambers (FTC) are situated in the angular regions $12° < \theta < 34°$ and $146° < \theta < 168°$ behind the 0.7 radiation length thick TEC end flange. They are made of two orthogonal layers of cylindrical multi-wire drift chambers. Because of the presence of the TEC end flange, the resolution is limited to 200 μm.

4.4 The electromagnetic calorimeter

The electromagnetic calorimeter consists of about 11000 crystals of bismuth germanate ($Bi_4Ge_30_{12}$ indicated also as BGO) which are both the showering and the detecting medium. All the crystals point to the interaction region and each crystal has the form of a 24 cm long truncated pyramid with a section of 2×2 cm^2 at the inner and 3×3 cm^2 at the outer end. Each crystal is housed in its own cell of a carbon fiber structure and kept against the front end of the structure by a spring-loaded holding device. Since the calorimeter is inside the magnetic field, the BGO scintillation light is read out on each crystal by two photodiodes.

As shown in Figure 4.11, the electromagnetic calorimeter consists of a barrel part

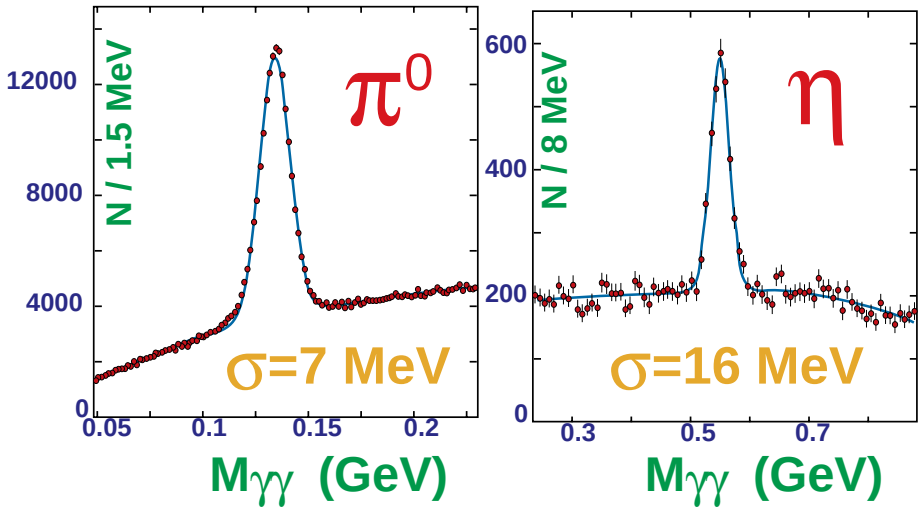

Figure 4.12: The signals of π^0 and η mesons.

and two end-caps covering approximately 94% of the solid angle. The barrel part of the calorimeter covers the polar angular range $42° < \theta < 138°$ and the endcaps the ranges $12° < \theta < 38°$ and $142° < \theta < 168°$.

The main advantages of BGO are the high light yield, the high energy resolution and the very short radiation length of 1.12 cm which allows the construction of a very compact calorimeter. The precision on the energy measurement for an electromagnetic shower in the barrel region can be parametrized as

$$\frac{\sigma(E)}{E} = \sqrt{\left(\frac{a}{\sqrt{E}} + b\right)^2 + d^2 + \frac{c^2}{E^2}} \tag{4.2}$$

where E is the energy expressed in GeV and

$$\begin{aligned} a &= 1.54 \times 10^2 \mathrm{GeV}^{0.5} \\ b &= 0.38 \times 10^{-2} \\ c &= 0.25 \pm 0.15 \times 10^{-2} \\ d &= 1.18 \pm 0.11 \times 10^{-2}. \end{aligned}$$

The parameters a and b are measured in a test beam facility and are due to the BGO shower statistics. The intercalibration term d and the electronic noise term c

are obtained directly from the data [77]. This leads to a resolution of 5% at 100 MeV and of 1.4% above 2 GeV. The angular precision is of 0.5° for energies above 1 GeV.

The BGO electromagnetic calorimeter has an angular gap of 4° between the barrel and the endcaps. In order to improve the hermeticity of the calorimeter, this gap has been instrumented in 1996 with a " spaghetti" calorimeter made of lead absorber filled with scintillating fibers [78].

In the study of two-photon interactions, the high precision and the high sensitivity for low energy photons of the BGO electromagnetic calorimeter is very important. In particular the calorimeter can be used to veto photons in the study of exclusive final states with only charged particles and to reconstruct mesons like π^0 and η, as shown in Figure 4.12.

4.5 The scintillators

A layer of plastic scintillation counters is located between the electromagnetic calorimeter and the hadron calorimeter. The scintillators have the main task to distinguish cosmic muons from di-muon events. The time-of-flight difference between two opposite counters is zero for di-muon events and 5.8 ns for cosmic muons. With a resolution of less than 1 ns a good cosmic muon rejection is achieved.

4.6 The hadron calorimeter

The hadron calorimeter is shown in Figure 4.13. It consists of a barrel and two end-caps covering 99.5% of the solid angle. The calorimeter is made of 5 mm thick depleted uranium absorber plates and rectangular proportional wire chambers with a 80% Ar and 20% CO_2 gas mixture.

The barrel covers the angular region $35° < \theta < 145°$ and has a modular structure consisting of 9 rings of 16 modules each. The three central rings are made up of 910 mm length modules containing 60 multiwire proportional chambers and 58 uranium plates. The other modules have a length of 816 mm and contain 53 chambers and 51 uranium plates.

The two end-caps cover the polar angular ranges $5.5° < \theta < 35°$ and $145° < \theta < 174.5°$, respectively. Each end-cap consists of 3 rings, an outer ring and two inner

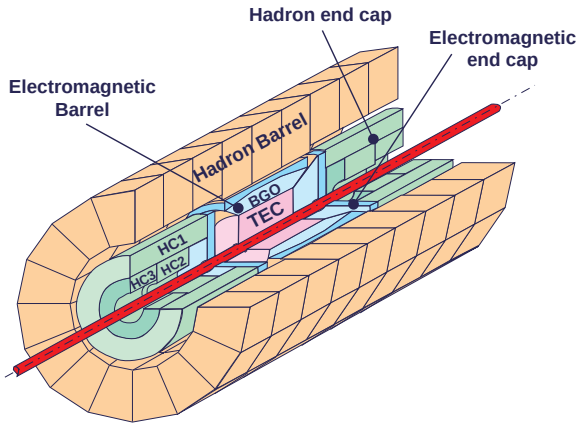

Figure 4.13: Perspective view of the hadron calorimeter.

rings, of 12 modules each.

The energy resolution is given by

$$\frac{\sigma(E)}{E} = \left(\frac{55}{\sqrt{E}} + 5\right)\% \tag{4.3}$$

where E is expressed in GeV.

4.6.1 The muon filter

The muon filter is located between the hadron calorimeter and the support tube and consists of eight identical octants, each made of six 1 cm absorber plates (65% Cu and 35% Zn) interleaved with five layers of proportional chambers. A 1.5 cm thick absorber is then used to match the circular shape of the support tube. With its 1.03 absorption lengths it prevents the tails of the hadronic showers to enter the muon chambers.

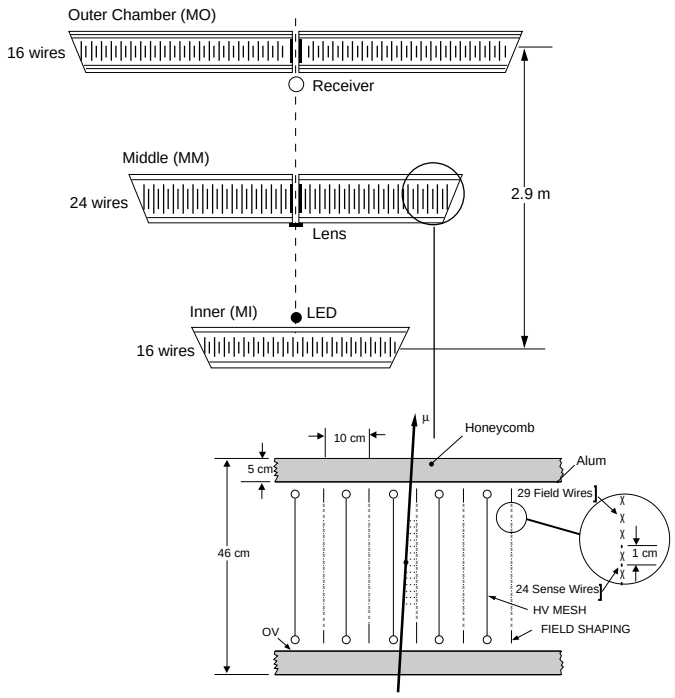

Figure 4.14: Scheme of one octant of the muon spectrometer.

4.7 The muon spectrometer

The muon spectrometer is composed by two parts, one in the positive and one in the negative z direction, composed by 8 octants mounted on the support tube. As shown in Figure 4.14, each octant consists of a mechanical structure supporting three layers of drift chambers allowing the determination of the sagitta of a muon track with a lever arm of 2.9 m. The inner and the outer layers of every octant are equipped with z-measuring drift chambers.

The muon spectrometer has a precision of 2.5% for a 45 GeV muon. In this case the sagitta is of 3.5 mm which is measured with an accuracy less than 88 μm. To obtain this high precision a UV laser system is used for the alignment of the spectrometer.

In order to extent the angular coverage, the L3 detector has been equipped in 1995 with a forward-backward muon spectrometer [79]. It consists of 96 drift chambers

organized in three layers allowing a θ angular coverage down to 24°.

4.8 The forward-backward detectors

To maximize the solid angle coverage and to tag beam scattered electrons and positrons for the study of tagged two-photon collisions, the L3 detector is equipped with three forward-backward subdetectors.

4.8.1 The Very Small Angle Tagger

The Very Small Angle Tagger (VSAT) [80] was installed in 1996 and consists of four aluminum boxes containing 24 BGO crystals each. These boxes are installed two-by-two at each side of the interaction point at a distance of 8.05 m. The angular acceptance in θ is from 5 to 10 mrad and in ϕ from -1 to 1 rad and from $\pi - 1$ and $\pi + 1$ rad.

4.8.2 The luminosity monitor

The luminosity monitor has been designed to measure precisely the low angle Bhabha scattering cross section used to determine the integrated luminosity [81]. It is also used to tag scattered beam particles in two-photon collisions. The luminosity monitor is composed of two cylindrical detectors composed by a matrix of BGO crystals installed at 2.65 m away from the interaction point. The angular coverage in θ is from 24.7 to 69.3 mrad. Each cylindrical detector is divided into two parts that can be moved away from the beam pipe by an hydraulic system to protect the crystals from radiation damage caused by unstable beam during the filling and the acceleration phases of LEP.

4.8.3 The Active Lead Rings

The Active Lead Rings [82] are composed of three layers of scintillator of 10 mm thickness placed behind 18.5 mm of lead. The scintillators have the form of truncated equilateral triangles and are read out by photodiodes. Each scintillator subtends 22.5° in ϕ and, since the successive layers are shifted of 1/3 of the width of the

scintillator, the effective segmentation in ϕ is 7.5°. The angular coverage in θ is between 4° and 9° and between 171° and 176°.

4.9 The trigger system

In the 4×4 bunch mode, the electron and positron beams cross each other every 22 μs. This corresponds to a frequency of 45 kHz that doubles for the 8×8 bunch mode adopted only in 1995. Of all the beam crossings only a rate of 1-2 Hz corresponds to a genuine e^+e^- interaction. Since it takes about 500 μs to read out all the information coming from the L3 detector, it is very important to select which events are physically interesting and which events can be discarded and considered as background. This task is performed by the trigger system which consists of three subsequent filtering algorithms. The main background sources which the trigger system has to reduce are due to beam-wall and beam-gas interactions, cosmic rays and noise in electronic channels.

The level-one trigger decides if the event is a good candidate to be kept within the time between two beam crossings and reduces the rate to approximately 10 Hz. The level-two and the level-three triggers take their decision in less then 1 ms and 100 ms respectively and reduce the rate below 2 Hz, keeping the livetime above 95%.

4.9.1 The level-one trigger

The level-one trigger is the logical OR of five subtriggers: the muon trigger, the luminosity trigger, the scintillator trigger, the energy trigger and the charged particle trigger. This fast trigger is based on the analog signals coming from the subdetectors which are processed by a system of FASTBUS, VME and CAMAC crates.

The muon trigger searches for single muon and back-to-back muon tracks in the muon spectrometer with a momentum larger than 1 GeV. To reduce the high rate due to cosmic rays, the coincidence with a signal from the scintillators is required.

The scintillator trigger is used to select high multiplicity events. This trigger requires a coincidence of 5 out of 16 scintillator pairs.

The luminosity trigger is integrated in the electronics of the energy trigger and requires the presence of more than 15 GeV in both the luminosity monitors. This

trigger is used to collect small angle Bhabha events for the measurement of the luminosity.

The energy trigger [83] uses signals from the calorimeters and has a rate of about 5 Hz. For the electromagnetic calorimeter the BGO barrel crystals are grouped into clusters of 30 crystals, giving a total of 256 analog signals. For each endcap 128 trigger clusters are formed. For the hadron calorimeter the trigger gets two signals per module, one for the first interaction length and one for the rest. Based on this information the following trigger algorithms are applied:

- Cluster trigger – The trigger cells from the electromagnetic and hadron calorimeters with the same θ and ϕ coordinates are defined as a cluster which is required to have at least 7 GeV. The threshold is lowered to 3 GeV if a track detected by the charged particle trigger is present in the direction of the cluster.

- Total Energy trigger – There must be at least 10 GeV in the barrel of the electromagnetic calorimeter or 15 GeV in the barrel of the electromagnetic and the hadron calorimeters or 20 GeV in total including the endcaps.

- Single photon trigger – There must be only a single isolated cluster in the electromagnetic calorimeter with an energy larger than 2 GeV. The anticoincidence with tracks seen by the charged particle trigger is required.

- Hit counting trigger – At least two trigger cells with more than 5 GeV are required.

The main trigger which collects the events produced by two-photon interactions is the charged particle trigger since the energy deposited in the calorimeters is too low for the criteria of the energy trigger. The charged particle trigger is composed by the Outer TEC and the Inner TEC triggers and is described in detail in Chapter5.

4.9.2 The level-two trigger

The level-two trigger is based on a system of transputers and its algorithm [84] has the function to combine all the level-one information and to reduce the number of background events which have been triggered by the level-one algorithm. Its rejection

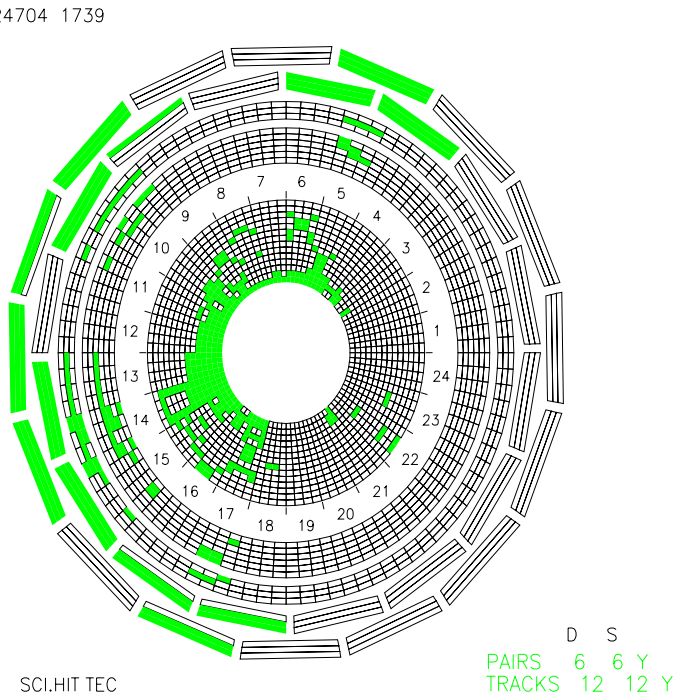

Figure 4.15: A typical beam gas event as it is seen and accepted by the level-one Outer TEC trigger.

factor is about 30%. Events which are selected by more than one level-one triggers pass the level-two algorithm automatically.

Three are the filtering algorithms applied at level-two.

- The energy algorithm is based on a more precise energy estimation and rejects events with an energy lower than a programmable threshold.
- The TEC algorithm is based on the information from the Charge Division wires and is designed to reject events due to electronic noise in the TEC and to beam-gas and beam-wall interactions. This algorithm is based on the fact that these events are characterized by the presence of many low momentum tracks producing a high hit multiplicity concentrated in the inner part of the drift chamber, as shown in Figure 4.15.

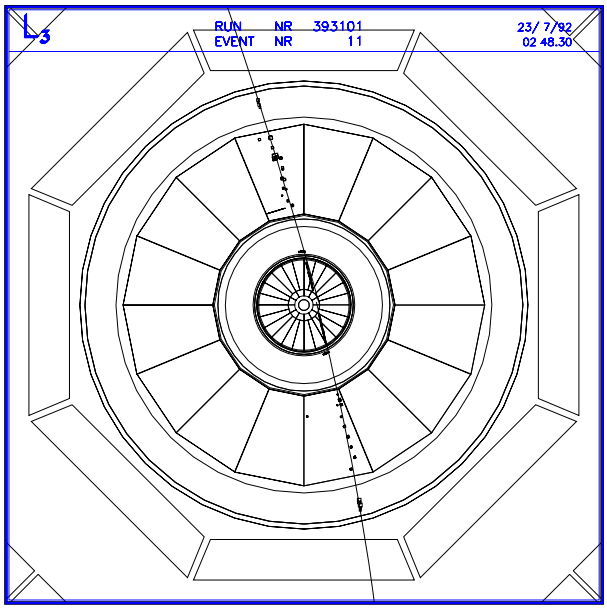

Figure 4.16: A cosmic muon event accepted by the level-one muon trigger.

- The muon algorithm rejects events with a too small number of hits in the TEC and with no scintillator hits in time. A typical cosmic muon event is shown in Figure 4.16.

One out of every 20 events rejected at level-two is kept and flagged as such to monitor the efficiency.

4.9.3 The level-three trigger

The level-three algorithm [85] is based on digitized data and is therefore able to perform a much more precise selection of the events. The trigger is based on three software implemented algorithms and on two ALPHAVAX stations running in parallel.

- The energy algorithm reconstructs the energy in the electromagnetic and in the hadron calorimeters. More precise thresholds are applied since fine digitized data are used.

- The TEC algorithm reconstructs tracks using the Charge Division wire information coming from the level-two TEC algorithm. At least one track is required to come from the primary vertex and correlations between tracks and clusters in the calorimeters are searched for. For the events which are triggered only by the charged particle trigger at level-one, at least one track correlated with a deposit of 200 MeV or two tracks correlated with deposits of 50 MeV are required.

- The muon algorithm requires a muon track with a coincidence within ± 10 ns between the scintillator hits and the beam crossing.

As for the level-two trigger, one out of every 20 events rejected at level-three is kept and flagged as such to monitor the efficiency.

The level-three TEC algorithm has been considerably improved in 1999. Due to the improvement on the speed of data processing, the algorithm has been modified in order to rely completely on the fully reconstructed data as in the off-line analysis. This makes the level-three trigger completely independent from the level-one and the level-two triggers and significantly improves its precision and its efficiency.

4.10 The data acquisition system

The data acquisition system (DAQ) of L3 [86] is shown in Figure 4.17. The data coming from the subdetectors are divided into two streams: the full data stream and the trigger stream which contains less information to be processed within the time between two successive beam crossings. Each subdetector uses a different system of readout and digitization according to its properties. Each subdetector can operate in two modes. In the local mode the subdetector is separated from the rest of the experiment for calibration and debugging purposes. In the global mode the subdetector is part of the L3 DAQ system and runs in parallel with all the other subdetectors. All the digitized data are stored in event memories based on FASTBUS crates. These data are merged together and sent to the central event builder. The information of the whole event, if the decision of the level-three trigger is positive, is transferred to the main VAX 8800. Here a program called producer writes the

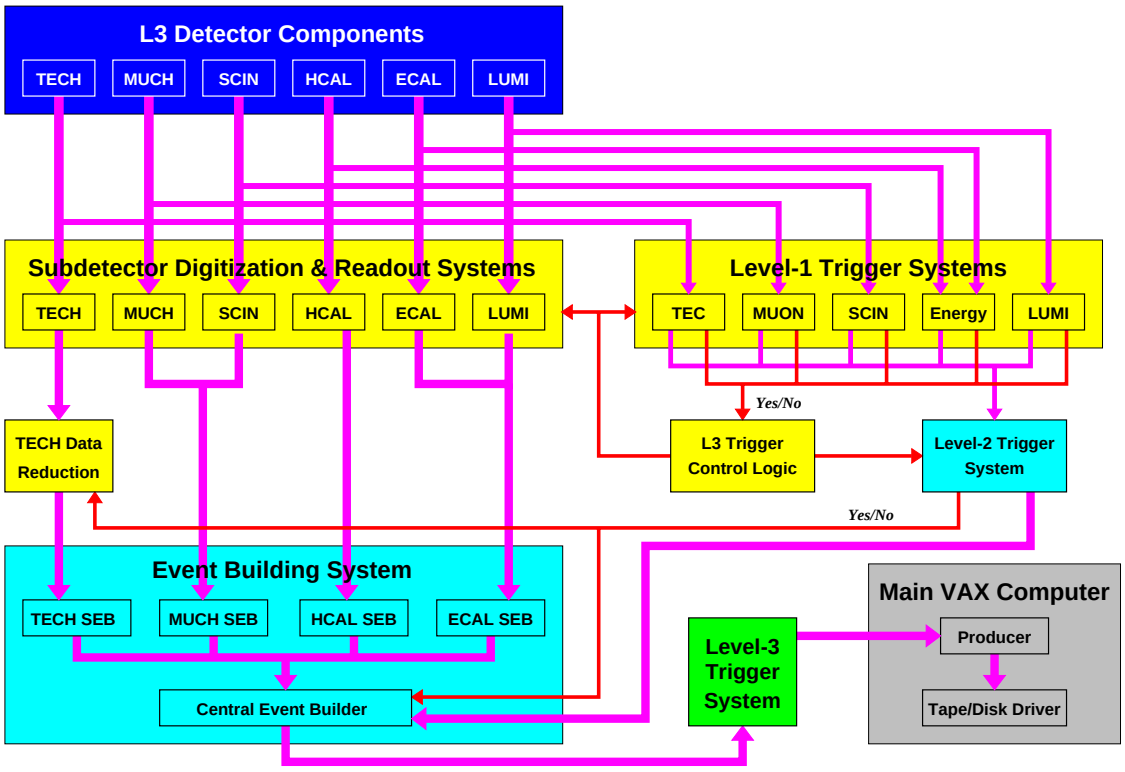

Figure 4.17: Scheme of the structure of the data acquisition system of L3.

raw data information into a tape and sends them via network to the L3 main off-line cluster.

4.11 Event reconstruction

Within a few hours after the event is recorded, it is processed by the L3 off-line reconstruction program (REL3). Information from databases such as calibration constants and alignment parameters is used to convert digitized raw information into physical quantities such as energies and momenta. The fully reconstructed events are stored in three different formats (DVN, DSU and DAQ) of increasing sizes. The larger formats contain some or the full raw data information and are used to refine the calibrations and the alignments of the subdetectors after the end of each data

taking period. When the final calibration and alignment parameters are calculated, all the data are reprocessed in order to improve the quality and the precision of the measurements.

Not all the events which are selected by the level-three trigger are available for the physical analyses in the three formats mentioned above. The REL3 program contains in fact some selection routines which ensure the interest of the events and classify them into different categories such as muon pair, Bhabha, hadronic, two-photon events etc. The events produced by the interaction of two photons are selected by two dedicated routines, denominated AAGGSEL and ABGGSEL, to assure some redundancy. AAGGSEL selects events according to the following criteria used as a logical OR:

- two charged tracks with charge balance and an effective mass larger than a programmable threshold
- two charged tracks with charge balance matched with BGO clusters
- four charged tracks with charge balance
- at least two charged tracks matched with BGO clusters and a total charge less than a programmable threshold
- at least a tag in the endcaps of the BGO, in the luminosity monitor, in the ALR or in the VSAT.

ABGGSEL selects events with a total detected energy and a total effective mass less then programmable threshold values. On these events

- at least two good clusters in the BGO
- at least two good tracks in the TEC

are required.

Chapter 5

The level-one charged particle trigger

5.1 Introduction

The level-one charged particle trigger is composed by the Outer TEC and the Inner TEC triggers. The Outer TEC trigger is based on the information coming from charged particles detected by the Outer TEC. This system has been conceived, constructed and maintained by the University of Geneva [87] and has been one of my main responsibilities within the L3 Collaboration. This system is described in detail throughout this chapter.

The Outer TEC trigger has been designed to be flexible and programmable according to the different energies, luminosities and background conditions of the LEP machine. The importance of this apparatus is due to two main reasons. First, it is a backup trigger for the other level-one triggers such as the energy, the muon and the scintillator trigger and is essential to calculate their efficiencies. Second, it is the main trigger for two-photon physics, allowing to exploit LEP as a photon-photon collider.

5.2 Description of the apparatus

The Outer TEC trigger processes the analog signals generated by the Outer TEC and its algorithm is composed of three main steps.

- The hit pattern of the event is first reconstructed from the analog signals coming from the TEC wires.
- Tracks pointing to the interaction point in the transverse plane are searched for in the hit pattern.
- Pairs of back-to-back tracks are searched for and the presence of one of these pairs is sufficient to trigger the event.

The background events produced by beam halo, synchrotron radiation and off-momentum electrons are characterized by a high multiplicity of low momentum tracks concentrated near the beam pipe and usually with an asymmetric configuration with respect to the interaction point. This is why the information from the Inner TEC is not used and the algorithm is based on back-to-back tracks pointing to the interaction point.

The outer TEC trigger uses signals from the 14 Left-Right anode wires of the 24 sectors of the Outer TEC. These wires are located approximately as $\approx 1/R$, between $R_i = 178$ mm and $R_o = 413$ mm. The trigger is software programmable and different configurations are possible based on the following quantities:

- The polar angle range - Two different polar angle ranges can be chosen by using the full set of 14 wires or only the first 7.
- Track definition - A minimum number of hits are required to form a track.
- The minimum transverse momentum - Three sets of predefined masks are used to select tracks in three different transverse momentum ranges.
- Wire grouping - Wires can be grouped in each subsector through AND or OR functions, to maximize the efficiency.
- The acoplanarity angle - Pairs are counted according to a programmable acoplanarity angle.

Wire Number for SD	TEC Wire Number	Radius (mm)	Drift Time (ns)
1	59	412.8	9211
2	55	393.6	8783
3	51	374.4	8354
4	47	355.2	7926
5	43	336.0	7497
6	39	316.0	7069
7	35	297.6	6641
8	31	278.4	6212
9	27	259.2	5784
10	24	244.8	5463
11	21	230.4	5141
12	18	216.0	4820
13	15	201.6	4498
14	12	187.2	4177

Table 5.1: The list of TEC wires used by the trigger. The drift time is calculated by assuming a uniform drift velocity of 5.9 μm/ns.

Each step of the trigger algorithm is carried out by a different set of electronic FASTBUS modules:

- The segment divider modules (SD) reconstruct the hit pattern in the transverse plane. There are 24 segment divider modules, one for each sector of the Outer TEC.
- The track finder modules (TF) receive the hit pattern information from the SD modules and search for tracks. There are 24 track finder modules, one for each sector of the Outer TEC.
- The track adder module (TA) receives all the information from the track finder modules, searches for pairs of back-to-back tracks and takes the trigger decision.

5.2.1 The Segment Divider Modules

The SD modules digitize the data received from the Outer TEC to form a 14×96 hit pattern matrix on which the search for tracks is performed. Each SD module

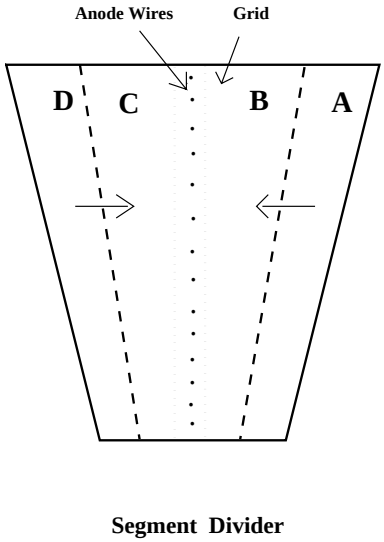

Figure 5.1: The SD modules divide the two drift regions of each sector into two parts.

receives the information from the 14 anode wires of the corresponding sector. The list of wires is given in the Table 5.1, where the distance of the wires in mm from the interaction point and the drift time are also shown.

At each beam crossing, a counter is started in each SD module and the value of the counter is assigned to each signal coming from the TEC according to its arrival time. A programmable threshold value of the counter is used to divide the drift region into two parts, as shown in Figure 5.1. Each sector is therefore divided into four subsectors, two internal (B and C) and two external (A and D). Since the left-right ambiguity is not resolved, each signal is assigned either to both B and C or to both A and D by comparing the result of the counter with the threshold value. The global output of the 24 SD modules is therefore a 14×96 hit pattern matrix in which the 14×4 sub-matrices, corresponding to each sector, are symmetric with respect to the anode plane.

The module is very flexible in operation because all parameters, the thresholds of the discriminators, the width of the pickup signal, the timing of the anode-pickup coincidence and the time cuts to define the subsectors, are software programmable. The module completely conforms to the FASTBUS protocol and it is based on the

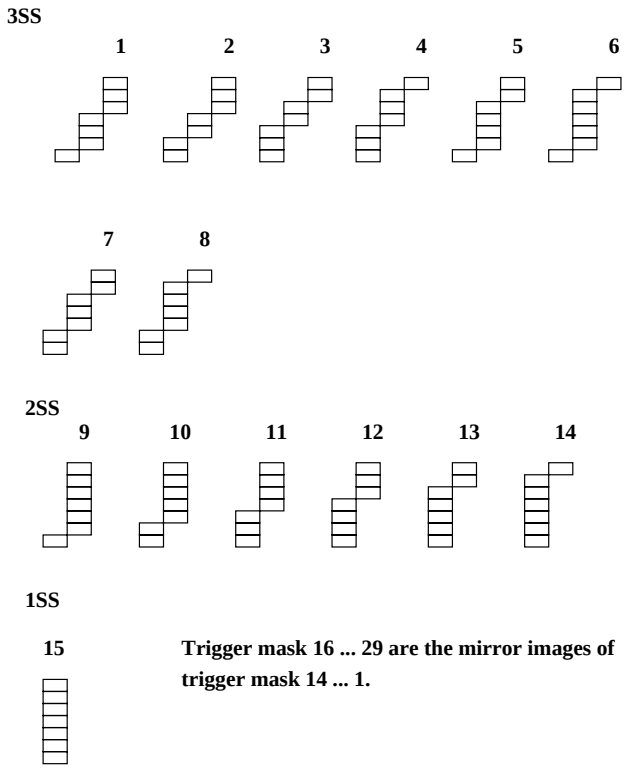

Figure 5.2: The different type of tracks searched by the TF modules.

ECL technology. The processing time is determined by the maximum drift time required in the TEC which is about 9 μs.

5.2.2 The Track Finder Modules

A TF module contains four TF circuits implemented in a FASTBUS protocol. There are 24 TF modules and 96 TF circuits which correspond to the 96 subsectors. The search for tracks is carried out in $\approx$ 330 nsec and is performed in the following way. From the 96 $\times$ 14 hit pattern matrix two 96 $\times$ 7 matrices are formed: one by using only the 7 innermost wires and one by OR-ing or AND-ing the 14 wire output two-by-two. If background conditions are bad, the AND option can be chosen in order to increase the rejection of spurious tracks. The good background conditions of LEP always allowed the use of the OR option. Each TF circuit examines the part of

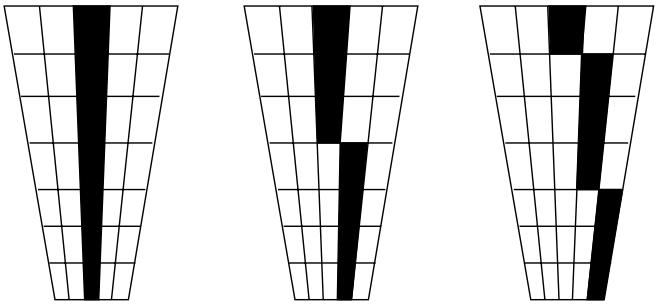

Figure 5.3: Some examples of tracks reconstructed by the Outer TEC trigger.

the two matrices around the corresponding reference subsector and compares the hit pattern with 29 configurations which are stored in a memory and correspond to different kinds of tracks. These configurations are called trigger masks and are shown in Figure 5.2. The masks are divided into three categories according to the number of subsectors they cross: 3SS, 2SS and 1SS tracks cross 3,2 and 1 subsectors, respectively. To allow some inefficiency of the TEC wires at least 6 out of 7 hits are required to be present. The result of the search consists on a 96 $\times$ 6 bit matrix containing the results of the following six categories: 1css, 2css, 3css, 1fss, 2fss and 3fss where "c" stands for central and "f" for forward tracks. The forward tracks are searched for in the 96 $\times$ 7 matrix formed using only the 7 innermost wires and the central tracks are searched for in the other matrix. Examples of tracks as seen by the trigger are shown in Figure 5.3.

The six categories of tracks correspond roughly to the transverse momentum regions shown in Table 5.2. The central region corresponds approximately to $37^\circ \leq \theta \leq 143^\circ$ and the forward region to $28^\circ \leq \theta \leq 162^\circ$.

Category	Forward Region	Central Region
1ss	$p_t > 400$ MeV	$p_t > 600$ MeV
2ss	200 MeV $< p_t <$ 400 MeV	300 MeV $< p_t <$ 600 MeV
3ss	100 MeV $< p_t <$ 200 MeV	150 MeV $< p_t <$ 300 MeV

Table 5.2: Track categories and corresponding transverse momentum regions.

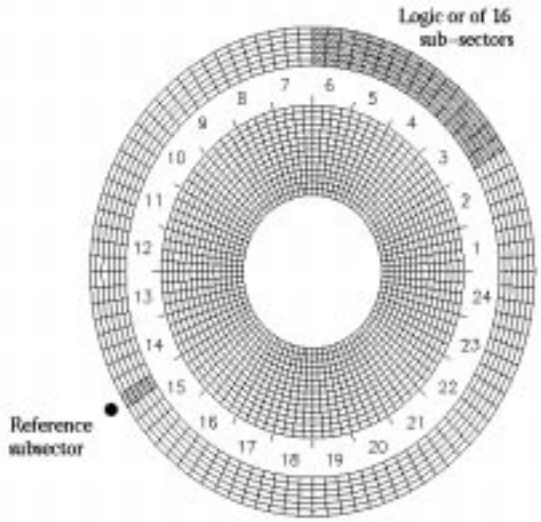

Figure 5.4: The search for a pair of coplanar tracks. The subsectors on the other side with respect to the reference subsector are taken only on one side to avoid double counting.

5.2.3 The Track Adder Module

The Track Adder (TA) consists of two modules: the TA receiver and TA processor. The TA receiver receives the data from the 24 TF modules, forms the 96×6 TF output matrix and transfers it to the TA processor which stores the information in six different shift registers. The TA processor can be configured in order to use only some of the six different categories of tracks and a logic OR is performed with the bits of the selected categories to have only one bit per subsector. The number of tracks is first computed and the result, between 0 and 96, is sent to the energy trigger and to the Inner TEC trigger. Then, pairs of back-to-back tracks are searched for as shown in Figure 5.4. If a track is found in a given subsector, a programmable number of subsectors on the other side of the TEC are considered and their logic OR is calculated. If the result of the OR is one, a coplanar pair is found. This operation is done for all the 96 subsectors. There can be a maximum of 96 coplanar pairs of tracks but only one is sufficient for a positive decision of the trigger.

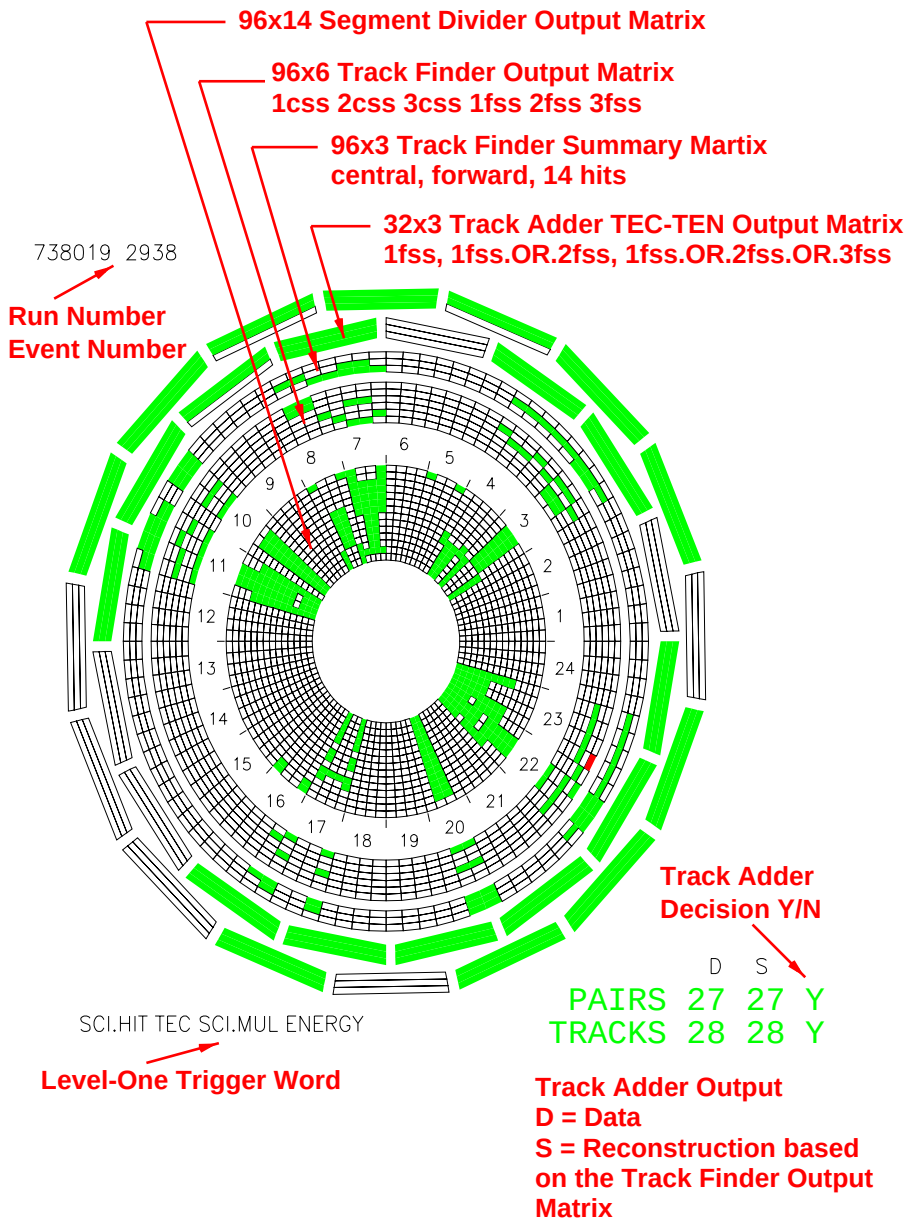

Figure 5.5: One event shown by the on-line TEC trigger event display. The inner ring represents the 96 × 14 matrix provided by the SD modules. The second ring is the result of the track search in the categories 1css, 2css, 3css, 1fss, 2fss and 3fss, respectively (96 × 6 Track Finder output matrix). The third ring represents the logic OR of the three central categories, the logic OR of the three forward categories and the presence of 14 hit tracks. The 32 external segments represent the information sent by the Outer TEC trigger to the level-one energy trigger.

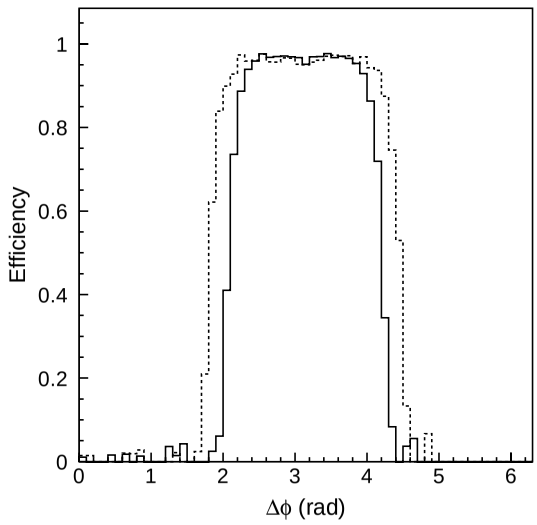

Figure 5.6: The Outer TEC trigger efficiency as a function of the acoplanarity angle $\Delta\phi$. The two lines correspond to the two different configurations used in 1996 for the acoplanarity angle cut.

Using only the forward tracks, the TA processor builds up tracking information to be sent to the energy trigger for the TEC-Energy correlation algorithm. As shown in Figure 5.5, a 32×3 matrix is formed corresponding to 32 blocks in ϕ. For each block, the 3 bits correspond to the 1fss, to the logical OR of the 1fss and 2fss and to the logical OR of the 1fss, 2fss and 3fss categories, respectively.

5.3 The efficiency of the Outer TEC trigger

The efficiency of the Outer TEC trigger can be measured directly on the data if the physical sample under study is triggered also by another independent trigger. This is the case for instance of the processes $e^+e^- \to e^+e^-, \mu^+\mu^-$. For most of the processes produced by photon-photon interactions, only the charged particle trigger is present and the efficiency have to be obtained by using the Outer TEC trigger simulation program on the Monte Carlo events.

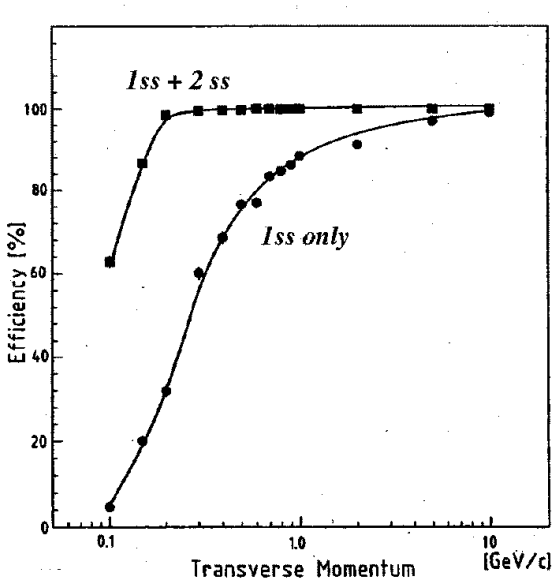

Figure 5.7: Efficiency for track detection as a function of the transverse momentum.

To measure the efficiency on the data, a sample of events with two tracks with opposite charge and transverse momentum larger than 1 GeV is selected. On this sample the Outer TEC trigger efficiency is calculated with respect to the energy trigger as

$$\varepsilon = \frac{N_{T.and.E}}{N_E} \tag{5.1}$$

where $N_{T.and.E}$ is the number of events collected by the Outer TEC and the energy trigger and N_E is the number of events collected by the energy trigger.

Figure 5.6 shows the Outer TEC trigger efficiency as a function of the acoplanarity angle $\Delta\phi$ for the 1996 data taking period in which two different acoplanarity cut conditions, 12 and 16 subsectors, have been used. Within the $\Delta\phi$ fiducial region the efficiency is flat and its value is about 98%. As soon as the borders of the acoplanarity region are approached, the efficiency drops very rapidly to zero. The two acoplanarity conditions correspond to fiducial regions of approximately $\pm 40°$ and $\pm 60°$, respectively.

Figure 5.7 shows the efficiency for the detection of a track by the Outer TEC

trigger as a function of p_t. Low transverse momentum tracks are often contained in two subsectors and the category 2ss is needed to assure a high efficiency.

5.4 The Inner TEC trigger

The Inner TEC trigger has been installed [88] in 1997 with the purpose of improving the efficiency for low multiplicity events with acoplanar tracks. This trigger is based on the information from the 6 standard anode wires of the 12 Inner TEC sectors. The information from the wires is examined by a neural network algorithm which divides the 12 sectors into "good" and "bad", according to their hit pattern. The value of the threshold of the neural network output is software programmable. The event is triggered if there are at least two good sectors, more good than bad sectors and at least one track seen by the Outer TEC trigger. The neural network is trained to regard hit patterns from background events as bad and from two-photon, Bhabha and $e^+e^- \to q\bar{q}$ events as good.

5.5 Improvement of the Outer TEC trigger configuration

The data acquisition system (DAQ) of the L3 experiment has an intrinsic limitation of about 25 Hz for the total level-one trigger rate. As shown in Figure 5.8, the live-time reduces to a very low value if this threshold is crossed. Due to the continuously improving performance of the LEP machine, and in particular the increasing luminosity, rates of about 20 Hz were reached at the beginning of high luminosity fills at the end of 1997 data taking. A higher luminosity was expected for the 1998 data taking and, to cope with this situation, a reduction of the level-one trigger rate was mandatory.

The rate of the Outer TEC trigger rises linearly with the luminosity, as shown in Figure 5.9, and is mainly due to beam-gas and beam-wall background events. The physical events, mainly produced by two-photon collisions, give a rate of approximately 1 Hz. To reduce the rate of the Outer TEC trigger, new configurations have been conceived and a study of their effect on the trigger rate and on the efficiency for

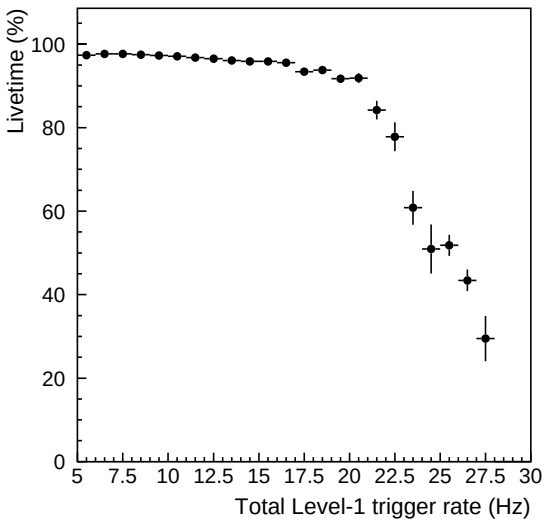

Figure 5.8: The livetime of the DAQ efficiency versus the total level-one trigger rate.

physical channels has been performed during the 1997-1998 shut down period [89].

The configuration of the Outer TEC trigger, which was used up to 1997 data taking, is denominated Version 20.0 and corresponds to the following set-up:

- Track categories - 1css, 2css and 1fss
- Acoplanarity cut - 16 subsectors (12 before 1996)

Three new configurations have been studied by modifying the Version 20.0:

- Version 20.1 - Track categories: 1css and 1fss. Excludes low momentum central tracks.
- Version 20.2 - Track categories: 1css and 2css. Excludes the forward region.
- Version 20.3 - Track categories: only 1css. Only high momentum central tracks are considered.

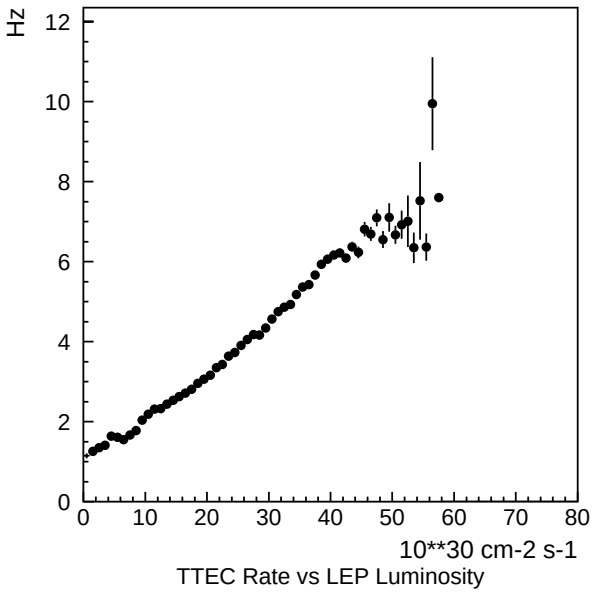

Figure 5.9: The Outer TEC trigger rate versus the luminosity of LEP for the 1997 data sample.

Since a significant increase of the trigger rate was not observed in 1996 by changing the acoplanarity cut from 12 to 16 sub-sectors, the acoplanarity cut has not been considered as a good parameter to reduce the rate.

5.5.1 Trigger rate and trigger configurations

In order to study the effect of the three new configurations on data, a "level-1 unbiased" event sample was extracted from 1997 raw data. These events correspond to a pure output of the level-one trigger. The sample consists on 19699 events, 6154 of them are triggered by the TEC trigger. The effect of the new configurations on this sample is reported in Table 5.3. From the rate reduction factor it can be immediately seen that the 20.3 configuration is unreliable since it practically eliminates the TEC trigger. Only the 20.1 and 20.2 configuration were then investigated further on.

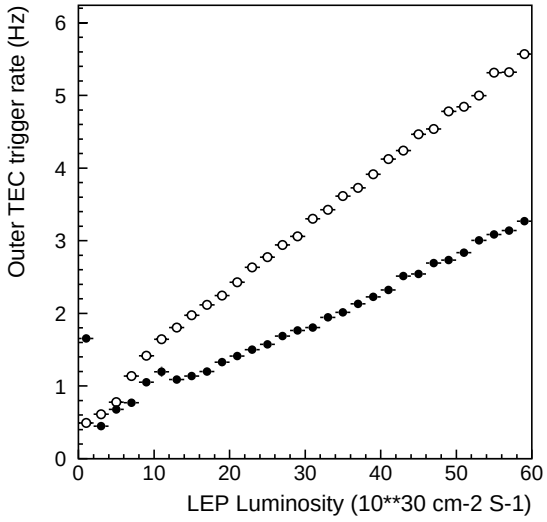

Figure 5.10: The Outer TEC trigger rate versus the luminosity of LEP for the 1997 (Version 20.0 - open circles) and 1998 (Version 20.1 - black dots) data.

5.5.2 Trigger efficiency and trigger configurations

For the configurations 20.0, 20.1 and 20.2, the trigger efficiency is examined for the most typical two-photon physics channels with a Monte Carlo study. A complete analysis selection procedure is applied to the completely reconstructed Monte Carlo events and the simulation of the Outer TEC trigger is applied to all the selected events, according to the different configurations.

Setup	Version	Configuration	Triggered Events	Rate Reduction Factor
36	20.0	1css 2css 1fss	6154	—
40	20.1	1css 1fss	4114	0.69
41	20.2	1css 2css	3612	0.58
42	20.3	1css	1008	0.16

Table 5.3: Rate reduction factor and TEC trigger configurations.

Physical Process	E_{beam}	Events	Trigger Efficiency %					
			TEC			TEC.OR.ITEC		
			20.0	20.1	20.2	20.0	20.1	20.2
$\gamma\gamma \to a_2(1320) \to \pi^+\pi^-\pi^0$	91.36	3500	23	16	10	78	75	67
$\gamma\gamma \to \xi(2230) \to K^0_S K^0_S$	92.0	3498	84	77	70	94	90	90
$\gamma\gamma \to f'_2(1525) \to K^0_S K^0_S$	92.0	3000	80	69	57	92	87	86
$\gamma\gamma \to \eta_c(2980) \to \rho^0\rho^0$	91.36	3496	92	86	80	98	98	97
$\gamma\gamma \to \Lambda\bar{\Lambda}$	92.0	2996	83	74	62	85	83	77
$\gamma\gamma \to \rho^0\rho^0$	91.36	4500	86	82	72	98	98	98
$\gamma\gamma \to \eta'(958) \to \pi^+\pi^-\gamma$	91.36	3494	36	27	21	80	74	69
$e^+e^- \to e^+e^- q\bar{q}$ (PJQ31)	91.36	2500	81	74	63	96	95	92
$e^+e^- \to e^+e^- q\bar{q}$ (PJQ29)	91.36	2493	85	79	70	97	97	95
$e^+e^- \to e^+e^- q\bar{q}$ (QPH41)	92.00	2998	81	74	62	96	95	93
$e^+e^- \to e^+e^- q\bar{q}$ (PFC07)	91.36	4789	75	70	58	96	94	92
$\gamma\gamma \to f_2(1270) \to \pi^+\pi^-$	45.6	3500	78	70	45	95	93	86
$\gamma\gamma \to f'_2(1525) \to K^0_S K^0_S$ (16)	45.6	3500	78	63	59	92	87	87
$\gamma\gamma \to f'_2(1525) \to K^0_S K^0_S$ (12)	45.6	3500	76	59	55	91	87	87

Table 5.4: Trigger efficiencies and Outer TEC trigger configurations for various two-photon physics typical channels. The efficiencies are evaluated for the Outer TEC trigger alone and for the Outer TEC trigger together with the Inner TEC trigger.

The results are shown in Table 5.4. The TEC trigger efficiencies are reported for the three configurations as well as the global efficiency of the TEC and the Inner TEC trigger.

Looking at the TEC trigger efficiency, it can be seen that the 20.1 configuration produces a loss in efficiency from 5% to 10% with respect to the version 20.0 and the 20.2 produces a loss in efficiency from 20% to 30%. It is clear that the 20.1 configuration is better for two-photon physics than 20.2. This is straightforward since two-photon collisions are characterized by a boost along the beam direction producing tracks in the forward region.

It is clear also that the Inner TEC trigger will recover many events; the efficiency increases from 10% up to 25%. For channels with two acollinear tracks, like the formation of the η' or the a_2, the gain is more than a factor two. The Inner TEC trigger is quite inefficient for the $\gamma\gamma \to \Lambda\bar{\Lambda}$ process; this is not surprising since, due

to their large lifetime, Λ particles decay often outside the Inner TEC. The last two lines of Table 5.4 show the little effect produced by the change of the acollinearity cut from 16 to 12 sub-sectors for the channel $\gamma\gamma \to f_2' \to K_S^0 K_S^0$.

The Version 20.1 was finally chosen and was used from 1998 up to the end of LEP. Figure 5.10 shows the Outer TEC trigger rate as a function of the LEP luminosity for the Version 20.0 in 1997 data and the new Version 20.1 in 1998 data. The reduction of the trigger rate found on 1998 data is in very good agreement with the prediction of Table 5.3, based on 1997 data.

Chapter 6

Track and vertex reconstruction and measurement of the specific ionization loss

6.1 Track reconstruction

The central tracking system is used to measure the position, the momentum and the ionization loss of charged particles. The trajectory of a charged particle in a homogeneous magnetic field is a helix curling around the direction of the field. According to the L3 reference system, this trajectory can be regarded as the superposition of a circular motion in the transverse plane with a constant drift along the z direction.

The signals collected by the SMD and by the TEC, indicated as hits, are used by the pattern recognition program to determine the position and the momentum while the charge collected by the TEC wires is used to measure the specific ionization loss, indicated as $\mathrm{dE}/\mathrm{d}x$.

The pattern recognition program [90] is integrated in the reconstruction program of the L3 experiment (REL3) and proceeds in two steps.

- Charged tracks are first searched for in the transverse plane: their transverse momentum and their azimuthal angle ϕ are determined.
- The information on the z direction is considered and the polar angle θ is measured.

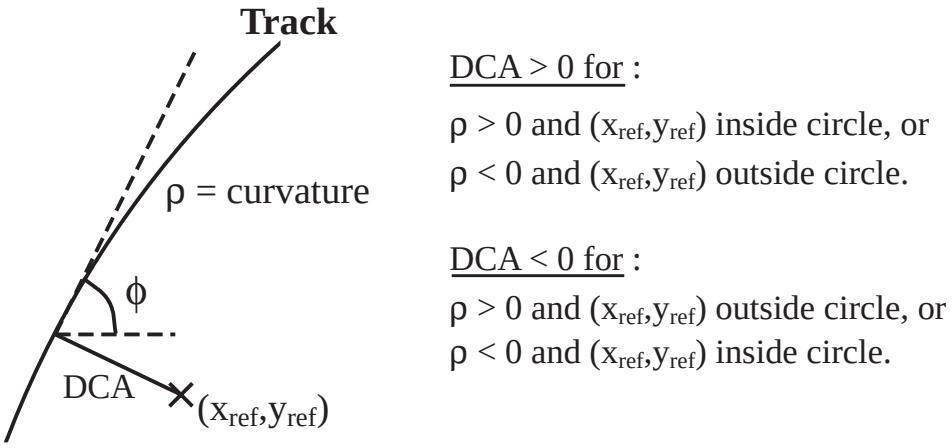

Figure 6.1: The quantities which characterize a charged track in the transverse plane. (x_{ref}, y_{ref}) is the position of the primary vertex.

The hits are first coupled two-by-two to form doublets which are grouped together to form long chains called segments. Segments pointing towards the interaction point are first considered to search for high momentum tracks produced by the e^+e^- interaction. In this procedure the left-right ambiguity is resolved by using the LR wire information and the geometrical difference between the Outer and the Inner TEC. Once high momentum tracks are found, the remnant segments are considered to form low momentum tracks. At the end, a procedure is applied to try to attach the unused hits to one of the already formed tracks. In order to measure the physical quantities, a circular fit is then performed to all the tracks. In this fit a different weight is assigned to every hit, according to the precision on the measurement of its position. As shown in Figure 6.1, from the fit the distance of closest approach (DCA) with respect to the primary vertex, the azimuthal angle ϕ at closest approach and the radius of curvature ρ are determined. The sign of ρ corresponds to the charge of the particle and the meaning of the sign of the DCA is explained in Figure 6.1.

From the radius of curvature, the signed transverse momentum p_t of the particle is obtained as

$$p_t = qB|\rho| \tag{6.1}$$

where q is the charge of the particle and B the magnetic field produced by the magnet.

Once the tracks are reconstructed in the transverse plane, the information on the z direction is considered. From the information coming from the charge division wires of the TEC a first measurement of the direction of the track in the longitudinal plane is performed. The hits of the z-chambers and the z-hits of the SMD are then attached to the track in order to have a final measurement of the azimuthal angle θ and of z_0 which is the z position of the point of closest approach in the xy plane.

6.2 Primary vertex reconstruction

The region where the electron and the positron beams collide has the shape of a three dimensional ellipsoid and the density of the collisions is approximately normally distributed around its center. The determination of its position is very important for several measurements like, in our case, for the reconstruction of the secondary vertex produced by a neutral K^0_S meson.

The position of the primary vertex is determined by computing a common vertex for a set of tracks belonging to a group of consecutive hadronic events [91]. Tracks with a transverse momentum larger then 1 GeV, more than 15 hits and a polar angle between 45° and 135° are selected and the common vertex of these tracks is calculated by finding the point which minimizes the weighted sum

$$\chi^2 = \sum_i \frac{\delta_i^2}{\sigma_{\delta_i}^2} \tag{6.2}$$

where δ_i is the distance of closest approach of the i-th track and σ_{δ_i} is the error on δ_i. The primary vertex is determined with an iterative procedure. First a common vertex is found for all the tracks, then the tracks with $|\delta| > 1$ mm with respect to this point are removed and a new point is calculated with the remaining tracks. The procedure is repeated until the shift of the vertex from one iteration to the next is

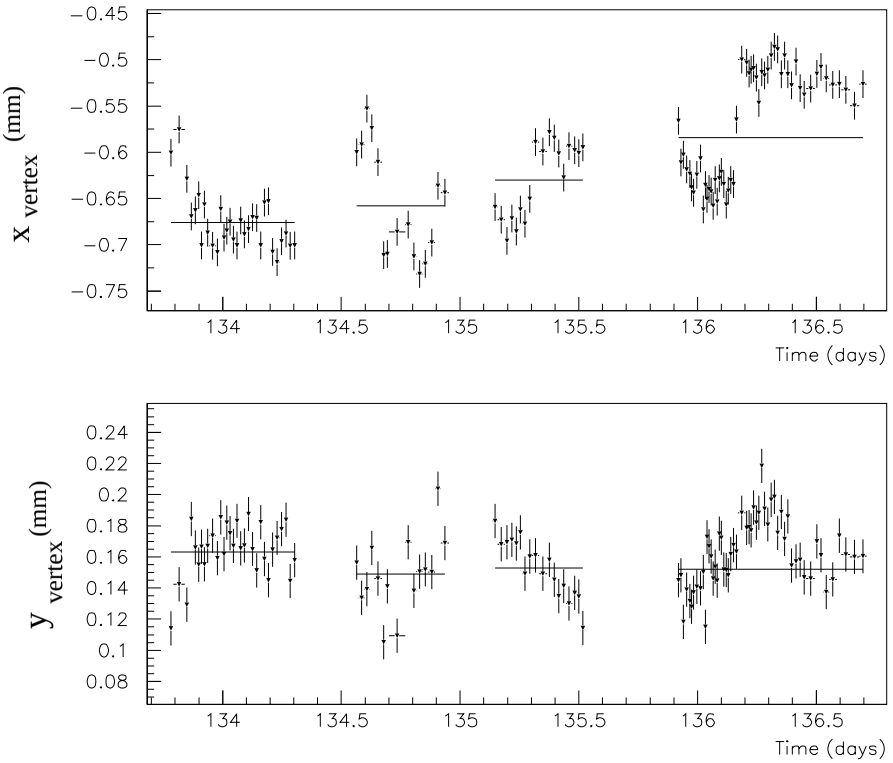

Figure 6.2: The time evolution of the primary vertex for some fills of the 1994 data taking period. The upper plot shows the horizontal beam position and the lower plot the vertical beam position. The lines correspond to the average value computed for the whole fill.

less than 1μm. The choice of the number of events used for the determination of the primary vertex is based on two considerations.

- A large number of tracks, and hence of events, is necessary to reduce the statistical error.
- The events must be as near as possible in time to follow the variations of the beam position due to synchrotron radiation and orbit corrections.

A good compromise is to take groups of 200 consecutive hadronic events. The average time for their collection is about 16 minutes at LEP2 and an average of 1700 tracks are used for the measurement of the primary vertex which is determined with a

precision of 15 μm in x and of 10 μm in y. Figure 6.2 shows an example of the measurement of the position of the primary vertex as a function of time.

6.3 Secondary vertex reconstruction

The reconstruction of secondary vertices is essential for the study of neutral particles with a lifetime of the order of 10^{-10} seconds such as K^0_S mesons and Λ baryons. The standard program of L3 for the reconstruction of secondary vertices is based on the tracks found by the pattern recognition program and searches for vertices formed by two oppositely charged tracks. This program is optimized for the study of high transverse momentum K^0_S mesons and Λ baryons produced in the hadronic decays of the Z boson [92]. In photon-photon interactions these particles are produced with low transverse momenta of the order of 1 GeV and a specific optimization of the program has been performed for this thesis work.

The algorithm of the secondary vertex reconstruction program is composed by two main steps.

- The secondary vertices are first searched for in the transverse plane.
- The longitudinal quantities of the tracks forming the secondary vertex are recalculated taking into account their common origin.

For each event, all the pairs of oppositely charged tracks passing some quality tests are considered and possible interceptions of their trajectories are calculated in the transverse plane. The selection criteria for the tracks are based on their kinematic quantities (for example $p_t > 50$ MeV and at least 10 hits) and are optimized according to the kind of decay under study. The two circular trajectories have zero, one or two points of interception. The case with one interception point corresponds to tangent circles and is quite rare in practice. In the usual case of two interceptions, the ambiguity is solved by applying the following criteria:

- Vertices falling outside the volume of the TEC are excluded.
- The total transverse momentum of the two outgoing tracks must be collinear with the vector joining the primary and the secondary vertex within a pre-

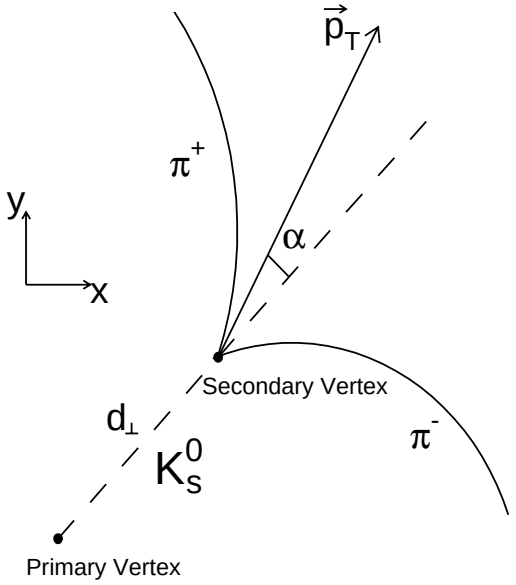

Figure 6.3: The reconstruction of the secondary vertex produced by the decay $K^0_S \rightarrow \pi^+\pi^-$.

defined range (for example ± 1.0 rad). Only one of the two secondary vertex candidates usually fulfills this requirement.

- Vertices which are located at a radial distance larger than the first hits of the tracks are excluded.

- If both the vertices are compatible with the previous conditions, the nearest to the first track hits is considered.

It is important to remark that in more than 99% of the cases the ambiguity is resolved before the last criterion.

As shown in Figure 6.3, the angle α between the total transverse momentum of the outgoing tracks and the vector joining the primary and the secondary vertex and the distance $d_\perp$ between the primary and the secondary vertex are calculated for each secondary vertex. These are the main parameters to be used for a further selection.

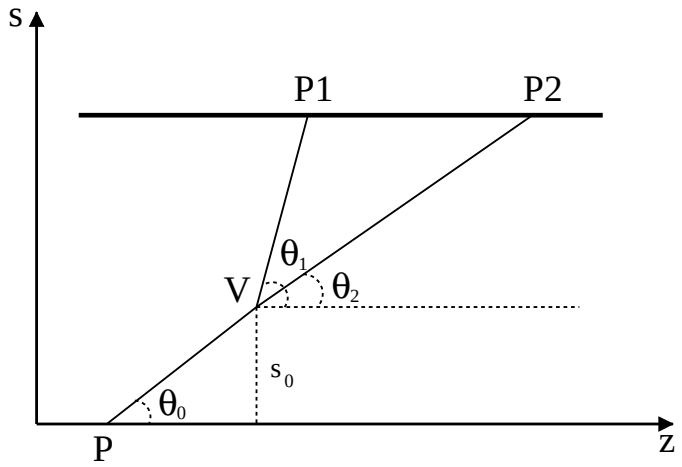

Figure 6.4: The quantities which characterize a secondary vertex in the longitudinal sz plane.

In order to reconstruct the effective mass of the neutral particle, the azimuthal angles ϕ of the two outgoing tracks are recalculated at the secondary vertex point.

After the reconstruction of the secondary vertex in the transverse plane, the longitudinal quantities are calculated in the following way. The conservation of the longitudinal momentum can be expressed as

$$p_{t0} \cot\theta_0 = p_{t1} \cot\theta_1 + p_{t2} \cot\theta_2 \tag{6.3}$$

where p_{t0}, θ_0, p_{ti} and θ_i are the transverse momenta and the azimuthal angles of the neutral particle and of the two outgoing tracks respectively. According to Figure 6.4, the common origin of the two tracks in the secondary vertex leads to the following relations in the sz longitudinal plane

$$\begin{aligned} z_V &= z_P + s_0 \cot\theta_0 \\ z_{P1} &= z_V + s_1 \cot\theta_1 \\ z_{P2} &= z_V + s_2 \cot\theta_2 \end{aligned} \tag{6.4}$$

where P and V are the primary and the secondary vertex, respectively. P1 and P2 are the points where the two outgoing tracks exit the volume of the TEC and s_i is the projection of the segment V$-$Pi on the s axis. From the Equations (6.3) and

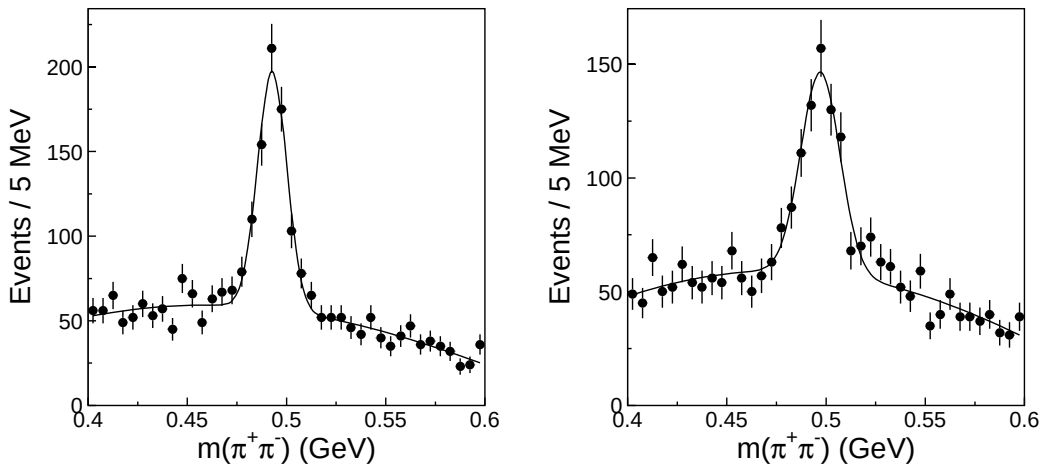

(a) **(b)**

Figure 6.5: The K^0_S signal without (a) and with (b) the correction applied to the transverse momentum for low energy charged particles.

(6.4) the polar angles θ_0, θ_1 and θ_2 and the position z_V of the secondary vertex in the longitudinal plane can be calculated on the basis of transverse quantities and of the position of P1 and P2.

Figure 6.5(a) shows the $\pi^+\pi^-$ mass spectrum for reconstructed secondary vertices formed by tracks with a transverse momentum of the order of 500 MeV produced by two-photon interactions. The K^0_S peak is found at a mass of 493.0±0.5 MeV, 0.9% less than the world average value of 497.672±0.031 MeV [28]. The resolution is $\sigma = 7.3 \pm 0.6$ MeV. The mass and the resolution values are consistent with the Monte Carlo simulation.

For low momentum tracks the effect of the energy loss due to multiple scattering in the material of the beam pipe, the SMD and the TEC results in a distortion of the circular trajectory of the charged particle and the measurement of its transverse momentum is underestimated by the circular fit.

If the transverse momentum of the charged particle is corrected according to the

formula [93]

$$p_t^{corr} = p_t + \Delta(p_t), \tag{6.5}$$

where the correction term $\Delta(p_t)$ is tuned on the Monte Carlo, the mass value of 497.5 ± 0.8 MeV is found, consistent with the world average. From the signal shown in Figure 6.5(b) a resolution of $\sigma = 9.8 \pm 0.7$ MeV is obtained. Since this correction produces a degradation of the resolution and of the signal to noise ratio, no correction to the transverse momentum is applied for the analyses presented in this thesis.

An interesting feature of the secondary vertex reconstruction is the possibility to put in evidence the presence of beam-wall events. When the particles of the beam halo hit the beryllium beam pipe, pairs of oppositely charged tracks are often produced. Figure 6.6(a) shows the distribution of the reconstructed secondary vertices for a sample of low energy events with four charged tracks. The accumulation at a distance of 55 mm corresponds to the beam pipe. The density is not constant around the circumference of the beam pipe because of the effect of the focusing quadrupoles on the beam halo. In the radial projection shown in Figure 6.6(b), the peak corresponding to the radius of the beam pipe is clearly visible. The tail above 55 mm is due to the structure of the SMD. A typical beam-wall event with reconstructed secondary vertices in the beam pipe is shown in Figures 6.6(c) and (d).

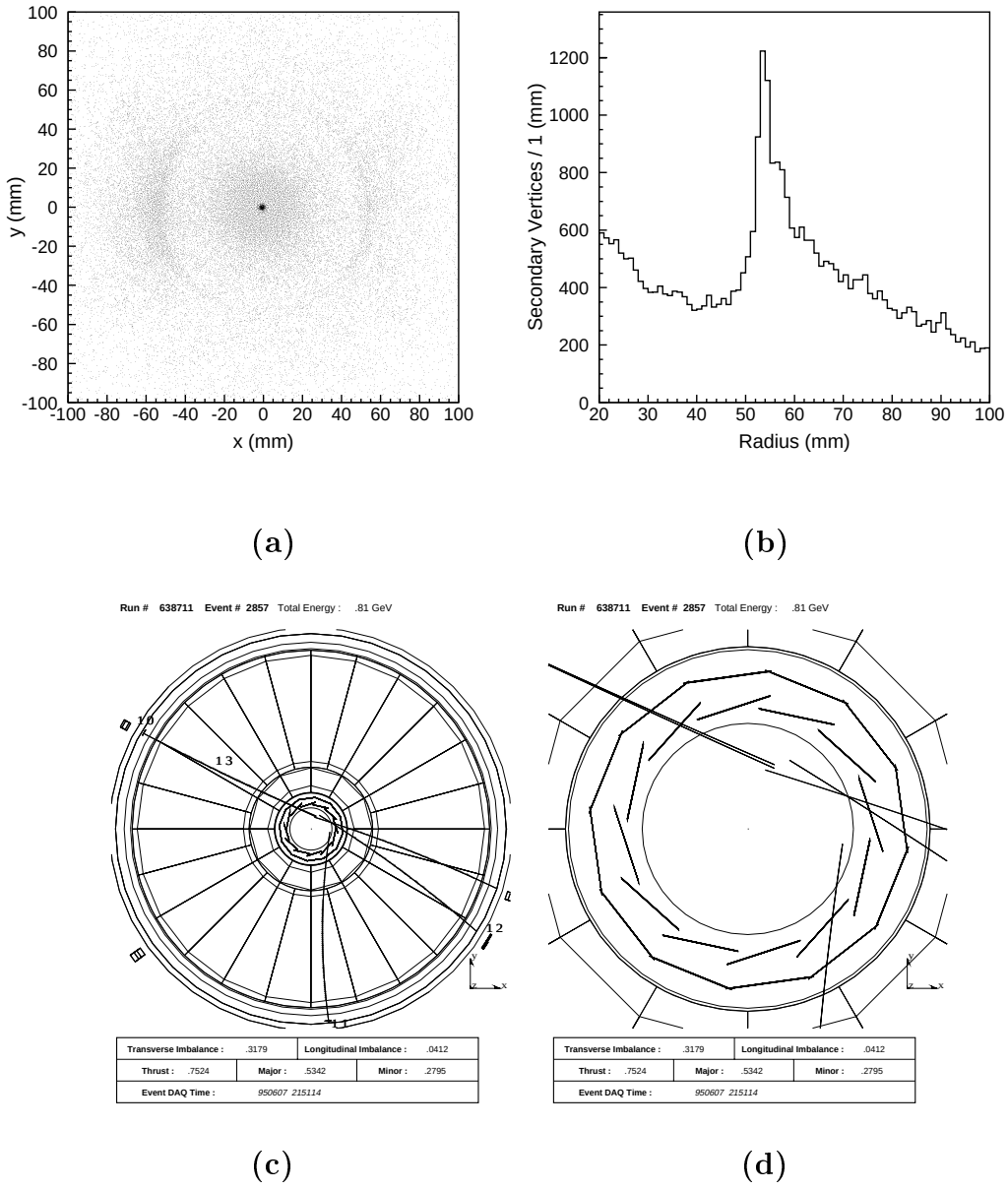

Figure 6.6: (a) The xy position of the reconstructed secondary vertices in low energy events and (b) their radial distribution. (c) A typical beam-wall event with reconstructed secondary vertices in the beam pipe and (d) a zoom of the same event at the level of the SMD.

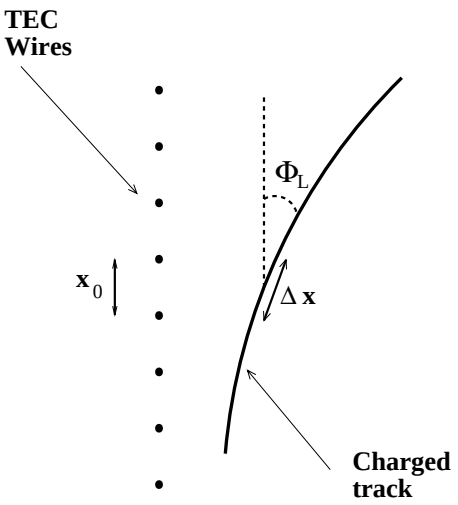

Figure 6.7: Scheme of the geometrical parameters used for the measurement of the specific ionization loss in the TEC.

6.4 Measurement of the ionization loss

The integral of the charge collected by TEC anode wires corresponding to each single hit is measured by flash ADC's. This charge Q is proportional to the energy loss ΔE of the charged particle in the gas and can be expressed as

$$Q \propto \Delta E = \frac{dE}{dx} \cdot \Delta x \tag{6.6}$$

where $\frac{dE}{dx}$ is the specific ionization loss. The quantity Δx is given by

$$\Delta x = \frac{x_0}{\cos \Phi_L \cdot \sin \theta} \tag{6.7}$$

where x_0 is the distance between two consecutive anode wires, as shown in Figure 6.7. Since there are differences in the gas amplification, in the geometry, in the high voltage and in the electronics, a calibration constant g_{wire} is calculated for each wire and for each year of data taking. The measurement of the specific ionization loss and the calculation of the calibration constants have been one of my personal responsibilities within the L3 Collaboration [94].

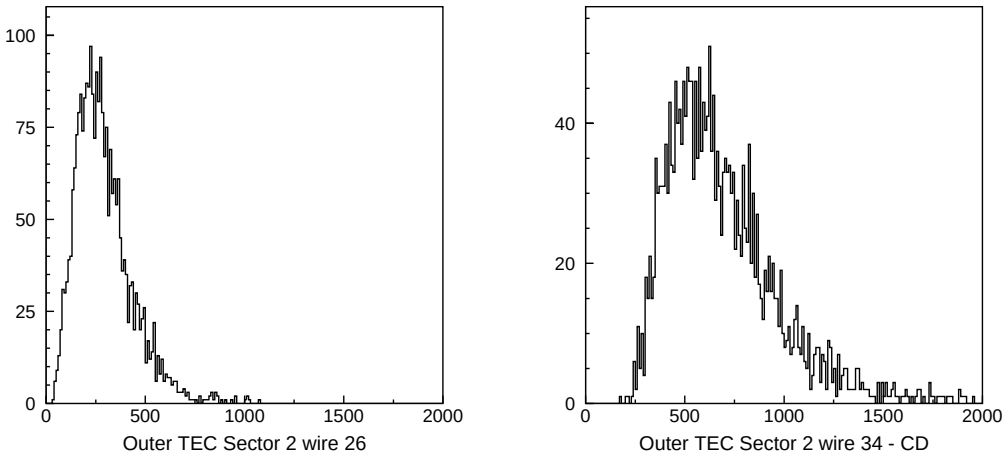

(a) **(b)**

Figure 6.8: Landau distributions for the quantity $Q \cos\Phi_L \sin\theta$ for a normal wire (a) and for a charge division (CD) wire (b) of the Outer TEC.

For each hit i, the specific ionization loss is measured according to

$$\left(\frac{dE}{dx}\right)_i = \frac{Q_i \cdot \cos\Phi_L \cdot \sin\theta}{g_{wire}} \tag{6.8}$$

where Q_i is the value measured by the flash ADC. Since the ionization loss follows a Landau distribution, characterized by large fluctuations, it is not convenient to calculate the ionization loss of a charged track as the average of all the $\left(\frac{dE}{dx}\right)_i$ values. In order to reduce the effect of the fluctuations a $\sim 60\%$ truncated mean is usually applied [95]. Since only a maximum of 62 hits is possible for the TEC, a truncated mean at 80% has been chosen [96] to avoid a too large loss of information.

6.4.1 The calibration constants

To calculate the calibration constants g_{wire}, a sample of particles of known specific ionization loss is used. Electrons and muons with an energy larger than 30 GeV sit in the relativistic plateau [96] of the Bethe-Block curve and are well suited for

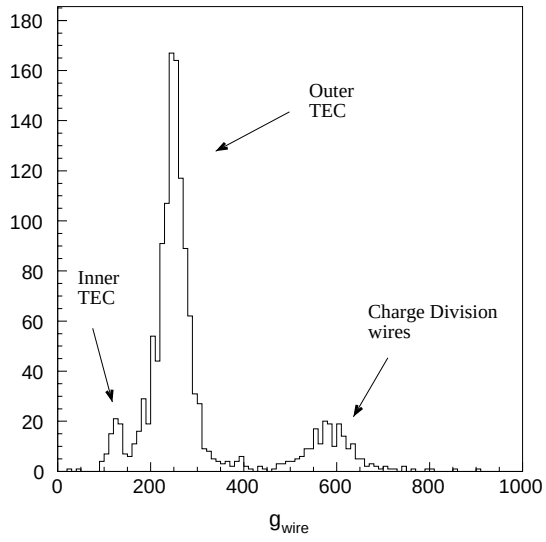

Figure 6.9: Distribution of the calibration constants g_{wire} for the 1998 data taking period. The Inner TEC, the Outer TEC and the charge division wires have similar values of g_{wire}.

this purpose. The calibration constants are calculated in such a way that the 80% truncated mean value of the $\frac{dE}{dx}$ for this reference sample is forced to be one.

With this selected sample of tracks the distribution of the quantity $Q \cos \Phi_L \sin \theta$ is computed for each wire of the TEC and the 80% truncated mean is calculated. This value is the calibration constant g_{wire} that is used to calculate the specific ionization loss for all the tracks according to Equation (6.8).

Figure 6.8 shows the Landau distributions for the quantity $Q \cos \Phi_L \sin \theta$ for two different wires and Figure 6.9 shows the distribution of the calibration constants. Similar values of the calibration constant characterize wires of the same category such as Inner TEC, Outer TEC and charge division but large differences are observed for different categories of wires.

At LEP1 the calibration was performed using only $\mu^+\mu^-$ pairs from the decay of the Z boson. Since at LEP2 only an integrated luminosity of about 5 pb^{-1} is available each year at the Z pole for calibration purposes, a sample of $\mathrm{e}^+\mathrm{e}^-$ and $\mu^+\mu^-$ pairs is used. The number of electron and muon tracks used for the calibration for each year of data taking at LEP2 is reported in Table 6.1.

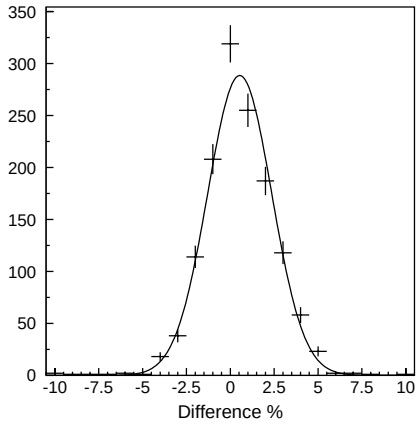

Figure 6.10: The difference between the calibration constants g_{wire} calculated only with high energy muons and with high energy electrons and muons for data at the Z pole taken in 1995.

Despite a different sample of events is used for the calibration at LEP2, no bias is introduced by the e^+e^- sample. Using the very large data sample at the Z pole taken in 1995, the calibration constants are calculated with the two methods. As shown in Figure 6.10, the distribution of their difference is well fitted by a Gaussian function with a mean value compatible with zero.

Year	Number of tracks
1996	9310
1997	9421
1998	10326
1999	11354
2000	11138

Table 6.1: High energy electron and muon tracks used for the calculation of the calibration constants g_{wire}.

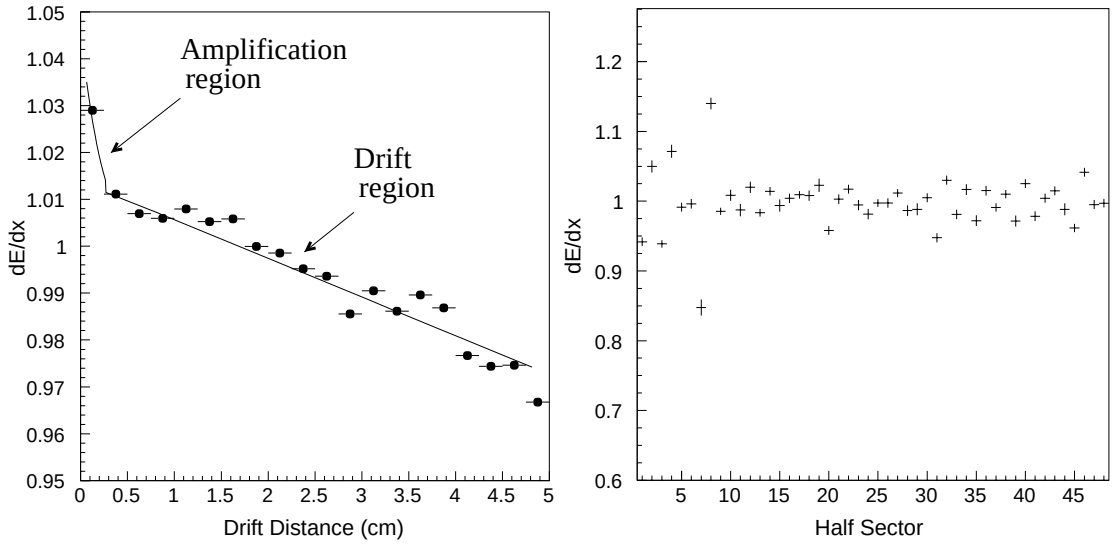

(a) (b)

Figure 6.11: The specific ionization loss as a function of the drift distance for the Outer TEC (a) and for the 48 halfsectors (b).

6.4.2 Corrections

The precision of the measurement of the specific ionization loss, calculated for each track according to Equation (6.8), is improved by taking into account some other effects.

During the drift towards the anode, the electrons produced by the ionization in the gas are partially lost due to recombination. If the primary ionization is produced in the amplification region, the recombination is partially prevented by the high electric field. Figure 6.11(a) shows the specific ionization loss for high energy electrons and muons as a function of the drift distance for the Outer TEC. The effect of the loss due to the recombination is responsible for the negative slope in the drift and in the amplification regions which are characterized by a different value of this quantity. To take the effect of the recombination into account, the value of the charge of each hit is corrected according to its drift distance by using the two segment function shown in Figure 6.11(a). An analogous correction is applied to all the Inner TEC hits.

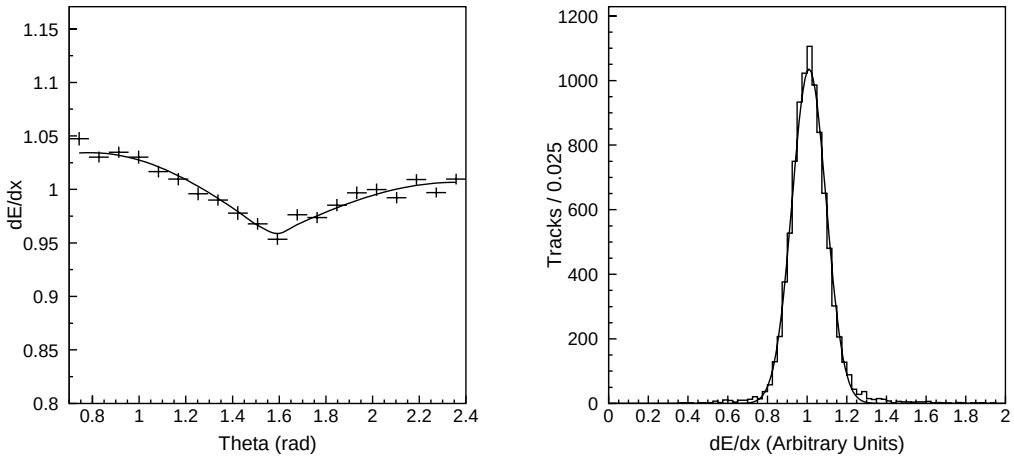

(a) **(b)**

Figure 6.12: The specific ionization loss as a function of θ (a). The distribution of the $\frac{dE}{dx}$ for high energy electrons and muons after the calibration and all the corrections for the 1998 data (b).

Since the calibration constant is obtained without taking into account in which halfsector the ionization is produced, small asymmetries of the TEC can introduce a dependence on the halfsector. Figure 6.11(b) shows the average values of the specific ionization loss obtained for high energy electrons and muons for all the halfsectors of the TEC. The asymmetry is usually of the order of a few per cent but can be larger for damaged sectors. This effect is corrected by dividing the value of the ionization loss of a track by the average value of Figure 6.11(b) for the same halfsector.

Figure 6.12(a) shows the specific ionization loss for the calibration sample as a function of the angle θ. The distribution shows a residual dependence on the polar angle, mainly due to the fact that the standard anode wires are read out only at one end and that high values of the charge are produced at small and large values of θ causing possible non linearities. This effect is corrected by dividing the value of the

Year	Mean	Sigma	Resolution (%)
1996	1.0188	0.1093	10.7
1997	1.0148	0.0863	8.5
1998	1.0100	0.0850	8.4
1999	1.0163	0.0837	8.1
2000	1.0119	0.0937	9.1

Table 6.2: The average value, the sigma and the resolution for the measurement of the $\frac{dE}{dx}$ for high energy electrons and muons at LEP2.

ionization loss of a track by the function

$$f = A_1 \cdot |\sin 2\theta| + C \quad \text{for} \quad \theta < \frac{\pi}{2} \tag{6.9}$$
$$f = A_2 \cdot |\sin 2\theta| + C \quad \text{for} \quad \theta \geq \frac{\pi}{2}$$

where the parameters A_1, A_2 and C are calculated from the fit shown in Figure 6.12(a) which is performed for each year of data taking.

After having applied all the corrections, the distribution of the specific ionization loss for 45 GeV electrons and muons shows a good Gaussian shape, as presented in Figure 6.12(b). The average value, the standard deviation and the resolution, calculated as the ratio between the standard deviation and the average value, are reported in Table 6.2 for all the years of data taking at LEP2.

6.4.3 The dE/dx for low energy particles

The specific ionization loss is a very important physical quantity to identify charged particles with momenta up to about 1 GeV and has been used in L3 in the study of two-photon interactions [97, 98] and in the search for heavy stable leptons [99].

Figure 6.13 shows the specific ionization loss versus the momentum for a sample of low energy events with four charged tracks. The bands corresponding to electrons, muons, charged pions, charged kaons, protons and deuterons are visible and their intensities are different with respect to the charge. The lines correspond to Bethe-Block curves [100] adjusted on the data.

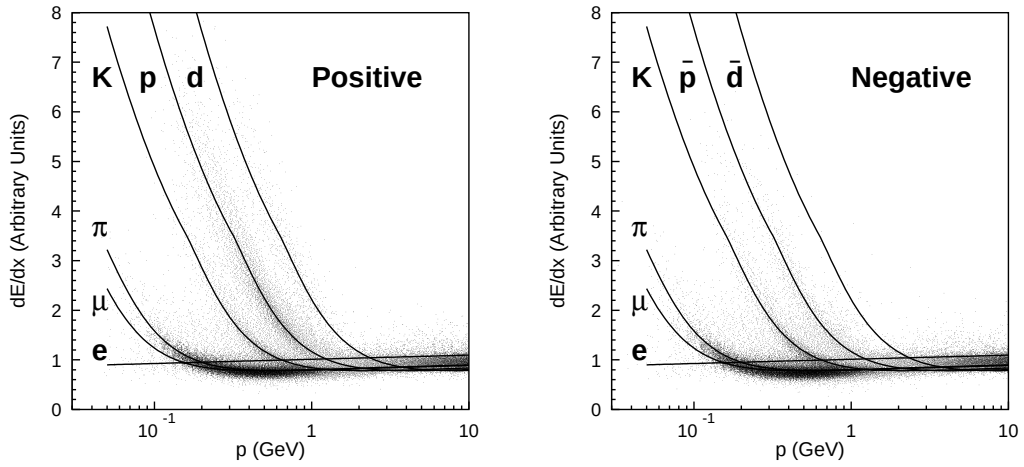

(a) (b)

Figure 6.13: The specific ionization loss versus the momentum for a sample of low momentum positively (a) and negatively (b) charged particles.

The abundance of protons and the presence of deuterons in Figure 6.13(a) is due to beam-gas and beam-wall background events. In Figure 6.13(b) the presence of antiprotons is visible.

From the Bethe-Block functions and from the Landau distributions for the TEC wires (Figure 6.8) a Monte Carlo simulation for the specific ionization loss has been developed by P. Déglon [98] and myself. For each hit of a track, a random value of its specific ionization loss is calculated on the basis of the Landau distribution of the corresponding wire. The average value of the distribution is fixed by the momentum of the particle and by the corresponding point in the Bethe-Block curve. Once the values of the specific ionization loss are calculated for all the hits, the $\frac{dE}{dx}$ of the track is calculated as the 80% truncated mean of these values.

Chapter 7

The inclusive K^0_S production

7.1 Introduction

LEP2 is well suited for the study of the reaction $e^+e^- \to e^+e^-$hadrons. As shown in Chapter 3, this process dominates the cross section and the high beam energies allow to explore high values of the two-photon mass $W_{\gamma\gamma}$, where QCD predictions can be compared to data. Moreover, being far away from the Z pole, the background from other processes is very low.

The study of single particle production provides fundamental information to understand the interplay of the different processes which contribute to the production of hadrons in two-photon collisions (Figure 3.14). The low transverse momentum range allows the study of soft processes while at large p_t the perturbative QCD contributions from the direct, the single-resolved and the double-resolved diagrams can be investigated. Moreover, the study of inclusive K^0_S meson production is a good testing ground for the charm sector since the production of K^0_S is due for a large fraction to the decay of primary charm quarks.

The OPAL Collaboration at LEP2 has performed a study of jet production [101] and a study of inclusive single charged particle and inclusive K^0_S meson production [69] in two-photon collisions, showing reasonable agreement with QCD Next-to-Leading Order (NLO) predictions.

The first study of the inclusive production of K^0_S mesons in untagged two-photon

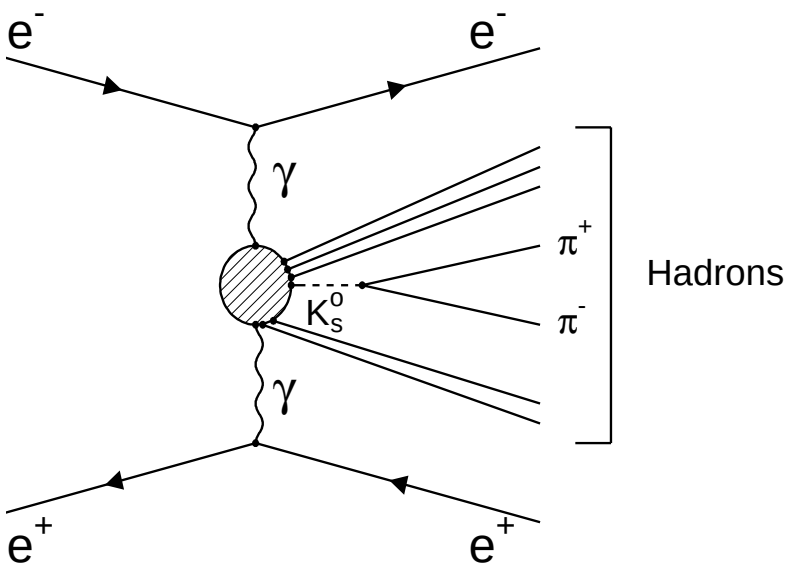

Figure 7.1: The reaction $e^+e^- \to e^+e^-$ hadrons, with a K^0_S decaying into $\pi^+\pi^-$.

collisions in L3 [102] is described here. The process

$$e^+e^- \to e^+e^-K^0_S X, \tag{7.1}$$

where X stands for the remnant hadrons, is shown in Figure 7.1. The selection of K^0_S mesons is based on the decay $K^0_S \to \pi^+\pi^-$.

The data sample used for this analysis corresponds to a total integrated luminosity of 410 pb^{-1} collected during the years 1998 and 1999 at LEP2, as shown in Table 7.1.

The $e^+e^- \to e^+e^-$hadrons processes are simulated with the PHOJET [62] and PYTHIA [63] Monte Carlo event generators. Only the events with $W_{\gamma\gamma} > 5$ GeV and $Q^2 < 8$ GeV^2 are considered, where Q^2 is the maximum four-vector squared of the two photons. For the annihilation processes $e^+e^- \to$ hadrons(γ) events are simulated using PYTHIA [63]; KORALZ [103] is used for $e^+e^- \to \tau^+\tau^-(\gamma)$ and KORALW [104] for $e^+e^- \to W^+W^-$. For the $e^+e^- \to e^+e^-\tau^+\tau^-$ channel the generator DIAG36 [105] is used. The events are simulated in the L3 detector using GEANT [106]

Year	$\sqrt{s}$ (GeV)	$\mathcal{L}$ (pb^{-1})
1998	189	177
1999	192 – 202	233

Table 7.1: The centre of mass energies and integrated luminosities for the full data sample.

and GHEISHA [107] programs and passed through the same reconstruction program as the data. Time dependent detector inefficiencies, as monitored during the data taking period, are also simulated for this analysis.

7.2 The $e^+e^- \to e^+e^-$hadrons event selection

In the process $e^+e^- \to e^+e^-$hadrons a large fraction of the centre of mass energy is carried by the outgoing electron and positron. This kind of events are characterized by a relatively low fraction of the available energy deposited in the calorimeters and by a total multiplicity smaller with respect to the annihilation process. For "no-tag" events, the outgoing electron and positron are not detected.

To select $\gamma\gamma \to$hadrons events, the following selection criteria are applied to the data sample:

- At least six particles must be detected. A particle can be a track, a photon or a pion cluster in the hadron calorimeter or in the luminosity monitor. A track must have a transverse momentum $p_t > 100$ MeV, at least 12 wire hits in the TEC and a distance of closest approach to the primary vertex less than 10 mm in the transverse plane. A photon candidate is a cluster in the electromagnetic calorimeter, with no nearby track in a 200 mrad cone. Its associated energy in the hadron calorimeter must be smaller than 20% of the electromagnetic energy. Clusters in the hadron calorimeter, without any track within a 300 mrad cone and with an energy greater than 20% of the electromagnetic energy are considered as pions, since they are mainly outside the tracking chamber detection region. Clusters in the luminosity monitor with energy less than 30 GeV are considered as pions if their energy is below 5 GeV and as photons

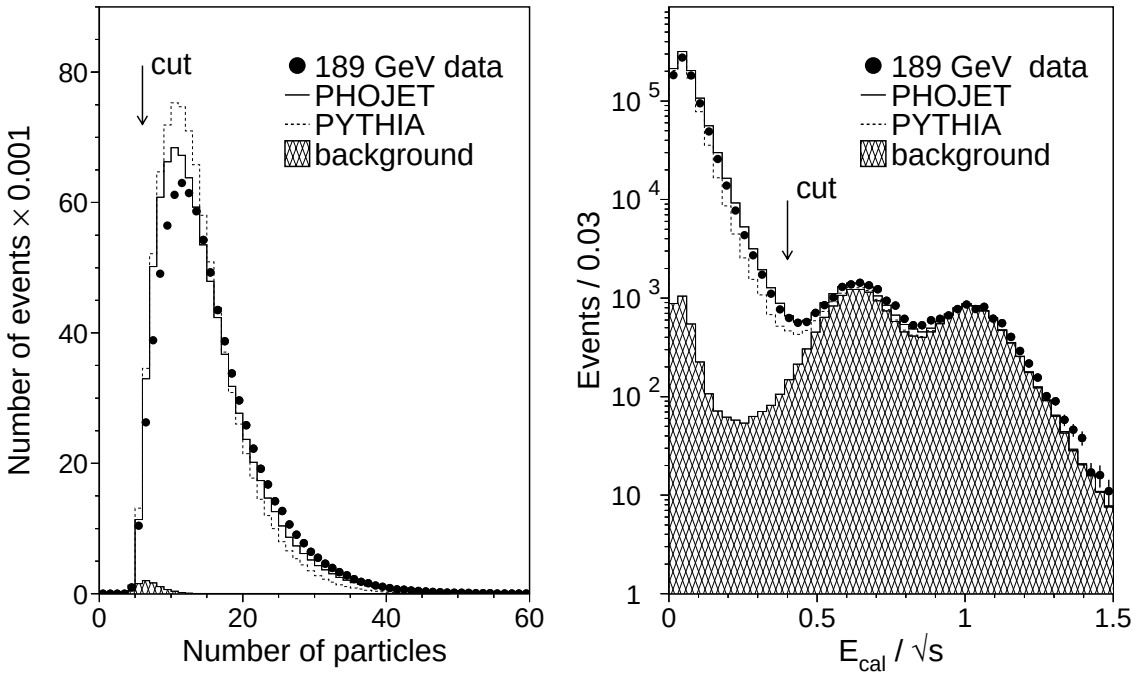

Figure 7.2: The distributions of the number of particles (a) and of the sum of the energies in the electromagnetic and in the hadronic calorimeters divided by $\sqrt{s}$ (b). The arrows correspond to the cuts applied.

above 5 GeV. Figure 7.2(a) shows the distribution of the number of particles. The two Monte Carlo programs produce a clear excess of events with a low multiplicity of particles. The PHOJET Monte Carlo is found to reproduce better the data with respect to PYTHIA.

- The total energy in the electromagnetic calorimeter is required to be greater than 500 MeV in order to suppress beam-gas and beam-wall backgrounds and smaller than 50 GeV , to exclude events from the process $e^+e^- \to \gamma Z$. The total energy deposited in the calorimeters must be less than 40 % of the centre of mass energy $\sqrt{s}$, to exclude annihilation events. Figure 7.2(b) shows the distribution of the sum of the energy deposited in the electromagnetic and in the hadronic calorimeters divided by $\sqrt{s}$. Both the Monte Carlo generators

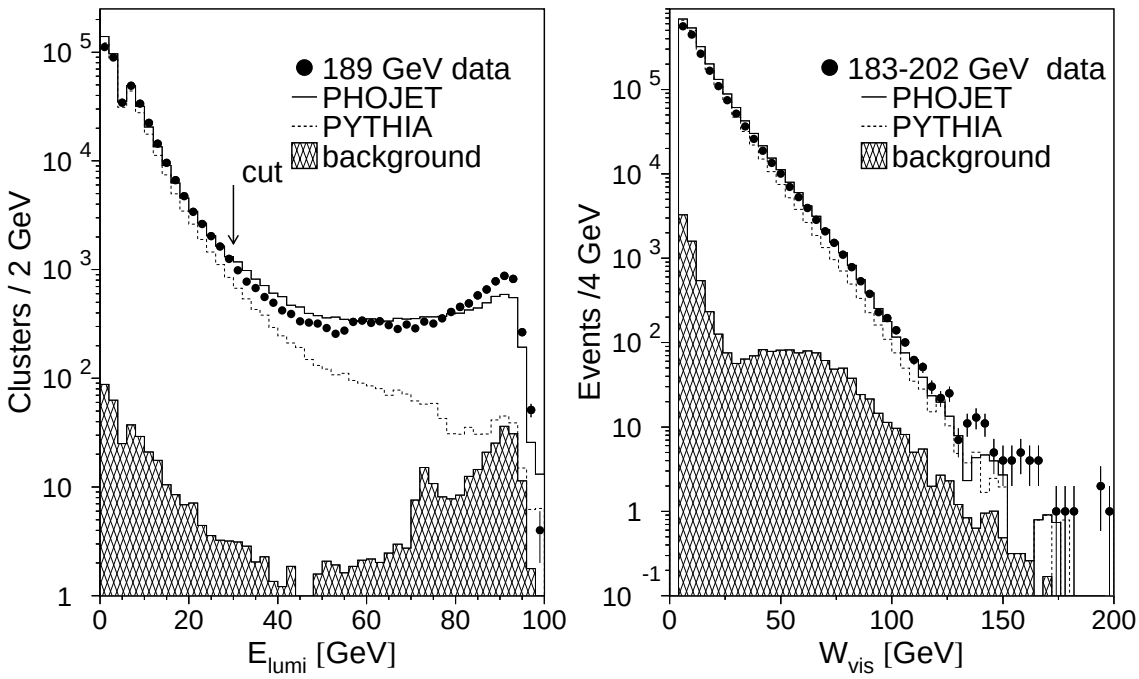

(a) (b)

Figure 7.3: The distributions of the maximum energy detected by one luminosity monitor (a) and of the visible effective mass W_{vis} (b). The arrows correspond to the cuts applied.

reproduce quite well the data.

- An anti-tag condition is imposed which excludes events with clusters having energy greater than 30 GeV in the luminosity monitor, in a fiducial region of 33−64 mrad. The Q^2 value of the selected events is thus less than 8 GeV^2, its average value being $< Q^2 > \sim 1.5 \times 10^{-2}$ GeV^2. Figure 7.3(a) shows the distribution for the maximum energy detected by one luminosity monitor. The PYTHIA Monte Carlo generator does not reproduce high Q^2 events because of a cutoff $Q^2 \leq m_\rho^2$ applied to the two-photon luminosity function. At low Q^2 both the generators reproduce well the data.

The visible effective mass W_{vis} of the event is calculated from the four-momentum

vectors of the measured particles according to the formula

$$W^2_{vis} = \Big(\sum_i E_i\Big)^2 - \Big(\sum_i \vec{p}_i\Big)^2 \tag{7.2}$$

where i ranges over all pions and photons. Events produced by resonance formation and by VDM diffractive processes, like $\gamma\gamma \to \rho^0\rho^0$, are characterized by low values of the visible effective mass. In order to remove these events,

- the condition $W_{vis} \geq 5$ GeV is required.

The distribution of W_{vis} is shown in Figure 7.3(b) and is found to be well reproduced either by PHOJET or by PYTHIA, except for high values of W_{vis} where the data are higher.

After these selection cuts 7.8×10^5 at $\sqrt{s} = 189$ GeV and 1.0×10^6 at $\sqrt{s} = 192 - 202$ GeV events are selected. The background from beam-gas and beam-wall interactions is found to be negligible. The background to the process $\gamma\gamma \to$hadrons is below 1% at low masses, dominated by two-photon τ production. It increases at high masses, due mainly to annihilation processes and reaches a maximum of $\simeq 15\%$ at 130 GeV.

7.3 The $e^+e^- \to e^+e^-$hadrons total cross section

The total cross section for all hadron-hadron interactions is characterized by a steep decrease at low centre of mass energies followed by a slow rise at high energies. According to Regge theory, this behaviour of the cross section is explained in terms of the exchange of Regge trajectories, $\alpha(t)$, in the t-channel. The total cross section can be written as

$$\sigma_{tot} \propto s^{(\alpha(0)-1)} \tag{7.3}$$

where $\alpha(0)$ is the intercept of the Regge trajectory

$$\alpha(t) = \alpha(0) + \alpha' \cdot t. \tag{7.4}$$

The low energy region is dominated by Reggeon R exchange, with R=$\rho, \omega, \phi, ...$, for which $\alpha_R(0) \simeq 0.5$. Pomeron exchange with $\alpha_P(0) \simeq 1$ dominates at high energies.

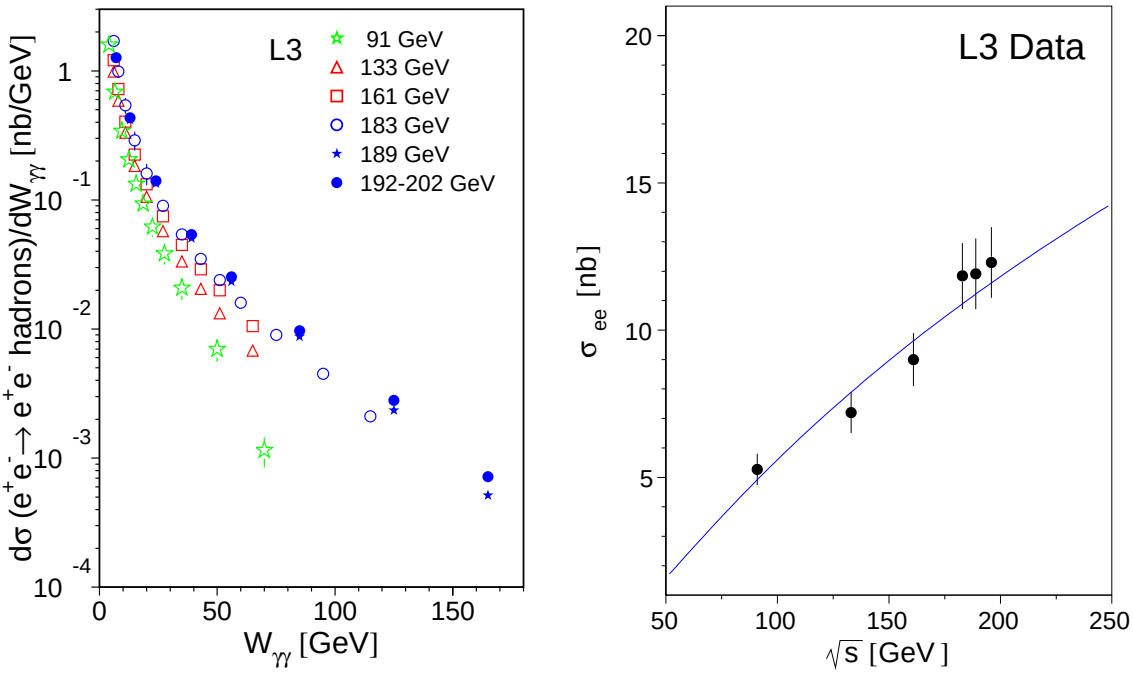

(a) (b)

Figure 7.4: The total cross section of the process $e^+e^- \to e^+e^-$hadrons as a function of $W_{\gamma\gamma}$ for several center of mass energies (a) and as a function of the center of mass energy (b).

This leads to the Donnachie and Landshoff [108] parameterization of the hadronic cross section

$$\sigma_{tot} = As^{\epsilon} + Bs^{-\eta} \tag{7.5}$$

that describes well all the known hadron-hadron cross sections [28]. The values of ϵ and η are found to be universal. The values $\epsilon = 0.093 \pm 0.002$ and $\eta = 0.358 \pm 0.015$ are consistent with pp, πp and γp data. If the photon behaves like a hadron, Equation (7.5) is expected to be valid also for the photon-photon hadronic cross section. Before LEP, only the region of $W_{\gamma\gamma}$ below 10 GeV was explored and the data could not put in evidence any consistence or inconsistence with the Donnachie and Landshoff parameterization. The total cross section for the process $e^+e^- \to e^+e^-$hadrons is measured by L3 [109] and OPAL [110]. The total cross section as a

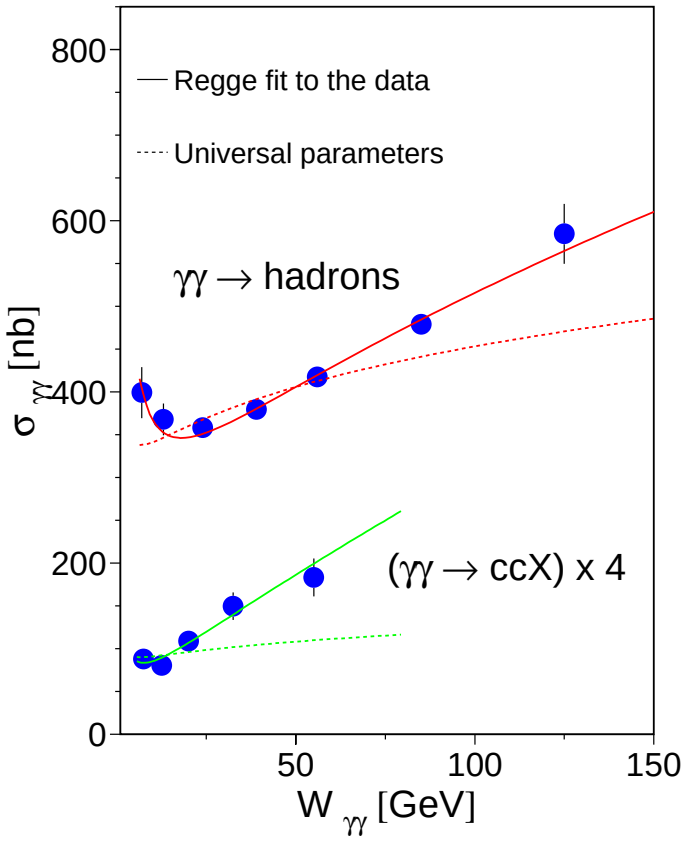

Figure 7.5: The total cross section of the processes $\gamma\gamma$ →hadrons [109] and $\gamma\gamma \rightarrow c\bar{c}X$ [111] as a function of $W_{\gamma\gamma}$.

function of $W_{\gamma\gamma}$ is measured by L3 for several values of the center of mass energy, as shown in Figure 7.4(a). For a given value of $W_{\gamma\gamma}$, the cross section rises with the beam energy because of the luminosity function. The total cross section as a function of the center of mass energy is shown in Figure 7.4(b) and is found to rise as $(\log E_{beam})^2$, as expected. The data are in fact well fitted by the function

$$\sigma = a + b \cdot (\log \sqrt{s} - 4)^2 \tag{7.6}$$

where the values $a = 3.66$ and $b = 5.03$ are obtained from the fit. The χ^2 of the fit is 2.9 for 4 degrees of freedom.

Figure 7.5 shows the cross section for the process $\gamma\gamma$ →hadrons as a function of

$W_{\gamma\gamma}$ measured by L3. The cross section for open charm production as a function of $W_{\gamma\gamma}$ is also shown. The data are well fitted by the Donnachie and Landshoff parameterization of Equation (7.5) but a value of $\epsilon = 0.225 \pm 0.021$ is found for $\gamma\gamma \rightarrow$hadrons, more than a factor two higher than the universal value. The value $\epsilon = 0.40 \pm 0.03 \pm 0.07$ is found in the case of charm production. These results are not dependent on the Monte Carlo model used to correct the data and put in evidence a steeper rise of the photon-photon hadronic total cross section with respect to the hadron-hadron and photon-proton processes. This indicates the importance of QCD phenomena due to the $q\bar{q}$ component in the photon wave function. When a hard scale, as the charm quark, is present, the soft processes are suppressed and the energy dependence of the cross section can be reproduced by perturbative QCD calculations [111].

7.4 K^0_S selection

Once hadronic two-photon events are selected, K^0_S candidates are searched for by reconstructing the secondary vertex produced by the decay $K^0_S \rightarrow \pi^+\pi^-$. The following selection criteria are applied to the reconstructed secondary vertices:

- The distance $d_\perp$ between the primary and the secondary vertex in the transverse plane must be greater than 3 mm.
- The angle α between the flight direction of the K^0_S candidate and the total transverse momentum vector of the two outgoing tracks must be less than 0.075 rad.

After all these selection criteria 516540 events are selected. A typical event is presented in Figures 7.6 and 7.7. Considering the K^0_S signal, the background due to non two-photon fusion processes is estimated to be negligible.

In Figure 7.8 the $\pi^+\pi^-$ mass spectrum is shown for different intervals of the transverse momentum of the K^0_S candidates. A clear K^0_S signal is present over a smooth background. The width of the signal is found to be $\sigma = 8$ MeV for p_t below 1 GeV. It increases up to $\sigma = 13$ MeV for p_t around 4 GeV, consistent with the Monte Carlo.

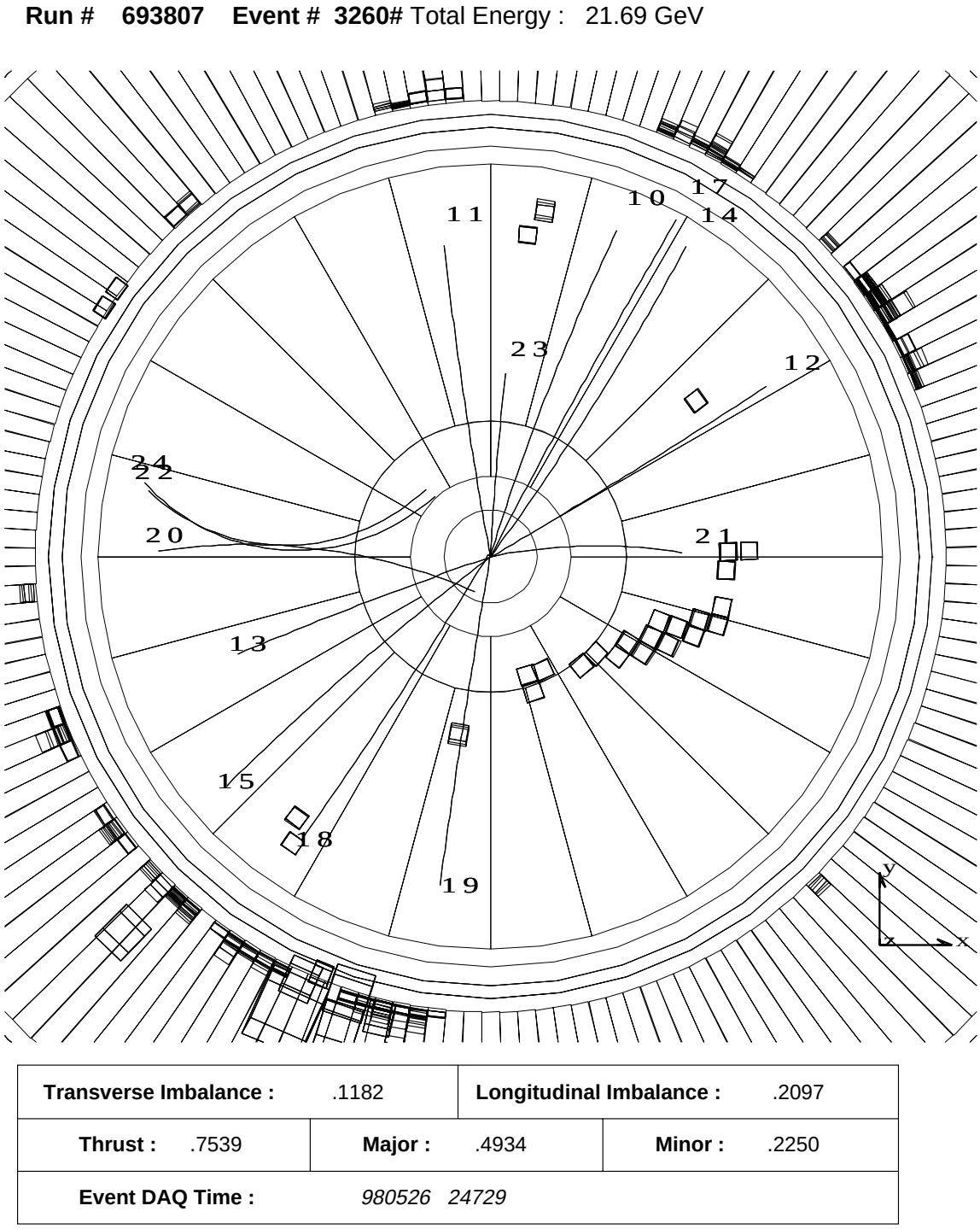

Figure 7.6: A typical hadronic event produced by the collision of two photons. The structure of the electromagnetic calorimeter, of the Outer and the Inner TEC are visible.

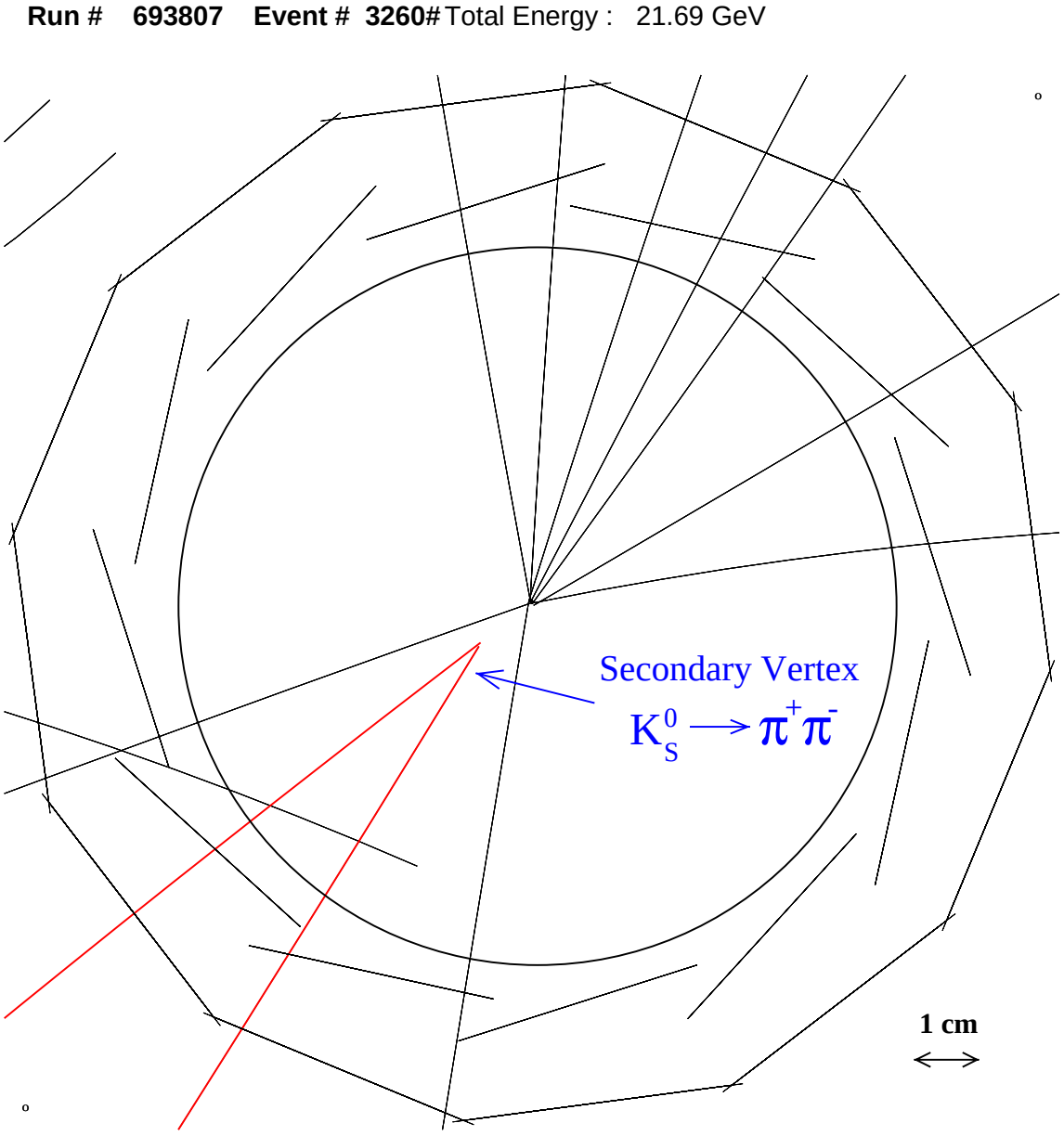

Figure 7.7: The event presented in Figure 7.6 shows the presence of a K^0_S meson. The structure of the SMD and the beam pipe are visible.

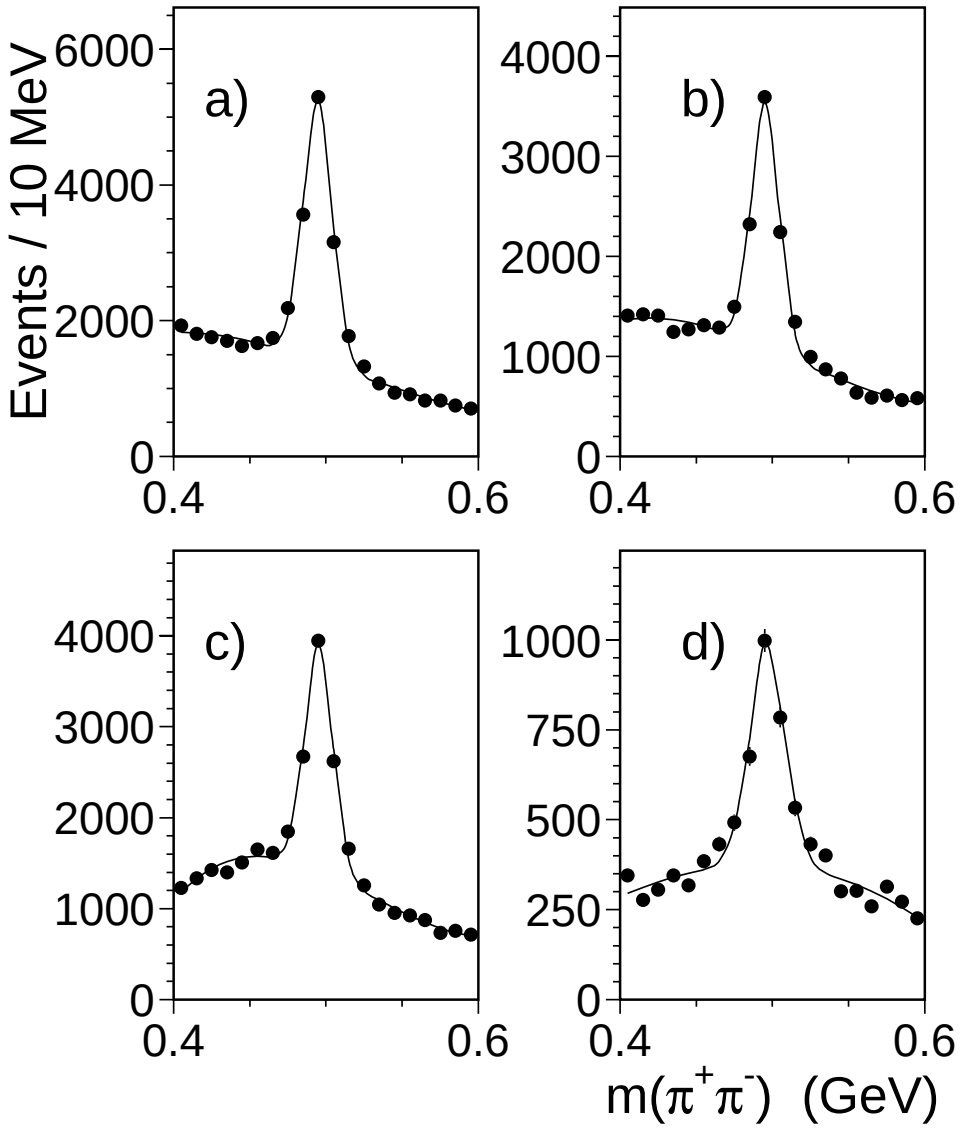

Figure 7.8: The $\pi^+\pi^-$ mass distribution for different values of the transverse momentum p_t of the K^0_S candidates: $0.6 < p_t < 0.8$ GeV (a), $0.8 < p_t < 1.0$ GeV (b), $1.0 < p_t < 1.5$ GeV (c) and $1.5 < p_t < 2.0$ GeV (d). The K^0_S signal is prominent over a smooth background. The line corresponds to the fit of a gaussian plus a third order Chebyshev polynomial for the background.

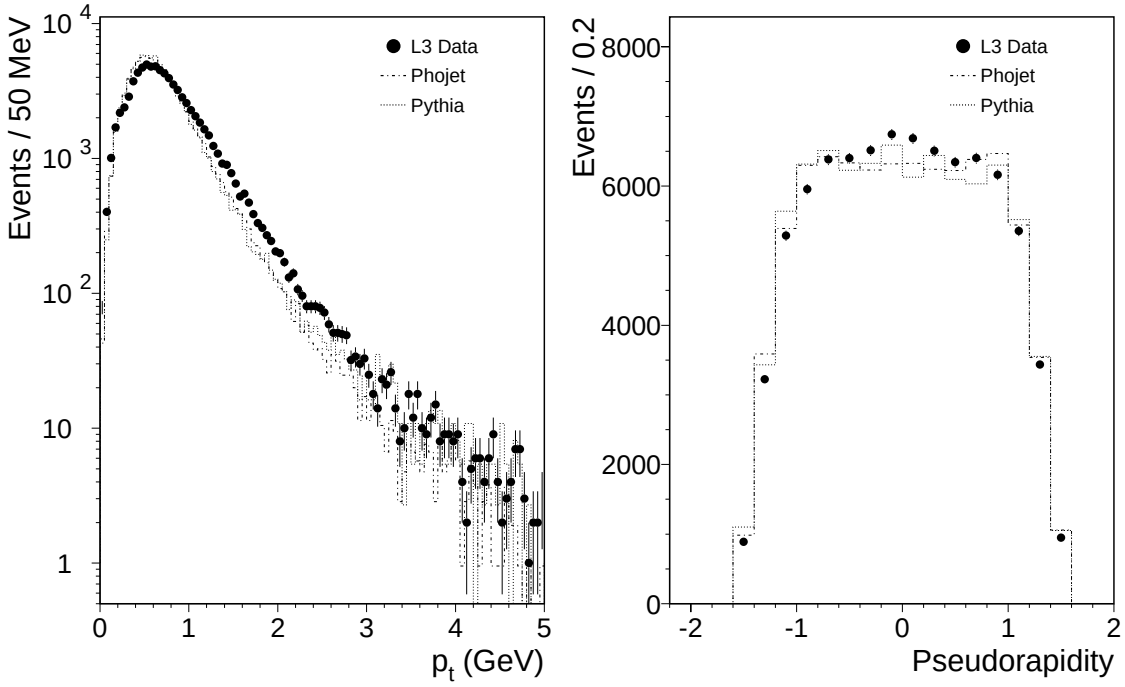

(a) (b)

Figure 7.9: The transverse momentum distribution (a) and the pseudorapidity distribution (b) for the K^0_S candidates in a mass window of ± 30 MeV around the K^0_S mass.

In Figure 7.9(a) and in Figure 7.9(b) the distributions are shown for the transverse momentum p_t and the pseudorapidity

$$\eta = -\log\left(\tan\frac{\theta}{2}\right) \tag{7.7}$$

of the K^0_S candidates selected in a mass window of $\pm$ 30 MeV around the K^0_S mass. Data are in reasonable agreement with respect to the PHOJET and PYTHIA Monte Carlo predictions.

7.5 The K^0_S inclusive production cross section

The differential cross sections as a function of the transverse momentum and of the pseudorapidity are measured for events with $W_{\gamma\gamma} > 5$ GeV and $W_{\gamma\gamma} > 10$ GeV. The selection cut on W_{vis} is set to 5 and 10 GeV, respectively.

To measure the differential cross section as a function of p_t, the K^0_S candidates with $|\eta| < 1.5$ are subdivided in nine bins of p_t with sufficient statistics in each bin. The differential cross section $(d\sigma/dp_t)_i$ is measured for every bin using the formula

$$\left(\frac{d\sigma}{dp_t}\right)_i = \frac{(N_{obs} - N_{bkg})_i}{\varepsilon_i \cdot \mathcal{L} \cdot \Delta p_t^i} \tag{7.8}$$

where i indicates the bin. Similarly the differential cross section as a function of $|\eta|$ is measured by subdividing the K^0_S candidates with $p_t > 1.5$ GeV in four bins and by evaluating the quantity

$$\left(\frac{d\sigma}{d|\eta|}\right)_i = \frac{(N_{obs} - N_{bkg})_i}{\varepsilon_i \cdot \mathcal{L} \cdot \Delta|\eta|_i} \tag{7.9}$$

in each bin. $(N_{obs} - N_{bkg})_i$ is the number of K^0_S in the bin, ε_i the total detection efficiency, $\mathcal{L}$ the integrated luminosity, Δp_t^i and $\Delta|\eta|_i$ the width of the bin. $(N_{obs} - N_{bkg})_i$ is evaluated by fitting the mass spectrum with a gaussian and a third order Chebyshev polynomial for the background. The total detection efficiency ε_i includes the effects of the acceptance, selection cuts, trigger and corrects for the branching fraction of the K^0_S into $\pi^+\pi^-$.

7.6 The trigger efficiency

Two-photon hadronic events are collected predominantly by the level-one charged particle trigger composed by the Outer TEC and the Inner TEC triggers.

Due to the small energy deposited in the calorimeters, only 11% of the events are collected also by the energy trigger. Since the charged particle and the energy trigger are independent, this sample can be used to evaluate the level-one trigger efficiency directly on the data. The level-one trigger efficiency is evaluated from the ratio

$$\varepsilon_{level-one} = \frac{N_{C.and.E}}{N_E} \tag{7.10}$$

Year	$\varepsilon_{level-one}$ %	$\varepsilon_{level-two}$ %	$\varepsilon_{level-three}$ %
1998	96	92	93
1999	92	91	99

Table 7.2: The trigger efficiencies for the two years of data taking.

where $N_{C.and.E}$ is the number of events collected by the charged particle and the energy trigger and N_E is the number of events collected by the energy trigger. The level-one efficiencies for the two years of data taking are reported in Table 7.2. The decrease in 1999 is due to a stricter condition applied to the Inner TEC trigger.

One event out of 20 which is rejected by the level-two or by the level-three trigger is written on tape and flagged as such. This allows to evaluate the level-two and level-three trigger efficiencies directly on data as reported in Table 7.2. The significant increase in the level-three efficiency in 1999 is due to a change in the level-three algorithm that was redesigned to improve the efficiency for the two-photon hadronic events.

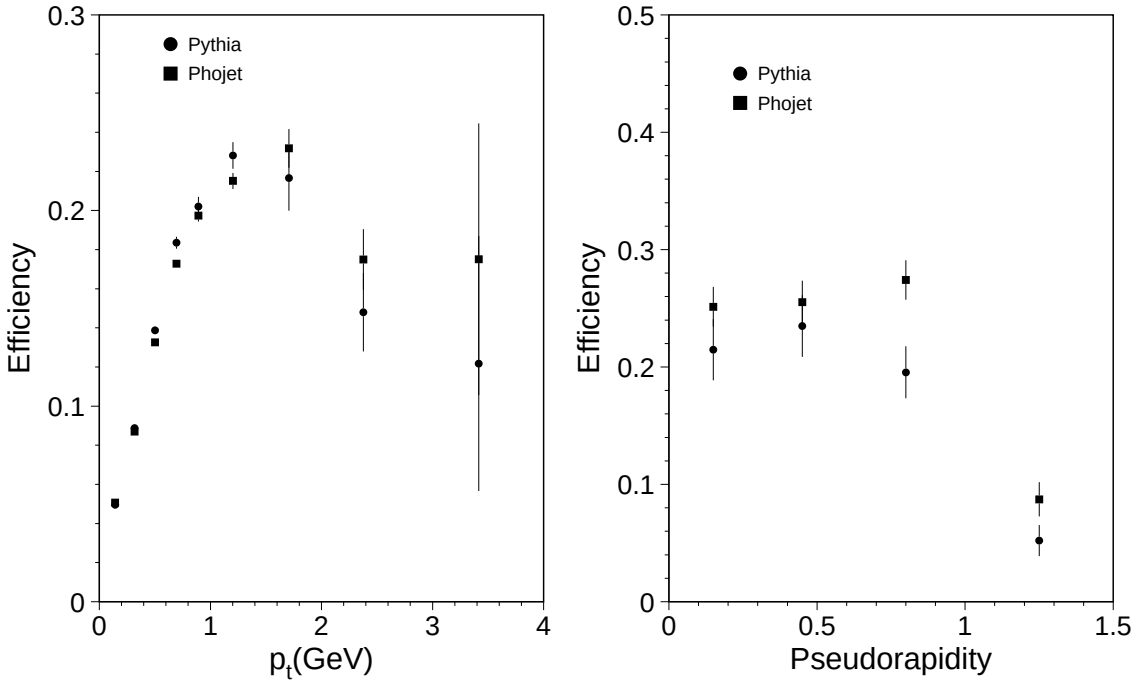

(a) (b)

Figure 7.10: The total detection efficiency as a function of the transverse momentum (a) and of the pseudorapidity (b) for the K^0_S candidates for events with $W_{\gamma\gamma} > 5$ GeV.

7.7 The total detection efficiency

The total detection efficiency is the product of the trigger efficiency and the selection efficiency. The selection efficiency is calculated using the PHOJET and the PYTHIA Monte Carlo programs as the ratio between the reconstructed and the generated K^0_S's. The number of the reconstructed K^0_S's is evaluated by performing a fit with a gaussian plus a third order Chebyshev polynomial for the background on the $\pi^+\pi^-$ mass spectrum for each bin of the transverse momentum and of the pseudorapidity.

Figures 7.10 and 7.11 show the total efficiency as a function of the transverse momentum and of the pseudorapidity for the two Monte Carlo generators. Since PHOJET and PYTHIA reproduce reasonably well the data and since the values of the total efficiencies are compatible within about one standard deviation, the average

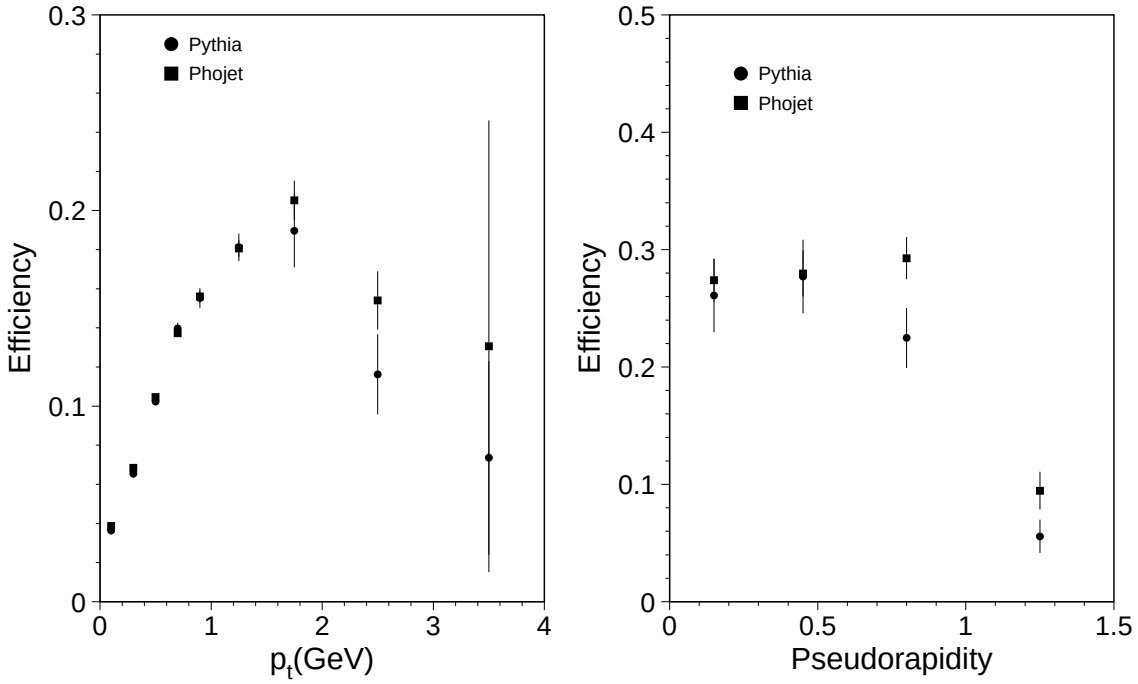

(a) (b)

Figure 7.11: The total detection efficiency as a function of the transverse momentum (a) and of the pseudorapidity (b) for the K^0_S candidates for events with $W_{\gamma\gamma} > 10$ GeV.

of the two Monte Carlo generators is used to correct the data.

The efficiency as a function of the transverse momentum drops at low p_t due to the secondary vertex reconstruction efficiency and at high values of p_t because of the K^0_S's which decay inside the volume of the TEC. The efficiency as a function of the pseudorapidity is rather flat and it drops at large values of $|\eta|$ due to the limited acceptance of the TEC in the forward-backward region.

7.8 Systematic uncertainties

The difference between the two Monte Carlo generators introduces a systematic uncertainty on the selection efficiency. The corresponding systematic uncertainty is

estimated as

$$\left(\frac{\Delta\varepsilon}{\epsilon}\right)_{sys} = \sqrt{\left(\frac{\varepsilon_{PHOJET} - \varepsilon_{PYTHIA}}{\varepsilon_{PHOJET} + \varepsilon_{PYTHIA}}\right)^2 - \left(\frac{\sigma_{PHOJET}}{\varepsilon_{PHOJET}}\right)^2 - \left(\frac{\sigma_{PYTHIA}}{\varepsilon_{PYTHIA}}\right)^2} \quad (7.11)$$

where the two negative terms take into account the statistical error on the two selection efficiencies. If the negative terms are larger than the positive term, no systematic uncertainty is assigned. In the limit of infinite statistics, these two terms reduce to zero and the systematic uncertainty is just half of the difference between PHOJET and PYTHIA.

Another source of systematic uncertainty is the fitting procedure. The cross sections are recalculated by assuming a second order polynomial for the background in the fits of the $\pi^+\pi^-$ mass spectra. Half of the difference between the two results is considered and a systematic uncertainty is assigned with the same procedure used for the selection efficiency.

A systematic uncertainty of 2.0% is assigned to the trigger efficiency which takes into account the stability with respect to time.

The systematic uncertainty introduced by the analysis selection criteria is evaluated by varying the values of the cuts applied. A systematic uncertainty of 7.5% is assigned to the hadronic selection and of 2.5% to the K^0_S selection.

Despite the data sample is collected at different centre of mass energies, no systematic effect is introduced and the effects related to the beam energy can be neglected. The differential cross section as a function of the transverse momentum is measured for the two data samples collected in 1998 and in 1999 separately. The two measurements are shown in Figure 7.12 where only the statistical errors are drawn.

Source	Contribution %
MC Difference	1 - 6
Fitting procedure	1 - 7
Trigger efficiency	2.0
Hadronic selection	7.5
K^0_S selection	2.5

Table 7.3: The sources of systematic uncertainty and the corresponding contributions.

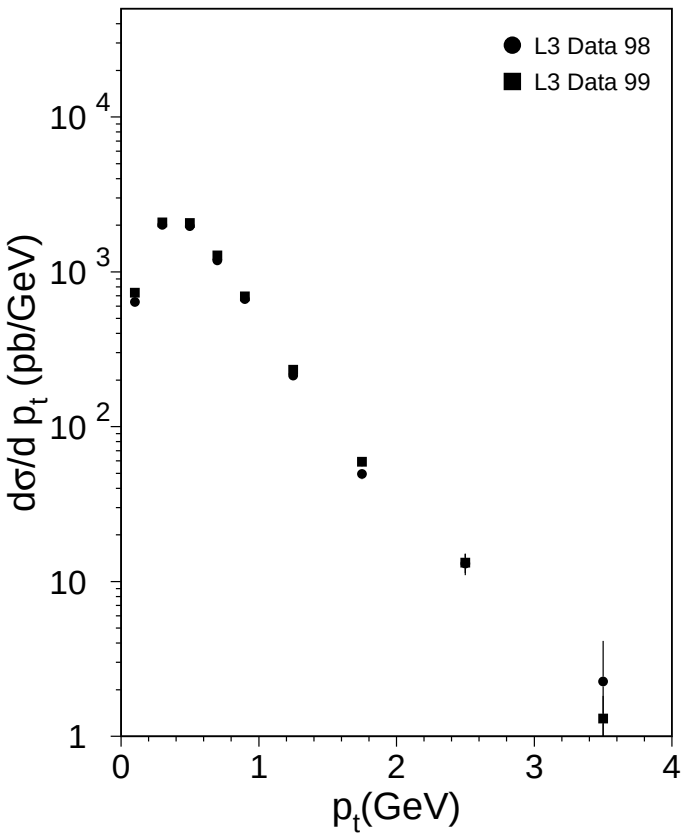

Figure 7.12: The differential cross section as a function of p_t for $|\eta| < 1.5$ for the 1998 and the 1999 data samples separately. Only the statistical uncertainties are shown.

The overlapping of the data points, within the statistical uncertainties, shows that the data are homogeneous and can be considered as a unique sample.

The total systematic uncertainty is calculated in each bin of the transverse momentum and of the pseudorapidity by adding in quadrature all the contributions reported in Table 7.3.

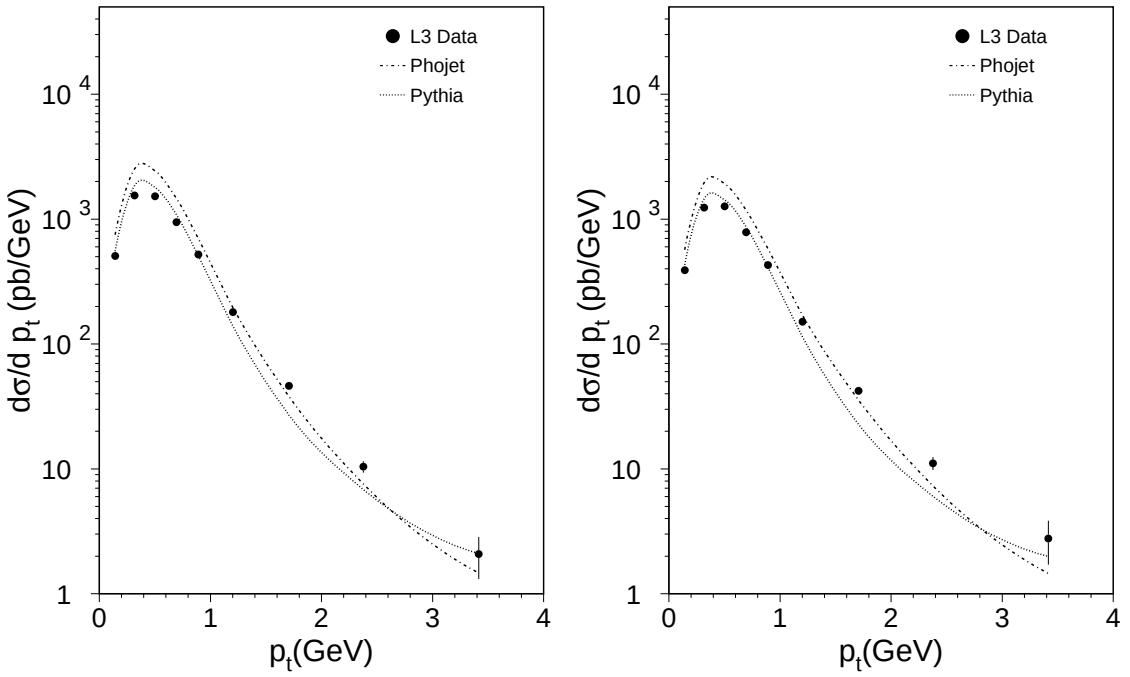

Figure 7.13: The measured differential cross section as a function of p_t for $|\eta| < 1.5$ and for $W_{\gamma\gamma} > 5$ GeV (a) and for $W_{\gamma\gamma} > 10$ GeV (b) is compared to the predictions of the PHOJET and PYTHIA Monte Carlos.

7.9 The cross section as a function of the transverse momentum

The measurement of the cross section as a function of the transverse momentum for $|\eta| < 1.5$ is shown in Figure 7.13 and is reported in Table 7.4. In Figure 7.13 the results are compared with the predictions of the PHOJET and PYTHIA Monte Carlos. The p_t distribution is not well reproduced by both the Monte Carlo models. The cross section drops for values of the transverse momentum smaller than the mass of the K^0_S meson because of the phase space factor.

$W_{\gamma\gamma} > 5$ GeV										
p_t Range (GeV)	$< p_t >$ (GeV)	N_{signal}			ϵ (%)	$d\sigma/dp_t$ (pb/GeV)				
0.0 − 0.2	0.142	2084	±	83	5.0	507.8	±	20.3	±	25.8
0.2 − 0.4	0.317	11109	±	151	8.8	1541.3	±	20.9	±	78.5
0.4 − 0.6	0.501	16935	±	218	13.6	1521.6	±	19.5	±	80.7
0.6 − 0.8	0.695	13837	±	210	17.8	946.9	±	14.3	±	53.0
0.8 − 1.0	0.893	8532	±	173	20.0	520.8	±	10.6	±	26.5
1.0 − 1.5	1.203	8184	±	184	22.2	180.1	±	4.0	±	9.1
1.5 − 2.0	1.708	2120	±	114	22.4	46.1	±	2.5	±	2.3
2.0 − 3.0	2.378	689	±	72	16.1	10.4	±	1.0	±	0.6
3.0 − 4.0	3.417	126	±	46	14.8	2.0	±	0.7	±	0.2
$W_{\gamma\gamma} > 10$ GeV										
p_t Range (GeV)	$< p_t >$ (GeV)	N_{signal}			ϵ (%)	$d\sigma/dp_t$ (pb/GeV)				
0.0 − 0.2	0.142	1200	±	1200	3.8	390.0	±	21.5	±	19.8
0.2 − 0.4	0.317	6791	±	6791	6.7	1237.3	±	22.4	±	63.0
0.4 − 0.6	0.501	10707	±	10707	10.4	1261.5	±	21.4	±	64.3
0.6 − 0.8	0.695	8923	±	8923	13.8	786.0	±	15.5	±	40.0
0.8 − 1.0	0.893	5460	±	5460	15.6	427.8	±	11.2	±	21.8
1.0 − 1.5	1.203	5576	±	5576	18.1	150.7	±	4.2	±	7.6
1.5 − 2.0	1.708	1707	±	1707	19.7	42.2	±	2.3	±	2.1
2.0 − 3.0	2.378	615	±	615	13.5	11.1	±	1.3	±	0.6
3.0 − 4.0	3.417	115	±	115	10.2	2.8	±	1.0	±	0.3

Table 7.4: The $e^+e^- \rightarrow e^+e^-K^0_S X$ differential cross section as a function of the transverse momentum for $|\eta| < 1.5$. The first error is statistical and the second is systematic.

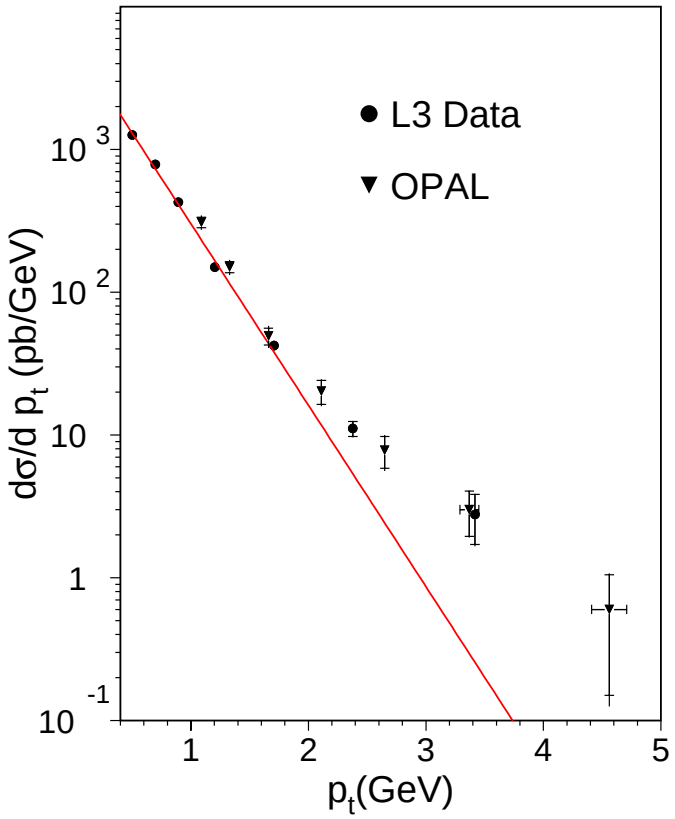

Figure 7.14: The differential cross section as a function of p_t for $|\eta| < 1.5$ and for $W_{\gamma\gamma} > 10$ GeV measured by L3 and OPAL. The line corresponds to the exponential fit performed on L3 data in the interval $0.4 < p_t < 2$ GeV.

In Figure 7.14 our measurement for $W_{\gamma\gamma} > 10$ GeV is compared to the results published by OPAL [69] at LEP2 at $\sqrt{s} = 161$ and 172 GeV. OPAL data are multiplied by a factor 1.1 to take into account the effect of the different beam energy on the luminosity function. Good agreement is found between the two measurements.

It is important to note that L3 data cover also the p_t region below 1 GeV where the cross section shows an exponential behaviour, typical of the soft processes in the strong interactions [112]. An exponential fit of the form

$$\frac{d\sigma}{dp_t} = A \times \exp\left(-\frac{p_t}{\langle p_t \rangle}\right) \tag{7.12}$$

is performed in the low range of p_t from 0.4 to 2 GeV, as shown in Figure 7.14. The

value

$$\langle p_t \rangle = 342 \pm 8 \ \text{MeV} \tag{7.13}$$

is obtained. The χ^2 of the fit is 3.1 for 3 degrees of freedom. If the fit is performed for $W_{\gamma\gamma} > 5$ GeV, a similar value $\langle p_t \rangle = 337 \pm 8$ MeV is obtained.

At high p_t the cross sections are higher than the exponential and show a different behaviour of the photon with respect to other hadrons. As shown in Chapter 3, the photon can interact directly as a point-like particle and hard QCD processes like photon-gluon fusion must be taken into account to describe the high p_t spectrum of hadrons produced in photon-photon collisions.

7.9.1 The multiplicity

The multiplicity m of K^0_S mesons per two-photon hadronic event is calculated in the range $p_t < 4$ GeV and $|\eta| < 1.5$ and for $W_{\gamma\gamma} > 5$ GeV. Using the measurement of the $e^+e^- \to e^+e^-$hadrons total hadronic cross section [109] for $W_{\gamma\gamma} > 5$ GeV, the average number of K^0_S mesons per hadronic two-photon event is evaluated as

$$m = \frac{\sum_i \frac{N^i_{signal}}{\varepsilon_i}}{\sigma_{e^+e^- \to e^+e^- \text{hadrons}} \cdot \mathcal{L}} \tag{7.14}$$

where i indicates the bin in p_t and $\mathcal{L}$ is the total integrated luminosity. The value

$$m = 0.094 \pm 0.009 \pm 0.005 \quad \frac{K^0_S}{\text{Event}} \tag{7.15}$$

is obtained. The first error is statistical and the second is systematic. This result is in good agreement with the Monte Carlo predictions of 0.11 K^0_S/Event by PHOJET and 0.10 K^0_S/Event by PYTHIA.

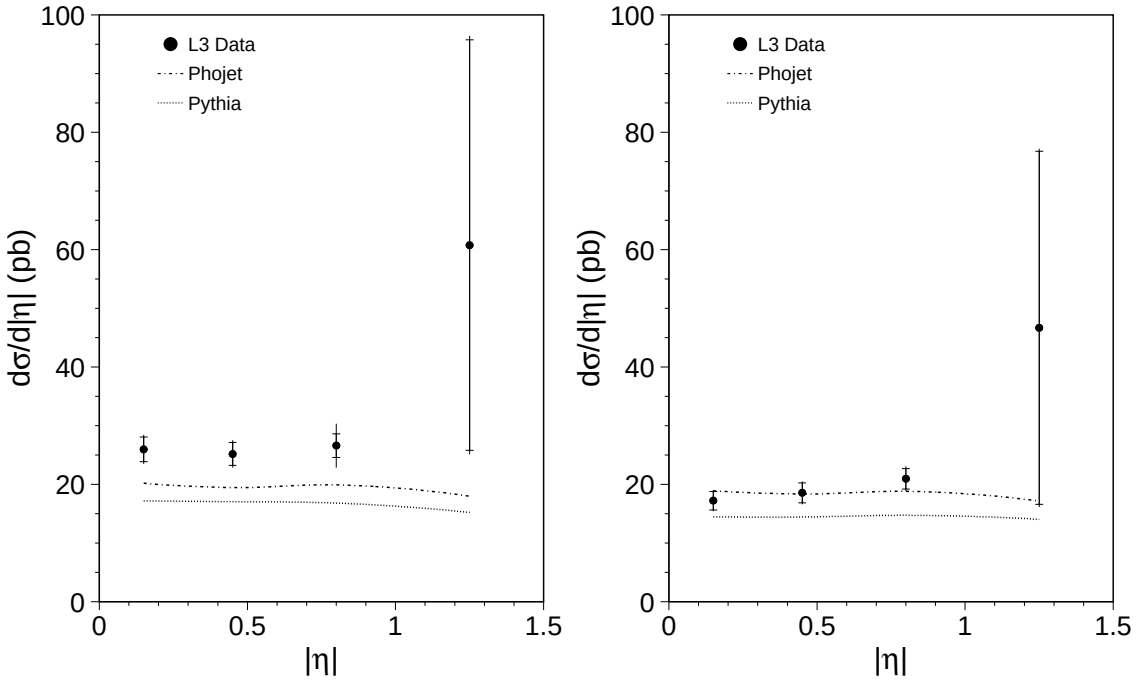

Figure 7.15: The measured differential cross section as a function of $|\eta|$ for $p_t > 1.5$ GeV and for $W_{\gamma\gamma} > 5$ GeV (a) and $W_{\gamma\gamma} > 10$ GeV (b) is compared to the predictions of the PHOJET and PYTHIA Monte Carlos.

7.10 The cross section as a function of the pseudorapidity

The measurement of the cross section as a function of the pseudorapidity for $p_t > 1.5$ GeV is performed for $W_{\gamma\gamma} > 5$ GeV and $W_{\gamma\gamma} > 10$ GeV. The results are reported in Table 7.5.

In Figure 7.15 L3 data are compared with the predictions of the PHOJET and PYTHIA Monte Carlos. The shape of the $|\eta|$ distribution is well in agreement with the two Monte Carlo generators. For $W_{\gamma\gamma} > 5$ GeV, PHOJET and PYTHIA are $\sim$25% and $\sim$35% too low, respectively. For $W_{\gamma\gamma} > 10$ GeV, PHOJET agrees not only in the shape but also in the value of the cross section while PYTHIA is $\sim$15% too low.

$W_{\gamma\gamma} > 5$ GeV									
$\|\eta\|$ Range	N_{signal}			ϵ (%)	$d\sigma/d\|\eta\|$ (pb)				
0.0 − 0.3	744	±	60	23.3	25.9	±	2.0	±	1.3
0.3 − 0.6	759	±	58	24.5	25.1	±	1.9	±	1.2
0.6 − 1.0	1024	±	77	23.5	26.6	±	2.0	±	3.1
1.0 − 1.5	868	±	499	7.0	60.7	±	35.0	±	6.7
$W_{\gamma\gamma} > 10$ GeV									
$\|\eta\|$ Range	N_{signal}			ϵ (%)	$d\sigma/d\|\eta\|$ (pb)				
0.0 − 0.3	566	±	51	26.7	17.2	±	1.6	±	0.8
0.3 − 0.6	635	±	58	27.8	18.6	±	1.7	±	0.9
0.6 − 1.0	889	±	74	25.9	21.0	±	1.7	±	1.1
1.0 − 1.5	719	±	463	7.5	46.7	±	30.1	±	5.2

Table 7.5: The $e^+e^- \to e^+e^-K^0_S X$ differential cross section as a function of the pseudorapidity for $p_t > 1.5$ GeV. The first error is statistical and the second is systematic.

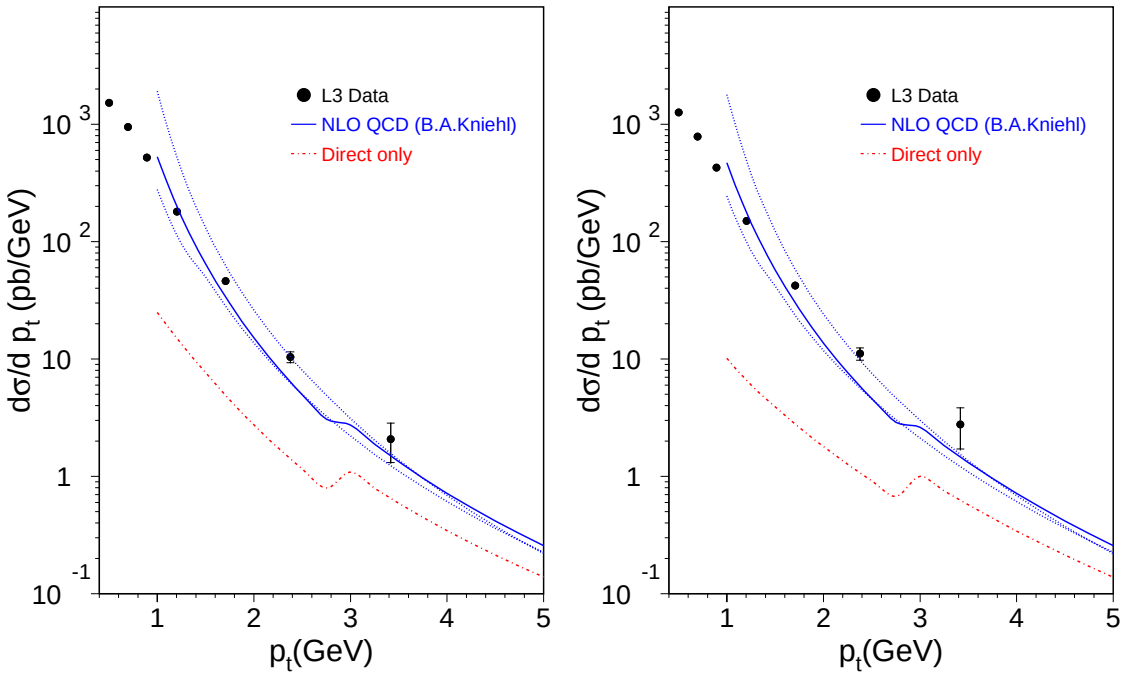

Figure 7.16: The measured differential cross section as a function of p_t for $|\eta| < 1.5$ and for $W_{\gamma\gamma} > 5$ GeV (a) and for $W_{\gamma\gamma} > 10$ GeV (b) is compared to the NLO QCD predictions by Kniehl. The solid line corresponds to the scale factor $x = 1$ while the upper dotted line to $x = 0.5$ and the lower dotted line to $x = 2$. The dash-dotted line corresponds to the direct contribution.

7.11 Comparison with QCD predictions

The measurements of the cross section as a function of the transverse momentum and of the pseudorapidity represent a good test for Next-to-Leading Order (NLO) QCD predictions. The results of the calculations shown in this Section have been performed by Kniehl [113] considering all the elementary $2 \to 2$ and $2 \to 3$ subprocesses and using the parton density function of the photon. According to the author, the predictions are reliable for values of p_t larger than 1.5 GeV. The factorization and the renormalization scales are set equal to xp_t and predictions for $x = 0.5$, 1 and 2 are provided.

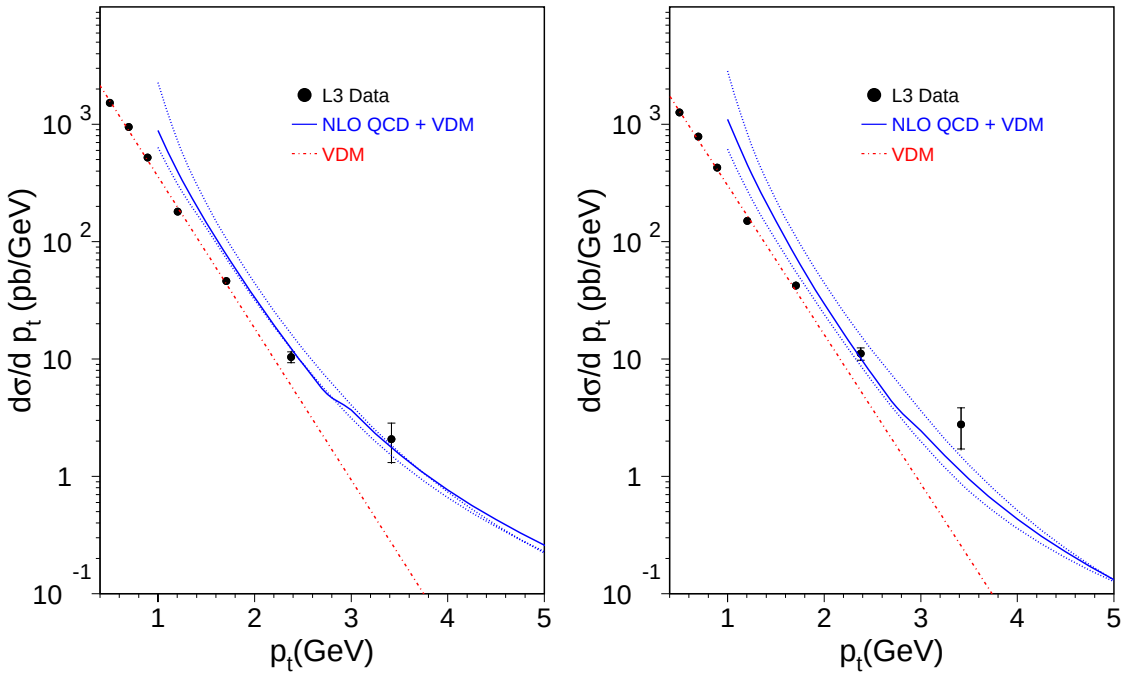

Figure 7.17: The measured differential cross section as a function of p_t for $|\eta| < 1.5$ and for $W_{\gamma\gamma} > 5$ GeV (a) and for $W_{\gamma\gamma} > 10$ GeV (b) is compared to the sum of the NLO QCD predictions and the VDM exponential fit (dash-dotted line). The solid line corresponds to NLO QCD prediction for a scale factor $x = 1$ while the upper dotted line to $x = 0.5$ and the lower dotted line to $x = 2$.

Figure 7.16 shows the measurement of the cross section as a function of the transverse momentum and the theoretical prediction by Kneihl for the three values of the x renormalization scale factor. Data at $p_t > 2$ GeV are higher than the theoretical prediction for $x = 1$. A better agreement is found with the prediction for $x = 0.5$. The dot-dashed line corresponds to the contribution from the direct process with an enhancement at 3 GeV due to the charm-anticharm production threshold. Figure 7.16 shows clearly that the direct process is insufficient to describe the data and that photon-gluon fusion processes cannot be neglected.

It is important to remark that Next-to-Leading Order QCD calculations do not include soft (VDM) contributions to the cross section. The exponential fit of Fig-

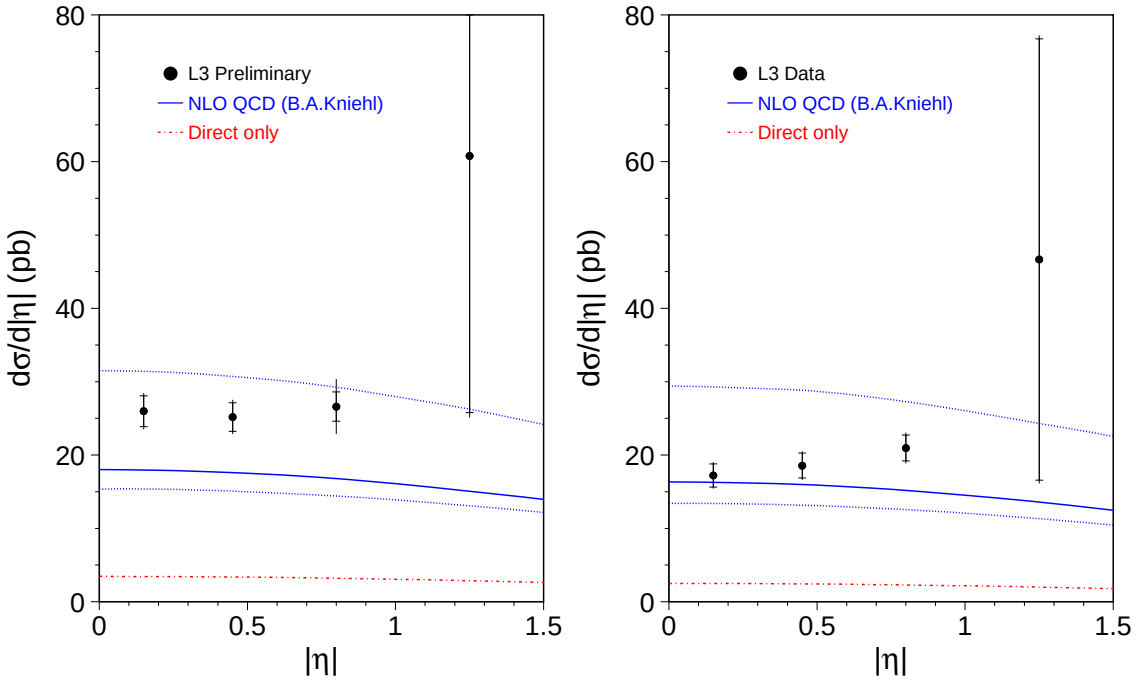

(a) (b)

Figure 7.18: The measured differential cross section as a function of $|\eta|$ for $p_t > 1.5$ GeV and for $W_{\gamma\gamma} > 5$ GeV (a) and for $W_{\gamma\gamma} > 10$ GeV (b) is compared to the NLO QCD predictions by Kniehl. The solid line corresponds to the scale factor $x = 1$ while the upper dotted line to $x = 0.5$ and the lower dotted line to $x = 2$. The dash-dotted line corresponds to the direct contribution.

ure 7.14 shows that the soft contributions in the p_t range corresponding to our data points is not negligible with respect to the QCD predictions. Around 2 GeV the fit and the QCD predictions are of the same order of magnitude. If the exponential fit is added to the Next-to-Leading Order QCD predictions by Kniehl, a better agreement at high p_t is observed, as shown in Figure 7.17.

Figure 7.18 shows the measurement and the theoretical predictions by Kneihl for the cross section as a function of the pseudorapidity. The theoretical predictions reproduce well the shape of the distribution. The data are in between the QCD calculations for $x = 1$ and $x = 0.5$. Also here the direct contribution alone is not sufficient to describe the data. This clearly puts in evidence the necessity of including

QCD partonic processes.

Chapter 8

The $K^0_S K^0_S$ final state in two-photon collisions

8.1 Introduction

The $K^0_S K^0_S$ final state in two-photon collisions is well suited for the search and for the study of J^{PC}=(even)$^{++}$ resonant states. In particular, scalar and tensor mesons can be formed, giving fundamental and unique information on the search for the scalar and tensor glueball. As shown in Chapter 3, this channel has the advantage to be dominated by resonance formation, having only a small contribution from the continuum $K^0_S K^0_S$ production mechanism.

The study of the exclusive reaction

$$e^+e^- \rightarrow e^+e^-R \rightarrow e^+e^-K^0_S K^0_S \tag{8.1}$$

is based on the decay $K^0_S \rightarrow \pi^+\pi^-$, as shown in Figure 8.1. K^0_S's are characterized [28] by a lifetime of 0.89×10^{-10} seconds, a decay branching fraction of 68.6% into $\pi^+\pi^-$ and of 31.4% into $\pi^0\pi^0$. The outgoing electron and positron carry nearly the full beam energy, are scattered at very low angles and are usually undetected. The two K^0_S are emitted approximately back-to-back in the transverse plane and have a boost along the beam direction. Since the $K^0_S K^0_S$ system has an energy of a few GeV, these events can be collected only by the charged particle trigger of L3. The reaction (8.1) and the decay of the K^0_S mesons lead to three different final states with zero, two or

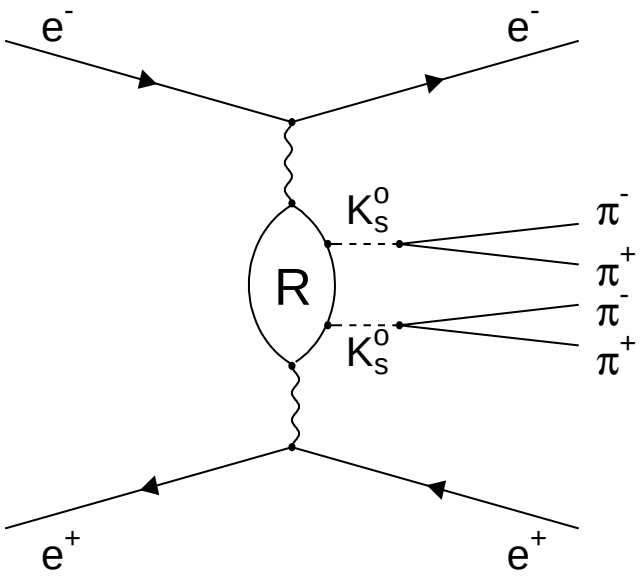

Figure 8.1: The reaction $e^+e^- \to e^+e^-R \to e^+e^-K^0_S K^0_S$, with $K^0_S \to \pi^+\pi^-$.

four charged pions. The events with four π^0's are not collected by the energy trigger and the events in which only one K^0_S decays into charged pions cannot be collected by the charged particle trigger because of the acoplanarity condition. The only suitable final state is therefore the one with four charged pions.

In the reaction (8.1), K^0_S's are produced with momenta of the order of 1 GeV that corresponds to decay lengths of about 5 cm. The decay $K^0_S \to \pi^+\pi^-$ produces therefore a secondary vertex that can be reconstructed using the charged pion tracks detected by the TEC. This characteristic topology makes this channel almost free from backgrounds from other channels.

A resonant state decaying into $K^0_S K^0_S$ can also decay into $K^0_L K^0_L$. Since the K^0_L are characterized by a lifetime of 5.17×10^{-8} seconds, their decay length is of the order of 30 m in this kind of process. Effects of the $K^0_L K^0_L$ channel as well as of CP violation can be neglected in this study.

The data sample used in this analysis corresponds to to an integrated luminosity of 588 pb^{-1}collected by the L3 detector over the years from 1991 to 1999. The full data sample is subdivided into three different subsamples, as shown in Table 8.1.

Years	LEP Phase	$\sqrt{s}$ (GeV)	$\mathcal{L}$ (pb^{-1})
1991 - 1995	LEP1	$\sim$m(Z)	143
1997	LEP2	183	52
1998 - 1999	LEP2	189-202	393

Table 8.1: The three data subsamples and the corresponding years of data taking, centre of mass energies and integrated luminosities.

The first data sample corresponds to the full luminosity collected around the Z pole at LEP1. Despite their similar centre of mass energy, the other two data subsamples are kept separated because of the different trigger conditions. Up to the 1997 data taking period only the Outer TEC trigger was present and from 1998 on the Inner TEC trigger come into operation. In this analysis, all the periods in which the TEC or the charged track trigger were not fully working are excluded.

The EGPC [22] Monte Carlo program is used to model the process of resonance formation in two-photon collisions. A VDM form factor with a ρ pole is used, according to Equation (3.25). This program calculates also the $\mathcal{K}$ factor that allows to obtain the two-photon width of the resonance from the measurement of the cross section (Equation (3.29)). The angular distribution of the two K^0_S's in the two-photon centre of mass system is generated uniformly in $\cos\theta^*$ and in ϕ^*, the polar and azimuthal angles defined by the beam line. This corresponds to the decay of a spin zero resonant state. In order to take into account the helicity of a spin-two resonance, a weight w is assigned to each generated event:

$$w = \left(\cos^2\theta^* - \frac{1}{3}\right)^2 \tag{8.2}$$

for spin-two helicity-zero (J=2, λ=0) and

$$w = \sin^4\theta^* \tag{8.3}$$

for spin-two helicity-two (J=2, λ=2). These weight functions correspond to the spherical harmonics described in Chapter 3. All the generated events are passed through the full detector simulation program based on GEANT [106] and GHEISHA [107] and are reconstructed following the same procedure used for the data.

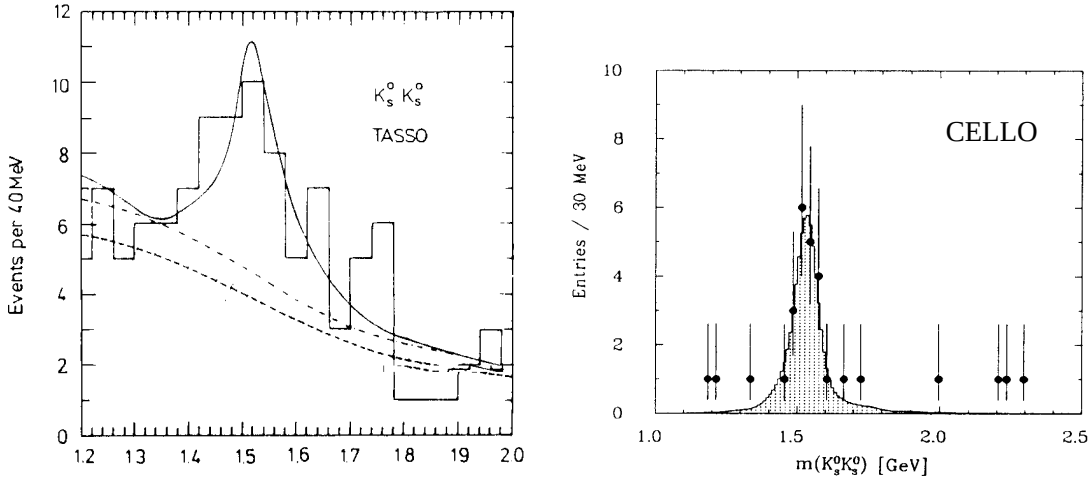

(a) (b)

Figure 8.2: The $K^0_S K^0_S$ mass spectra reported by TASSO (a) and by CELLO (b).

Since gluons do not couple directly to photons, the two-photon width is expected to be small for a glueball. To make this statement more quantitative, a parameter called stickiness [114] is introduced for a state X

$$\frac{|<X|gg>|^2}{|<X|\gamma\gamma>|^2} \sim S_X = N_l \left(\frac{m_X}{k_{J/\psi\to\gamma X}}\right)^{2l+1} \frac{\Gamma(\mathrm{J}/\psi \to \gamma X)}{\Gamma(X \to \gamma\gamma)} \tag{8.4}$$

where m_X is the mass of the state, $k_{J/\psi\to\gamma X}$ is the energy of the photon from a radiative J/ψ decay in the J/ψ rest frame and l is the orbital angular momentum between the two gluons. For spin-two states $l = 0$. N_l is a normalization factor that can be calculated assuming by definition the stickiness of the $f_2(1270)$ tensor meson to be one. Glueball candidates are expected to be characterized by values of the stickiness much larger than one.

The study reported in this chapter was recently published by the L3 Collaboration [115] and supersedes a previous study [116] performed at LEP1 with a luminosity of 114 pb^{-1}.

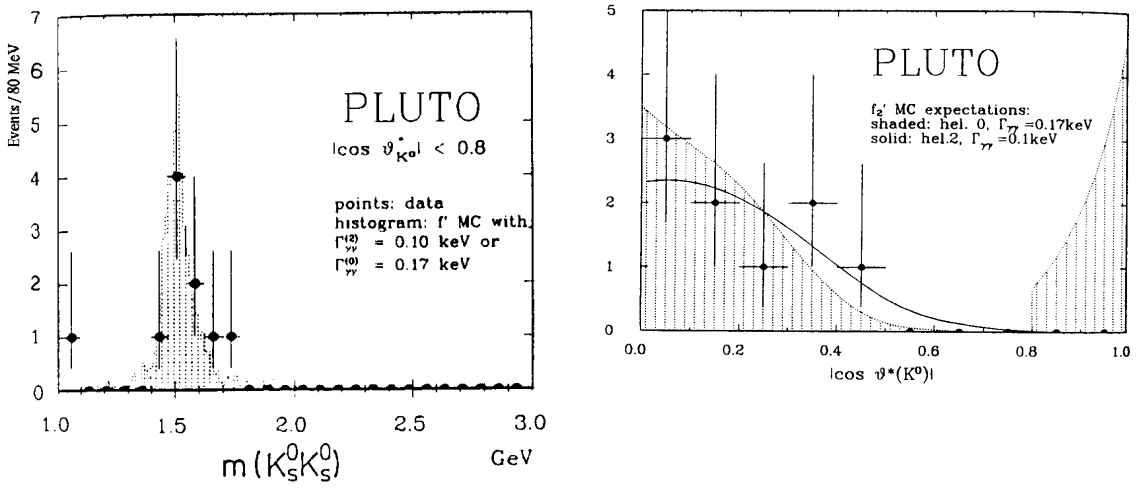

Figure 8.3: The $K^0_S K^0_S$ mass spectrum and the decay polar angle distribution reported by PLUTO.

8.2 Results by other experiments

The first studies of the $K^0_S K^0_S$ final state in two-photon collisions were performed at the PETRA e^+e^- collider at DESY at a beam energy of 17.5 GeV. The $K^0_S K^0_S$ mass spectra reported by the TASSO [117], CELLO [118] and PLUTO [119] Collaborations are shown in Figures 8.2(a), 8.2(b) and 8.3, respectively. The study of the prominent signal due to the formation of the tensor meson $f_2'(1525)$ lead to the measurements of the two photon width reported in Table 8.2. Despite the very low statistics, the

Experiment	Ref.	$\mathcal{L}$ (pb^{-1})	Decay modes	$\Gamma_{\gamma\gamma}(f_2'(1525))\times Br(f_2'(1525) \to KK)$ (keV)
TASSO	[117]	79	$K^0_S K^0_S$, K^+K^-	$0.11 \pm 0.02 \pm 0.04$
CELLO	[118]	86	$K^0_S K^0_S$	$0.11^{+0.03}_{-0.02} \pm 0.02$
PLUTO	[119]	45	$K^0_S K^0_S$	$0.10^{+0.04\ +0.03}_{-0.03\ -0.02}$

Table 8.2: The measurements of the two photon width of the tensor meson $f_2'(1525)$ performed at PETRA.

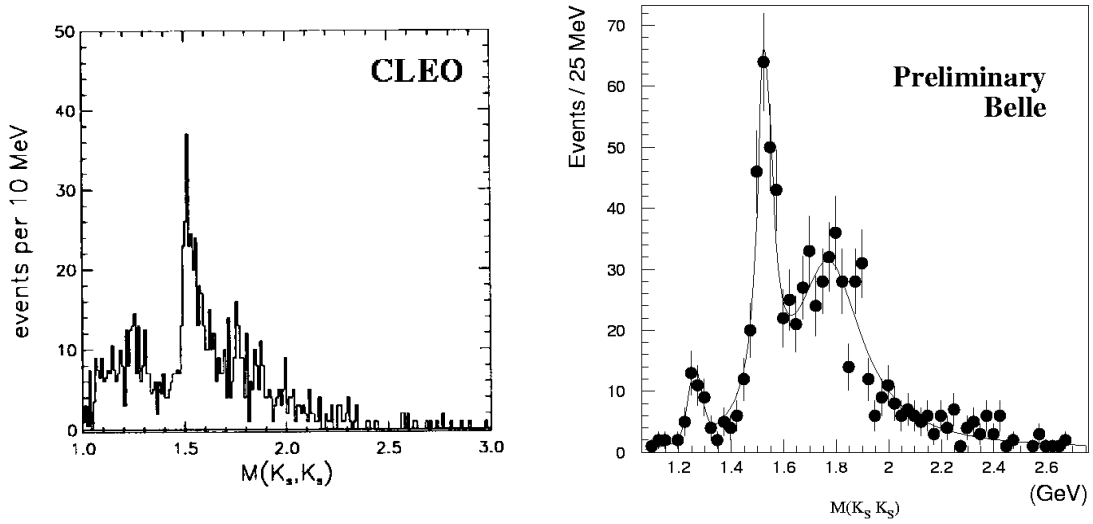

(a) (b)

Figure 8.4: The $K^0_S K^0_S$ mass spectra reported by CLEO (a) and BELLE (b).

PLUTO Collaboration performed a study of the angular distribution which favoured the spin-two helicity-two state, as shown in Figure 8.3.

The CLEO Collaboration [120] at CESR storage ring in Cornell performed a search of the $\xi(2230)$ in the $K^0_S K^0_S$ final state with a luminosity of 3.0 fb^{-1} collected at centre of mass energies around the $\Upsilon(4S)$. The $K^0_S K^0_S$ mass spectrum is reported in Figure 8.4(a). The upper limit $\Gamma_{\gamma\gamma}(\xi(2230)) \times \mathrm{BR}(\xi(2230) \to K^0_S K^0_S) < 1.3$ eV at 95% C.L. is obtained. A lower limit of 102 is obtained for the stickiness of the $\xi(2230)$ combining the $K^0_S K^0_S$ and the $\pi^+\pi^-$ final states.

Very recently the BELLE Collaboration [121] at KEK presented very interesting preliminary results. The $K^0_S K^0_S$ mass spectrum shown in Figure 8.4(b) has been obtained with a luminosity of 5.0 fb^{-1} collected during the year 2000 at centre of mass energies around the $\Upsilon(4S)$. In particular, the signal of the $f_J(1710)$ is visible. Considering the fact that BELLE is just at the beginning of the data taking, we may expect that the study of the $K^0_S K^0_S$ final state in two-photon collisions will be continued in future with high statistics.

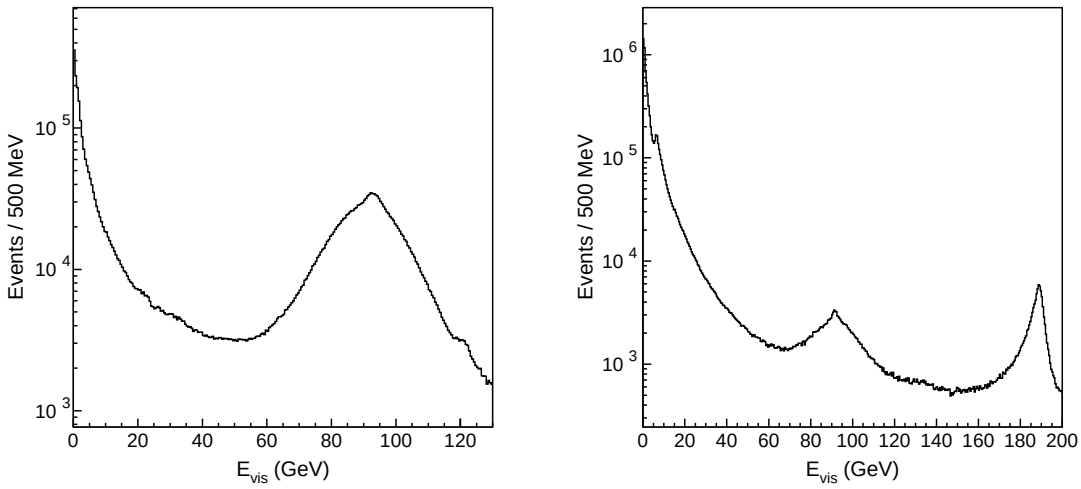

(a) **(b)**

Figure 8.5: The visible energy at LEP1 (a) and at LEP2 (b) for data collected at $\sqrt{s} = 189$ GeV.

8.3 Event selection

To select events produced by two-photon interactions, the sum of the energies detected by the electromagnetic and the hadron calorimeter, indicated as E_{vis}, is required to be

- $E_{vis} < 30$ GeV.

Figure 8.5 shows the visible energy for LEP1 (a) and LEP2 (b) data. At LEP1 the peak at the Z pole is clearly visible. At LEP2 annihilation events produce two peaks. One peak corresponds to the full centre of mass energy and one peak to the mass of the Z boson. This is due to the "return to the Z" process, where the emission of initial state radiation favours the e^+e^- annihilation around the Z resonance. The events produced by photon-photon collisions dominate the low values of E_{vis}. In particular, events due to the formation of a resonant state are characterized by a visible energy of only a few GeV and sit far below the cut at 30 GeV either at LEP1 or at LEP2.

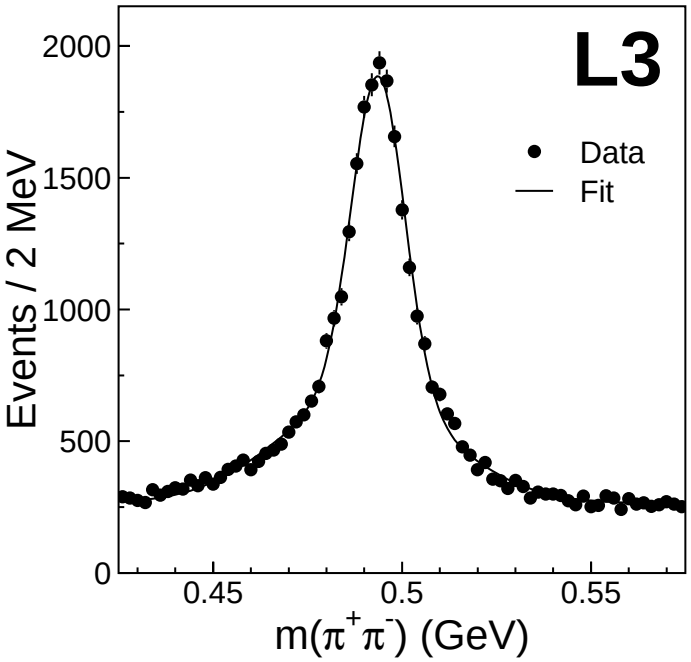

Figure 8.6: The $\pi^+\pi^-$ mass spectrum for reconstructed secondary vertices with a transverse separation of more than 3 mm from the interaction point.

Charged tracks with a transverse momentum greater than 100 MeV and more than 12 hits in the TEC and are selected. The condition on the number of hits limits the polar angle θ in the range $24° < \theta < 156°$.

To select $\pi^+\pi^-\pi^+\pi^-$ final state events

- four tracks with a net charge of zero

are required.

At this level the selected sample contains events produced by several processes. The $\pi^+\pi^-\pi^+\pi^-$ final state is dominated by the diffractive $\rho^0\rho^0$ production. Besides exclusive final states, non-exclusive events with four detected tracks plus undetected charged particles or photons are also present. The photons are predominantly produced by the decay of π^0 mesons. Since the beam-gas and beam-wall events are not

completely eliminated by the level-two and level-three triggers, a small contribution of this kind of background is also present.

K^0_S's are selected by reconstructing the secondary vertex of the decay $K^0_S \to \pi^+\pi^-$, as discussed in Chapter 6. Figure 8.6 shows the $\pi^+\pi^-$ mass spectrum for reconstructed secondary vertices with $d_\perp > 3$ mm and $|\alpha| < 0.1$ rad for the full data sample, according to the event selection described up to this point. The signal due to the production of K^0_S mesons is very clear over a smooth background. Fitting the distribution with a Gaussian for the signal and a Gaussian plus a constant for the background, a mass value of 493 ± 1 MeV and mass resolution $\sigma = 8.0 \pm 0.5$ MeV are found. The mass value is slightly lower with respect to the world average value of 497.7 MeV [28], as discussed in Chapter 6. The values of the mass and of the resolution, reported in Table 8.3, are stable over the years of data taking and are consistent with the Monte Carlo simulation.

To search for events with two K^0_S,

- two secondary vertices with $d_\perp > 1$ mm

are required. With the selection criteria described up to this point, 260023 events are selected.

The selection of $K^0_S K^0_S$ exclusive events is based on the specific topology of this process. It is important to remark that the selection criteria for the K^0_S's are different with respect to the previous chapter.

- Since the two quasi-real photons are approximately collinear with respect to the beam axis, the total transverse momentum imbalance squared $|\sum \overrightarrow{p_t}|^2$ of the four pions is required to be less than 0.1 GeV^2. This cut selects quasi-real

Years	Mass (MeV)	Sigma (MeV)
1991 - 1995	493.7 ± 1.0	8.5 ± 1.0
1997	493.1 ± 0.8	7.9 ± 1.3
1998 - 1999	493.0 ± 0.5	7.3 ± 0.6
Monte Carlo	493.0 ± 0.9	7.9 ± 1.0

Table 8.3: Mass and resolution for the K^0_S signal.

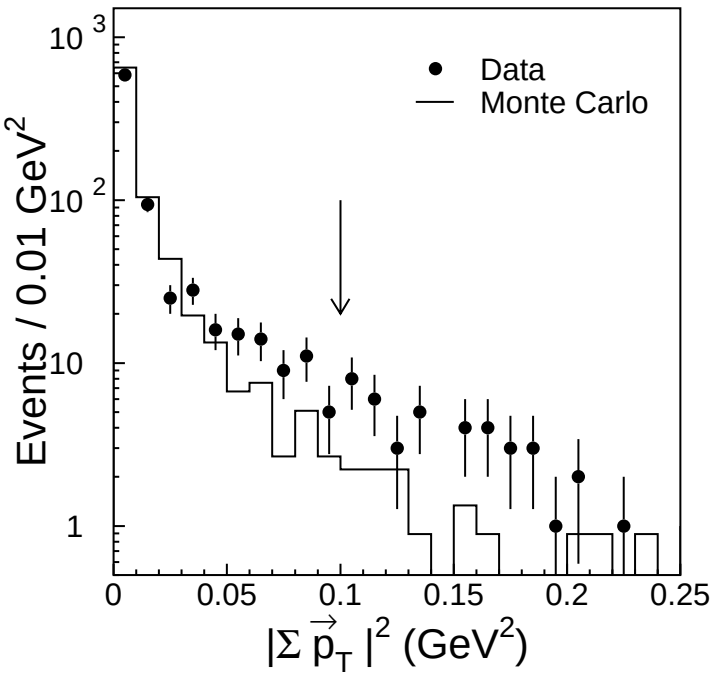

Figure 8.7: The distribution of the total transverse momentum squared of the measured charged particles. The Monte Carlo is normalized to the same number of events as the data and the arrow indicate the cut applied.

two-photon events and removes non-exclusive events in which some particles are not detected. In Figure 8.7 the $|\sum \overrightarrow{p_t}|^2$ distribution is compared to the Monte Carlo prediction for exclusive $K^0_S K^0_S$ formation. The excess in the data at high values is due to non-exclusive final states.

- No photon must be detected. A photon is defined as an isolated shower in the electromagnetic calorimeter with a total energy larger than 100 MeV distributed in more than two crystals. The ratio between the energies deposited in the hadronic and electromagnetic calorimeters must be less than 0.2 and there must be no charged track within 200 mrad from the shower direction.

- Two secondary vertices with transverse distances from the interaction point

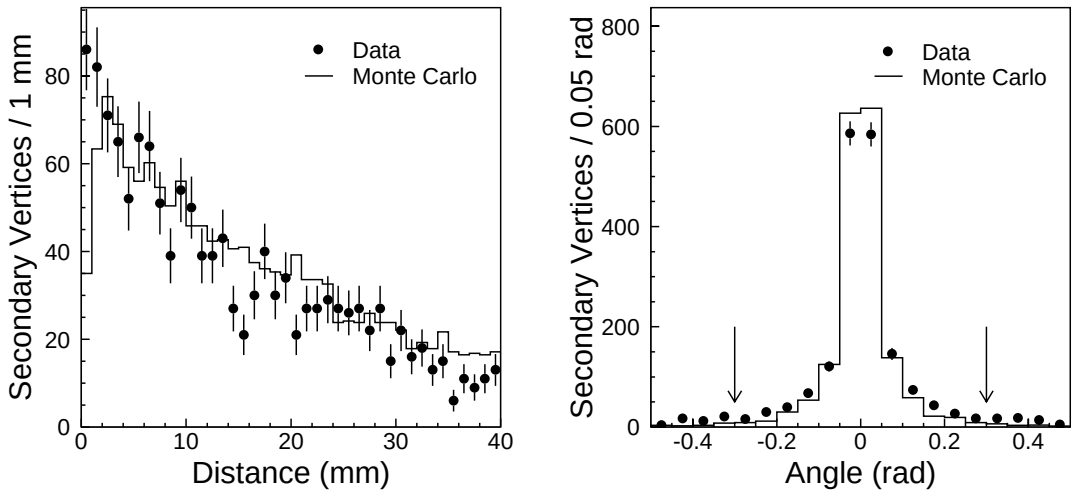

(a) (b)

Figure 8.8: The distribution of the transverse decay length $d_\perp$ (a), where an asymmetric cut of 1 mm and 3 mm is applied, and of the angle α (b) for the K^0_S candidates after the other selection cuts have been applied. The Monte Carlo is normalized to the same number of events as the data and arrows indicates the cut applied.

greater than 1 mm and 3 mm are required. In Figure 8.8(a) the data are compared to the Monte Carlo prediction for exclusive $K^0_S K^0_S$ formation. The excess in the data at low values is due to the dominant $\gamma\gamma \to \rho^0\rho^0$ channel.

- The angle α between the flight direction of each K^0_S candidate and the total transverse momentum vector of the two outgoing tracks in the transverse plane must be less than 0.3 rad, as presented in Figure 8.8(b).

- Since the two K^0_S's are produced back-to-back in the transverse plane, the angle $\Delta\phi_N$ between the flight directions of the two K^0_S candidates in this plane is required to be $\pi \pm 0.3$ rad, as presented in Figure 8.9.

Figure 8.10 shows the distribution of the mass of one K^0_S candidate versus the mass of the other candidate. The two candidates are ordered randomly. There is a strong enhancement corresponding to the $K^0_S K^0_S$ exclusive formation over a small

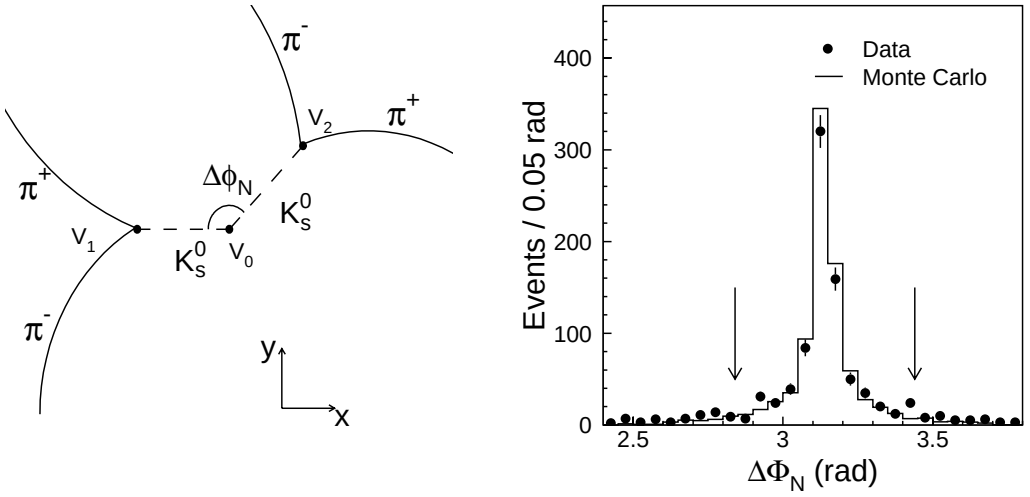

Figure 8.9: The distribution of the angle $\Delta\phi_N$ between the flight directions of the two K^0_S candidates in the transverse plane after the other selection cuts have been applied. The Monte Carlo is normalized to the same number of events as the data and arrows indicates the cut applied.

background.

- The $\pi^+\pi^-$ effective masses of the two K^0_S candidates are required to be inside a circle of 40 MeV radius centered on the peak of the $K^0_S K^0_S$ signal.

With these selection criteria, 802 events are found in the full data sample. In the three data subsamples 118, 85 and 599 events are selected, respectively. The effect of the selection criteria on the data of the subsample collected at $\sqrt{s} = 189 - 202$ GeV and on the Monte Carlo are reported in Table 8.4. The number of selected $K^0_S K^0_S$ events after each cut is reported together with the corresponding reduction factor. The first line corresponds to the events passing the preselection and the requirement on the two $\pi^+\pi^-$ masses. The effect of the first two cuts is very different on the data and on the Monte Carlo. This is due to the non-exclusive final states which are not simulated in the Monte Carlo.

One selected event is shown in Figures 8.11 and 8.12. Figure 8.11 shows the $r - \phi$ view of the event with the four charged pions detected by the TEC. The

Cut	Events Data	Red. factor (%)	Events MC	Red. factor (%)
Preselection	3871	-	6932	-
$\lvert\Sigma\overrightarrow{pt}\rvert^2$	1740	45	4922	71
No photons	1286	74	4823	98
$d_\perp$	912	71	3859	80
$\lvert\alpha\rvert$	665	73	2894	75
$\Delta\phi_N$	599	90	2663	92

Table 8.4: The effect of the selection criteria on the data collected at $\sqrt{s} = 189 - 202$ GeV and on the Monte Carlo.

formation of two back-to-back K^0_S mesons in the transverse plane is visible and the two secondary vertices are very well distinct from the primary interaction point. The use of the silicon micro-vertex detector SMD is very important for a high precision determination of the secondary vertices, as presented in Figure 8.12(a).

Two-photon events are characterized by a typical boost along the beam direction. The distribution of the rapidity r

$$r = \frac{1}{2} \cdot \ln \frac{E + p_z}{E - p_z} \tag{8.5}$$

of the $K^0_S K^0_S$ system is shown in Figure 8.13(a) for the selected events. The distribution is rather flat around zero due to the boost of the $K^0_S K^0_S$ system along the beam line and drops at values around ± 0.5 due to the limited acceptance of the detector in the forward-backward region.

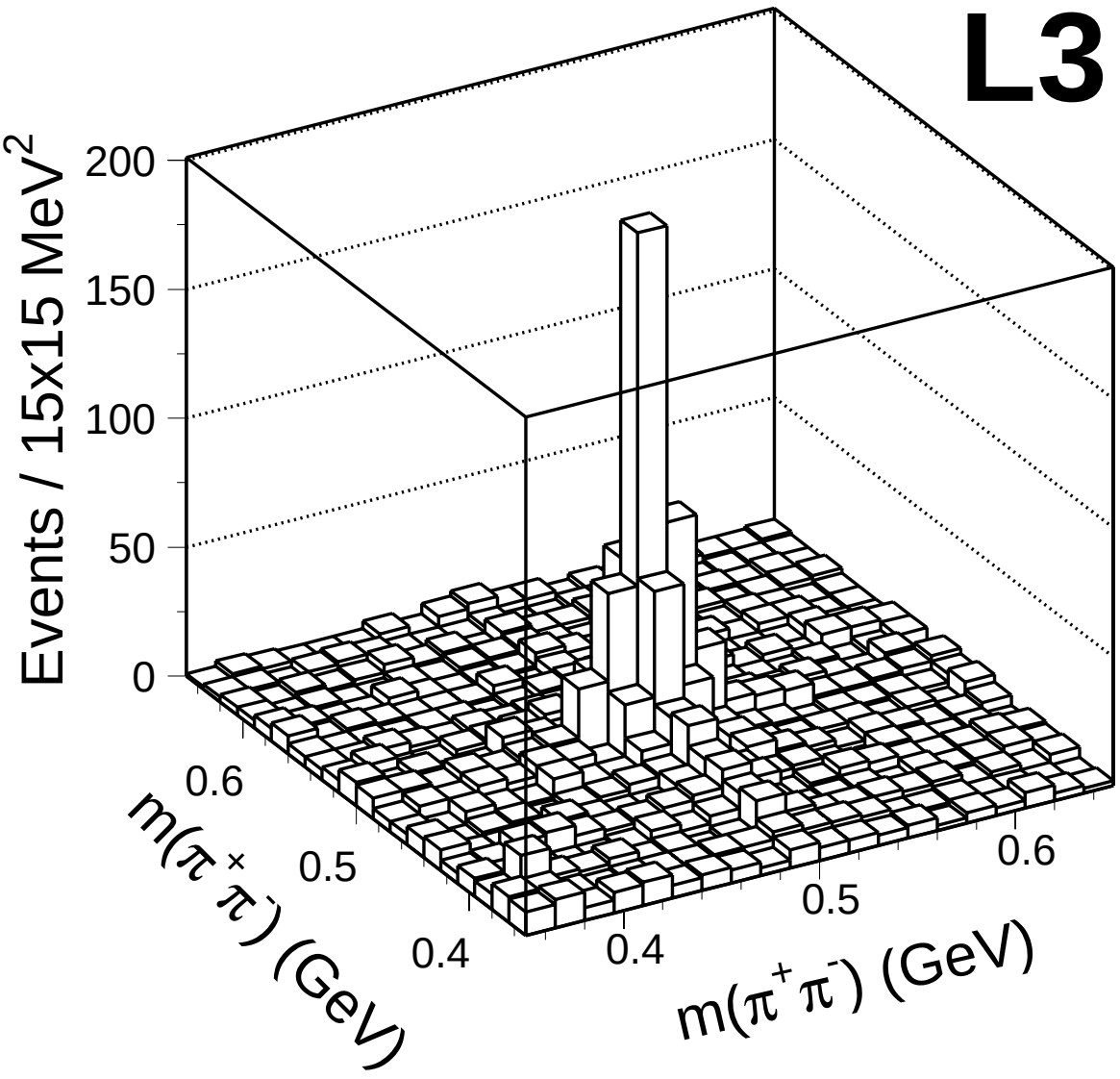

Figure 8.10: The mass distribution of a K^0_S candidate versus the mass of the other candidate for the full data sample.

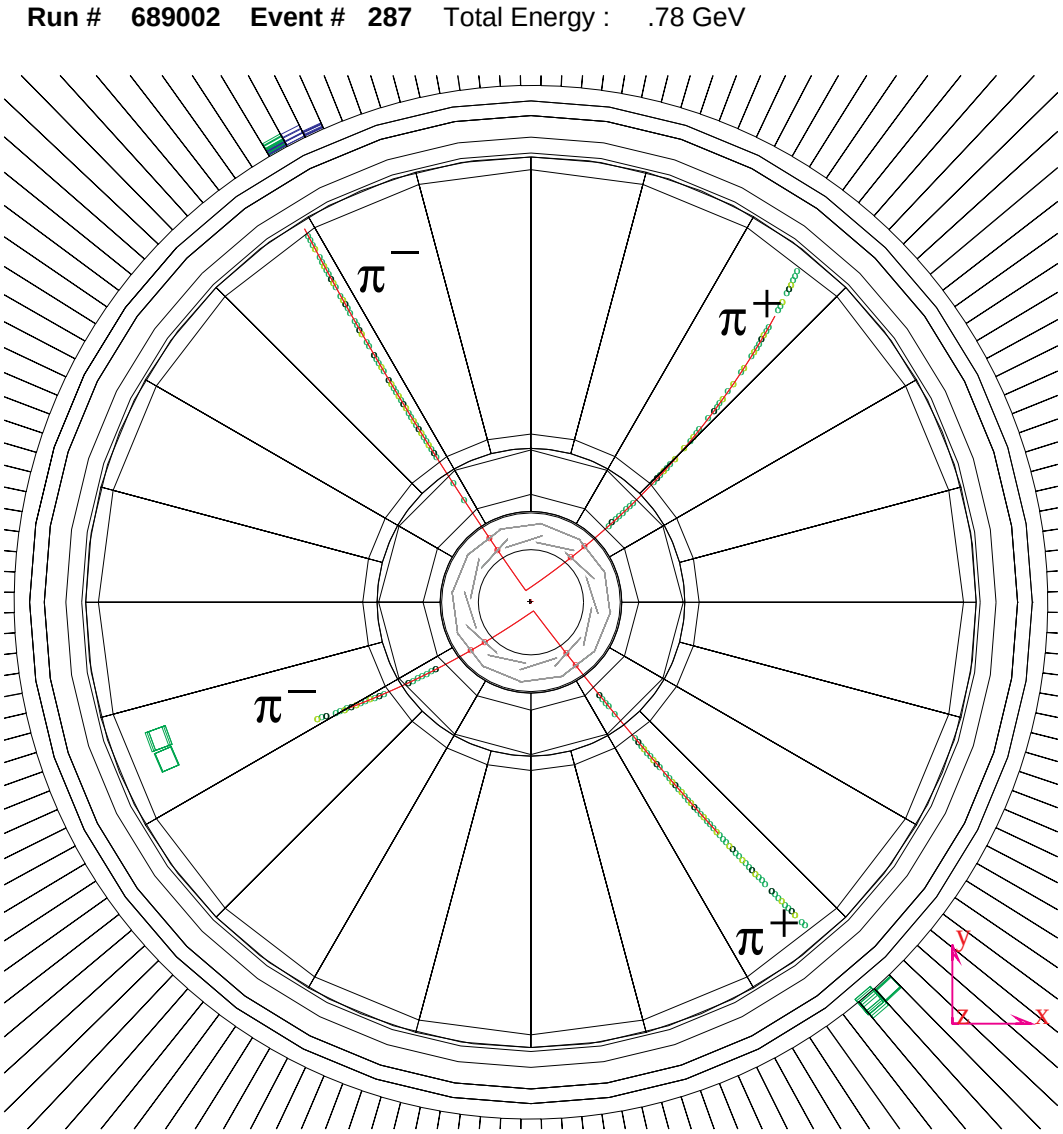

Figure 8.11: One selected $\gamma\gamma \to K^0_S K^0_S$ exclusive event. The two K^0_S with the corresponding secondary vertices are visible.

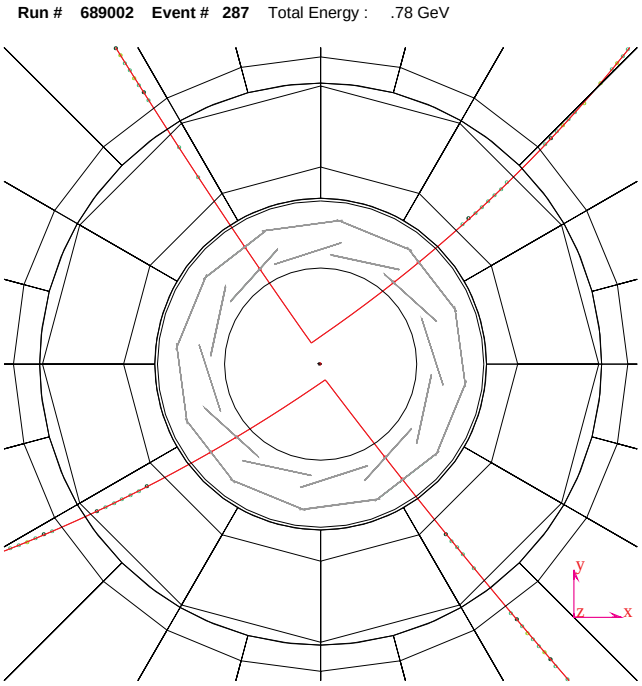

(a)

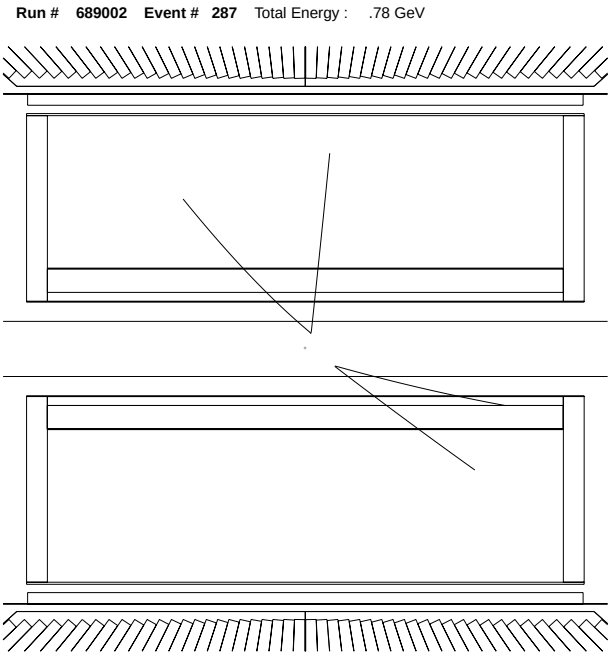

(b)

Figure 8.12: (a) A zoom at the SMD dimension level shows the precise reconstruction of the secondary vertices. (b) The transverse view of the event shows the typical boost along the beam line.

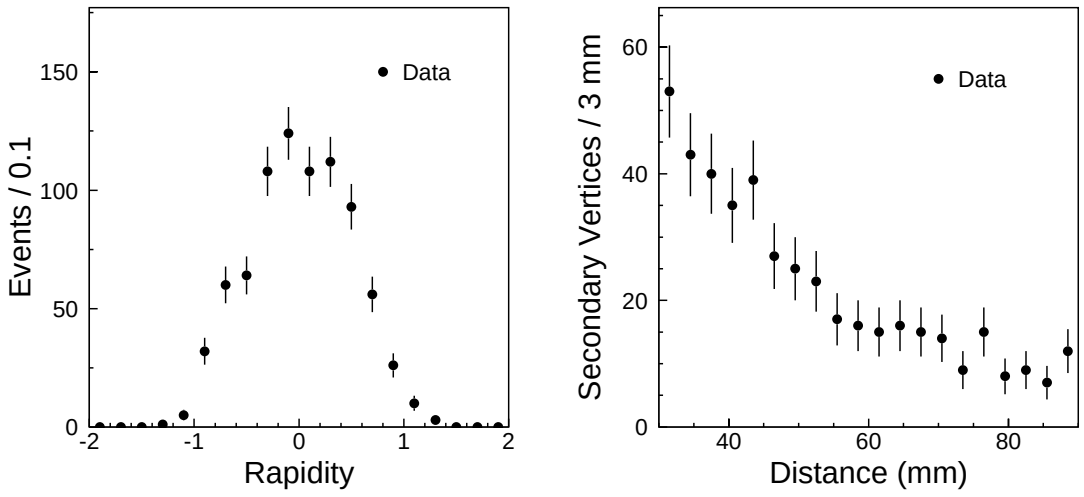

(a) (b)

Figure 8.13: The distribution of the rapidity (a) and of the decay distance (b) for the selected events.

The background due to misidentified K^0_S pairs and non-exclusive events is estimated to be less than 5% by a study of the K^0_S mass sidebands (Figure 8.10) and of the $|\sum \overrightarrow{p_i}|^2$ distribution (Figure 8.7). The background due to $K^0_S K^{\pm}\pi^{\mp}$ final state, producing only one secondary vertex, is found to be negligible by a Monte Carlo study. Due to its very low cross section [122], the $\Lambda\bar{\Lambda}$ channel is a negligible background source for the $K^0_S K^0_S$ final state. The background contributions due to beam-gas and beam-wall interactions are found to be negligible by an inspection of the distance of closest approach of the tracks along the beam line direction and by the absence of any accumulation of secondary vertices in the position of the beam pipe. Figure 8.13(b) shows the distribution of the K^0_S decay length for the selected events. No excess is observed at 55 mm, in correspondence of the beam pipe.

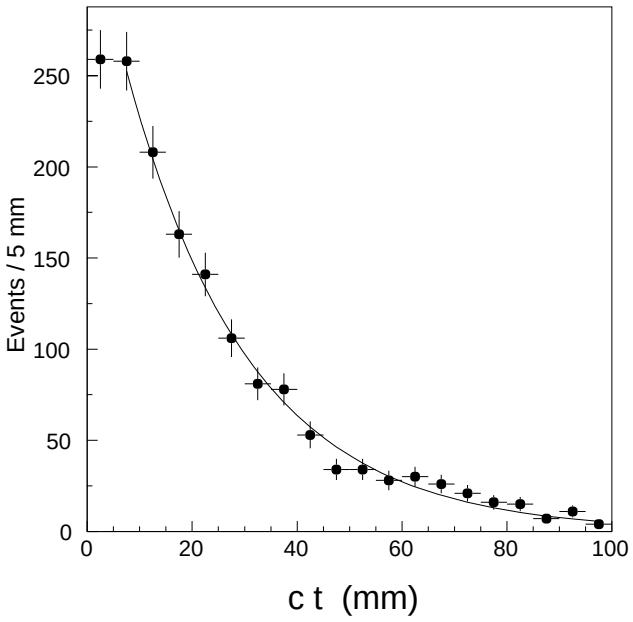

Figure 8.14: Distribution of the lifetime $c \cdot t$ for the selected K^0_S. The line corresponds to the exponential fit. Since the first bin is affected by the $d_\perp$ cut, it is excluded from the fit.

8.3.1 A quality test: the lifetime of the K^0_S

A good test for the quality of the K^0_S selection is to check the lifetime value. Since the selected sample has a very high purity, a simple exponential fit on the distribution of

$$c \cdot t = m_{K^0_S} \cdot \frac{d_\perp}{p_t} \tag{8.6}$$

is expected to give a value $c\tau$ for the lifetime times the speed of light in agreement with the world average $c\tau = 26.8$ mm [28]. Here t is the lifetime measured in the centre of mass system of the K^0_S candidate. The quantities $d_\perp$ and p_t are measured in the laboratory system. The distribution of $c \cdot t$ is shown in Figure 8.14. The value $c\tau = 25.7 \pm 1.5$ mm is found by fitting the distribution with the function

$$f = A \cdot \exp\left(-\frac{ct}{c\tau}\right). \tag{8.7}$$

This result is in agreement with the world average value.

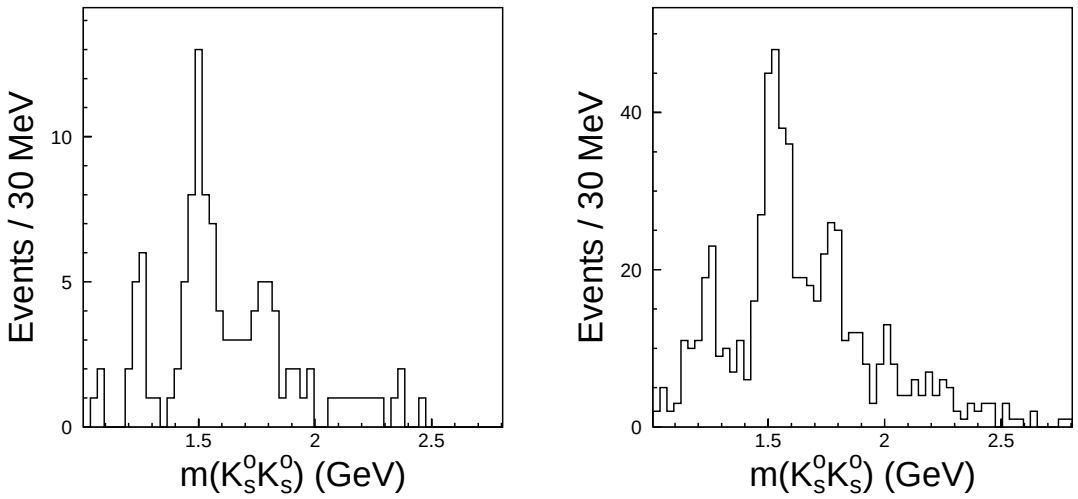

(a) (b)

Figure 8.15: The $K^0_S K^0_S$ mass spectra for LEP1 (a) and LEP2 (b) data.

8.4 The $K^0_S K^0_S$ mass spectrum

The $K^0_S K^0_S$ effective mass is calculated for the selected events by assigning the mass of the K^0_S to each $\pi^+\pi^-$ pair. The $K^0_S K^0_S$ mass spectra obtained with LEP1 and LEP2 data are shown in Figure 8.15(a) and (b), respectively. The $K^0_S K^0_S$ mass spectrum for the full data sample is presented in Figure 8.16. All the spectra show three distinct peaks over a low background.

Despite their large two-photon widths, the $f_2(1270)$ and the $a^0_2(1320)$ tensor mesons produce a small signal in the $K^0_S K^0_S$ final state due to their destructive interference, as explained in Chapter 3. The spectrum is dominated by the formation of the $f'_2(1525)$ tensor meson, in agreement with previous observations. A signal for the formation of the $f_J(1710)$ is present while no resonance is observed in the mass region of the $\xi(2230)$. It is important to remark that the $f_J(1710)$ is observed here for the first time in two-photon collisions.

A maximum likelihood fit using three Breit-Wigner functions plus a second order polynomial for the background is performed on the full $K^0_S K^0_S$ mass spectrum. The

Mass Region	$f_2(1270)-a_2(1320)$	$f_2'(1525)$	$f_J(1710)$	Background
Mass (MeV)	1239 ± 6	1523 ± 6	1767 ± 14	–
Width (MeV)	78 ± 19	100 ± 15	187 ± 60	–
Integral (Events)	123 ± 22	331 ± 37	221 ± 55	149 ± 21

Table 8.5: The parameters of the three Breit-Wigner functions and the parabolic background from the fit on the $K^0_S K^0_S$ mass spectrum.

Mass (MeV)	Resolution (MeV)
1525	29 ± 4
1750	35 ± 4
2230	60 ± 6

Table 8.6: The resolution for three different values of the $K^0_S K^0_S$ mass evaluated by Monte Carlo.

results of the fit are shown in Figure 8.16 and reported in Table 8.5. The confidence level is 31.7%. The parameters of the $f_2'(1525)$ are in good agreement with the PDG [28], once the experimental resolution $\sigma = 29 \pm 4$ MeV is taken into account. The experimental resolution for three $K^0_S K^0_S$ mass values is reported in Table 8.6. It is evaluated using the Monte Carlo and is found to be constant within the errors with respect to the beam energy.

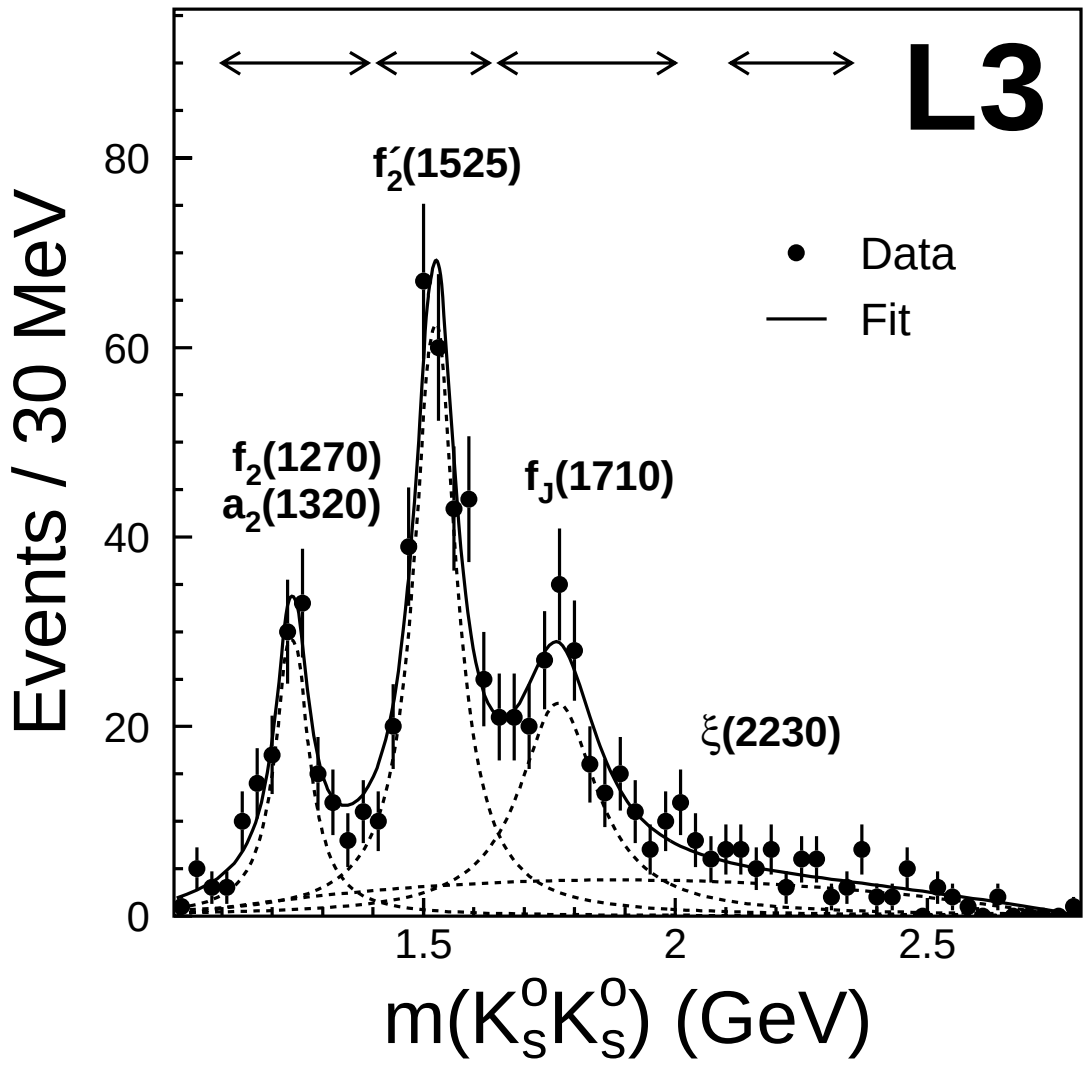

Figure 8.16: The $K^0_S K^0_S$ mass spectrum: the solid line corresponds to the maximum likelihood fit. The background is fitted by a second order polynomial and the three peaks by Breit-Wigner functions (dashed lines). The horizontal arrows define the mass regions used in the analysis for the $f_2(1270)$–$a_2^0(1320)$, the $f_2'(1525)$, the $f_J(1710)$ and the $\xi(2230)$. The mass spectrum is not corrected for the detection efficiency.

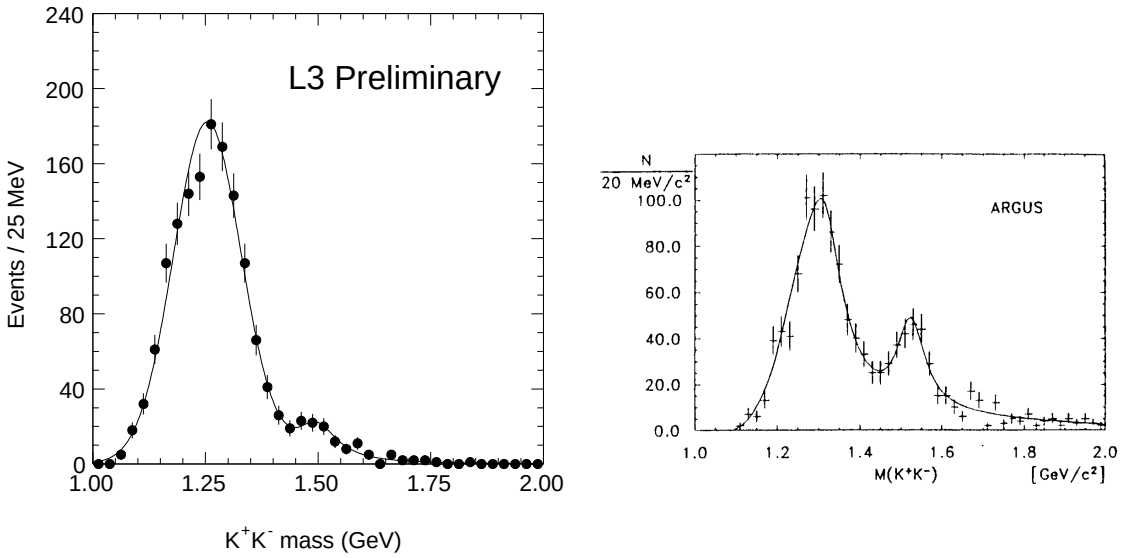

(a) (b)

Figure 8.17: The K^+K^- mass spectra by L3 (a) and by ARGUS (b).

8.5 The f_2-a_2 interference

As discussed in Chapter 3 and observed in the previous Section, the $f_2(1270)$ and the $a_2(1320)$ tensor mesons interfere destructively in the $K^0_S K^0_S$ final state. It is interesting to see if it is possible to put in evidence, as expected, the constructive interference in the K^+K^- final state.

Exclusive $e^+e^- \to e^+e^-K^+K^-$ events are selected by applying the following criteria.

- Two oppositely charged tracks back-to-back within 0.2 rad, with a DCA less than 5 mm and at least 40 hits for a good measurement of the dE/dx are required.

- The dE/dx of the two tracks must be inside a band of $\pm 30\%$ around the Bethe-Block curve for charged kaons, shown in Figure 6.13. For at least one track the condition $dE/dx > 1.2$ is required in order to have at least one unambiguously identified charged kaon.

	$f_2(1270)$ - $a_2(1320)$	$f_2'(1525)$
Mass (MeV)	-	1500±15
Width (MeV)	-	115±25
Events	1370±40	157±19

Table 8.7: Results of the fit on the K^+K^- mass spectrum.

- Events with photons are rejected.
- The total transverse momentum squared must be $|\vec{p_{t1}} + \vec{p_{t2}}|^2 < 0.01$ GeV^2 to select exclusive events.

With these selection criteria 877 events are selected on the data collected in 1998 and corresponding to a luminosity of 177pb^{-1}. The K^+K^- mass spectrum is shown in Figure 8.17(a). The large signal due to the $f_2(1270)-a_2(1320)$ constructive interference is visible together with the signal due to the formation of the $f_2'(1525)$. A fit with a gaussian in the 1300 MeV mass region and a Breit-Wigner function for the $f_2'(1525)$ is performed. The results of the fit are reported in Table 8.7. Unfortunately the condition on the dE/dx limits the efficiency at high masses and no events are found already in the 1750 MeV mass region.

The only published study of the K^+K^- final state in two-photon collisions was performed at the e^+e^- storage ring DORIS II at DESY by the ARGUS Collaboration [123]. The K^+K^- mass spectrum, obtained with a beam energy between 4.7 and 5.3 GeV and a luminosity of 281 pb^{-1}, is shown in Figure 8.17(b). The preliminary results of L3 [124] are in good agreement with ARGUS.

8.6 The detection efficiency

The total detection efficiency is the product of the selection efficiency and the trigger efficiency. The selection efficiency is defined as the number of Monte Carlo events after the final selection divided by the total number of generated events for the $\pi^+\pi^-\pi^+\pi^-$ final state. The trigger efficiency is the product of the level-one, level-two and level-three trigger efficiencies. The level-one trigger efficiency is evaluated

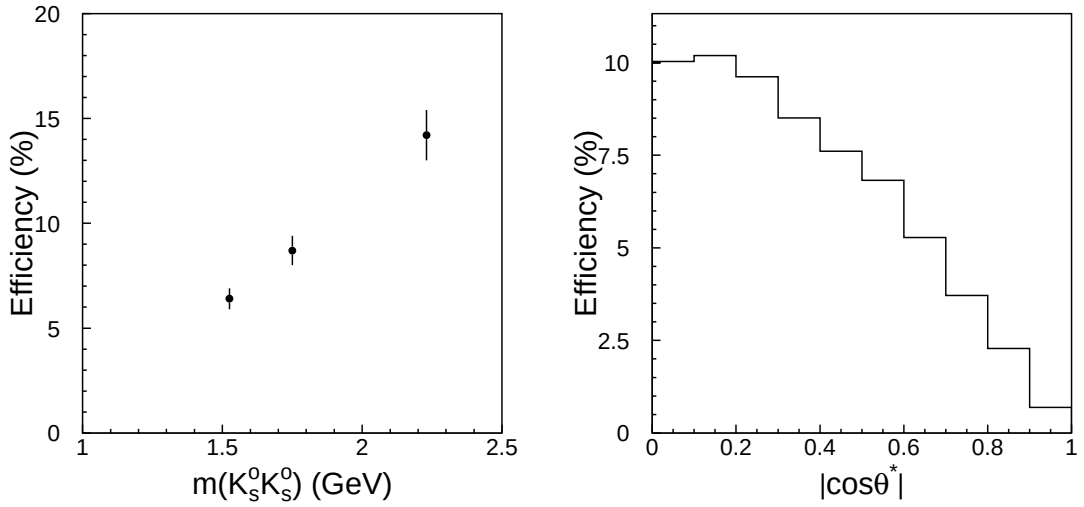

(a) **(b)**

Figure 8.18: (a) The total detection efficiency as a function of the $K^0_S K^0_S$ mass at $\sqrt{s} = 189$ GeV for spin-two helicity-two. (b) The total detection efficiency as a function of $|\cos\theta^*|$ for the 1525 MeV mass region at $\sqrt{s} = 189$ GeV.

by Monte Carlo. The selection and the level-one trigger efficiencies are calculated according to the weight function for different spin-helicity states.

Since a simulation program for the level-two and level-three triggers does not exist, the respective efficiencies are evaluated directly on the data. One out of 20 events rejected by the the level-two and by the level-three trigger are stored and flagged as such. These events are used to estimate the efficiency of these two filtering algorithms. Since none of the events of the final $K^0_S K^0_S$ selected sample is flagged as a level-two or level-three rejected event, this suggests that the level-two and level-three inefficiencies are small and that a larger sample with a similar topology has to be used for their evaluation. For this purpose, events with four charged tracks, charge balance and total transverse momentum imbalance squared less then 0.1 GeV^2 are used. The level-two and level-three trigger efficiencies are reported in Table 8.8. The total detection efficiency as a function of the $K^0_S K^0_S$ mass and of $|\cos\theta^*|$ is shown in Figures 8.18(a) and (b), respectively.

$\sqrt{s}$ (GeV)	$\varepsilon_{level-two}$ (%)	$\varepsilon_{level-three}$ (%)
Z pole	99	95
183	98	95
189-202	96	94

Table 8.8: The level-two and level-three trigger efficiencies.

For the data at the Z pole the selection efficiency includes also a preselection efficiency factor of 70%. The two-photon selection routine in REL3 contained in fact a cut of 10 mm for the minimum distance of closest approach for all the tracks in the event, reducing significantly the efficiency of the $K^0_S K^0_S$ final state. The filtering algorithm was modified in 1995 and the selection cut on the minimum distance of closest approach removed.

8.7 Systematic uncertainties

The systematic uncertainties on the study of the $K^0_S K^0_S$ final state in two-photon collisions come from different sources.

Since the Monte Carlo used to evaluate the selection efficiency does not reproduce perfectly the data, a selection cut may have a different effect on the data and on the Monte Carlo. Because of the small statistics of the $K^0_S K^0_S$ selected sample, the data are not subdivided into three different subsamples for the evaluation of the systematic uncertainties that are assumed to be the same for the three cases. A cut variation method is applied by varying each selection cut and by evaluating the relative difference on the number of events selected in the data and in the Monte Carlo. The systematic uncertainties assigned to each selection cut are reported in Table 8.9. The total systematic uncertainty on the selection efficiency is 7.5%. The main contribution comes from the exclusion of the photons, since the Monte Carlo does not reproduce perfectly the shower shapes of low energy pions in the electromagnetic calorimeter.

Systematic uncertainties related to the level-one trigger are evaluated by comparing the results of the charged particle trigger simulation with a direct measurement of the charged particle trigger efficiency [80]. Systematic effects on the level-two and

Cut	Contribution %
$\lvert\Sigma\overrightarrow{p_t}\rvert^2$	1.5
No photons	6.0
$d_\perp$	2.9
$\lvert\alpha\rvert$	0.3
$\Delta\phi_N$	0.5
m($\pi^+\pi^-$)	3.1
Total	7.5

Table 8.9: The contributions to the systematic uncertainty on the selection efficiency.

level-three trigger efficiencies are difficult to be evaluated. They are estimated to be much smaller then the ones affecting the level-one trigger. A 5% systematic uncertainty is assigned to the trigger efficiency that takes into account also the stability with respect to time.

The main source of systematic uncertainty comes from the fitting procedure. A contribution of 10% is evaluated by varying the shape of the background and by allowing no background at all. Figure 8.19 shows the $K^0_S K^0_S$ mass spectrum fitted with three Breit-Wigner functions for the three peaks plus another Breit-Wigner function for modeling the high mass background. The confidence level is 30.1%, very similar to the reference fit shown in Figure 8.16. The results of the fit are reported in Table 8.10. The mass and the width of the fourth Breit-Wigner function can be an indication of the formation of one or more high mass mesons. According to PDG [28], the $f_2(2010)$ has a mass of 2011 MeV and a width of 202 MeV and the the $f_4(2050)$ has a mass of 2034 MeV and a width of 222 MeV. The limited statistics of the $K^0_S K^0_S$ selected sample does not allow to draw any conclusion on this subject.

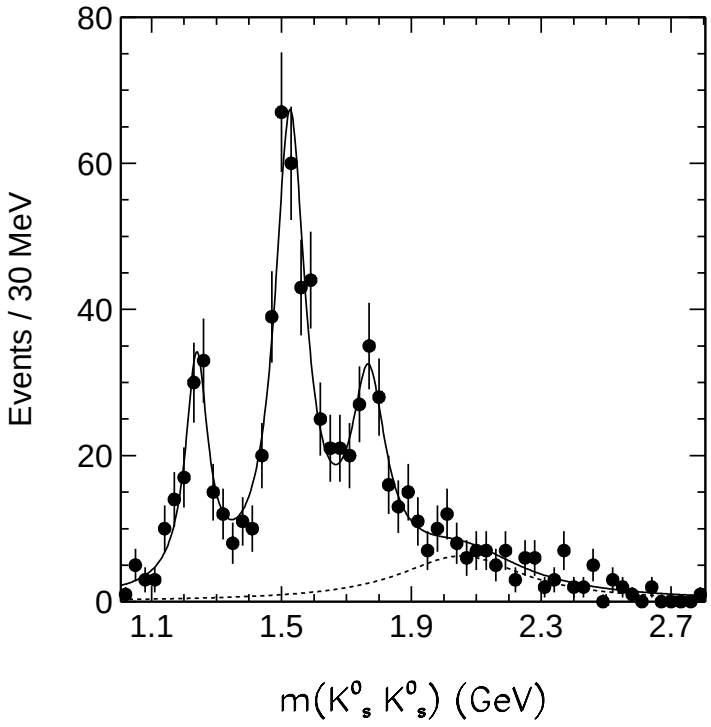

Figure 8.19: The fit of the $K^0_S K^0_S$ mass spectrum with four Breit-Wigner functions, three for the signals and one for the background (dashed line).

Mass Region	$f_2(1270)$–$a_2(1320)$	$f_2'(1525)$	$f_J(1710)$	Background
Mass (MeV)	1239 ± 6	1526 ± 6	1768 ± 10	2053 ± 8
Width (MeV)	83 ± 15	115 ± 15	140 ± 60	472 ± 115
Integral (Events)	135 ± 17	385 ± 37	177 ± 63	154 ± 56

Table 8.10: The parameters of the three Breit-Wigner functions for the signal and the Breit-Wigner function for the high mass background from the fit on the $K^0_S K^0_S$ mass spectrum. This fit is used only to evaluate the systematic uncertainty.

8.8 The $f'_2(1525)$ tensor meson

To study the $f'_2(1525)$ tensor meson Monte Carlo events are generated according to the world average values of the mass, total width and two-photon width [28]. About 100000 events are generated for each of the three data subsamples, according to the different beam energies, detector and trigger conditions.

To determine the spin and the helicity composition in the $f'_2(1525)$ mass region, events are selected between 1400 and 1640 MeV (Figure 8.16). For these events the experimental polar angle distribution as a function of $|\cos\theta^*|$ is is compared with the normalized Monte Carlo expectations for the (J=0), (J=2, λ=0) and (J=2, λ=2) states, as presented in Figure 8.20. A χ^2 is calculated for each hypothesis, after grouping bins in order to have at least 10 entries both in the data and in the Monte Carlo. The confidence levels for the (J=0) and (J=2, λ=0) hypotheses are less then 10^{-6}. For the (J=2, λ=2) hypothesis, a confidence level of 99.9% is obtained. The contributions of (J=0) and (J=2, λ=0) are found to be compatible with zero when fitting the three waves simultaneously. The contribution of (J=2, λ=2) is found to be compatible with unity within 7%. This result is in agreement with the theoretical predictions [33] and allows to consider the formation of the $f'_2(1525)$ in a pure helicity-two state.

The two-photon width times the branching ratio into $K\bar{K}$ is determined from the cross section, as discussed in Chapter 3. The cross section for the reaction $e^+e^- \to e^+e^- f'_2(1525)$ is given by

$$\sigma = \frac{N(f'_2)}{\mathcal{L} \cdot \varepsilon \cdot Br} \tag{8.8}$$

where $\mathcal{L}$ is the integrated luminosity, ε is the total detection efficiency and Br is the branching fraction into the observed final state. The total detection efficiency is reported in Table 8.11. The number of signal events $N(f'_2)$ is determined from the maximum likelihood fit performed on the $K^0_S K^0_S$ mass spectrum. From our data only $\sigma \times Br(f'_2 \to K^0_S K^0_S \to \pi^+\pi^-\pi^+\pi^-)$ is directly measured.

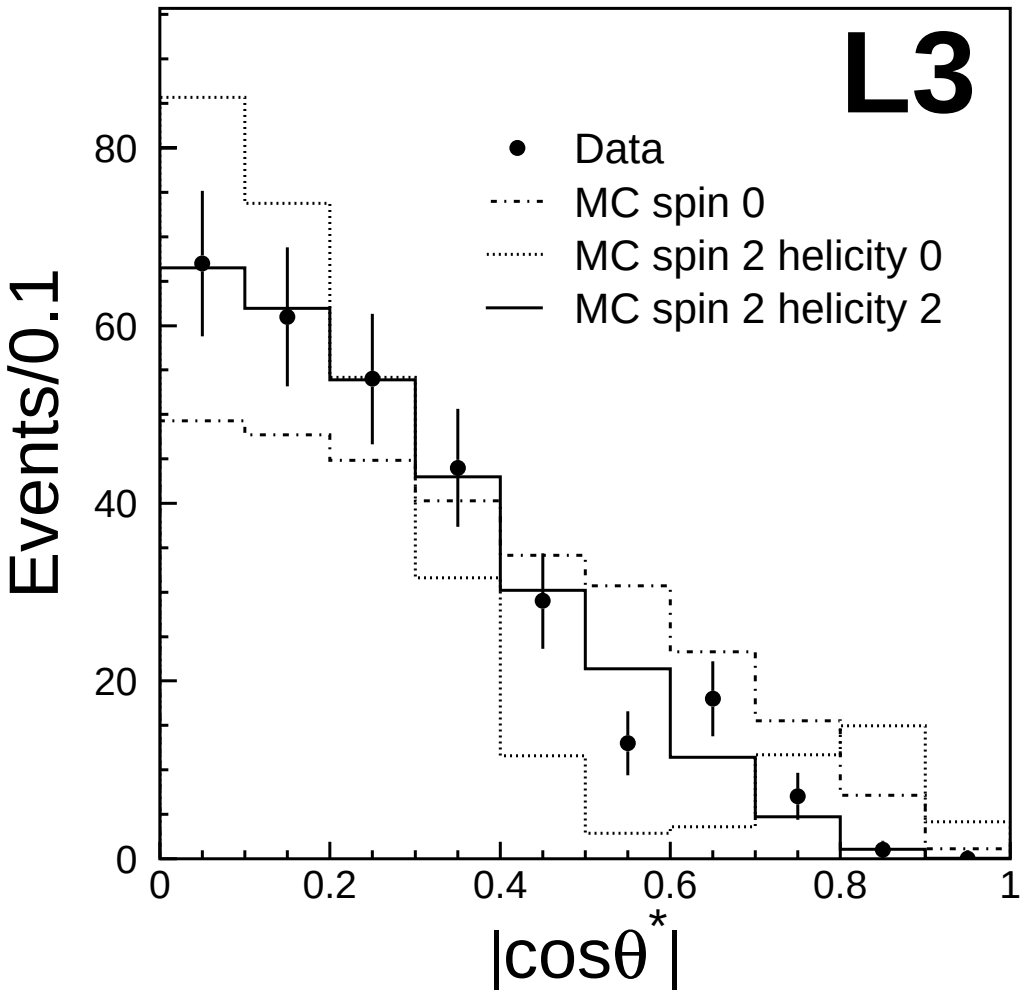

Figure 8.20: The $K^0_S K^0_S$ polar angle distribution compared with the Monte Carlo distributions for the hypothesis of a pure spin zero, spin-two helicity-zero and spin-two helicity-two states for the $f_2'(1525)$. The Monte Carlo expectations are normalized to the same number of events as the data.

$\sqrt{s}$ (GeV)	$\varepsilon_{selection}$ %	$\varepsilon_{level-one}$ %	$\varepsilon_{level-two}$ %	$\varepsilon_{level-three}$ %	ε %
Z pole	6.4	83	99	95	5.0
183	8.0	86	98	95	6.4
189-202	7.9	90	96	94	6.4

Table 8.11: The efficiencies for the $f'_2(1525)$ for the three data subsamples.

Using the PDG [28] value for $Br(K^0_S \to \pi^+\pi^-)$ and $Br(f'_2 \to K\bar{K}) = 4\times Br(f'_2 \to K^0_S K^0_S)$ from isospin symmetry, $\sigma\times Br(f'_2 \to K\bar{K})$ is determined. Combining Equations (3.29) and (8.8), the product $\Gamma_{\gamma\gamma}(f'_2)\times Br(f'_2 \to K\bar{K})$ is given by

$$\Gamma_{\gamma\gamma}(f'_2) \times Br(f'_2 \to K\bar{K}) = \frac{N(f'_2)}{\mathcal{L}\cdot\varepsilon\cdot\mathcal{K}} \cdot \frac{4}{[Br(K^0_S \to \pi^+\pi^-)]^2} \tag{8.9}$$

where the proportionality factor $\mathcal{K}$ is evaluated by Monte Carlo integration using the EGPC program.

Three distinct measurements are performed for the three data subsamples. The results are reported on Table 8.12. The three values obtained for the two-photon width of the $f'_2(1525)$ are consistent within errors, allowing their combination. The value

$$\Gamma_{\gamma\gamma}\Big(f'_2(1525)\Big) \times Br\Big(f'_2(1525) \to K\bar{K}\Big) = 76 \pm 6 \pm 11 \text{ eV} \tag{8.10}$$

is obtained, where the first uncertainty is statistical and the second is systematic. This value is in good agreement with the world average value of 86 ± 12 eV [28].

$\sqrt{s}$ (GeV)	$\mathcal{L}$ (pb^{-1})	$\mathcal{K}$ (pb/keV)	ε (%)	$N(f'_2)$	$\Gamma_{\gamma\gamma}(f'_2) \times Br(f'_2 \to K\bar{K})$ (keV)
Z pole	142.6	605	5.0	42.0 ± 7.8	$0.083 \pm 0.015 \pm 0.012$
183	51.9	841	6.4	24.4 ± 6.2	$0.074 \pm 0.018 \pm 0.011$
189-202	392.8	846	6.4	188.5 ± 20.5	$0.075 \pm 0.008 \pm 0.011$

Table 8.12: The measurement of the two-photon width of the $f'_2(1525)$ times the branching fraction into $K\bar{K}$ for the three data subsamples.

It agrees with and supersedes the value of $93 \pm 18 \pm 22$ eV previously published by L3 [116].

Using the result (8.10) and the world average values reported by the Particle Data Group [28], the stickiness of the $f_2'(1525)$ can be calculated according to Equation (8.4). The value

$$S_{f_2'(1525)} = 14.1 \pm 3.2 \tag{8.11}$$

is obtained. This value is typical for a $s\bar{s}$ state and is due to the smaller coupling to photons of the s quark with respect to the u quark.

8.9 The mixing angle of the tensor meson nonet

The ratio between the two-photon widths of the $f_2'(1525)$ and the $f_2(1270)$ is sensitive to the mixing angle θ_M of the tensor meson nonet, as discussed in Chapter 3.

From Equation (3.42), the expression

$$\frac{\Gamma_{\gamma\gamma}(f_2')}{\Gamma_{\gamma\gamma}(f_2)} = \frac{m^3_{f_2'(1525)}}{m^3_{f_2(1270)}} \cdot \frac{(\cos\theta_M - 2\sqrt{2}\sin\theta_M)^2}{(\sin\theta_M + 2\sqrt{2}\cos\theta_M)^2} \tag{8.12}$$

is obtained.

Using the world average values [28]

$$\begin{aligned} \Gamma_{\gamma\gamma}(f_2) &= (2.60 \pm 0.24) \text{ keV} \\ \mathrm{Br}(f_2' \to K\bar{K}) &= (88.8 \pm 3.1)\%, \end{aligned}$$

the value

$$\frac{\Gamma_{\gamma\gamma}(f_2')}{\Gamma_{\gamma\gamma}(f_2)} = 0.0329 \pm 0.0062$$

is obtained. Figure 8.21 shows this ratio and its expected value as a function of θ_M. The value

$$\theta_M = (27.5^{+0.7}_{-0.8})^\circ$$

is obtained showing a small but significant deviation from ideal mixing ($\theta_M \simeq 35^\circ$), in agreement with the value $\theta_M = 28^\circ \pm 3^\circ$ obtained with the Gell-Mann-Okubo mass formula. This result is also in agreement with the value of $\theta = (28 \pm 2)^\circ$ found in a recent analysis by Klempt and Peters [125] which fits all the results of the tensor nonet.

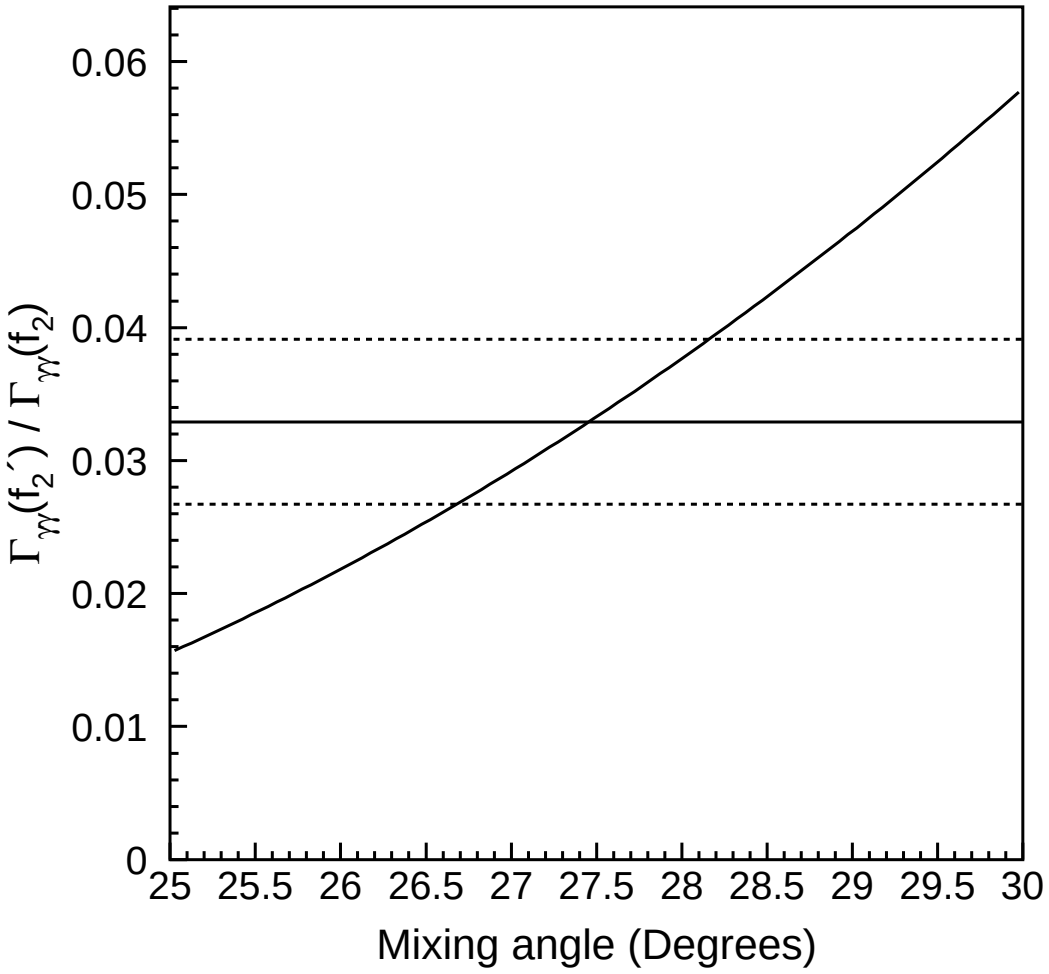

Figure 8.21: The ratio between the two photon widths of the $f_2'(1525)$ and the $f_2(1270)$ as a function of the mixing angle. The horizontal full line corresponds the experimental measurement of $\frac{\Gamma_{\gamma\gamma}(f_2')}{\Gamma_{\gamma\gamma}(f_2)}$ and the horizontal dashed lines represent the one standard deviation band.

8.10 The 1750 MeV region

The signal we observe in the 1750 MeV region, with a mass of 1767 ± 14 MeV and a total width of 187 ± 60 MeV, provides important information on the $f_J(1710)$. This state is observed in hadronic processes like J/ψ radiative decays and proton-proton central production and the determination of its scalar or tensor nature is at present controversial [28]. A summary of the results of the spin-parity assignments for the $f_J(1710)$ is reported in Table 8.13. The presence of both spin-zero and spin-two waves in the 1750 MeV mass region is reported by several analyses [126, 127, 128]. The two components are not resolved by these analyses. The presence of two resonant states, a scalar and a tensor, in the 1750 MeV mass region is reported by the BES Collaboration [129] in the study of the K^+K^- system in the reaction $e^+e^- \to J/\psi \to K^+K^-\gamma$. The K^+K^- mass spectrum reported by BES is shown in Figure 8.22 together with the decomposition into the 0^{++} and 2^{++} waves. In the 1525 MeV mass region only the 2^{++} wave is present due to the formation of the $f_2'(1525)$. In the 1750 MeV mass region a scalar is found at 1781 MeV and a tensor at 1696 MeV. The 0^{++} fraction in the 1750 MeV mass region is estimated to be $30 \pm 10\%$.

The first study of the $f_J(1710)$ in two-photon collisions is reported here. As discussed in Chapter 3, the first radial excitations of the tensor meson nonet are expected in this mass region. Moreover, according to lattice QCD predictions, the low lying glueball is a scalar with $J^{PC} = 0^{++}$ and a mass between 1400 and 1800 MeV. The scalar glueball is expected to mix with nearby states belonging to the scalar meson nonet and several predictions are based on the presence of a scalar state in the 1750 MeV region, the $f_0(1710)$.

Experiment	Reaction	Mass (MeV)	Width (MeV)	J^P	Reference
Crystal Ball	$J/\psi \to \gamma\eta\eta$	1640 ± 50	220^{+100}_{-70}	2^+	[130]
Mark III	$J/\psi \to \gamma K^+K^-$	$1720 \pm 10 \pm 10$	130 ± 20	2^+	[131]
WA76	$pp \to p_f K^0_S K^0_S p_s$	1713 ± 10	181 ± 30	2^+	[132]
WA102	$pp \to p_f K^0_S K^0_S p_s$	1730 ± 15	100 ± 25	0^+	[133]

Table 8.13: Observation of the states in the $f_J(1710)$ mass region with their spin parity assignments.

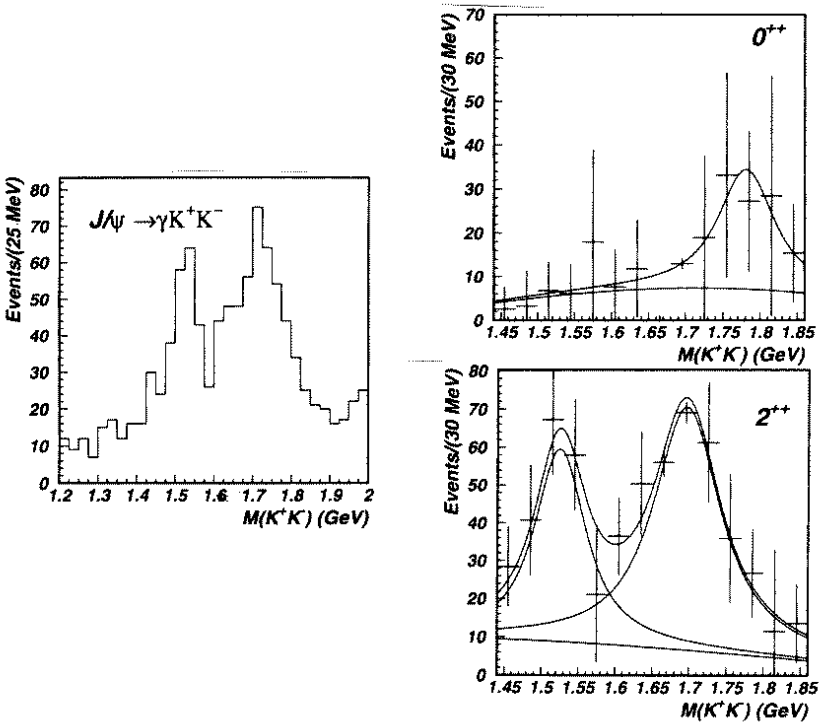

Figure 8.22: The K^+K^- mass spectrum reported by BES from the reaction $e^+e^- \to J/\psi \to K^+K^-\gamma$ together with the decomposition into the 0^{++} and 2^{++} waves.

To investigate the spin composition in the mass region of the $f_J(1710)$, the angular distribution of the two K^0_S's is studied in the mass region between 1640 and 2000 MeV (Figure 8.16). A resonance with a mass of 1750 MeV and a total width of 200 MeV is generated using the EGPC Monte Carlo generator. A VDM form factor with a ρ pole is used like for the $f'_2(1525)$. The total detection efficiencies for the three data subsamples and for the various spin and helicity hypotheses are reported in Table 8.14.

A fit of the angular distribution is performed using a combination of the two waves (J=0) and (J=2, λ=2) for the signal plus the distribution of the tail of the $f'_2(1525)$. Contributions from the (J=2, λ=0) wave are not considered, based on theoretical predictions [33] and on our experimental results for the $f'_2(1525)$. The tail of the $f'_2(1525)$ is modeled by Monte Carlo, assuming a pure (J=2, λ=2) state. The

$\sqrt{s}$ (GeV)	J=0	J=2, $\lambda = 2$	J=2, $\lambda = 0$
Z pole	6.0%	8.2%	4.1%
183	6.1%	8.4%	4.2%
189-202	6.3%	8.8%	4.5%

Table 8.14: The total detection efficiency in the 1750 MeV mass region for the various spin and helicity hypotheses.

$f_J(1710)$ wave	χ^2	d. o. f.	C. L. (%)
J=0 only	9.8	5	8
J=2, λ=2 only	6.7	5	24
Both	2.3	4	68

Table 8.15: The results of the fits on the polar angle distribution in the 1750 MeV mass region.

fraction of the events belonging to the $f_2'(1525)$ in the 1750 MeV mass region is found to be 14%. The fit is performed according to the formula

$$\mathcal{A}(|\cos\theta^*|) = C_1 \cdot \mathcal{A}_{f_2'(1525)}(|\cos\theta^*|) + F \cdot \mathcal{A}_{J=0}(|\cos\theta^*|) + (C_2 - F) \cdot \mathcal{A}_{J=2}^{\lambda=2}(|\cos\theta^*|) \tag{8.13}$$

where C_1 and C_2 are fixed to 14% and 86%, respectively. The spin-zero fraction F is the only free parameter of the fit. The three angular distributions $\mathcal{A}_i(|\cos\theta^*|)$ are obtained from the Monte Carlo and are normalized to the same number of events as the data. The bins are grouped in order to have at least 10 entries both in the data and in the Monte Carlo. The results of the fit are shown in Figure 8.23. The confidence level for the fit is 68.0% whereas the (J=0) fraction is $F = 24 \pm 16\%$.

If a fit is performed neglecting the (J=0) wave, a confidence level of 24.0% is obtained. A confidence level of 8% is found if only the (J=0) wave is considered. The possible (J=2, λ=0) contribution is found to be compatible with zero. The results of all these fits are reported in Table 8.15.

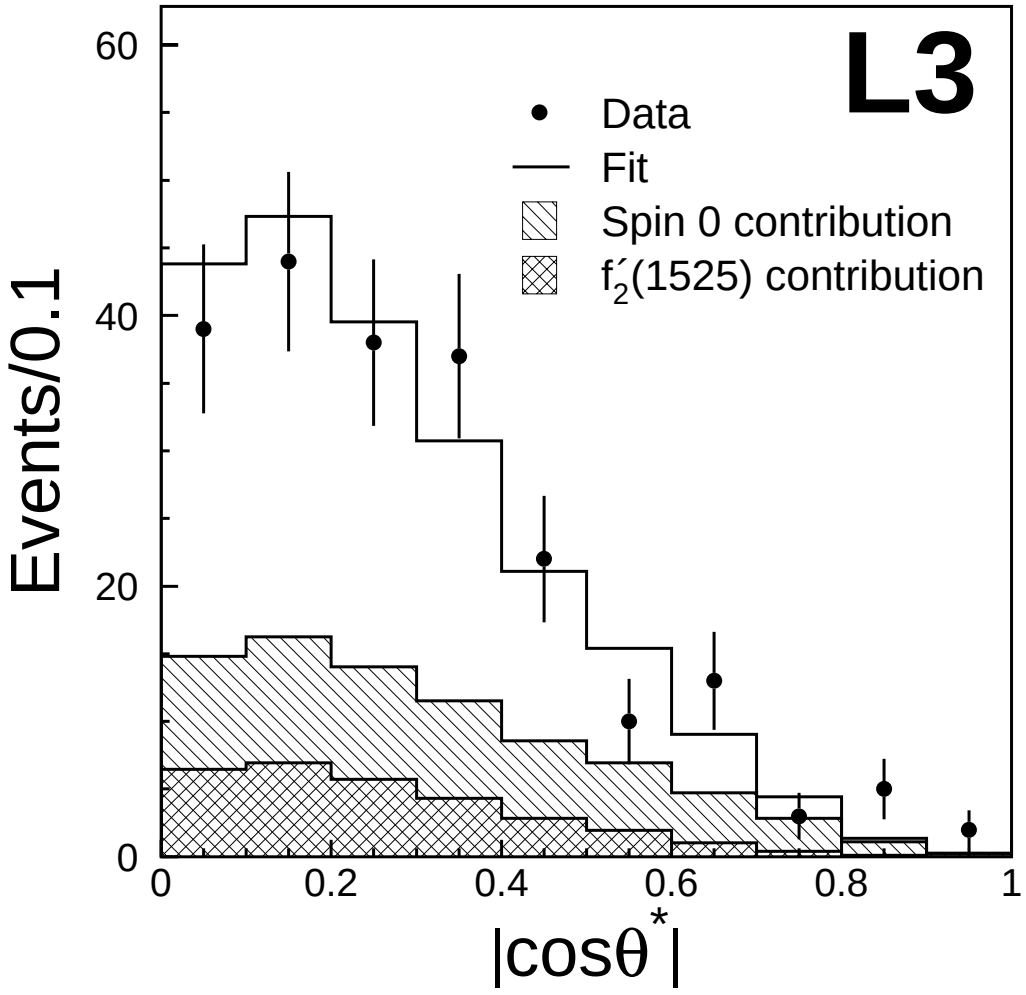

Figure 8.23: The fit of the $K^0_S K^0_S$ polar angle distribution in the 1640−2000 MeV mass region. The contributions of spin-zero and spin-two helicity-two waves are shown together with the 14% contribution of the tail of the $f_2'(1525)$.

Our data indicate therefore the presence of both spin zero and spin two in the 1750 MeV mass region where the (J=2, λ=2) wave largely dominates. The measured spin-zero fraction is in good agreement with the result reported by BES [129].

The spin-two fraction is large enough to allow an estimation if its two-photon width. Due to its low statistics, the second data subsample is not used for this measurement. Two different measurements are therefore effectuated with the same method adopted for the $f_2'(1525)$. Combining the two results, the two-photon width for the spin-two fraction is measured to be

$$\Gamma_{\gamma\gamma}\Big(f_2(1750)\Big) \times \mathrm{Br}\Big(f_2(1750) \to K\bar{K}\Big) = 49 \pm 11 \pm 13 \text{ eV}. \tag{8.14}$$

The systematic uncertainty includes also contributions from the total width (2%) and the (J=2, λ=2) fraction (10%).

Using this result and the world average values reported by the Particle Data Group [28], the stickiness of the $f_2(1750)$ can be evaluated according to Equation (8.4). The value

$$S_{f_2(1750)} = 32 \pm 15 \tag{8.15}$$

is obtained. This value is compatible within the errors with the value obtained for the $f_2'(1525)$ tensor meson.

The (J=2, λ=2) signal can be interpreted as the formation of the first radial excitation of a isoscalar tensor meson state, the f_2'', predicted at a mass of 1740 MeV [35, 36] with a surprisingly high value of the two-photon width of 1.04 keV [35]. Under this hypothesis and using the result (8.14), the f_2'' would be characterized by a branching ratio into $K\bar{K}$ of about 5%, very similar to the $f_2(1270)$.

The $K_S^0K_S^0$ final state leads also to isovector final states and the (J=2, λ=2) signal can be interpreted as the formation of the first radial excitation of the isovector tensor meson, the a_2'. The values of the mass and of the total width are in fact compatible with the a_2' signal reported by L3 [38] in the $\pi^+\pi^-\pi^0$ final state and discussed in Chapter 3. This state is probably observed also in $p\bar{p}$ annihilations. An isovector tensor state with a mass of 1698$\pm$44 MeV and a total width of 265$\pm$55 MeV decaying into $\pi^0\eta$ is recently reported by Crystal Barrel [134] in the reaction $p\bar{p} \to \pi^0\pi^0\eta$. Using the result (8.14) and the measurement by L3 in the $\pi^+\pi^-\pi^0$ final state, the

ratio

$$\frac{\mathrm{Br}(a_2'(1750) \to \pi^+\pi^-\pi^0)}{\mathrm{Br}(a_2'(1750) \to K\bar{K})} = 5.9 \pm 2.2 \tag{8.16}$$

is evaluated. This value is found to be about a factor 2.5 less with respect to the $a_2(1320)$. As for the $f_2(1270)$ and the $a_2(1320)$, the f_2'' and the a_2' are very close in mass and, leading to the same final state, interference effects are possible. In this case, the (J=2, λ=2) signal can be due to the interference of these two radially excited tensor states.

The spin-zero component of the signal in the 1750 MeV mass region can be interpreted as the formation of the $f_0(1710)$ scalar meson in agreement with the various interpretations of the scalar meson nonet mixed with the scalar glueball presented in Chapter 3. The spin-zero fraction is compatible with the theoretical predictions for the cross section of the 0^{++} wave in the $K^0_S K^0_S$ final state by Anisovich [135]. For the two-photon width, the limited statistics of our data allows only a very rough estimation. The value $\Gamma_{\gamma\gamma}(f_0(1710)) \times \mathrm{Br}(f_0(1710) \to K\bar{K}) = 130 \pm 96$ eV is obtained. The large error is dominated by the uncertainty on the (J=0) fraction.

8.11 Limits on the formation of the $\xi(2230)$ tensor glueball candidate

The $K^0_S K^0_S$ mass spectrum in Figure 8.16 shows no evidence for the formation of the $\xi(2230)$. This state is considered a good candidate for the tensor glueball and is

$\sqrt{s}$ (GeV)	$\mathcal{L}$ (pb^{-1})	$\mathcal{K}$ (pb/keV)	ε (%)	N_{ev}	N_{bkg}	N_{up-lim}	$\Gamma_{\gamma\gamma}(\xi) \times \mathrm{Br}(K^0_S K^0_S)$ (eV)
91	142.6	161	16.6	6	4.9	7.3	< 4.1
183	51.9	227	15.2	2	7.9	3.6	< 4.2
189-202	392.8	230	14.1	34	37.5	11.9	< 2.1

Table 8.16: The upper limits at 95% C.L. on the two-photon width of the $\xi(2230)$ for the three data subsamples.

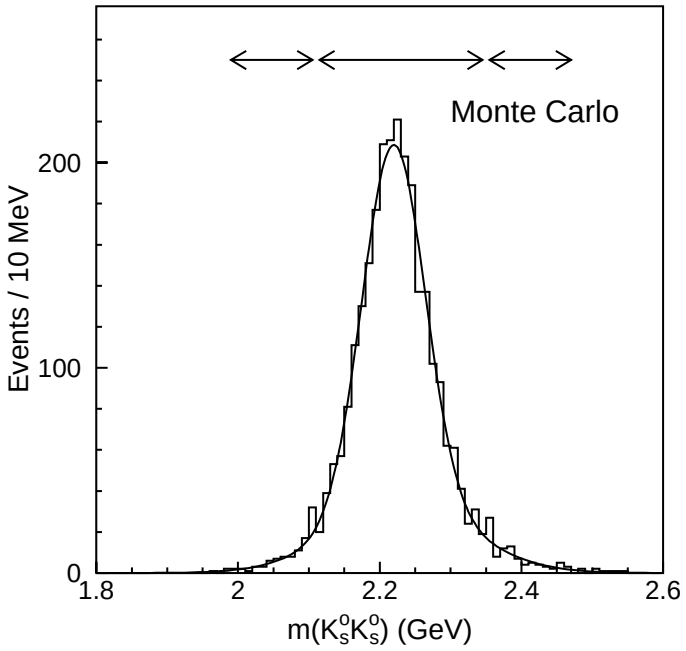

Figure 8.24: The $K^0_S K^0_S$ mass spectrum for the Monte Carlo simulation for the $\xi(2230)$. The solid line corresponds to the Gaussian fit and the arrows to the signal region and the two mass sidebands.

expected to be characterized by a very small two-photon width. This non-observation of the $\xi(2230)$ translates into an upper limit on its two-photon width.

Three Monte Carlo samples are generated using the EGPC generator to determine the detection efficiency for the $\xi(2230)$. For the simulation a mass of 2230 MeV and a total width of 20 MeV are used and the same procedure as for the $f_2'(1525)$ is adopted. A mass resolution of σ= 60 MeV is estimated by fitting the $K^0_S K^0_S$ mass distribution with a Gaussian function, as shown in Figure 8.24.

The total detection efficiency is reported in Table 8.16 for the three different data samples, under the hypothesis of a pure (J=2, λ=2) contribution. The signal region is chosen to be $\pm 2\sigma$ around the $\xi(2230)$ mass, as shown in Figure 8.16. In order to evaluate the background two sidebands of 2σ are considered. The number

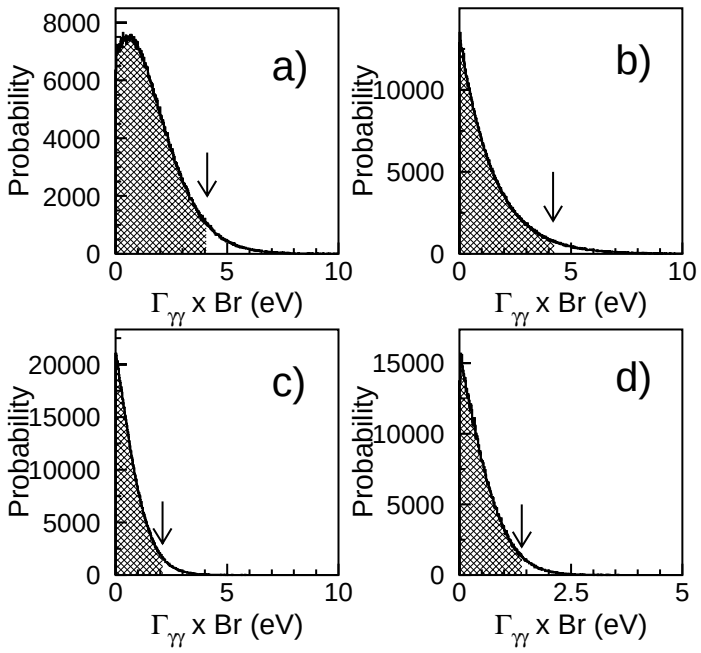

Figure 8.25: The probability distributions for $\Gamma_{\gamma\gamma}(\xi(2230))\times\mathrm{Br}(\xi(2230) \to K^0_S K^0_S)$ for the three data subsamples (a, b and c) and for their combination (d). The probability is expressed in arbitrary units. The hatched area corresponds to 95% of the total probability and the arrows to the 95% upper limits.

of events in the signal region (N_{ev}) and the expected background (N_{bkg}) evaluated with a linear fit in the sideband region are reported in Table 8.16. The upper limit on the number of events N_{up-lim} is determined using a Poisson distribution with background, following the method proposed by Helene [136]. The confidence level is fixed at 95%. The resulting upper limits are reported in Table 8.16.

Using the same method adopted for measuring the two-photon width of the $f_2'(1525)$, an upper limit of $\Gamma_{\gamma\gamma}(\xi(2230))\times\mathrm{Br}(\xi(2230) \to K^0_S K^0_S)$ is derived for each data subsample. From the three probability distributions for the number of events, the probability distributions for $\Gamma_{\gamma\gamma}(\xi(2230))\times\mathrm{Br}(\xi(2230) \to K^0_S K^0_S)$ are calculated. To take the error on the detection efficiency into account, the Poisson distribution

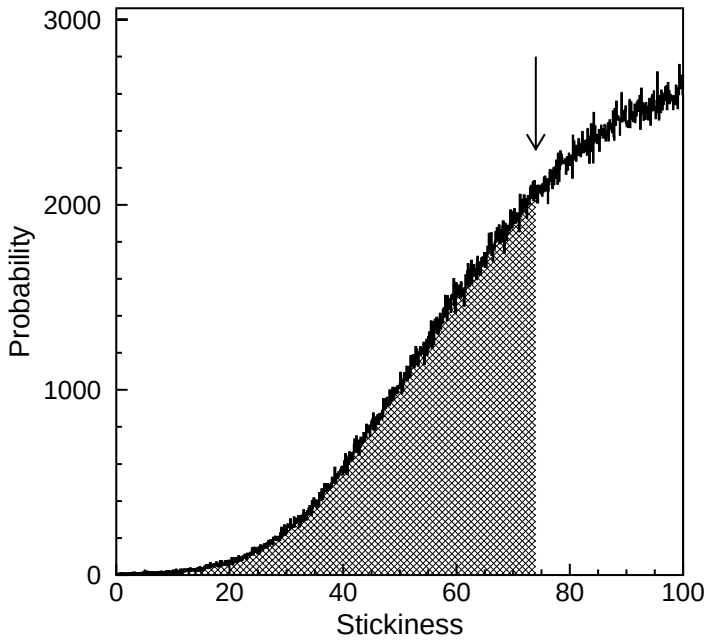

Figure 8.26: The probability distribution for the stickiness of the $\xi(2230)$ expressed in arbitrary units. The hatched area corresponds to the 5% of the total and the arrow corresponds to the 95% lower limit.

with background is convoluted with the Gaussian function corresponding to the detection efficiency. The convolution is performed with a Monte Carlo technique. The tree probability distributions for $\Gamma_{\gamma\gamma}(\xi(2230))\times \mathrm{Br}(\xi(2230) \to \mathrm{K^0_S K^0_S})$ are shown in Figure 8.25(a, b and c) from which the three upper limits reported in Table 8.16 are derived.

A combination of these three probability distributions is obtained by multiplying them, as shown in Figure 8.25(d). From the combined distribution the value

$$\Gamma_{\gamma\gamma}(\xi(2230)) \times \mathrm{Br}(\xi(2230) \to \mathrm{K^0_S K^0_S}) < 1.4 \text{ eV} \tag{8.17}$$

at 95% C.L. is obtained under the hypothesis of a pure helicity-two state.

Combining the world average values [28] for $\Gamma(\mathrm{J} \to \gamma\xi(2230))\times \mathrm{Br}(\xi(2230) \to$

$K^0_S K^0_S) = 1.9 \pm 0.5$ eV and our upper limit on $\Gamma(\xi(2230) \to \gamma\gamma) \times \mathrm{Br}(\xi(2230) \to K^0_S K^0_S)$, a lower limit on the stickiness of the $\xi(2230)$ is obtained. This is done by calculating the probability distribution for the stickiness from the combined probability distribution for $\Gamma_{\gamma\gamma}(\xi(2230)) \times \mathrm{Br}(\xi(2230) \to K^0_S K^0_S)$ and the Gaussian probability distributions for the other quantities. The probability distribution for the stickiness is shown in Figure 8.26. It leads to the lower limit

$$S_{\xi(2230)} > 74 \tag{8.18}$$

at 95% C.L.

This lower limit on $S_{\xi(2230)}$ is much larger than the values measured for all the well established $q\bar{q}$ states and supports the interpretation of the $\xi(2230)$ as the tensor glueball. A further confirmation of its existence in gluon rich environments becomes now very important.

Chapter 9

Conclusions

In this thesis two experimental studies on two-photon interactions are reported.

In the reaction $e^+e^- \to e^+e^-$hadrons the inclusive production of K^0_S mesons is studied. The data sample corresponds to a total integrated luminosity of 410 pb^{-1} collected by the L3 detector at LEP at e^+e^- centre of mass energies from 189 to 202 GeV. The differential production cross sections as a function of the transverse momentum p_t and of the pseudorapidity η are measured for events with two-photon centre of mass energy $W_{\gamma\gamma} > 5$ GeV and $W_{\gamma\gamma} > 10$ GeV. For $0.4 < p_t < 2.0$ GeV and $|\eta| < 1.5$, the differential cross section as a function of p_t is well reproduced by an exponential fit with $\langle p_t \rangle = 342 \pm 8$ MeV, typical of soft hadronic interactions. For $p_t > 2.0$ GeV the K^0_S production cross section is higher than the exponential fit due to QCD hard processes. A reasonable agreement is found between our measurement and the Next-to-Leading order QCD predictions by Kniehl.

The $K^0_S K^0_S$ exclusive final state in two-photon collisions is studied using a total integrated luminosity of 588 pb^{-1}collected at e^+e^- center of mass energies from the Z pole to 202 GeV. In the full data sample 802 events are selected. The $K^0_S K^0_S$ mass spectrum shows the presence of three peaks over a small and smooth background.

- Around 1300 MeV a small peak is due to the $f_2(1270)-a_2(1320)$ destructive interference.

- The spectrum is dominated by the formation of the $f_2'(1525)$ tensor meson in a pure spin-two helicity-two state. For the two-photon width of the $f_2'(1525)$ we

obtain

$$\Gamma_{\gamma\gamma}\left(\mathrm{f}_2'(1525)\right) \times \mathrm{Br}\left(\mathrm{f}_2'(1525) \to \mathrm{K}\bar{\mathrm{K}}\right) = 76 \pm 6 \pm 11 \text{ eV}.$$

This value is at present the most accurate measurement of this quantity. This result leads to the evaluation of the mixing angle θ_M of the tensor meson nonet

$$\theta_M = (27.5^{+0.7}_{-0.8})^\circ$$

which shows a small but significant deviation from ideal mixing ($\theta_M \simeq 35^\circ$).

- A clear signal for the formation of the $\mathrm{f_J}(1710)$ is observed and the first study of this state in two-photon collisions is performed. This signal is found to be dominated by the spin-two helicity-two state. A fraction of 24±16% of a 0^{++} wave is also found in the $\mathrm{K^0_S K^0_S}$ mass region between 1640 and 2000 MeV. The spin-two component can be interpreted as the formation of the first radial excitation of a tensor meson state for which we measure

$$\Gamma_{\gamma\gamma}\left(\mathrm{f}_2(1750)\right) \times \mathrm{Br}\left(\mathrm{f}_2(1750) \to \mathrm{K}\bar{\mathrm{K}}\right) = 49 \pm 11 \pm 13 \text{ eV}.$$

- No resonance is observed in the mass region around 2.2 GeV and the upper limit

$$\Gamma_{\gamma\gamma}(\xi(2230)) \times \mathrm{Br}(\xi(2230) \to \mathrm{K^0_S K^0_S}) < 1.4 \text{ eV}$$

at 95% C.L. is derived for the glueball candidate $\xi(2230)$. This translates into the lower limit on the stickiness

$$S_{\xi(2230)} > 74$$

at 95% C.L., much larger than the values measured for all the well established $q\bar{q}$ states. If the $\xi(2230)$ will be confirmed in gluon rich environments, this result supports the interpretation of this state as the tensor glueball.

List of Figures

List of Tables

Bibliography

[1] M. I. Sobel, *Light*, The University of Chicago Press, 1987.

[2] G. N. Lewis, *Nature* **118** (1926) 874.

[3] H. Euler and B. Kockel, *Naturwissenschaften* **23** (1935) 246.

[4] A. L. Huges and G. E. M. Jauncey, *Phys. Rev.* **36** (1930) 773.

[5] G. Breit and J. A. Wheeler, *Phys. Rev.* **46** (1934) 1087.

[6] E. Fermi, *Z. Phys.* **29** (1924) 315.

[7] F. E. Low, *Phys. Rev.* **120** (1960) 582.

[8] F. Calogero and C. Zemach, *Phys. Rev.* **120** (1960) 1860.

[9] V. Bolakin *et al.*, *Phys. Lett.* **B 34** (1971) 663.

[10] L.D. Landau and E. Lifshitz, *Sov. Phys.* **6** (1934) 244.

[11] G. Barbiellini *et al.*, *Phys. Rev. Lett.* **32** (1974) 385.

[12] *Physics at LEP 2*, CERN 96-01, G. Altarelli *et al.* editors.

[13] D. L. Burke *et al.*, *Phys. Rev. Lett.* **79** (1997) 1626.

[14] D. J. Miller, *Real photon physics at the linear collider*;
V. Telnov, *Status of gamma-gamma and gamma-electron colliders*;
I. F. Ginzburg, *Physics at $\gamma\gamma$ and $e\gamma$ colliders*,
Proceedings of *Photon99*, *Nucl. Phys.* **B 82**, March 2000.

[15] V. M. Budnev *et al.*, *Phys. Rep.* **C 15** (1975) 181.

[16] H. Kolanoski, *Two-photon physics at e^+e^- storage rings*, Springer-Verlag, 1984.

[17] C. Berger and W. Wagner, *Phys. Rep.* **146** (1987) 1.

[18] H. Kolanoski and W. Zerwas, *Two-photon physics*, World Scientific, 1993.

[19] J. H. Field, *Photon-photon collisions*, L.P.N.H.E., University of Paris, 84-04, 1984.

[20] G. A. Schuler, *Improving the equivalent-photon approximation in electron-positron collisions*, CERN-TH/96-297 and hep-ph/9610406.

[21] L3 Collab., M. Acciarri *et al.*, *Phys. Lett.* **B 438** (1998) 363.

[22] F. L. Linde, *Charm production in two-photon collisions*, Ph. D. thesis, Rijksuniversiteit Leiden, The Netherlands, 1988.

[23] L. D. Landau, *Dokl. Akad. Nauk. USSR* **60** (1948) 207;
C. N. Yang, *Phys. Rev.* **77** (1950) 242.

[24] D. Morgan, M. R. Pennington and M. R. Whalley, *J. Phys.* **G 20** (1994) A1-A147.

[25] M. Poppe, *Exclusive hadron production in two-photon reactions*, *Int. J. Mod. Phys.* **1** (1986) 545.

[26] S. Braccini, *Resonance formation in two-photon collisions*, *Acta Physica Polonica* **31** (2000) 2143 and hep-ex/0007010.

[27] A. V. Anisovich and V. V. Anisovich, *Phys. Lett.* **B 467** (1999) 289;
A. V. Anisovich and V. V. Anisovich, hep-ph/9906448;
A. V. Anisovich, private communication.

[28] Particle Data Group, D. E. Groom *et al.*, *Eur. Phys. J.* **C 15** (2000) 1.

[29] H. J. Lipkin, *Nucl. Phys.* **B 7** (1968) 321.

[30] D. Faiman *et al.*, *Phys. Lett.* **B 59** (1975) 269.

[31] M. Gell-Mann, *Phys. Rev.* **125** (1962) 1067.

[32] S. Okubo, *Prog. Theor. Phys.* **27** (1962) 949.

[33] B. Schrempp-Otto *et al.*, *Phys. Lett.* **36 B** (1971) 463;
G. Köpp *et al.*, *Nucl. Phys.* **B 70** (1974) 461;
P. Grassberger and R. Kögerler, *Nucl. Phys.* **B 106** (1976) 451.

[34] T. Barnes, *Radial excitations*, Frascati Physics Series Vol.XV (1999) 645.

[35] C. R. Münz, *Nucl. Phys.* **A 609** (1996) 364.

[36] L. S. Celenza *et al.*, *Phys. Rev.* **C 60** (1999) 035206.

[37] S. Godfrey and N. Isgur, *Phys. Rev.* **D 32** (1985) 189.

[38] L3 Collab., M. Acciarri *et al.*, *Phys. Lett.* **B 413** (1997) 147;
S. Braccini, *The 1500-1700 MeV mass region and glueball searches in two-photon collisions with the L3 detector at LEP*, Frascati Physics Series Vol.XV (1999) 53.

[39] CERN-IHEP Collab., *Nucl. Phys.* **B 63** (1973) 153.

[40] H. Fritzsch and M. Gell-Mann, *Current algebra: quarks and what else?*, Proceedings of the XVI International Conference on High Energy Physics, Chicago, Batavia, Vol. 2, 1972.

[41] H. Fritzsch and P. Minkowski, *Il Nuovo Cimento* **A 30** (1975) 393.

[42] C. Michael, *Nucl. Phys.* **A 655** (1999) 12, and references therein.

[43] UKQCD Collab., G. Bali *et al.*, *Phys. Lett.* **B 314** (1993) 378.

[44] C. J. Morningstar and M. Peardon, *Phys. Rev.* **D 60** (1999) 034509 and hep-lat/9901004.

[45] A. Vaccarino and D. Weingarten, *Phys. Rev.* **D 60** (1999) 114501 and hep-lat/9910007

[46] C. Amsler and F. E. Close, *Phys. Lett.* **B 353** (1995) 385;
C. Amsler and F. E. Close, *Phys. Rev.* **D 53** (1996) 295;
C. Amsler, *Scalar mesons in the 1500 MeV mass region*, Frascati Physics Series Vol.XV (1999) 609.

[47] C. Amsler, *Nucl. Phys.* **A663&664** (Proc. Suppl.) (2000) 93c.

[48] F. E. Close and A. Kirk, *Phys. Lett.* **B 483** (2000) 345.

[49] L. Burakowsky and P. R. Page, *Scalar glueball mixing and decay*, hep-ph/9807400.

[50] W. Lee and D. Weingarten, *Phys. Rev.* **D 61** (2000) 014015 and hep-lat/9910008

[51] F. E. Close *et al.*, *Phys. Rev.* **D 55** (1997) 5749;
F. E. Close, hep-ph/9610426.

[52] P. Minkowski and W. Ochs, *Eur. Phys. J.* **C 9** (2000) 283;
P. Minkowski and W. Ochs, *The $J^{PC}=0^{++}$ scalar meson nonet and glueball of lowest mass*, Frascati Physics Series Vol.XV (1999) 245.

[53] U. Gastaldi, *The 0^{++} gluonium ground state: experimental survey*, Proceedings of QCD'00, Montpellier, France, July 2000;
U. Gastaldi, *Observation of the 0^{++} gluonium ground state in antiproton annihilations at rest*, Proceedings of *Rencontres de Physique de la Vallee d'Aoste*, La Thuille, Italy, March 2000;
V. Ableev *et al.*, *Nucl. Phys.* **B 86** (2000) 351.

[54] Mark III Collab., R. M. Baltrusaitis *et al.*, *Phys. Rev. Lett.* **56** (1986) 107.

[55] DM2 Collab., J. E. Augustin *et al.*, *Phys. Rev. Lett.* **60** (1988) 2238.

[56] BES Collab., J. Z. Bai *et al.*, *Phys. Rev. Lett.* **76** (1996) 3502.

[57] BES Collab., J. Z. Bai *et al.*, *Phys. Rev. Lett.* **81** (1998) 1179.

[58] W. Roethel for the Crystal Barrel Collab., *Nucl. Phys.* **A655** (Proc. Suppl.) (1999) 137c;

K. K. Seth for the Crystal Barrel Collab., *Nucl. Phys.* **A663&664** (Proc. Suppl.) (2000) 600c;
Crystal Barrel Collab., in preparation.

[59] E. H. Kada, P. Kessler and J. Parisi, *Phys. Rev.* **D 39** (1989) 2657.

[60] M. R. Perl, *High energy hadron physics*, John Wiley & Sons, 1974.

[61] P. D. B. Collins and A. D. Martin, *Hadron interactions*, Adam Hilger, 1984.

[62] R. Engel, *Z. Phys.* **C 66** (1995) 203 ;
R. Engel and J. Ranft, *Phys. Rev.* **D 54** (1996) 4246;
R. Engel, private communication.

[63] T. Sjöstrand, *Comput. Phys. Commun.* **82** (1994) 74.

[64] A. Capella *et al.*, *Phys. Rep.* **236** (1994) 227.

[65] G. A. Schuler and T. Sjöstrand, *Phys. Rev.* **D 49** (1994) 2257.

[66] J. Binnewies, B. A. Kniehl and G. Kramer, *Phys. Rev.* **D 53** (1996) 6110.

[67] L. E. Gordon and J. K. Storrow, *Nucl. Phys.* **B 489** (1997) 405.

[68] TOPAZ Collab., R. Enomoto *et al.*, *Phys. Lett.* **B 341** (1994) 238.

[69] OPAL Collab., K. Ackerstaff *et al.*, *Eur. Phys. J.* **C 6** (1999) 253.

[70] LEP Design Report Vol. 1, CERN-LEP/TH 83-29 (1983);
LEP Design Report Vol. 2, CERN-LEP/TH 84-01 (1984);
S. Meyers, *The LEP collider, from design to approval and commissioning*, CERN 91-08 (1991).

[71] L. Camilleri *et al.*, *Physics with very high energy e^+e^- colliding beams*, CERN 76-18, November 1976.

[72] The LEP Energy Working Group, R. Assmann *et al.*, *Eur. Phys. J.* **C 6** (1999) 187;
The LEP Energy Working Group, A. Blondel *et al.*, *Eur. Phys. J.* **C 11** (1999) 573.

[73] L3 Collab., *The L3 technical proposal*, L3 Note 211, 1983;
L3 Collab., B. Adeva *et al.*, *Nucl. Instr. Meth.* **A 289** (1990) 35;
L3 Collab., O. Adriani *et al.*, *Phys. Rep.* **236** (1993) 1.

[74] R. Battiston, *Nucl. Instr. Meth.* **A 315** (1992) 197;
M. Acciarri *et al.*, *Nucl. Instr. Meth.* **A 351** (1994) 300.

[75] G. Viertel, *Nucl. Instr. Meth.* **A 263** (1988) 1.

[76] G. Viertel, *Nucl. Instr. Meth.* **A 273** (1989) 471.

[77] J. Wenninger, Ph. D. thesis, University of Geneva, Switzerland, 1992.

[78] G. Basti *et al.*, *Nucl. Instr. Meth.* **A 374** (1996) 293.

[79] A. Adam *et al.*, *Nucl. Instr. Meth.* **A 383** (1996) 342.

[80] T. van Rhee, Ph. D. thesis, University of Utrecht, The Netherlands, 2000.

[81] I. C. Brock *et al.*, *Nucl. Instr. Meth.* **A 381** (1996) 236.

[82] M. Chemarin *et al.*, *Nucl. Instr. Meth.* **A 349** (1994) 345.

[83] R. Bizzarri *et al.*, *Nucl. Instr. Meth.* **A 283** (1989) 799;
R. Bizzarri *et al.*, *Nucl. Instr. Meth.* **A 317** (1992) 463.

[84] S. P. Beingessner *et al.*, *Nucl. Instr. Meth.* **A 340** (1994) 322;
J. J. Blaising *et al.*, *The L3 second level trigger implemented for LEP2 with ST T9000 transputer and the ST C104 asynchronous packet switch from SGS-Thomson*, L3 Note 2150, August 1997.

[85] C. Dionisi *et al.*, *Nucl. Instr. Meth.* **A 336** (1993) 78.

[86] M. Fukushima, *The trigger and data acquisition system of the L3 experiment*, L3 Note 520, 1987.

[87] P. Béné *et al.*, *Nucl. Instr. Meth.* **A 306** (1991) 150.

[88] D. Haas *et al.*, *Nucl. Instr. Meth.* **A 420** (1999) 101.

[89] S. Braccini, *Study of the level-one TEC trigger configurations, efficiencies and rates*, L3 Note 2261, May 1998.

[90] B. Schroers, *Track reconstruction in the L3 vertex detector*, L3 Note 713, 1988;
J. Alcaraz, *Helicoidal tracks*, L3 Note 1666, February 1995;
J. Alcaraz, *SZ reconstruction in the L3 detector*, L3 Note 2318, August 1998.

[91] J. C. Sens and P. Vikas, *Reconstruction of the L3 fill vertex*, L3 Note 1027, 1992;
A. J. Barczyk, Diploma thesis, ETH-Zürich, Switzerland, 1996;
V. Brigljevic, Ph. D. thesis, ETH-Zürich, Switzerland, 1999.

[92] J. C. Sens, *Structure and use of the standard L3 software for finding secondary vertices*, L3 Note 1244, 1992;
F. Becattini, Ph.D. thesis, University of Florence, Italy, 1996.

[93] I. Vodopianov, private communication.

[94] S. Braccini, *Measurement of the specific ionization loss with the TEC at LEP2*, L3 Note 2631, January 2001.

[95] A. H. Walenta, *Performance and development of dE/dx counters*, *Physica Scripta*, **23** (1981) 354;
R. Fernow, *Introduction to experimental particle physics*, Cambridge University Press, 1990;
Experimental techniques in high-energy nuclear and particle physics, T. Ferbel editor, World Scientific, 1991;
C. Groupen, *Particle detectors*, Cambridge University Press, 1996.

[96] G. Schwering, *Measurement of energy loss with the TEC*, L3 Note 1541, 1993.

[97] L3 Collab., M. Acciarri *et al.*, *Phys. Lett.* **B 461** (1999) 155;
L3 Collab., M. Acciarri *et al.*, *Phys. Lett.* **B 467** (1999) 137;
L3 Collab., M. Acciarri *et al.*, *Phys. Lett.* **B 501** (2001) 1.

[98] P. Déglon, Diploma thesis, University of Geneva, Switzerland, 1997.

[99] L3 Collab., M. Acciarri *et al.*, *Phys. Lett.* **B 412** (1997) 189;
L3 Collab., M. Acciarri *et al.*, *Phys. Lett.* **B 462** (1999) 354.

[100] R. M. Sternheimer and R. F. Peierls, *Phys. Rev.* **B 3** (1971) 3681.

[101] OPAL Collab., G. Abbiendi *et al.*, *Eur. Phys. J.* **C 10** (1999) 547 and references therein.

[102] S. Braccini, *Inclusive K^0_S meson production in two-photon collisions*, L3 Note 2589, July 2000, Submitted to ICHEP2000, Osaka, Japan, July 2000;
L3 Collab., in preparation.

[103] S. Jadach, B. F. L. Ward and Z. Wąs, *Comput. Phys. Commun.* **79** (1994) 503.

[104] M. Skrzypek, S. Jadach, W. Placzek and Z. Wąs, *Comput. Phys. Commun.* **94** (1996) 216.

[105] F. A. Berends, P. H. Daverfeldt and R. Kleiss, *Nucl. Phys.* **B 253** (1985) 441.

[106] R. Brun *et al.*, GEANT 3.15 preprint CERN DD/EE/84-1 (1984); Revised 1987.

[107] H. Fesefeldt, RWTH Aachen report PITHA 85/2 (1985).

[108] A. Donnachie and P. V. Landshoff, *Phys. Lett.* **B 296** (1992) 227.

[109] L3 Collab., M. Acciarri *et al.*, PL **B 408** (1997) 450;
M. N. Focacci-Kienzle, L3 Note 2570, June 2000;
L3 Collab., M. Acciarri *et al.*, CERN-EP/2001-012, accepted by *Phys. Lett.* **B**.

[110] OPAL Collab., K. Ackerstaff *et al.*, *Eur. Phys. J.* **C 14** (2000) 199.

[111] L3 Collab., M. Acciarri *et al.*, *Phys. Lett.* **B 503** (2001) 10;
L3 Collab., M. Acciarri *et al.*, CERN-EP/2000-155, accepted by *Phys. Lett.* **B**.

[112] A. Zieminski, *Multiparticle production*, proceedings of the 1977 European Conference on Particle Physics.

[113] B. A. Kniehl, G. Kramer and B. Pötter, hep-ph/0011155;
B. A. Kniehl, private communication.

[114] M. Chanowitz, *Resonances in photon-photon scattering*, Proceedings of the VIth International Workshop on Photon-Photon Collisions, World Scientific (1984).

[115] L3 Collab., M. Acciarri *et al.*, *Phys. Lett.* **B 501** (2001) 173.

[116] L3 Collab., M. Acciarri *et al.*, *Phys. Lett.* **B 363** (1995) 118.

[117] TASSO Collab., M. Althoff *et al.*, *Phys. Lett.* **B 121** (1982) 216;
TASSO Collab., M. Althoff *et al.*, *Z. Phys.* **C 29** (1985) 189.

[118] CELLO Collab., H. J. Behrend *et al.*, *Z. Phys.* **C 43** (1989) 91.

[119] PLUTO Collab., C. Berger *et al.*, *Z. Phys.* **C 37** (1988) 329.

[120] CLEO Collab., R. Godang *et al.*, *Phys. Rev. Lett.* **79** (1997) 3829;
CLEO Collab., M. S. Alam *et al.*, *Phys. Rev. Lett.* **81** (1998) 3328;
H. P. Paar, *Study of the glueball candidate $f_J(2220)$ at CLEO*, *Nucl. Phys.* **B 82** (Proc. Suppl.) (2000) 337.

[121] BELLE Collab., A. Abashian *et al.*, BELLE-CONF-0018, Submitted to ICHEP2000, Osaka, Japan, July 2000.

[122] S. Braccini, $K^0_S K^0_S$ *final state and glueball searches and* $\Lambda\bar{\Lambda}$ *production in two-photon collisions in L3 at LEP*, proceedings of PHOTON2000, Ambleside, England, August 2000 and hep-ex/0010030.

[123] ARGUS Collab., H. Albrecht *et al.*, *Z. Phys.* **C 48** (1990) 183.

[124] S. Braccini, *Resonance formation in two-photon collisions with the L3 detector at LEP*, Proceedings of *Photon '97*, Egmond aan Zee, The Netherlands, May 1997, A. Buijs and F. C. Erné editors, p. 232, World Scientific;
S. Braccini, L3 Note 2422f, June 1999.

[125] K. Peters and E. Klempt, *Phys. Lett.* **352 B** (1995) 467.

[126] E690 Collab., M. A. Reyes *et al.*, *Phys. Rev. Lett.* **81** (1998) 4079.

[127] D. V. Bugg *et al.*, *Phys. Lett.* **B 353** (1995) 378.

[128] Yu. P. Gorin, *Nucl. Phys.* **B 309** (1988) 426.

[129] BES Collab., J. Z. Bai *et al.*, *Phys. Rev. Lett.* **77** (1996) 3959.

[130] Crystal Ball Collab., C. Edwards *et al.*, *Phys. Rev. Lett.* **48** (1982) 458.

[131] Mark III Collab., R. M. Baltrusaitis *et al.*, *Phys. Rev.* **D 35** (1987) 2077.

[132] WA76 Collab., T. A. Armstrong *et al.*, *Phys. Lett.* **B 227** (1989) 186.

[133] WA102 Collab., D. Barberis *et al.*, *Phys. Lett.* **B 453** (1999) 305.

[134] M. Heinzelmann, Ph.D. thesis, University of Zürich, Switzerland, 2000.

[135] A. V. Anisovich, private communication.

[136] O. Helene, *Nucl. Instr. Meth.* **212** (1983) 319.